

การสังเคราะห์และพิสูจน์เอกลักษณ์ของโครงอินทรีย์-โลหะฐานพอร์ไฟรินสำหรับการดูดซับแก๊ส

นางสาวสลิลทิพย์ เล่าห์เกริกเกียรติ

วิทยานิพนธ์นี้เป็นส่วนหนึ่งของการศึกษาตามหลักสูตรปริญญาวิทยาศาสตรมหาบัณฑิต

สาขาวิชาปิโตรเคมีและวิทยาศาสตร์พอลิเมอร์

คณะวิทยาศาสตร์ จุฬาลงกรณ์มหาวิทยาลัย

ปีการศึกษา 2554

ลิขสิทธิ์ของจุฬาลงกรณ์มหาวิทยาลัย

บทคัดย่อและแฟ้มข้อมูลฉบับเต็มของวิทยานิพนธ์ตั้งแต่ปีการศึกษา 2554 ที่ให้บริการในคลังปัญญาจุฬาฯ (CUIR)

เป็นแฟ้มข้อมูลของนิสิตเจ้าของวิทยานิพนธ์ที่ส่งผ่านทางบัณฑิตวิทยาลัย

The abstract and full text of theses from the academic year 2011 in Chulalongkorn University Intellectual Repository (CUIR)

are the thesis authors' files submitted through the Graduate School.

SYNTHESIS AND CHARACTERIZATION OF PORPHYRIN-BASED  
METAL-ORGANIC FRAMEWORKS FOR GAS ADSORPTION

Miss Salinthip Laokroekkiat

A Thesis Submitted in Partial Fulfillment of the Requirements  
for the Degree of Master of Science Program in Petrochemistry and Polymer Science  
Faculty of Science  
Chulalongkorn University  
Academic Year 2011  
Copyright of Chulalongkorn University

Thesis Title                   SYNTHESIS AND CHARACTERIZATION OF PORPHYRIN  
  -BASED METAL-ORGANIC FRAMEWORKS FOR GAS  
  ADSORPTION  
By                                 Miss Salinthip Laokroekkiat  
Field of Study                 Petrochemistry and Polymer Science  
Thesis Advisor                Associate Professor Buncha Pulpoka, Ph.D.  
Thesis Co-advisor            Duangamol Tungasmita, Ph.D.

---

Accepted by the Faculty of Science, Chulalongkorn University in Partial  
Fulfillment of the Requirements for the Master's Degree

..... Dean of the Faculty of Science  
(Professor Supot Hannongbua, Dr.rer.nat.)

#### THESIS COMMITTEE

.....Chairman  
(Associate Professor Supawan Tantayanon, Ph.D.)

.....Thesis Advisor  
(Associate Professor Buncha Pulpoka, Ph.D.)

.....Thesis Co-advisor  
(Duangamol Tungasmita, Ph.D.)

.....Examiner  
(Associate Professor Mongkol Sukwattanasinitt, Ph.D.)

.....External Examiner  
(Assistant Professor Ekasith Somsook, Ph.D.)

สถลิตทิพย์ เล่าห์เกริกเกียรติ : การสังเคราะห์และพิสูจน์เอกลักษณ์ของโครงอินทรีย์-โลหะ  
 ฐานพอร์ไฟรินสำหรับการดูดซับแก๊ส . (SYNTHESIS AND CHARACTERIZATION OF  
 PORPHYRIN-BASED METAL-ORGANIC FRAMEWORKS FOR GAS  
 ADSORPTION) อ.ที่ปรึกษาวิทยานิพนธ์หลัก : รศ. ดร.บัญญัติ พูลโกคา , อ.ที่ปรึกษา  
 วิทยานิพนธ์ร่วม : อ.ดร. ดวงกมล ตุงคะสมิต, 190 หน้า.

ในงานวิจัยนี้เกี่ยวข้องกับการสังเคราะห์สารประกอบพอร์ไฟรินเพื่อนำไปใช้ในการ  
 สังเคราะห์โครงอินทรีย์-โลหะฐานพอร์ไฟริน ส่วนแรกจะพิจารณาไปที่การสังเคราะห์อนุพันธ์ของ  
 พอร์ไฟรินซึ่งได้แก่ dicarboxyphenylporphyrin, 1,4-phenylene-bridged *meso-meso* linked  
 diporphyrin, *meso-meso*  $\beta-\beta$   $\beta-\beta$  triply linked (fused) diporphyrin และ  
 tetracarboxybiphenylporphyrin แต่อย่างไรก็ตามมีเฉพาะอนุพันธ์พอร์ไฟรินตัวสุดท้ายเท่านั้น  
 ที่นำมาใช้เป็นสารเชื่อมอินทรีย์ในการสังเคราะห์โครงอินทรีย์-โลหะ โดยใช้ซึ่งคี่ในเดรตหรือคอป  
 เปอร์ในเดรต และใช้ไดเมทิลพอร์มาไมด์เป็นตัวทำละลาย เปรียบเทียบระหว่างระบบที่มีและไม่มี  
 4,4'-bipyridine จากนั้นทำการศึกษาสัณฐานวิทยาและสมบัติในการดูดซับแก๊สของโครง  
 อินทรีย์-โลหะฐานพอร์ไฟรินที่สังเคราะห์ได้ โดยพบว่าสัณฐานวิทยาของโครงอินทรีย์-โลหะฐาน  
 พอร์ไฟรินจะแสดงเป็นอนุภาคขนาดไมครอน ซึ่งมีรูปร่างต่างๆกัน ทั้งแบบแท่ง ลูกบาศก์และ  
 แบบเกล็ด ไอโซเทอร์มของการดูดซับแก๊สไนโตรเจนเป็นแบบที่ 1 ซึ่งเป็นลักษณะเฉพาะสำหรับ  
 วัสดุรูพรุนที่มีขนาดเล็ก โดยมีพื้นที่ผิวอยู่ในช่วง 400-600 ตารางเมตรต่อกรัม และการกระจาย  
 ขนาดของรูพรุนค่อนข้างแคบโดยที่มีขนาดเส้นผ่าศูนย์กลางของรูพรุนเป็น 0.6 นาโนเมตร  
 นอกจากนี้ความทนต่อความร้อนของวัสดุนี้จะอยู่ที่อุณหภูมิไม่เกิน 300 องศาเซลเซียส การ  
 สังเคราะห์โครงอินทรีย์-โลหะฐานพอร์ไฟรินโดยใช้วิธี B เป็นวิธีที่ดีที่สุด ซึ่งใช้ พอร์ไฟรินที่มีโลหะ  
 อยู่กลางวงพอร์ไฟรินเป็นสารเชื่อมอินทรีย์ และใช้ 4,4'-bipyridine เป็นตัวเชื่อมระหว่างระนาบ  
 ของพอร์ไฟรินซึ่งจะช่วยลดการรวมตัวของพอร์ไฟริน และทำให้ได้โครงอินทรีย์-โลหะที่มีสมบัติที่ดี

สาขาวิชา...ปิโตรเคมีและวิทยาศาสตร์พอลิเมอร์ ลายมือชื่อนิสิต.....  
 ปีการศึกษา.....2554..... ลายมือชื่ออ.ที่ปรึกษาวิทยานิพนธ์หลัก.....  
 ลายมือชื่ออ.ที่ปรึกษาวิทยานิพนธ์ร่วม.....

# # 5172489623 : PETROCHEMISTRY AND POLYMER SCIENCE

KEYWORDS: PORPHYRIN / METAL-ORGANIC FRAMEWORK / GAS  
ADSORPTION

SALINTHIP LAOKROEKKIAT : SYNTHESIS AND  
CHARACTERIZATION OF PORPHYRIN-BASED METAL-ORGANIC  
FRAMEWORKS FOR GAS ADSORPTION ADVISOR : ASSOC. PROF.  
BUNCHA PULPOKA, Ph.D., CO-ADVISOR : DUANGAMOL  
TUNGASMITA, Ph.D., 190 pp.

In this research, synthesis of porphyrinic linkers, porphyrin-based Metal-Organic Frameworks construction and their physical properties were concerned. For the first one, four porphyrin derivatives, including dicarboxyphenylporphyrin, 1,4-phenylene-bridged *meso-meso* linked diporphyrin, *meso-meso*  $\beta$ - $\beta$   $\beta$ - $\beta$  triply linked (fused) diporphyrin and tetracarboxybiphenylporphyrin were synthesized. However, only the last porphyrin derivative was used as organic linker for MOFs synthesis in the presence of  $M(NO_3)_2$  (M= Zn, Cu) with or without 4,4'-bipyridine (as pillar) by using dimethylformamide as solvent. The obtained porphyrin-based MOFs were investigated their morphologies and gas adsorption properties for the potential use in gas storage. Morphology of synthesized MOFs exhibited as micro-particles of MOFs in various forms, such as cubic, rod and platelet shapes. The nitrogen adsorption-desorption isotherms performed as type I adsorption isotherm which was typical for microporous materials. Total specific surface areas were in range 400-600  $m^2/g$  and the quite narrow pore size distribution was found with the average pore diameter of 0.6 nm. Moreover, the stability of this framework was investigated by TGA with the temperature not over than 300°C. It should be concluded that the synthesized MOFs via pathway B, using M-TCBPP as organic linkers with 4,4'-bipyridine as a pillar between the porphyrin plane, was the suitable pathway to synthesize MOFs.

Field of Study: Petrochemistry and Polymer science Student's Signature.....

Academic Year: .....2011..... Advisor's Signature.....

Co-advisor's Signature.....

## ACKNOWLEDGEMENTS

I would like to begin by thanking Associate Professor Dr. Buncha Pulpoka and Dr. Duangamol Tungasmita for being the best advisors anyone could ever ask for. There no words that can express the depth of gratitude that I have toward them. They have supported me in everything that I set out to improve the synthetic skills, believe in me even at the moment of my life when I was down and help me to get back on my feet.

I also grateful to Associate Professor Dr. SupawanTuntayanon, for serving as the chairman, Associate Professor Mongkol Sukwattanasinitt and Assistant Professor Ekasith Somsook for serving as the members of my thesis committee, respectively, for their valuable suggestion and comments. Moreover, I also thank for Associate Professor Dr. Nongnuch Muangsin for solving the single crystal structure of my synthesized compound.

I would like to thank The National Center of Excellence for Petroleum, Petrochemicals and Advanced Materials (NCE-PPAM), The Center of Innovative Nanotechnology and graduate school of Chulalongkorn university for partial financial support of this research.

I also thank Supramolecular Chemistry Research Unit (SCRU), especially Professor Dr. Thawatchai Tuntulani for warm welcome into their family, great experience and laboratory facilities. I feel blessed and very privileged to have joined a group with great members who supported me throughout this course.

Finally, I am grateful to my family and my friends, especially Preecha Thiampunya, Preeyanut Duanglaor, Anusak Chaicham, Nutthaporn Labeung and Supachai Krajangsri for their love, understanding and great encouragement the entire course of my study.

# CONTENTS

	<b>Page</b>
<b>ABSTRACT (THAI)</b> .....	iv
<b>ABSTRACT (ENGLISH)</b> .....	v
<b>ACKNOWLEDGEMENTS</b> .....	vi
<b>CONTENTS</b> .....	vii
<b>LIST OF TABLES</b> .....	xiv
<b>LIST OF FIGURES</b> .....	xv
<b>LIST OF SCHEMES</b> .....	xxii
<b>LIST OF ABBREVIATIONS</b> .....	xxiii
<b>CHAPTER I INTRODUCTION</b> .....	1
1.1 Objectives of Research.....	3
1.2 Scope of Research.....	5
<b>CHAPTER II THEORY AND LITERATURE REVIEWS</b> .....	6
<b>THEORY</b> .....	6
2.1 Coordination polymer and Metal-Organic Frameworks (MOFs) .....	6
2.1.1 Coordination polymers .....	6
2.1.2 Metal-Organic Frameworks (MOFs) .....	8
2.1.2.1 Factors influencing on topologies and properties of MOFs .....	9
2.1.2.1.1 Metallic node .....	9
2.1.2.1.2 Organic linker .....	10
2.1.2.1.3 Secondary building unit or SBU .....	14
2.1.2.1.4 Parameters for MOFs synthesis .....	16
2.1.2.1.4.1 Metal salt .....	16
2.1.2.1.4.2 Metal to ligand ratio .....	17
2.1.2.1.4.3 Solvent .....	18
2.1.2.1.4.4 Concentration of reaction mixture ...	19
2.1.2.1.4.5 pH of reaction mixture .....	20
2.1.2.1.4.6 Reaction temperature and time .....	21

	<b>Page</b>
2.1.2.1.4.7 Synthetic method .....	21
2.1.2.1.4.7.1 Diffusion .....	21
2.1.2.1.4.7.2 Hydro/solvothermal .....	22
2.1.2.1.4.7.3 Microwave-assisted .....	23
2.1.2.1.4.7.4 Mechanochemical .....	23
2.1.2.2 Characterization of MOFs .....	24
2.1.2.2.1 Powder X-Ray Diffraction (XRD) .....	24
2.1.2.2.2 Scanning Electron Microscopy (SEM) .....	26
2.1.2.2.3 Nitrogen Adsorption-Desorption Isotherm .....	26
2.1.2.2.4 Fourier Transform Infrared Spectroscopy (FT-IR) .....	31
2.1.2.2.5 CHNS/O Elemental analysis (EA) .....	32
2.1.2.2.6 Thermogravimetric Analysis (TGA) .....	32
2.1.2.3 Application of MOFs .....	33
2.1.2.3.1 Gas storage .....	33
2.1.2.3.1.1 Adsorption force .....	34
2.1.2.3.1.2 Factors influencing on H <sub>2</sub> storage in MOFs .....	37
2.1.2.3.1.2.1 Surface area and pore volume.....	37
2.1.2.3.1.2.2 Pore size .....	38
2.1.2.3.1.2.3 Accessible metal site...	39
2.1.2.3.1.2.4 Polarizable ligand .....	40
2.1.2.3.2 Gas separation .....	41
2.1.2.3.3 Catalysis .....	42
2.1.2.3.4 Luminescence .....	43
2.1.2.3.5 Drug delivery .....	44
2.2 Porphyrin .....	44
2.2.1 Structure and nomenclature of porphyrins .....	45
2.2.2 Synthetic approach of Porphyrin .....	46



	<b>Page</b>
2.2.2.1 Synthesis of porphyrins via monopyrrole tetramerization	46
2.2.2.2 Synthesis of porphyrins via dipyrromethanes .....	48
2.2.3 Reactions of porphyrins .....	49
2.2.4 Spectroscopic properties of porphyrins and their derivatives ....	51
2.2.5 Complexation of porphyrin derivatives .....	52
2.2.6 Uses and Applications of Porphyrin Derivatives .....	53
2.2.7 Characterization of porphyrin derivatives .....	53
2.2.7.1 Nuclear Magnetic Resonance Spectroscopy (NMR) ...	53
2.2.7.2 Mass spectrometry (MS) .....	54
2.2.7.3 Ultraviolet/Visible Spectrophotometry (UV/VIS) .....	54
<b>LITERATURE REVIEWS</b> .....	55
<b>CHAPTER III EXPERIMENTAL</b> .....	60
3.1 Chemicals.....	60
3.2 Analytical Instruments.....	61
3.3 Experimental Procedure.....	63
3.3.1 <b>Part 1:</b> Synthesis of Zinc(II)-5,15-di(4-carboxyphenyl)-10,20-diphenylporphyrin (Zn-DCPP) .....	64
3.3.1.1 Synthesis of 5-phenyldipyrromethane ( <b>1</b> ) .....	65
3.3.1.2 Synthesis of Zinc(II)-5,15-di(4-carboxyphenyl)-10,20-diphenylporphyrin (Zn-DCPP, <b>2</b> ) .....	66
3.3.2 <b>Part 2:</b> Synthesis of 1,4-phenylene-bridged <i>meso-meso</i> linked di-5-(4-methoxycarbonylphenyl)-10,20-diphenyl porphyrin.....	68
3.3.2.1 Synthesis of 5-(4-carboxyphenyl)dipyrromethane ( <b>3</b> )	69
3.3.2.2 Synthesis of 1,4-bis(dipyrromethyl)benzene ( <b>4</b> ) .....	70
3.3.2.3 Synthesis of 1,4-phenylene-bridged <i>meso-meso</i> linked di-5-(4-methoxycarbonylphenyl)-10,20-diphenyl porphyrin ( <b>5</b> ) .....	71
3.3.3 <b>Part3:</b> Synthesis of <i>meso-meso</i> $\beta$ - $\beta$ $\beta$ - $\beta$ triply linked (fused) diporphyrin .....	72

	<b>Page</b>
3.3.3.1 Synthesis of <i>meso-meso</i> $\beta$ - $\beta$ $\beta$ - $\beta$ triply linked (fused) diporphyrin pathway I .....	72
3.3.3.1.1 Synthesis of dipyrromethane ( <b>6</b> ) .....	73
3.3.3.1.2 Synthesis of 5-(4-methoxycarbonylphenyl) dipyrromethane ( <b>7</b> ) .....	74
3.3.3.1.3 Synthesis of 5-(4-methoxycarbonylphenyl) 10,20-diphenylporphyrin ( <b>8</b> ) .....	75
3.3.3.1.4 Synthesis of Zinc(II)-5-(4-methoxycarbonyl phenyl)-10,20-diphenyl porphyrin ( <b>9</b> ) .....	76
3.3.3.1.5 Synthesis of <i>meso-meso</i> $\beta$ - $\beta$ $\beta$ - $\beta$ triply linked (fused) di-Zinc(II)-5-(4-methoxycarbonyl phenyl)-10,20-diphenylporphyrin ( <b>10</b> ) .....	77
3.3.3.2 Synthesis of <i>meso-meso</i> $\beta$ - $\beta$ $\beta$ - $\beta$ triply linked (fused) diporphyrin pathway II .....	78
3.3.3.2.1 Synthesis of 10,20-diphenyl porphyrin (H <sub>2</sub> DPP, <b>11</b> ) .....	79
3.3.3.2.2 Synthesis of 5-bromo-10,20-diphenyl porphyrin (H <sub>2</sub> DPP(Br), <b>12</b> ) .....	80
3.3.3.2.3 Synthesis of 5-(4-methoxycarbonyl phenyl)-10,20-diphenylporphyrin ( <b>8</b> ) .....	81
3.3.4 <b>Part 4:</b> Synthesis of tetracarboxybiphenylporphyrin derivative	82
3.3.4.1 Synthesis of 5,10,15,20-Tetra(4-bromophenyl) porphyrin (TPPBr, <b>13</b> ) .....	83
3.3.4.2 Synthesis of 5,10,15,20-Tetra(4-ethoxycarbonyl biphenyl)porphyrin (TEBPP, <b>14</b> ) .....	84
3.3.4.3 Synthesis of 5,10,15,20-Tetra(4-carboxybiphenyl) porphyrin (TCBPP, <b>15</b> ) .....	85
3.3.4.4 Synthesis of Zinc(II)-5,10,15,20-Tetra(4-ethoxy carbonylbiphenyl)porphyrin (Zn-TEBPP, <b>16</b> ).....	86

	<b>Page</b>
3.3.4.5 Synthesis of Copper(II)-5,10,15,20-Tetra(4-ethoxy carbonylbiphenyl)porphyrin (Cu-TEBPP, <b>17</b> ) .....	87
3.3.4.6 Synthesis of Zinc(II)-5,10,15,20-Tetra(4-carboxy biphenyl)porphyrin (Zn-TCBPP, <b>18</b> ) .....	88
3.3.4.7 Synthesis of Copper(II)-5,10,15,20-Tetra(4-carboxy biphenyl)porphyrin (Cu-TCBPP, <b>19</b> ) .....	89
3.3.4.8 Synthesis of Complex of Zinc(II)-5,10,15,20-Tetra(4-ethoxycarbonylbiphenyl)porphyrin with 4,4'-bipyridine ([Zn-TEBPP]-bpy, <b>20</b> ) .....	90
3.3.4.9 Synthesis of Complex of Copper(II)-5,10,15,20-Tetra(4-methoxycarbonylbiphenyl) porphyrin with 4,4'-bipyridine ([Cu-TEBPP]-bpy, <b>21</b> ) .....	91
3.3.4.10 Synthesis of Complex of Zinc(II)-5,10,15,20-Tetra(4-carboxybiphenyl)porphyrin with 4,4'-bipyridine ([Zn-TCBPP]-bpy, <b>22</b> ) .....	92
3.3.4.11 Synthesis of Complex of Copper(II)-5,10,15,20-Tetra(4-carboxybiphenyl)porphyrin with 4,4'-bipyridine ([Cu-TCBPP]-bpy, <b>23</b> ) .....	93
3.3.5 <b>Part 5</b> : Synthesis of Porphyrin- based MOFs using tetracarboxybiphenylporphyrin derivatives as organic linkers .....	94
3.3.5.1 Synthesis of Porphyrin- based MOFs Pathway <b>A</b> : Using free-base porphyrin (TCBPP) as organic linker (TCBPP + M(NO <sub>3</sub> ) <sub>2</sub> .nH <sub>2</sub> O +/- bpy) .....	94
3.3.5.1.1 Synthesis of MOF <b>2A</b> and MOF <b>6A</b> .....	94
3.3.5.1.2 Synthesis of MOF <b>3A</b> and MOF <b>7A</b> .....	95
3.3.5.1.3 Synthesis of MOF <b>5A</b> and MOF <b>8A</b> .....	95
3.3.5.2 Synthesis of Porphyrin- based MOFs Pathway <b>B</b> : Using metalloporphyrin (Zn-TCBPP and Cu-TCBPP) as organic linker (M-TCBPP + M(NO <sub>3</sub> ) <sub>2</sub> .nH <sub>2</sub> O + bpy) .....	96

	<b>Page</b>
3.3.5.2.1 Synthesis of <b>10B</b> and MOF <b>13B</b> .....	97
3.3.5.2.2 Synthesis of MOF <b>11B</b> and MOF <b>14B</b> .....	97
3.3.5.2.3 Synthesis of MOF <b>12B</b> and MOF <b>15B</b> .....	98
3.3.5.3 Synthesis of Porphyrin- based MOFs Pathway <b>C</b> : Using Complex of metalloporphyrin with 4,4'- bipyridine ( [Zn-TCBPP]-bpy and [Cu-TCBPP]-bpy) as organic linker ([M-TCBPP]-bpy + M(NO <sub>3</sub> ) <sub>2</sub> .nH <sub>2</sub> O +/- bpy) .....	99
3.3.5.3.1 Synthesis of MOF <b>16C</b> , MOF <b>20C</b> , MOF <b>21C</b> and MOF <b>23C</b> .....	99
3.3.5.3.2 Synthesis of MOF <b>19C</b> and MOF <b>22C</b>	101
<b>CHAPTER IV RESULTS AND DISCUSSION</b> .....	102
4.1 <b>Part 1</b> : Synthesis of Zinc(II)-5,15-di(4-carboxyphenyl)-10,20- diphenyl porphyrin (Zn-DCPP, <b>2</b> ) .....	102
4.2 <b>Part 2</b> : Synthesis of 1,4-phenylene-bridged <i>meso-meso</i> linked di-5-(4-methoxycarbonylphenyl)-10,20-diphenyl porphyrin ( <b>5</b> ) .....	103
4.3 <b>Part 3</b> : Synthesis of <i>meso-meso</i> $\beta$ - $\beta$ $\beta$ - $\beta$ triply linked (fused) diporphyrin ( <b>10</b> ) .....	104
4.3.1 Synthesis of <i>meso-meso</i> $\beta$ - $\beta$ $\beta$ - $\beta$ triply linked (fused) diporphyrin pathway I .....	104
4.3.2 Synthesis of <i>meso-meso</i> $\beta$ - $\beta$ $\beta$ - $\beta$ triply linked (fused) diporphyrin pathway II .....	105
4.3.3 UV-Vis study of <i>meso-meso</i> $\beta$ - $\beta$ $\beta$ - $\beta$ triply linked (fused) diporphyrin ( <b>10</b> ) .....	107
4.4 <b>Part 4</b> : Synthesis of tetracarboxybiphenylporphyrin derivatives	108
4.4.1 Synthesis of 5,10,15,20-Tetra(4-ethoxycarbonylbiphenyl) porphyrin (TEBPP, <b>14</b> ) .....	108
4.4.2 Metallation of 5,10,15,20-Tetra(4-ethoxycarbonyl biphenyl)porphyrin (TEBPP, <b>14</b> ) .....	109

	<b>Page</b>
4.4.3 Hydrolysis of TEBPP ( <b>14</b> ), Zn-TEBPP ( <b>16</b> ) and Cu-TEBPP ( <b>17</b> ) .....	109
4.4.4 Complexation studies of Zn-TEBPP ( <b>16</b> ), Cu-TEBPP( <b>17</b> ), Zn-TCBPP ( <b>18</b> ) and Cu-TCBPP( <b>19</b> ) with 4,4'-bipyridine	109
4.4.4.1 NMR Spectroscopic study .....	109
4.4.4.2 IR spectroscopic study .....	112
4.4.4.3 Mass spectrometric study .....	114
4.4.4.4 UV-Vis Spectrophotometric study .....	115
4.5 <b>Part 5</b> : Synthesis of Porphyrin- based MOFs using tetracarboxy biphenyl porphyrin derivatives as organic linkers .....	118
4.5.1 IR spectroscopic study .....	118
4.5.2 XRD study .....	121
4.5.3 SEM study .....	124
4.5.4 TGA study .....	130
4.5.5 Nitrogen Adsorption-Desorption study .....	130
<b>CHAPTER V CONCLUSION</b> .....	138
<b>REFERENCES</b> .....	139
<b>APPENDICES</b> .....	151
Appendix A.....	152
Appendix B.....	178
<b>VITA</b> .....	190

**LIST OF TABLES**

<b>Table</b>		<b>Page</b>
2.1	IUPAC classification of pores .....	28
2.2	Pore types of porous materials .....	29
2.3	Comparison of physisorption and chemisorptions .....	35
3.1	Code of Porphyrin-based MOFs via pathway A .....	94
3.2	Code of Porphyrin-based MOFs via pathway B .....	96
3.3	Code of Porphyrin-based MOFs via pathway C .....	99
4.1	SEM images of synthesized MOFs and particle size .....	125
4.2	Textural properties of synthesized MOFs with pretreatment temperature at 250°C .....	131

## LIST OF FIGURES

<b>Figure</b>		<b>Page</b>
1.1	Porphyrin-based MOFs .....	4
2.1	The structures of a) nickel(II) cyanide and b) Cd(II)-(4,4'-bipyridine)	6
2.2	Typical coordination polymers based on dimensionality .....	7
2.3	The structure of crystalline[Cu(4,4'-bipyridine) <sub>1.5</sub> ].NO <sub>3</sub> (H <sub>2</sub> O) <sub>1.25</sub> .....	8
2.4	Metal ions with various coordinations .....	9
2.5	Crystal structure of a) Zn <sub>3</sub> (BDT) <sub>3</sub> ; b) Mn <sub>2</sub> (BDT)Cl <sub>2</sub> ; and c) Cu(BDT)	10
2.6	Coordination modes of carboxylate ligand .....	11
2.7	Example of carboxylate ligands for MOFs .....	12
2.8	Example of nitrogen-based ligands for MOFs .....	13
2.9	Commonly secondary building units (SBUs) .....	15
2.10	Structure of MOF-5(or IRMOF-1) .....	15
2.11	Example of Isoreticular Metal-Organic Frameworks (IRMOFs) .....	16
2.12	Influence of different zinc(II) salts on the morphology of MOF-5 .....	17
2.13	Secondary Building Unit structure of PCN-131 and PCN-132 .....	17
2.14	X-ray crystal structure of Zn <sub>3</sub> (ntb) <sub>2</sub> .....	18
2.15	X-ray crystal structure of Zn <sub>4</sub> O(NTB) <sub>2</sub> .....	19
2.16	Noninterpenetrated and interpenetrated structure of Cd(bipy)(bdc) .....	20
2.17	Layering technique and vapor diffusion technique .....	22
2.18	Teflon-lined stainless steel autoclave .....	23
2.19	Ball mill: stainless steel vessel with a ball bearing .....	24
2.20	Schematic representation of X-Ray Diffraction .....	25
2.21	Example of Crystal structure and XRD pattern of PPF-4(Zn) .....	25
2.22	Example of SEM image of MOF-5 .....	26
2.23	Six types of adsorption isotherm .....	27
2.24	Example of IR spectrum of PPF-4 .....	32

<b>Figure</b>	<b>Page</b>
2.25	Example of Thermogravimetric analysis curve (TGA) of PPF-4 ..... 33
2.26	Proposed five binding sites for adsorbed argon in IRMOF-1 ..... 34
2.27	Schematic representation of temporary dipole in atom and electrostatic attraction ..... 36
2.28	Schematic representation of ion induced dipole force and dipole-induced dipole force ..... 37
2.29	Correlation of MOFs between surface area with pore volume and density ..... 38
2.30	Schematic representation of the repeat unit of a MOF with secondary building units (SBUs) and interpenetration of two identical frameworks ..... 39
2.31	Impregnated MOF-177 with C <sub>60</sub> molecules ..... 39
2.32	Schematic representation of removing water ligand at the axial coordination position ..... 40
2.33	Modelling of car using MOFs as hydrogen storage material ..... 41
2.34	The GC separation of alkanes with MOF-508 ..... 41
2.35	Structures of some naturally porphyrin derivatives ..... 45
2.36	Porphyrin macrocycle ..... 46
2.37	Typical UV-visible absorption spectrum of porphyrins ..... 51
2.38	Examples of bidentate ligands ..... 52
2.39	Schematic representation of metalloporphyrin-ligand coordinations ... 53
2.40	Construction of 2D coordination networks ..... 55
2.41	Crystal structure of PIZA-4 ..... 56
2.42	Scheme of PPF-3, PPF-4 and PPF-5 ..... 57
2.43	Paddle-wheel building units, Co <sub>2</sub> (COO) <sub>4</sub> with cis-ZnDCPP and 2D layer of PPF-6 ..... 58
2.44	2D porphyrinic assembled from trans-DCPP (PPF-25) and zinc paddlewheel cluster ..... 59



<b>Figure</b>	<b>Page</b>
4.1 Crystal structure of Zinc(II)-5,15-di(4-carboxyphenyl)-10,20-diphenylporphyrin(Zn-DCPP, <b>2</b> ) .....	102
4.2 UV-vis absorption spectra of zinc porphyrin <b>9</b> and triply-fused diporphyrin <b>10</b> .....	107
4.3 By products obtained from suzuki coupling reaction of TPPBr <b>13</b> and boronic acid derivative .....	108
4.4 Compared <sup>1</sup> H NMR spectra of Zn-TEBPP ( <b>16</b> ), 4,4'-bipyridine and [Zn-TEBPP]-bpy ( <b>20</b> ) in CDCl <sub>3</sub> .....	110
4.5 Complex of zinc porphyrin with 4,4'-bipyridine .....	110
4.6 Compared <sup>1</sup> H NMR spectra of [Zn-TEBPP]-bpy ( <b>20</b> ), 4,4'-bipyridine and [Zn-TCBPP]-bpy ( <b>22</b> ) in DMSO .....	111
4.7 Compared IR spectra of 4,4'-bipyridine, Zn-TEBPP( <b>16</b> ) and [Zn-TEBPP]-bpy ( <b>20</b> ).....	112
4.8 Compared IR spectra of 4,4'-bipyridine, Cu-TEBPP( <b>17</b> ) and [Cu-TEBPP]-bpy ( <b>21</b> ) .....	113
4.9 Compared IR spectra of 4,4'-bipyridine, Zn-TCBPP( <b>18</b> ) and [Zn-TCBPP]-bpy ( <b>22</b> ) .....	113
4.10 Compared IR spectra of 4,4'-bipyridine, Cu-TCBPP( <b>19</b> ) and [Cu-TCBPP]-bpy( <b>23</b> ) .....	114
4.11 Compared IR spectra of TEBPP( <b>14</b> ) and TCBPP( <b>15</b> ) .....	114
4.12 The job's plots of the complexations of metallated porphyrins ( <b>16</b> and <b>17</b> ) with 4,4'-bipyridine in CHCl <sub>3</sub> .....	116
4.13 The job's plots of the complexations of metallated porphyrins ( <b>18</b> and <b>19</b> ) with 4,4'-bipyridine in DMSO .....	117
4.14 Compared IR spectra of TCBPP( <b>15</b> ), MOFs <b>2A</b> , <b>3A</b> and <b>5A</b> .....	118
4.15 Compared IR spectra of TCBPP( <b>15</b> ), MOFs <b>6A</b> , <b>7A</b> and <b>8A</b> .....	119
4.16 Compared IR spectra of Zn-TCBPP( <b>18</b> ), MOFs <b>10B</b> , <b>11B</b> and <b>12B</b> ...	119
4.17 Compared IR spectra of Cu-TCBPP( <b>19</b> ), MOFs <b>13B</b> , <b>14B</b> and <b>15B</b> ...	120

<b>Figure</b>	<b>Page</b>
4.18 Compared IR spectra of [Zn-TCBPP]-bpy( <b>22</b> ), MOFs <b>16C</b> , <b>19C</b> and <b>20C</b> .....	120
4.19 Compared IR spectra of [Cu-TCBPP]-bpy( <b>23</b> ), MOFs <b>21C</b> , <b>22C</b> and <b>23C</b> .....	121
4.20 XRD patterns of the synthesized MOFs presented as <b>P1</b> , <b>P2</b> , <b>P3</b> and <b>P4</b> .....	122
4.21 XRD patterns of the synthesized MOFs presented as <b>P5</b> and <b>P6</b> .....	123
4.22 XRD patterns of the synthesized MOFs presented as <b>P7</b> , <b>P8</b> and <b>P9</b> ....	124
4.23 TGA and DTG of MOF <b>16C</b> .....	13
4.24 Example of the nitrogen adsorption-desorption isotherms with high surface area and MP pore-size distribution of porphyrin-based MOFs <b>8A</b> , <b>12B</b> , <b>22C</b> , <b>16C</b> , <b>17C</b> and <b>18C</b> .....	134
4.25 The nitrogen adsorption-desorption isotherms with low surface area and MP pore-size distribution of porphyrin-based MOFs <b>6A</b> , <b>13B</b> , and <b>23C</b> .....	136
A-1 <sup>1</sup> H NMR spectrum of compound <b>1</b> .....	153
A-2 <sup>1</sup> H NMR spectrum of compound <b>2</b> .....	153
A-3 <sup>13</sup> C NMR spectrum of compound <b>2</b> .....	154
A-4 Mass spectrum of compound <b>2</b> .....	154
A-5 IR spectrum of compound <b>2</b> .....	155
A-6 Crystallographic data of compound <b>2</b> .....	156
A-7 <sup>1</sup> H NMR spectrum of compound <b>3</b> .....	157
A-8 <sup>1</sup> H NMR spectrum of compound <b>4</b> .....	157
A-9 <sup>1</sup> H NMR spectrum of compound <b>6</b> .....	158
A-10 <sup>1</sup> H NMR spectrum of compound <b>7</b> .....	158
A-11 <sup>1</sup> H NMR spectrum of compound <b>8</b> .....	159
A-12 Mass spectrum of compound <b>8</b> .....	159
A-13 <sup>1</sup> H NMR spectrum of compound <b>9</b> .....	160

<b>Figure</b>		<b>Page</b>
A-14	Mass spectrum of compound <b>9</b> .....	160
A-15	<sup>1</sup> H NMR spectrum of compound <b>10</b> .....	161
A-16	Mass spectrum of compound <b>10</b> .....	161
A-17	<sup>1</sup> H NMR spectrum of compound <b>11</b> .....	162
A-18	<sup>1</sup> H NMR spectrum of compound <b>12</b> .....	162
A-19	Mass spectrum of compound <b>12</b> .....	163
A-20	<sup>1</sup> H NMR spectrum of compound <b>13</b> .....	163
A-21	<sup>13</sup> C NMR spectrum of compound <b>13</b> .....	164
A-22	Mass spectrum of compound <b>13</b> .....	164
A-23	<sup>1</sup> H NMR spectrum of compound <b>14</b> .....	165
A-24	<sup>13</sup> C NMR spectrum of compound <b>14</b> .....	165
A-25	Mass spectrum of compound <b>14</b> .....	166
A-26	<sup>1</sup> H-NMR spectrum of compound <b>15</b> .....	166
A-27	<sup>13</sup> C NMR spectrum of compound <b>15</b> .....	167
A-28	Mass spectrum of compound <b>15</b> .....	167
A-29	<sup>1</sup> H NMR spectrum of compound <b>16</b> .....	168
A-30	Mass spectrum of compound <b>16</b> .....	168
A-31	Mass spectrum of compound <b>17</b> .....	169
A-32	<sup>1</sup> H NMR spectrum of compound <b>18</b> .....	169
A-33	<sup>13</sup> C NMR spectrum of compound <b>18</b> .....	170
A-34	Mass spectrum of compound <b>18</b> .....	170
A-35	Mass spectrum of compound <b>19</b> .....	171
A-36	<sup>1</sup> H NMR spectrum of compound <b>20</b> in CDCl <sub>3</sub> .....	171
A-37	<sup>13</sup> C NMR spectrum of compound <b>20</b> in CDCl <sub>3</sub> .....	172
A-38	<sup>1</sup> H NMR spectrum of compound <b>20</b> in DMSO .....	172
A-39	Mass spectrum of compound <b>20</b> .....	173
A-40	Mass spectrum of compound <b>21</b> .....	173

<b>Figure</b>		<b>Page</b>
A-41	<sup>1</sup> H NMR spectrum of compound <b>22</b> .....	174
A-42	<sup>13</sup> C NMR spectrum of compound <b>22</b> .....	174
A-43	Mass spectrum of compound <b>22</b> .....	175
A-44	Mass spectrum of compound <b>23</b> .....	175
A-45	<sup>1</sup> H NMR spectrum of 4,4'-bipyridine in CDCl <sub>3</sub> .....	176
A-46	<sup>13</sup> C NMR spectrum of 4,4'-bipyridine in CDCl <sub>3</sub> .....	176
A-47	<sup>1</sup> H NMR spectrum of 4,4'-bipyridine in DMSO .....	177
A-48	<sup>13</sup> C NMR spectrum of 4,4'-bipyridine in DMSO .....	177
B-1	SEM image of MOF <b>2A</b> with magnification 2,000x .....	179
B-2	SEM image of MOF <b>3A</b> with magnification 500x .....	179
B-3	SEM image of MOF <b>5A</b> with magnification 1,600x .....	180
B-4	SEM image of MOF <b>8A</b> with magnification 10,000x .....	180
B-5	SEM image of MOF <b>10B</b> with magnification 4,000x .....	181
B-6	SEM image of MOF <b>11B</b> with magnification 4,000x .....	181
B-7	SEM image of MOF <b>12B</b> with magnification 6,000x .....	182
B-8	SEM image of MOF <b>13B</b> with magnification 10,000x .....	182
B-9	SEM image of MOF <b>14B</b> with magnification 20,000x .....	183
B-10	SEM image of MOF <b>15B</b> with magnification 6,000x .....	183
B-11	SEM image of MOF <b>16C</b> with magnification 10,000x .....	184
B-12	SEM image of MOF <b>19C</b> with magnification 3,000x .....	184
B-13	SEM image of MOF <b>20C</b> with magnification 4,000x .....	185
B-14	SEM image of MOF <b>21C</b> with magnification 16,000x .....	185
B-15	SEM image of MOF <b>22C</b> with magnification 8,000x .....	186
B-16	SEM image of MOF <b>23C</b> with magnification 8,000x .....	186
B-17	Nitrogen adsorption-desorption isotherm of porphyrin-based MOFs synthesized via pathway A: <b>2A</b> , <b>3A</b> , <b>5A</b> and <b>7A</b> .....	187

<b>Figure</b>		<b>Page</b>
B-18	MP pore-size distribution of porphyrin-based MOFs synthesized via pathway A: <b>2A</b> , <b>3A</b> , <b>5A</b> and <b>7A</b> .....	187
B-19	Nitrogen adsorption-desorption isotherm of porphyrin-based MOFs synthesized via pathway B: <b>10B</b> , <b>11B</b> , <b>14B</b> and <b>15B</b> .....	188
B-20	MP pore-size distribution of porphyrin-based MOFs synthesized via pathway B: <b>10B</b> , <b>11B</b> , <b>14B</b> and <b>15B</b> .....	188
B-21	Nitrogen adsorption-desorption isotherm of porphyrin-based MOFs synthesized via pathway C: <b>19C</b> , <b>20C</b> and <b>21C</b> .....	189
B-22	MP pore-size distribution of porphyrin-based MOFs synthesized via pathway C: <b>19C</b> , <b>20C</b> and <b>21C</b> .....	189

## LIST OF SCHEMES

Scheme	Page
2.1 Hydrolysis of DMF generating dimethylammonium ions .....	19
2.2 A unit cell of ZnPO-MOF .....	42
2.3 Synthetic reaction of ZnPO-MOF .....	42
2.4 Mechanism of acyl transfer using ZnPO-MOF as catalyst .....	43
2.5 Emission possibilities in a porous MOF .....	43
2.6 General scheme for using MOFs as drug delivery vehicles .....	44
2.7 Formation of TPP under Rothmund condition .....	47
2.8 Synthesis of TPP using Adler-Longo's procedure .....	47
2.9 Synthesis of TPP using Lindsey's procedure .....	48
2.10 Synthesis of porphyrin from dipyrromethane and aldehyde .....	48
2.11 Bromination and Suzuki coupling reaction of porphyrin .....	49
2.12 Metallation of porphyrin .....	50
2.13 Schematic representation of extended $\pi$ -electronic conjugated systems	51
3.1 Synthesis of Zinc porphyrin derivative ( <b>2</b> ) .....	64
3.2 Synthesis of 1,4-phenylene-bridged <i>meso-meso</i> linked diporphyrin ( <b>5</b> )	68
3.3 Synthesis of <i>meso-meso</i> $\beta$ - $\beta$ $\beta$ - $\beta$ triply linked (fused) diporphyrin ( <b>10</b> )	72
3.4 Synthesis of porphyrin derivative ( <b>8</b> ) .....	78
3.5 Synthesis of tetracarboxybiphenylporphyrin derivatives .....	82
4.1 Undesired products from synthesis of 1,4-phenylene-bridged <i>meso-meso</i> linked diporphyrin .....	103
4.2 Synthesis of 5-(4-methoxycarbonylphenyl)-10,20-diphenylporphyrin ( <b>8</b> ) .....	105
4.3 Product obtained from bromination of 5,15-diphenylporphyrin ( <b>11</b> )	106

**LIST OF ABBREVIATIONS**

$\lambda_{\text{abs}}$	:	absorption wavelength
CH <sub>3</sub> COOH	:	acetic acid
$\beta$	:	beta position
bpy	:	4,4'-bipyridine
PIFA	:	[bis(trifluoroacetoxy)iodo]benzene
br	:	broad (NMR)
BET	:	brunauer-emmett-teller
calcd	:	calculated
<sup>13</sup> C NMR	:	carbon-13 nuclear magnetic resonance spectroscopy
$\delta$	:	chemical shift
CHCl <sub>3</sub>	:	chloroform
Cu(OAc) <sub>2</sub>	:	copper acetate
Cu(NO <sub>3</sub> ) <sub>2</sub>	:	copper nitrate
<i>J</i>	:	coupling constant
cm <sup>3</sup> /g	:	cubic centimeter per gram
°C	:	degree Celsius
CDCl <sub>3</sub>	:	deuterated chloroform
MeOD	:	deuterated methanol
DEF	:	diethylformamide
DTG	:	differential thermogravimetric analysis
DMF	:	dimethylformamide
d	:	doublet (NMR)
dd	:	doublet of doublet (NMR)
EA	:	elemental analysis
EtOH	:	ethanol
EtOAc	:	ethyl acetate
FT-IR	:	fourier transform infrared spectroscopy
g	:	gram (s)
DMSO	:	hexadeuterated dimethylsulfoxide

Hz	:	hertz (s)
h	:	hour (s)
HCl	:	hydrochloric acid
IRMOF	:	isoreticular metal-organic framework
K	:	kelvin
MS	:	mass spectrometry
m/z	:	mass to charge
MALDI-TOF-MS	:	matrix-assisted laser desorption ionization mass spectrometry
MOF	:	metal-organic framework
m <sup>2</sup> /g	:	meter square per gram
MeOH	:	methanol
CH <sub>2</sub> Cl <sub>2</sub>	:	methylene chloride
μL	:	microliter (s)
μm	:	micrometer
mL	:	milliliter (s)
mg	:	milligram (s)
mmol	:	millimole (s)
min	:	minute
M	:	molar
m	:	multiplet (NMR)
NBS	:	N-bromosuccinimide
N <sub>2</sub>	:	nitrogen gas
nm	:	nanometer
obsd	:	observed
Pd(PPh <sub>3</sub> ) <sub>4</sub>	:	Tetrakis(triphenylphosphine)palladium(0)
ppm	:	parts per million
KBr	:	potassium bromide
K <sub>2</sub> CO <sub>3</sub>	:	potassium carbonate
KOH	:	potassium hydroxide
P	:	pressure
<sup>1</sup> H-NMR	:	proton nuclear magnetic resonance spectroscopy



q	:	quartet (NMR)
rt	:	room temperature
SBU	:	secondary building unit
s	:	singlet (NMR)
NaBH <sub>4</sub>	:	sodium borohydride
NaHCO <sub>3</sub>	:	sodium hydrogencarbonate
NaOH	:	sodium hydroxide
Na <sub>2</sub> SO <sub>4</sub>	:	sodium sulfate
T	:	temperature
θ	:	theta
TLC	:	thin layer chromatography
TEA	:	triethylamine
TFA	:	trifluoroacetic acid
THF	:	tetrahydrofuran
TGA	:	Thermogravimetric Analysis
TEA	:	triethylamine
t	:	triplet
UV/Vis	:	ultraviolet and visible spectrophotometry
v/v	:	volume by volume
SEM	:	scanning electron microscopy
XRD	:	x-ray diffraction
Zn(OAc) <sub>2</sub>	:	zinc acetate
Zn(NO <sub>3</sub> ) <sub>2</sub>	:	zinc nitrate

# CHAPTER I

## INTRODUCTION

Global economies and industries grow rapidly, thus the demand for energy is increased. Even though the government has supported to use alternative fuel such as biodiesel, compressed natural gas (CNG), liquefied petroleum gas (LPG), these carbonic fossil fuels also cause greenhouse gases that contribute to global warming. Several sustainable energy, especially the renewable energy such as wind, water and solar energy has been interesting for the future.

Jules Verne<sup>(1)</sup>, one of the world's greatest visionaries, wrote in 1874 in *The Mysterious Island* “I believe that water will one day be employed as fuel, that hydrogen and oxygen which constitute it, used singly or together will furnish an inexhaustible source of heat and light of an intensity of which coal is not capable...water will be coal of the future”. At the present, what he said comes true. Fuel cell technology<sup>(2)</sup> is one of the most interesting approaches to replace gasoline and diesel engines. This device can generate the electric power by chemical reaction between hydrogen and oxygen. However, hydrogen storage for fuel cell is a great challenge for development commercializing hydrogen powered vehicles. Many researchers seek for highly efficient and practical hydrogen storage methods<sup>(3)</sup>. Two different hydrogen storage technologies are conventionally used *i.e.* hydrogen gas in high pressure tanks made of steel and liquid hydrogen in cryogenic vessels. Both technologies possess disadvantages for mobile applications. Hydrogen gas occupies large volumes at room temperature and high pressures to be necessary to reach high storage capacities. Liquid hydrogen is successfully used for space shuttles propulsion, however the low condensation temperature about 20 K, the energy required for liquefaction is necessary at this temperature which is disadvantage for vehicles.

Thus an alternative solution is hydrogen storage in solid materials. There are two storage mechanisms of hydrogen storage which are chemisorption and physisorption. The chemisorption uses metal hydrides or complex hydride as a source of hydrogen gas while the physisorption normally employs porous materials to adsorb

hydrogen gas. Though physisorption exhibits several advantages over chemisorptions such as reversibility and fast kinetics, temperatures about 80 K are necessary to reach high storage capacities in physisorption due to weak interaction forces. Though room temperature hydrogen storage technologies are more desirable in vehicles, cryogenic tanks working at 80 K are easier to manage than hydrogen liquefaction at 20 K.

The well-known highly porous materials for storing hydrogen by physisorption are carbon materials, zeolites and metal-organic frameworks (MOFs).

Carbon nanostructures (CNT)<sup>(4)</sup> consist of benzene-like carbon hexagons with  $sp^2$ -hybridized carbon atoms with a cylindrical nanostructure. Although CNT can store hydrogen gas, synthesis of this material is still difficult with extremely high technology and high cost.

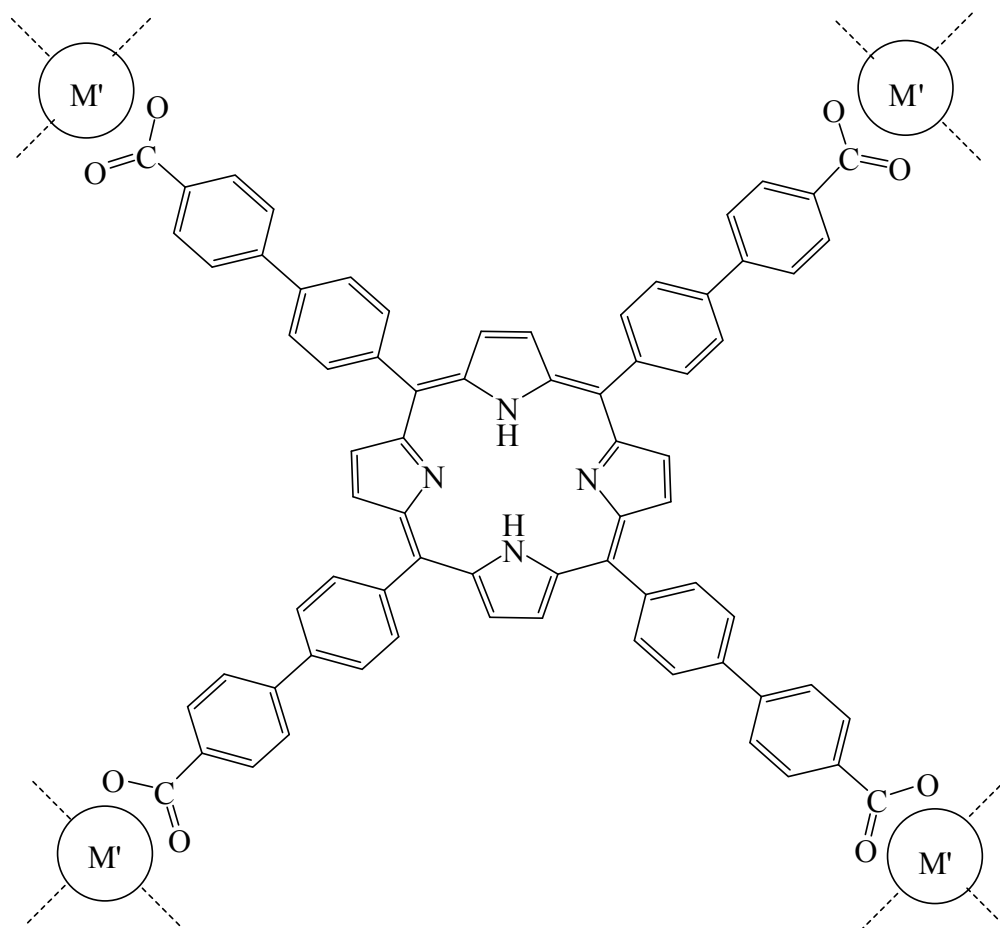
Zeolites<sup>(5)</sup> are porous materials with three dimensional silicate structures composing of  $TO_4$  ( $T = Si^{4+}$  and  $Al^{3+}$ ). Most of them are synthesized by hydrothermal crystallization of aluminosilicate gels. Zeolites are thermally stable and resistant under harsh chemical conditions.

Metal-organic frameworks (MOFs)<sup>(6)</sup> are the inter-penetrating network containing high porosity and large specific surface areas. MOFs are solid structures which compose of metal clusters and organic linkers such as dicarboxylate or bipyridyl compounds. Two compositions of MOFs play an important role in directing the topology and properties of framework. MOFs have an advantage over zeolites as they can be designed with specific chemical properties and a desired topology determined by building blocks, the coordination number or geometry of metals. Not only for gas storage, but MOFs also use in other applications such as gas purification, gas separation, heterogeneous catalysis and as sensor.

Porphyrin is one of the most popular supramolecular molecule which is flat and rigid structure. Porphyrins contain a lot of  $\pi$ -electron which can polarize molecular hydrogen resulting to the higher property to store gas. The gas storage capacity of MOFs depends on metal cluster, pore size and surface area. By keeping these factors in mind, porphyrinic compound<sup>(7)</sup> is being synthesized to use as organic linker for construction of new MOFs called porphyrin-based MOFs<sup>(8)</sup>.

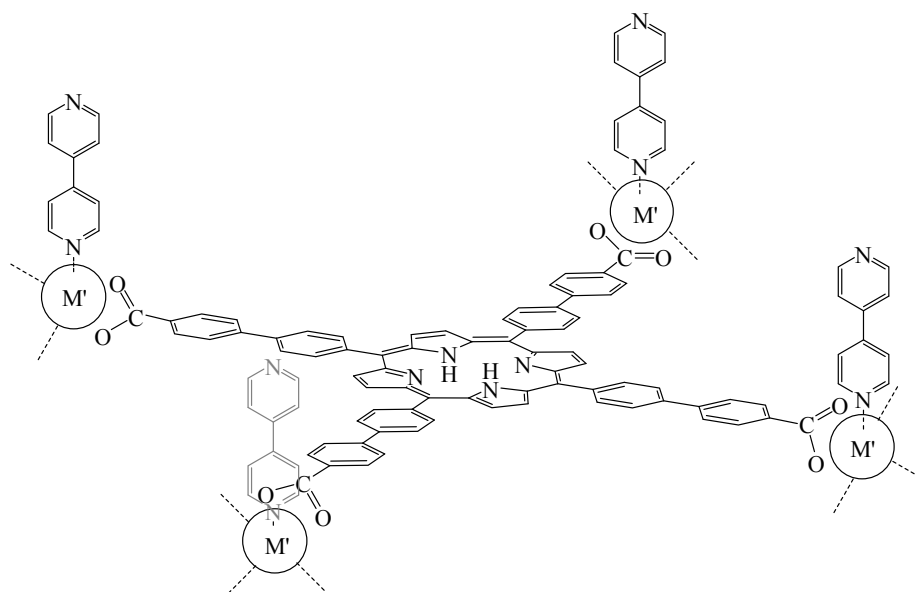
## 1.1 Objectives of Research

The objectives of this research are to synthesize porphyrin-based MOFs **1–6** (Figure 1.1), and to investigate their gas adsorption properties and morphology for the potential use in gas storage.



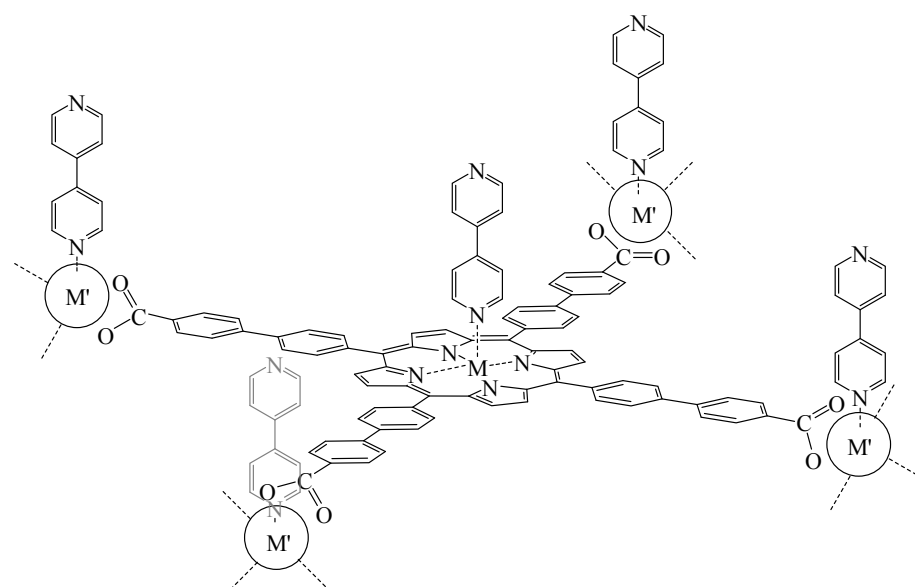
**1** : L-Zn ; M' = Zn

**2** : L-Cu ; M' = Cu



**3 : L-Zn-bpy ;  $M' = \text{Zn}$**

**4 : L-Cu-bpy ;  $M' = \text{Cu}$**



**5 : ZnL-Zn-bpy ;  $M \text{ and } M' = \text{Zn}$**

**6 : CuL-Cu-bpy ;  $M \text{ and } M' = \text{Cu}$**

**Figure 1.1** Porphyrin-based MOFs.

## 1.2 Scope of Research

The scope of this research covers the synthesis of porphyrin-based MOFs containing 5,10,15,20-Tetra(4-carboxybiphenyl)porphyrin (TCBPP) as organic linker. The synthesis of MOFs includes two steps. The first step is a synthesis of organic linkers including free base, their zinc and copper complexes. The second step concerns a construction of porphyrin-based MOFs from TCBPP and  $M(NO_3)_2$  ( $M = Zn, Cu$ ) with or without 4,4'-bipyridine (as a pillar) by using dimethylformamide as solvent. The 4,4'-bipyridine using as a spacer between the porphyrin plane may reduce the stacking of TCBPP in the framework and maybe increase surface area of the framework.

These organic compounds will be fully characterized by spectroscopic techniques, *i.e.*  $^1H$  NMR and  $^{13}C$  NMR spectroscopy, mass spectrometry and UV-Visible spectrophotometry. The gas adsorption properties and morphology of all porphyrin-based MOFs were investigated to evaluate their potential of being used in gas storage using Nitrogen adsorption-desorption isotherm, Powder X-ray diffraction (PXRD), Scanning electron microscopy (SEM), Fourier Transform Infrared Spectroscopy (FT-IR) and Thermogravimetric Analysis (TGA).

## CHAPTER II

### THEORY AND LITERATURE REVIEWS

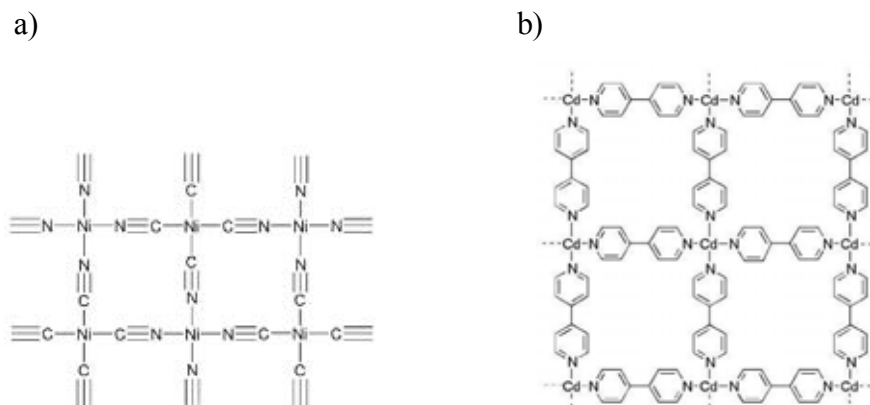
#### THEORY

#### 2.1 Coordination polymer and Metal-Organic Frameworks (MOFs)

##### 2.1.1 Coordination polymers

Coordination polymers (CPs)<sup>(9)</sup> are a class of organic-inorganic hybrid materials, in which metal ions are linked together by organic bridging ligands. The coordination polymers whose repeating unit is coordination complexes are also defined as molecular framework extending infinitely in at least one direction.

For example, the polymeric structures of nickel(II) cyanide<sup>(10)</sup> and Cd(II)-(4,4'-bipyridine)<sup>(11)</sup> as shown in Figure 2.1 was presented by John Bailar Jr. in 1964 and Fujita in 1994, respectively.



**Figure 2.1** The structures of a) nickel(II) cyanide and b) Cd(II)-(4,4'-bipyridine)

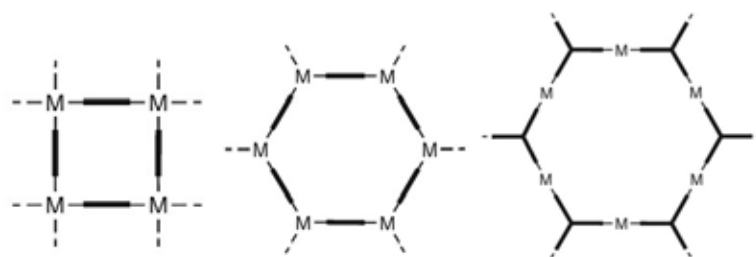
The classification<sup>(12)</sup> of coordination polymers are based on dimensionality which can be determined to be one, two or three dimension depending on the number of extended directions as shown in Figure 2.2. A one dimensional structure (1D) extends in a straight line (along the x axis), a two dimensional (2D) structure extends

in a plane with two directions (x and y axes) and a three dimensional (3D) structure extends in all three directions (x, y, and z axes).

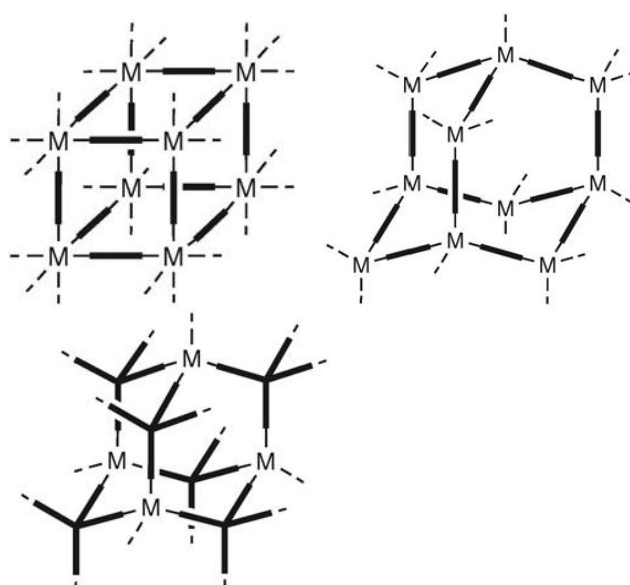
a) 1D coordination polymer



b) 2D coordination polymer



c) 3D coordination polymer



**Figure 2.2** Typical coordination polymers based on dimensionality; M = metal ion and black line represented as organic bridging ligand

Based on the concept of coordination polymers, in 1995, Omar Yaghi<sup>(13)</sup> firstly defined the term “Metal-Organic Frameworks” or “MOFs” for short to describe



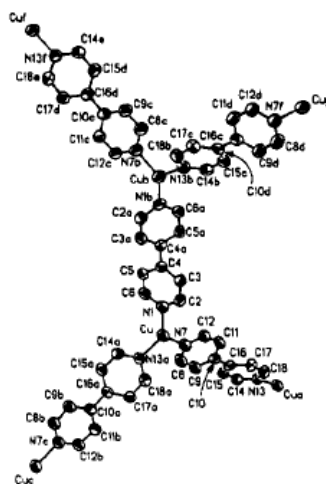
the new porous material. He found that the use of carboxylate or pyridyl as organic bridging ligands to aggregate metal ions could be formed extended frameworks with stability and high porosity structures.

A difference between MOFs and coordination polymers is in doubt. Biradha *et al.*<sup>(14)</sup> suggested that this discrimination may be based on structural features that the term MOFs is suitable to use for three-dimensional networks with potential porosity, it is inappropriate to use for extended one-dimensional or two-dimensional networks.

### 2.1.2 Metal-Organic Frameworks (MOFs)

Metal-organic frameworks<sup>(15)</sup> are crystalline porous materials containing high porosity and large specific surface area which compose of metal ions or clusters and organic linkers such as carboxylate or bipyridyl<sup>(16)</sup> organic ligands which play an important factors in directing the topologies and properties of frameworks that lead to versatile applications such as gas storage and separation<sup>(17)</sup>, heterogeneous catalysis<sup>(18)</sup>, luminescence<sup>(19)</sup>, drug delivery<sup>(20)</sup> etc.

Metal-organic frameworks or MOFs was first introduced by Yaghi<sup>(13)</sup> in 1995 to describe the newly synthesized compound  $[\text{Cu}(4,4'\text{-bipyridine})_{1.5}]\cdot\text{NO}_3(\text{H}_2\text{O})_{1.25}$ , which formed porous 3-D network structure as illustrated in Figure 2.3.

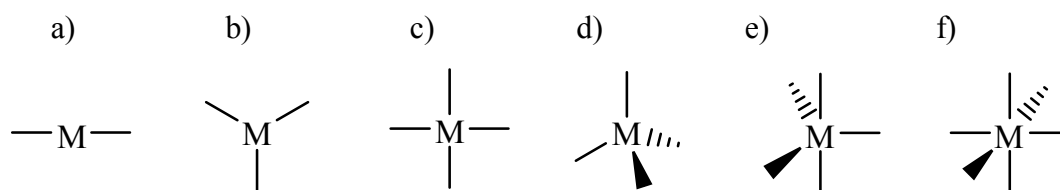


### 2.1.2.1 Factors influencing on topologies and properties of MOFs

In the construction of MOFs, many factors should be concerned about metallic node, organic linker, parameters for synthesis such as the metal salt, metal to ligand ratio, solvent, concentration, pH of reaction mixture, reaction temperature, reaction time and synthetic methods. These parameters play an important role in directing the topology and property of frameworks leading to their applications.

#### 2.1.2.1.1 Metallic node

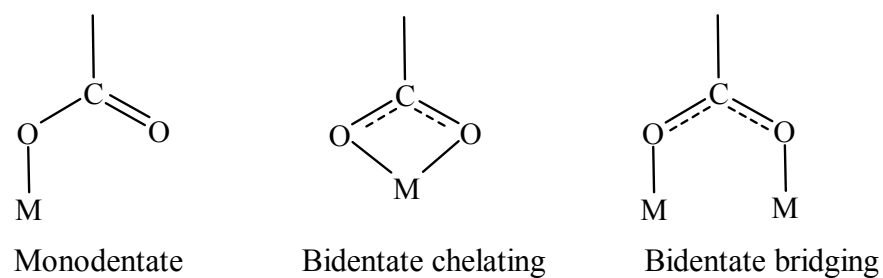
Transition metals such as copper(II), cadmium(II) and zinc(II)<sup>(21)</sup> are often used in MOF construction by introducing to the nodal positions of MOFs. Lanthanide metals are also used to provide luminescence property of the frameworks. The coordination of a metal often varies with its oxidation state. The coordination geometry<sup>(22)</sup> is linear, when two ligands are coordinated to the metal in a symmetrical distribution. Other common coordination geometries are trigonal planar for three-coordination, square planar or tetrahedral for four-coordination, trigonal bipyramidal for five-coordination, octahedral for six-coordination represented in Figure 2.4 a) to f) respectively.



**Figure 2.4** Metal ions with various coordinations.

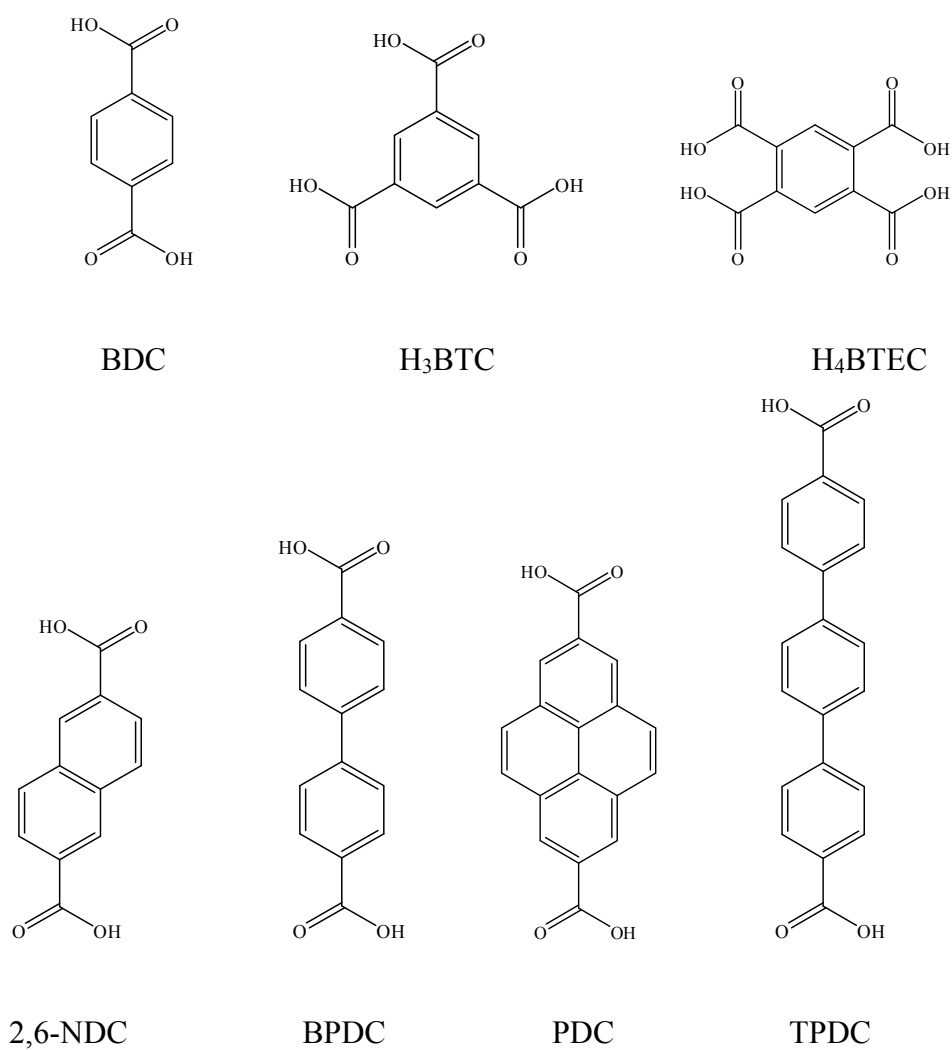
The potential of tetrazolate-based ligands with various metals including  $Zn^{2+}$ ,  $Mn^{2+}$  and  $Cu^{2+}$ <sup>(23)</sup> generated a series of 3D metal-organic frameworks with different structures and properties as displayed in Figure 2.5.

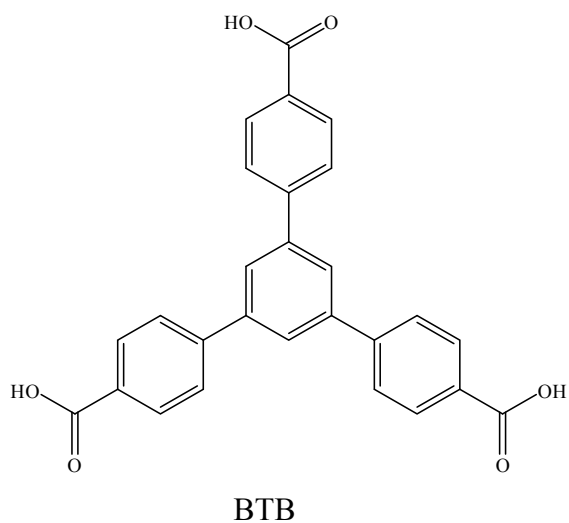




**Figure 2.6** Coordination modes of carboxylate ligand.

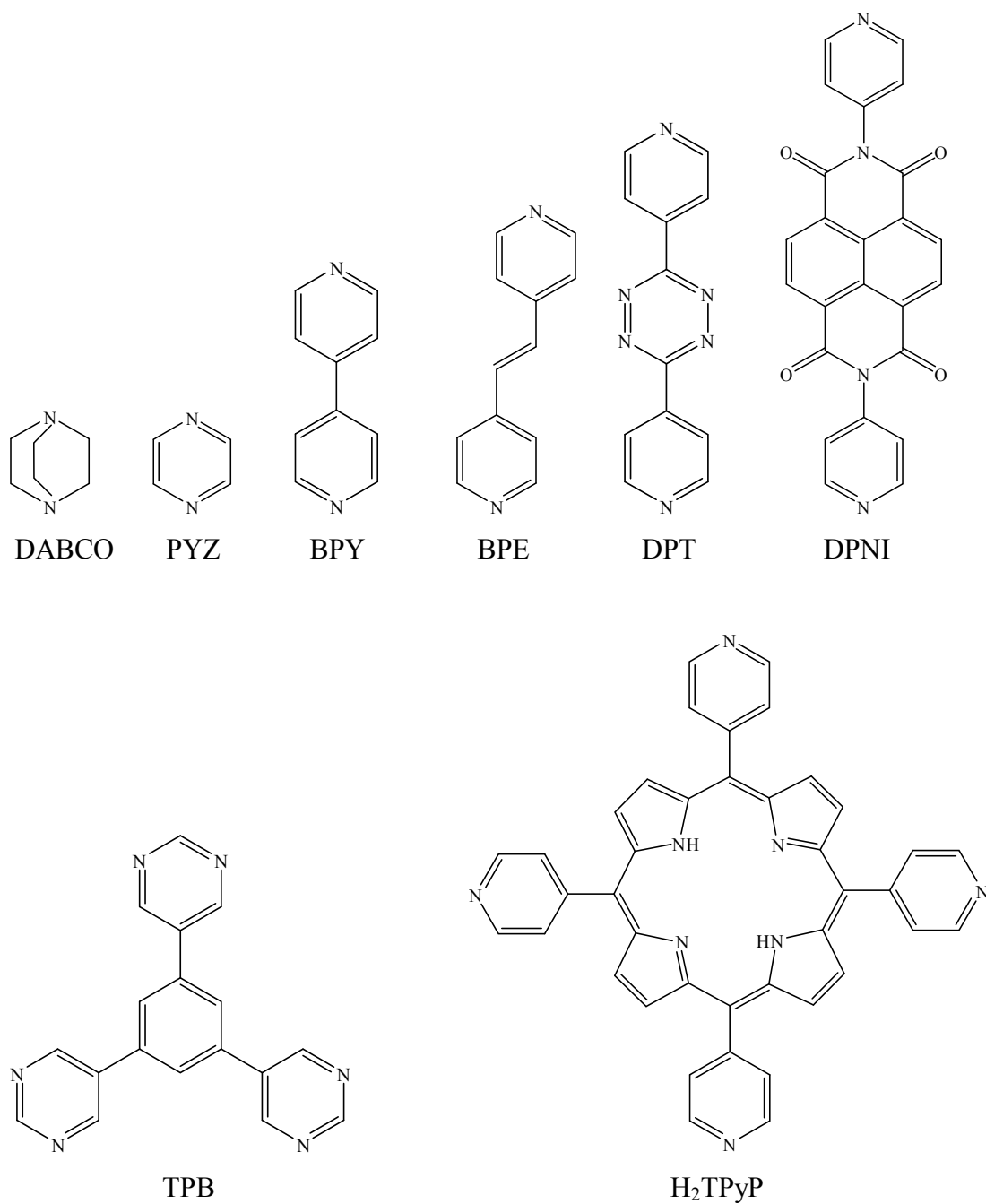
Examples of carboxylate<sup>(25)</sup> and nitrogen-based ligands<sup>(26)</sup> with ditopic ligands, tritopic ligands and tetratopic ligands were presented in Figure 2.7 and Figure 2.8, respectively. The expansion of the network can be used with long or polytopic ligands which enlarge the frameworks.





**Figure 2.7** Example of carboxylate ligands for MOFs.<sup>a</sup>

<sup>a</sup> BDC = 1,4-benzenedicarboxylic acid; H<sub>3</sub>BTC = 1,3,5-benzenetricarboxylic acid; H<sub>4</sub>BTEC = 1,2,4,5-benzenetetracarboxylic acid; 2,6-NDC = 2,6-Naphthalenedicarboxylic acid; BPDC = 4,4'-biphenyldicarboxylic acid; PDC = pyrene-2,7-dicarboxylic acid; TPDC = 1,1':4',1''-(terphenyl)-4,4''-dicarboxylic acid; BTB = 1,3,5-benzenetricarboxylic acid.



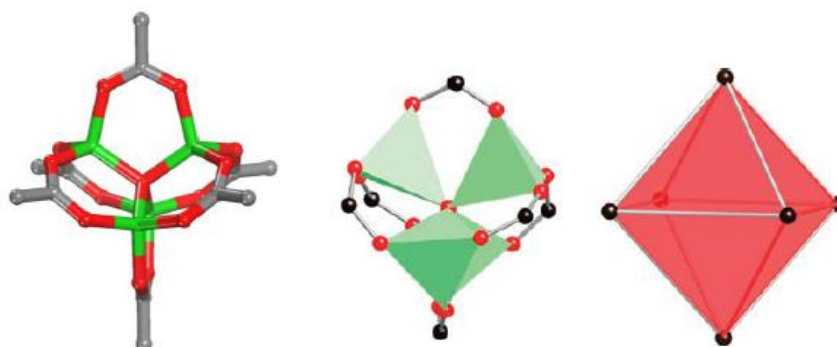
**Figure 2.8** Example of nitrogen-based ligands for MOFs.<sup>b</sup>

<sup>b</sup> DABCO = 1,4-Diaza-bicyclo[2.2.2]octane; PYZ = pyrazine; BPY = 4,4'-bipyridine; BPE = *trans*-bis(4-pyridyl)ethylene; DPT = 3,6-di-4-pyridyl-1,2,4,5-tetrazine; DPNI = *N,N'*-di-(4-pyridyl)-1,4,5,8-naphthalenetetracarboxydiimide; TPB = 1,3,5-tris(3,5-pyrimidyl)benzene; H<sub>2</sub>TPyP = 5,10,15,20-tetrakis(4-pyridyl)porphyrin.

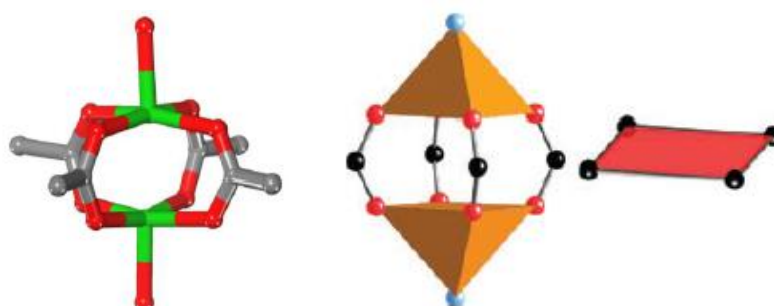
### 2.1.2.1.3 Secondary building unit (SBU)

The term “secondary building unit” or “SBU”<sup>(27)</sup> which refers to molecular clusters is useful for the topology prediction of MOFs. The topology of MOFs relates to both the coordination environment of the metal ion and the geometry of the organic linker. For example,  $M_4O(RCO_2)_6$  cluster (Figure 2.9 a) can be presented as a 6-connected octahedral building unit consisting of a single O atom bonded to four metal ions to form a  $M_4O$  tetrahedron whose edges are capped by carboxylates to form the octahedron. The  $M_2(RCO_2)_4$  cluster called *paddlewheel* (Figure 2.9 b.) can be acted as a square building unit that the two metal ions are bridged by four carboxylates. And the  $M_3O(RCO_2)_6$  cluster (Figure 2.9 c) shows as a trigonal prismatic building unit which consists of three metal ions, each coordinated by four bridging carboxylate groups, there are six carboxylate points of extension.<sup>(28, 29)</sup>

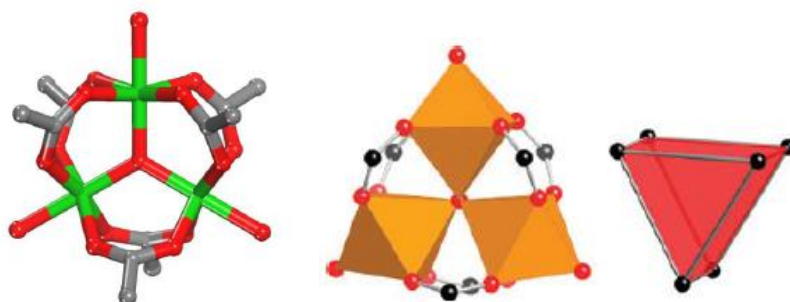
a)



b)



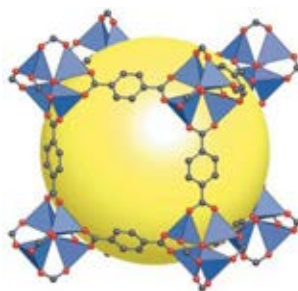
c)



**Figure 2.9** Common secondary building units (SBUs): a) octahedral building units; b) square building units; c) trigonal prism units. Hydrogen atoms are omitted for clarity, the metal is shown in green, and C and O are presented in grey and red, respectively.

An example of MOFs is presented by the structure of MOF-5 or IRMOF-1 (Figure 2.10), which was the most studied of all MOFs due to its high specific surface area and cheap starting material. In MOF-5,  $Zn^{2+}$  ion and 1,4-benzenedicarboxylate formed octahedral  $Zn_4O(CO_2)_6$  cluster to generate cubic framework.

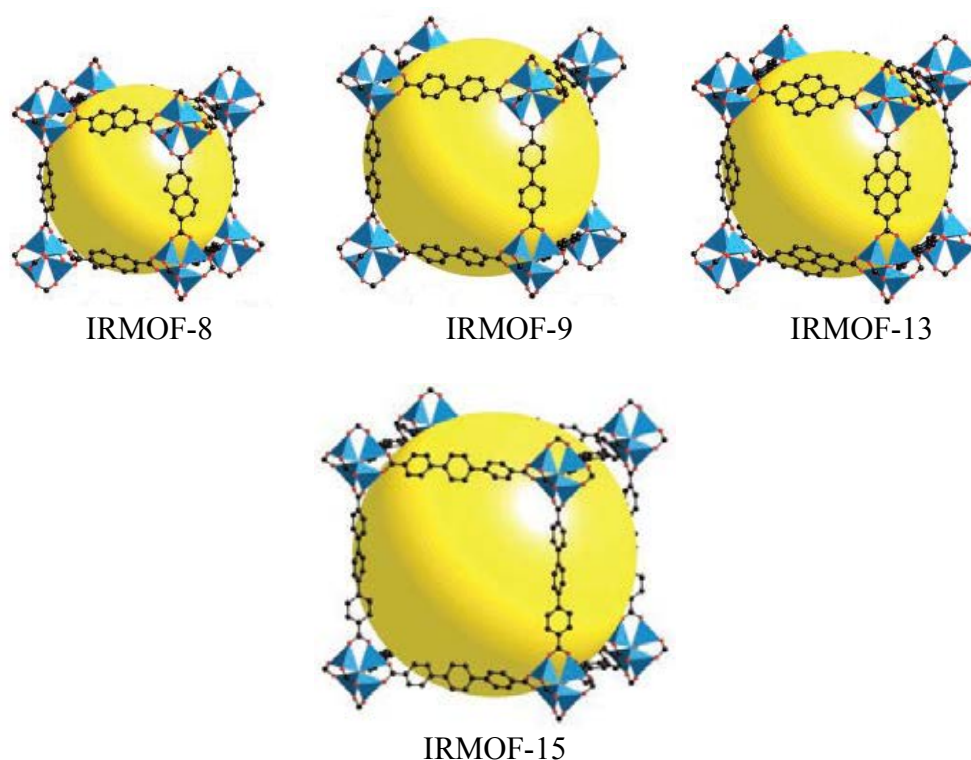
The term “MOF- $n$ ”<sup>(30, 31)</sup> stems from “Metal-Organic Framework” while “ $n$ ” is an integer assigned in chronological order. The word isorecticular means the same net or having the same topology, thus the term “Isorecticular MOF” (IRMOF- $n$ ;  $n$  is an integer referring to a member of the series) refers to a simple cubic topology.



**Figure 2.10** Structure of MOF-5(or IRMOF-1); yellow spheres represented the large void regions with diameters equal to the distance of Van der Waals surface.<sup>(31)</sup>



Using different organic linkers with the same metal in the case of octahedral  $Zn_4O(CO_2)_6$  clusters to form cubic frameworks can generate manifold IRMOFs with various properties. In figure 2.11, IRMOF-8, IRMOF-9, IRMOF-13 and IRMOF-15 using 2,6-NDC, BPDC, PDC and TPDC as organic linkers were illustrated, respectively.



**Figure 2.11** Example of Isoreticular Metal-Organic Frameworks (IRMOFs).

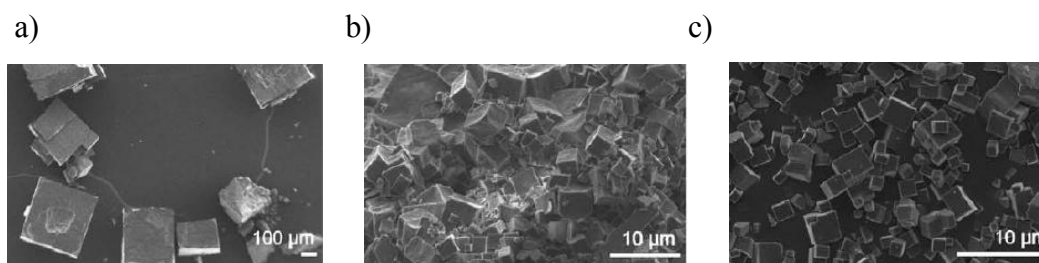
#### 2.1.2.1.4 Parameters for MOFs synthesis

The optimized conditions for the synthesis of metal-organic framework concern the systematic variation of many parameters, including the metal salt, metal to ligand ratio, solvent, concentration, pH of reaction mixture, reaction temperature, reaction time and synthetic method.

##### 2.1.2.1.4.1 Metal salt

The effect of the Zn salts<sup>(32)</sup> such as zinc(II) nitrate, zinc(II) oxide and zinc(II) acetate on the morphology of MOFs was found that zinc nitrate and zinc oxide generated bigger cubic crystals than that of zinc acetate (<10  $\mu\text{m}$ ) as presented in Figure 2.12. Owing to higher basicity compared with zinc nitrate

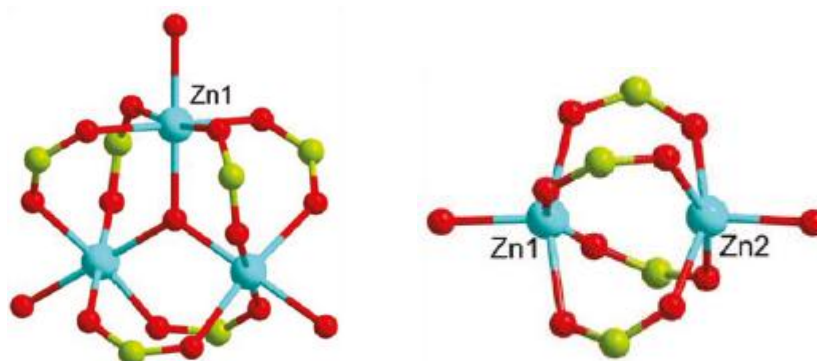
and better solubility compared with zinc oxide, zinc acetate led to a higher nucleation rate.



**Figure 2.12** Influence of different zinc(II) salts on the morphology of MOF-5. The samples were synthesized at 373 K under solvothermal condition for 24 h, using zinc(II) nitrate (a); zinc(II) oxide (b); and zinc(II) acetate (c), respectively.

#### 2.1.2.1.4.2 Metal to ligand ratio

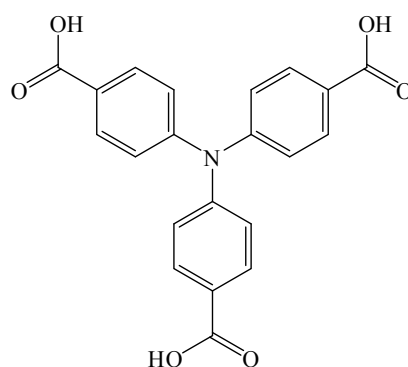
Altering metal to ligand ratio could effect to different forms of SBUs, affecting the structural formation of MOFs. In such a case, PCN-131 and PCN-132<sup>(33)</sup> (Figure 2.13) were synthesized using anthracene-9,10-dicarboxylic acid ( $H_2adc$ ) as organic linker and zinc(II) nitrate as metal salt but differing in metal to ligand ratio which were 2:1 and 3:1, respectively. PCN-131 was built on a  $\mu_3$ -oxo-trizinc basic carboxylate SBU as  $Zn_3O(COO)_6$ , whereas PCN-132 was a distorted paddle-wheel SBU as  $Zn_2(CO_2)_4$ .



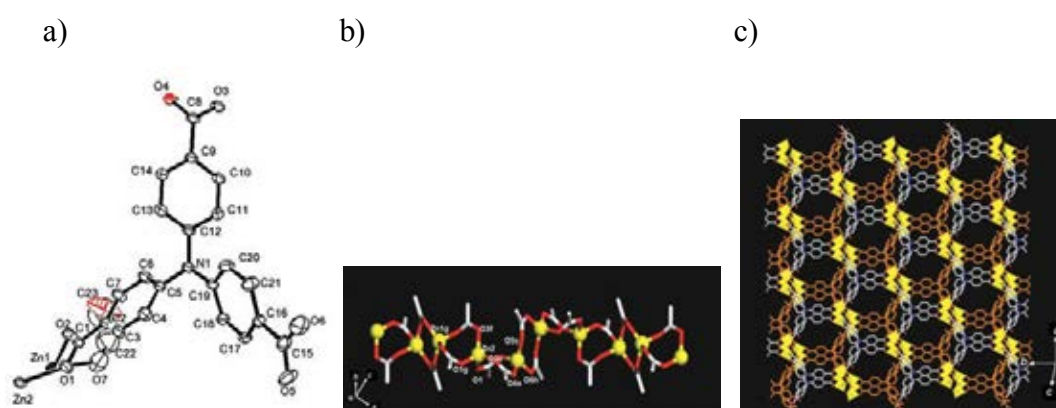
**Figure 2.13** Secondary Building Unit structures of PCN-131 and PCN-132, respectively

### 2.1.2.1.4.3 Solvent

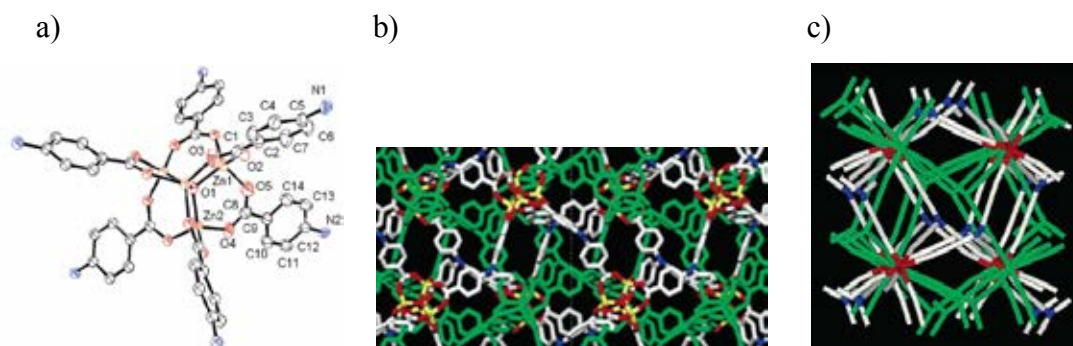
The influence of solvents on the formation of MOFs was discovered to be due to the polarity of the solvent and the solubility of the organic linker. In the case of the solvent effect, two different geometries of MOFs, which were synthesized using 4,4',4''-nitrilotrisbenzoic acid ( $H_3NTB$ ) as organic linker and zinc(II) nitrate as metal salt in distinct solvothermal reactions (EtOH and DEF/EtOH/ $H_2O$  (5:3:2, v/v)), were named  $Zn_3(ntb)_2$ <sup>(34)</sup> and  $Zn_4O(NTB)_2$ <sup>(35)</sup> as shown in Figure 2.14 and Figure 2.15, respectively.



4,4',4''-nitrilotrisbenzoic acid ( $H_3NTB$ )

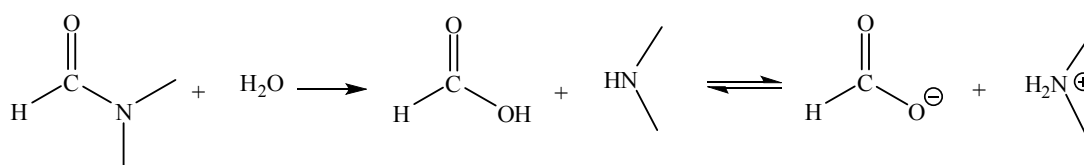


**Figure 2.14** X-ray crystal structures of a) original crystal of  $Zn_3(ntb)_2$ ; b) 1D chain of  $[Zn_3(ntb)_2]_n$ ; c) bilayers of the honeycomb formed of  $Zn_3$  pillars; Color scheme: Zn (tetrahedron), yellow; N, blue; O, red, C of two different bilayers, white and brown.



**Figure 2.15** X-ray crystal structures of a) original crystal of  $\text{Zn}_4\text{O}(\text{NTB})_2$ , the  $\text{Zn}_4\text{O}(\text{CO}_2)_6$  cluster; b) doubly interpenetrated 3D network structure of  $\text{Zn}_4\text{O}(\text{NTB})_2$ ; Color scheme: Zn, yellow; O, red; N, blue; C, gray; Green represents another interpenetrated 3D net; c) line drawing of doubly interpenetrated structure of  $\text{Zn}_4\text{O}(\text{NTB})_2$ ; Color scheme as same as b).

Hydrolysis of the solvent<sup>(36)</sup> in the case of organic amides such as dimethylformamide (DMF) and diethylformamide (DEF) has been noticed especially under solvothermal conditions. Hydrolysis of DMF leads to the formation of dimethylammonium ions as presented in Scheme 2.1 which suggests that  $\text{NH}_2\text{Et}_2^+$  plays as template in the crystallization of this material. Solvent molecule coordinates to the zinc node and acts as terminal ligands, preventing the layer linking to form 3D network.

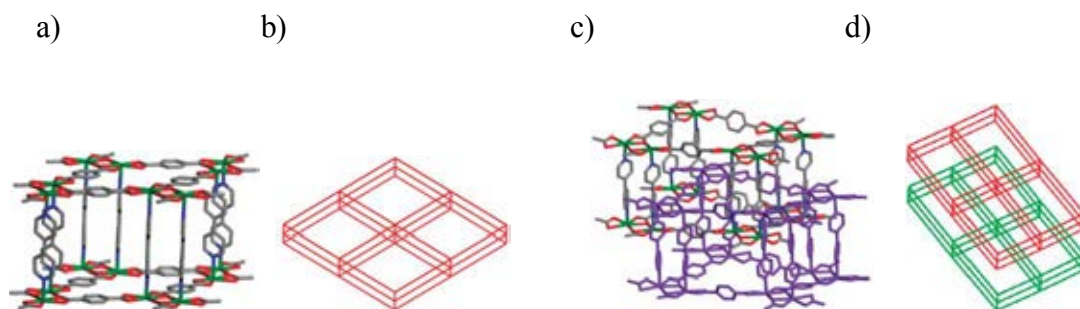


**Scheme 2.1** Hydrolysis of DMF generating dimethylammonium ions.

#### 2.1.2.1.4.4 Concentration of reaction mixture

The effect of reaction mixture concentration<sup>(37)</sup> is expected that low concentration of starting materials will shorten the growth of framework resulting in a decrease of particle size, due to a reduction of the possibility

in forming a sub-lattice in the voids of structure, called *non-interpenetrated structure*. High concentration favors an interpenetrated form as illustrated in Figure 2.16.



**Figure 2.16** a) non-interpenetrated structure of Cd(bipy)(bdc); b) simple diagram showing the primitive cubic (*pcu*) structure of a); c) 2-fold interpenetrated structure of Cd(bipy)(bdc) and d) simple diagram of c).

There are advantages and disadvantages of interpenetration upon the desired application. The interpenetrated form may exhibit high thermal stability and selective molecular recognition; however it possesses a low free volume, causing limit applications such as catalysis and separation of large molecules. On the other hand, the non-interpenetrated structure may contain a high free volume but low thermal stability and absence of proper cavity to trap small molecules.

#### 2.1.2.1.4.5 *pH* of reaction mixture

As for many polar solvents usage, base may be necessarily add to avoid competition with the organic linkers to coordinate to the available metal sites. The reaction mixture with high *pH* causes deprotonation of carboxylate organic linker which increases in nucleation rate and as a result to decrease in particle size.<sup>(38)</sup> In some cases of MOFs synthesis, acetic acid is added as a modulator<sup>(39)</sup> that acts as competitive ligand in the coordination equilibrium to control morphology of MOFs. Little amount of acetic acid induces rapid crystallization, producing low crystallinity or small particle size. Increasing the amount of acetic acid decelerates the rate of nucleation, resulting in fewer nuclei, causing larger crystal or

preventing the crystal growth. In the latter case, a modulator may be called in term of “capping agents”.

#### **2.1.2.1.4.6 Reaction temperature and time**

In growth of crystalline material, there are three steps concerning about: (a) incubation of the reaction solution; (b) initiation of nucleation by heating at high temperature; and (c) initiation of growth by cooling down to low temperature. Even though the crystal size increases at high temperatures and prolongs reaction time, the crystal is observed in low quality.<sup>(40)</sup> Moreover, increasing the reaction temperature causes the formation of copper(II) oxide (CuO) as a side product.<sup>(41)</sup>

#### **2.1.2.1.4.7 Synthetic method**

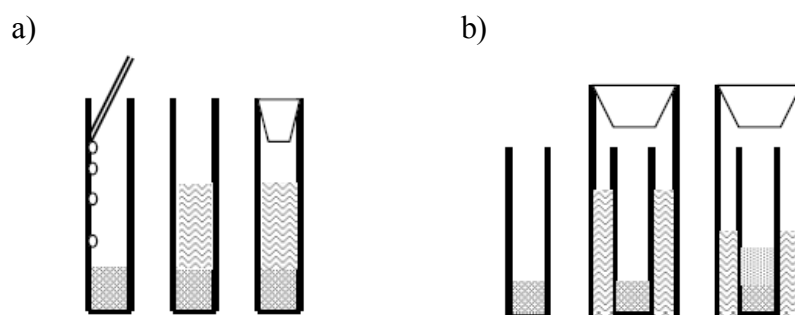
The principal concept of high quality in MOFs formation is to reduce the crystalline nucleation rate. The most commonly crystal growth method is solvent evaporation or cooling a saturated precursor solution. A wide variety of other methods to attain metal-organic frameworks have been explored,<sup>(42,43)</sup> such as diffusion method, hydro/solvothermal method, microwave assisted method and mechanochemical method.

##### **2.1.2.1.4.7.1 Diffusion method**

This method can be divided in two main techniques: solvent diffusion and vapor diffusion techniques (Figure 2.17). These techniques rely on different properties of the solutions to grow the crystals, suitable for X-ray diffraction analysis instead of non- or poly-crystalline products.<sup>(44)</sup>

In case of solvent diffusion or layering technique, a small amount of metal solution is placed in a tube and organic ligand solution gradually layers on the top of the earlier solution. The tube is sealed without disturbance. Later on, some crystals will form. It should be cautioned that the organic ligand solution will be less dense than the metal solution and an appropriate volume ratio of metal solution/organic solution is typically 1:4 or 1:5. For the case of vapor diffusion technique, it has the same principle as the previous technique but another

solution diffuses to the first solution by the vapor. For example, the mixed solution of metal and organic ligand in a tube is placed into the beaker, which contains triethylamine (TEA) as volatile amine, then a slow diffusion will occur and result in crystal formation.<sup>(45,46)</sup>

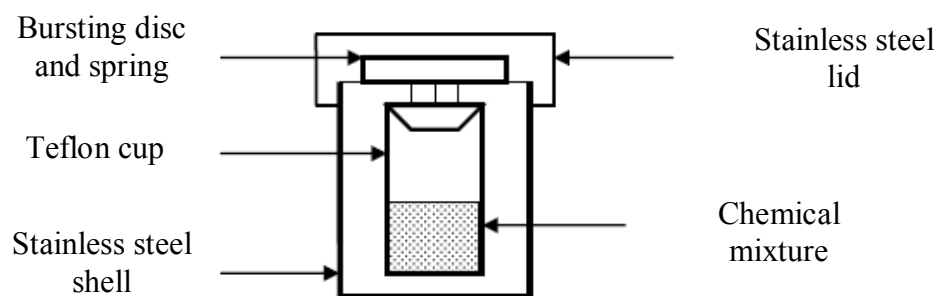


**Figure 2.17** Scheme of a) layering technique and b) vapor diffusion technique.<sup>(47)</sup>

The advantages of these techniques are using a small amount of reactant and setting up many experiments by altering experimental conditions at one time. However, these techniques are time consuming owing to slow diffusion and crystal growth with a few days up to several months.

#### 2.1.2.1.4.7.2 Hydro/solvothermal method

This method is originally used for the synthesis of zeolites, but has been widely used for synthesis of several MOFs. Hydrothermal<sup>(48)</sup> and solvothermal<sup>(49,50)</sup> syntheses are employed water and other solvents such as DMF, respectively at the temperature range of 110-240 °C in sealed vessel such as a Teflon-lined stainless steel autoclave under autogenous pressure (Figure 2.18), while the viscosity and dielectric constant of the solvent are reduced which enhance the diffusion process and crystal growth.



**Figure 2.18** Scheme of a Teflon-lined stainless steel autoclave.<sup>(51)</sup>

#### 2.1.2.1.4.7.3 Microwave-assisted method

Microwave heating<sup>(52,53)</sup> has been employed as a mean of accelerating the chemical reaction rate technique to perform high speed synthesis in under seconds to minutes, which is the same quality as those produced by the standard solvothermal process. Though the microwave method usually cannot yield big crystals enough for single X-ray analysis, it can create a uniform seeding. Thus, the size and shape of the crystals can be well controlled for many practical applications.

#### 2.1.2.1.4.7.4 Mechanochemical method

Mechanochemical synthesis<sup>(54,55)</sup> is a solvent-free methodology. In this technique, the mixtures of organic linker with lower melting points and metal salts, that are hydrated, are placed in a stainless steel vessel with a ball bearing, mixed and grinded in a ball mill mixer (Figure 2.19) to produce the desired MOFs. The formation of acetic acid as a by-product in the reactions may promote reaction by the solvent effect. Even though acetic acid presents in the pores of MOFs, it can be easily removed by thermal activation.





**Figure 2.19** Ball mill: stainless steel vessel with a ball bearing.<sup>(12)</sup>

Alternative synthetic methods for metal-organic framework can lead to various particle sizes and morphologies that influence on the material properties. In such a case, the diffusion of guest molecules in porous materials affects the catalytic reactions, the adsorption and separation of molecules.

### **2.1.2.2 Characterization of MOFs**

Metal-organic frameworks (MOFs) are porous materials which require many techniques to characterize the structures which may concern:

- (a) Powder X-ray diffraction (XRD)
- (b) Scanning electron microscopy (SEM)
- (c) Nitrogen adsorption-desorption
- (d) Fourier Transform Infrared Spectroscopy (FT-IR)
- (e) CHNS/O Elemental analysis (EA)
- (f) Thermogravimetric Analysis (TGA)

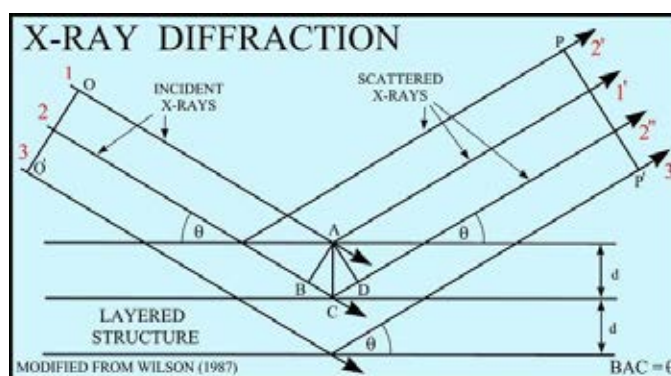
#### **2.1.2.2.1 Powder X-Ray Diffraction (XRD)**

Powder X-Ray Diffraction (XRD)<sup>(56)</sup> is an instrumental technique used to identify crystalline materials such as minerals and inorganic compounds. X-ray diffraction is concerned about the constructive interference of monochromatic X-rays and crystallinity of the sample. These generated X-rays by a cathode ray tube were filtered to result the monochromatic radiation, collimated to concentrate toward the sample. Both of the constructive interference and the

diffracted ray were produced by the interaction of the incident rays with the sample (Figure 2.20). Bragg's Law presents as following equation:

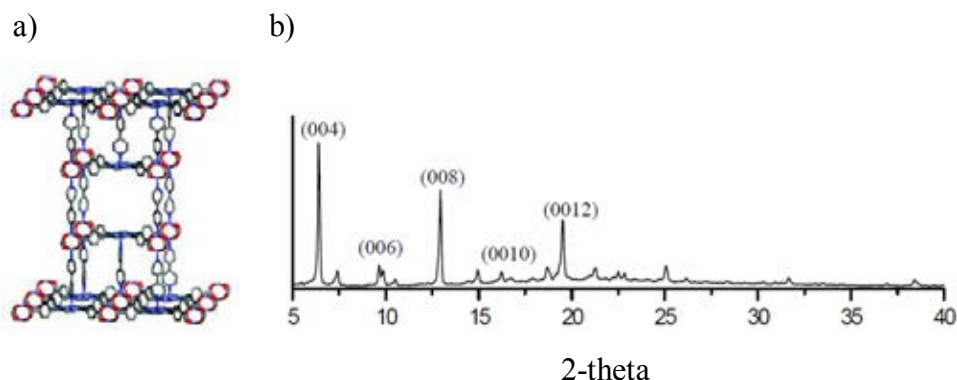
$$n\lambda = 2d \sin \theta$$

This equation relates the electromagnetic radiation wavelength ( $\lambda$ ) to the diffraction angle ( $\theta$ ) and the lattice spacing ( $d$ ) in a crystalline sample.



**Figure 2.20** Schematic representation of X-Ray Diffraction<sup>(57)</sup>

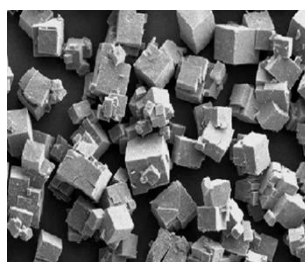
These diffracted X-rays are then detected and counted. By scanning the sample through a range of  $2\theta$  angles, all possible diffraction directions of the lattice should be obtained owing to the random orientation of the powder material. Conversion of the diffraction peaks to  $d$ -spacings identifies the mineral which has a set of unique  $d$ -spacings, then comparing with standard reference patterns (Figure 2.21).



**Figure 2.21** Example of a) crystal structure and b) XRD pattern of PPF-4(Zn).<sup>(58)</sup>

### 2.1.2.2.2 Scanning Electron Microscopy (SEM)

Scanning Electron microscope (SEM)<sup>(59)</sup> is concerning about a focused beam of high-energy electrons to produce a variety of signals at the specimen surface.. The signals deriving from electron-sample interactions show the external morphology (texture), chemical composition, crystalline structure and orientation of materials. The data from a selected area of the sample surface are collected and scanning mode of conventional SEM techniques resulted in the 3-dimensional image (magnification ranging from 20X to approximately 30,000X, spatial resolution of 50 to 100 nm) (Figure 2.22). The SEM is also able to analyse of selected point on the sample to determine the chemical compositions (using EDS), crystalline structure and crystal orientations (using EBSD).

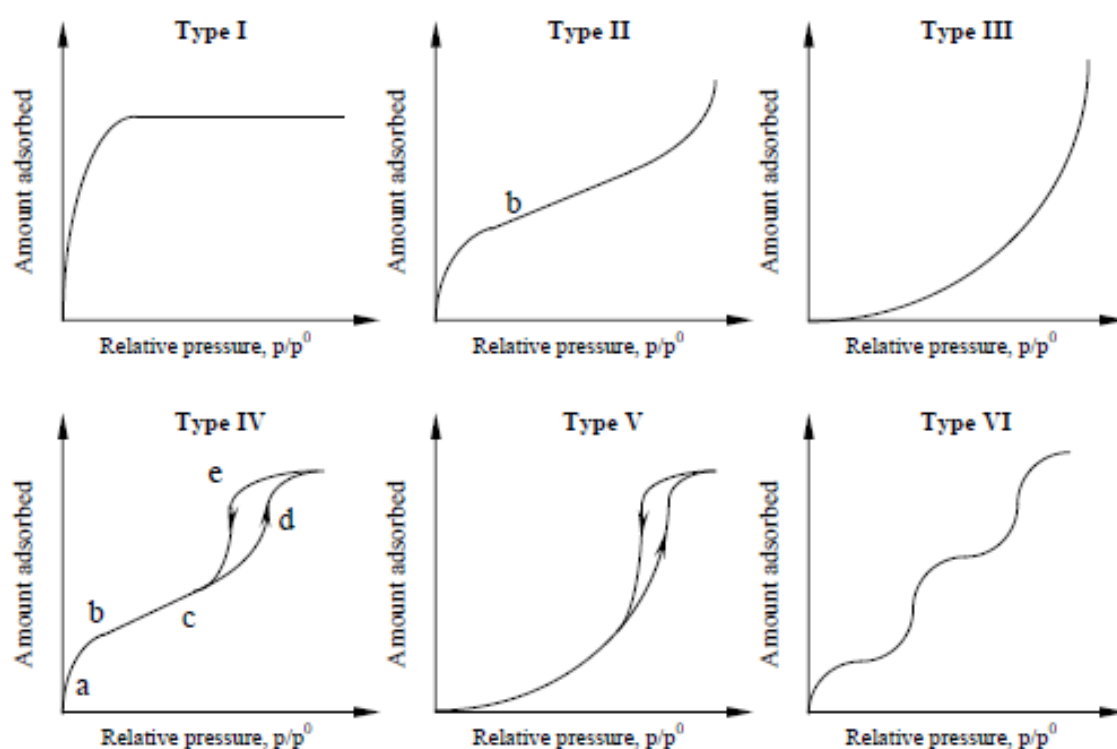


**Figure 2.22** Example of SEM image of MOF-5.<sup>(60)</sup>

### 2.1.2.2.3 Nitrogen Adsorption-Desorption Isotherm

The nitrogen adsorption technique<sup>(61)</sup> is used to determine the physical properties of porous materials, such as surface area, pore volume, pore diameter and pore size distribution. Adsorption of gas by porous material is described by an adsorption isotherm, the amount of adsorbed gas by material at a fixed temperature as a function of pressure. The temperature used for recording isotherms is the temperature of the boiling point of the adsorbate i.e. 77.3 K for nitrogen. At pressures below the saturation pressure ( $P/P_0 < 1$  which the saturation pressure ( $P_0$ ) is 760 mmHg for  $N_2$ ), a dense monolayer of adsorbate can be formed on the surface and a multilayer of increasing thickness can be formed when the pressure increases and approaches  $P_0$ .

Porous materials are frequently characterized in terms of pore size derived from gas sorption data. IUPAC conventions have been proposed to classify pore sizes and gas sorption isotherms that reflect the relationship between porosity and sorption properties. The IUPAC classification of adsorption isotherms is illustrated in Figure 2.23. Six types of isotherms are characteristic of adsorbents that are microporous (type I), nonporous or macroporous (type II, III and VI) or mesoporous (type IV and V).



**Figure 2.23** Six types of adsorption isotherm. <sup>(62)</sup>

**Table 2.1** IUPAC classification of pores. <sup>(63)</sup>

Type	Features	
	Interaction between sample surface and gas adsorbate	Porosity
I	Relatively strong	Microporous
II	Relatively strong	Nonporous
III	weak	Nonporous
IV	Relatively strong	Mesoporous
V	weak	Microporous or Mesoporous
VI	Relatively strong sample surface has an even distribution of energy	Nonporous

Type I adsorption isotherm of IUPAC classification is typical for microporous material which is controlled by stronger interaction between the adsorbate and adsorbent. This type shows a rapid increase in the amount of gas adsorbed over the low relative pressure range which is often attributed to micropore filling in porous solids and then reaches a plateau in the high pressure range which indicates that the micropores are filled and no further adsorption will take place.

Type II isotherm is characteristic of strong adsorbate-adsorbent interaction which indicates an multi-layer formation after completion of the monolayer. Near to the first point of inflexion (point B), a monolayer is completed following with adsorption in successive layers.

Type III isotherm represents characteristic of weak adsorbate-adsorbent interaction that lead to low uptakes at low relative pressures. However, once a molecule has become adsorbed at a primary adsorption site, the adsorbate-adsorbate interaction, which is much stronger, becomes the driving force of the adsorption process resulting in accelerated uptakes at higher relative pressure.

Type IV isotherm, which is common for mesoporous materials, usually exhibits hysteresis that is associated to capillary condensation. At this initial state, adsorption of molecules on to the walls of porous material occurs at a very low

relative pressure until a monolayer (a to b) is formed. Then, the multilayer adsorption occurs as pressure increases (b to c) and follows by capillary condensation at high relative pressure below  $p/p_0$  (c to d). In the capillary condensation process, gas/vapor molecules tend to form a liquid-like layer with a curved meniscus at pore entrances (d). As pressure decreases, the angle of the curve of the meniscus also changes. The liquid meniscus blocks the liquid condensed in pores from evaporating. This blocking results in a high mass of adsorbate remaining in the porous material which then creates the hysteric loop (e). For simply description, the quantity adsorbate is different when gas is added than it is removed.

Type V isotherm is characteristic of weak adsorbate-adsorbent interaction. This isotherm indicates of microporous or mesoporous solids that usually exhibit hysteresis. The shape of this class of isotherm is similar to type III.

The last type is the type VI isotherm. This isotherm shows stepwise multilayer adsorption. The height of the steps is associated with the monolayer capacity for each adsorbed layer.

Adsorption isotherms are described as shown in Table 2.1 based on the strength of the interaction between the sample surface (adsorbent) and gas (adsorbate) and the existence or absence of pores. Pore types are classified as shown in Table 2.2.

**Table 2.2** Pore types of porous materials.

Pore type	Pore diameter (nm)
Micropore	Up to 2
Mesopore	2 to 50
Macropore	50 to up

The two mostly used methods of surface area evaluation for MOFs are the Langmuir method and the BET method. Langmuir method<sup>(64)</sup> is able to describe the type I isotherm with the assumption that adsorption is limited to a monolayer of adsorbate. The Langmuir equation can be written as following equation:

$$\frac{P}{V_a} = \frac{1}{KV_m} + \frac{P}{V_m}$$

Where P is the pressure. V and  $V_m$  are the amount of adsorbed gas at a certain pressure and the amount of adsorbed gas at monolayer coverage, respectively, and K is the Langmuir adsorption constant (related to the strength of adsorption). The plot of  $P/V_a$  versus P is called the Langmuir plot, which gives a linear relationship with the intercept of  $1/KV_m$  and the slope of  $1/V_m$ . The two constants ( $V_m$  and K) of the Langmuir equation can be calculated.

However, later Brunauer, Emmett and Teller<sup>(65)</sup> extended the Langmuir's monolayer theory to multilayer adsorption. The BET equation is shown as the following equation:

$$\frac{1}{V \left[ \left( \frac{P_0}{P} \right) - 1 \right]} = \frac{1}{V_m C} + \frac{C-1}{V_m C} \left( \frac{P}{P_0} \right)$$

Where V is the volume of nitrogen adsorbed at a given  $P/P_0$  ( $\text{cm}^3/\text{g}$ ),  $V_m$  is the gas volume at the monolayer coverage ( $\text{cm}^3/\text{g}$ ) and C is a constant that is related to the heat of adsorption.

The plot of  $1/V[(P_0/P)-1]$  against  $P/P_0$  is called the BET plot, should give a linear relationship and intercept (i) and slope(s) of the BET plot give  $1/V_m C$  and  $(C-1)/V_m C$ , respectively. The two constants ( $V_m$  and C) of the BET equation can be calculated using following equation:

$$V_m = \frac{1}{s+i}$$

$$C = \left( \frac{s}{i} \right) + 1$$

In many adsorbents, the BET plot gives a good linear line in relative pressure range 0.05-0.35, but it deviates from the linear line in low or high

pressure range.  $V_m$  can be used to calculate the total specific surface area of the adsorbent ( $A_s$ ) as following equation:

$$A_s = \frac{V_m}{22414} \times L \times \sigma$$

Where  $V_m$  is the gas volume at the monolayer coverage ( $\text{cm}^3/\text{g}$ ),  $L$  is Avogadro number and  $\sigma$  is the cross-section area of an adsorbate molecule, in the case of nitrogen adsorption at liquid nitrogen temperature,  $\sigma(\text{N}_2) = 0.162 \text{ nm}^2$

$\sigma$  is defined as the average area that one adsorbed molecule occupies on the solid surface, which is based on assumption that adsorbed molecules make the closest packing on solid surface.

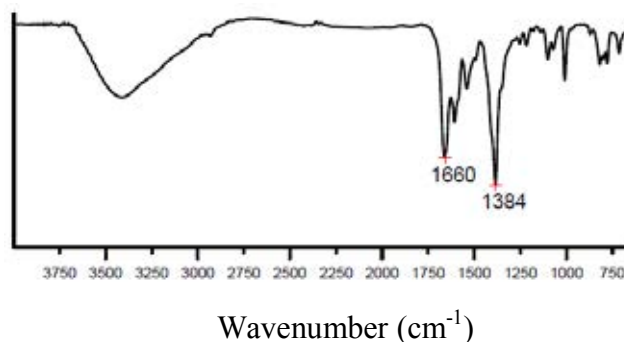
Pore size distribution is measured by the use of nitrogen adsorption-desorption isotherm at liquid nitrogen temperature and relative pressures ( $P/P_0$ ) ranging from 0.05-0.1. The large uptake of nitrogen at low  $P/P_0$  indicates filling of micropore ( $< 2 \text{ nm}$ ) in the adsorbent. The linear portion of the curve represents multilayer adsorption of nitrogen on the surface of the sample and the concave upward portion of the curve shows filling of mesopores and macropores. Various models have been proposed to evaluate the pore size and the pore size distribution. For examples, the t-method of Halsey, the MP method, the Barrett, Joyner and Halenda (BJH) method, the Dollimore and Heal (DH) method, the Dubinin-Astakhov (DA) method, the Horvath-Kawazoe (HK) method, the Saito-Foley (SF) method, the density functional theory (DFT) and Monte Carlo simulation method. It is assumed that the total isotherm consist of a number of individual single pore isotherms multiplied by their relative distribution over a range of pore sizes<sup>(66)</sup>

#### **2.1.2.2.4 Fourier Transform Infrared Spectroscopy (FT-IR)**

Infrared (IR) spectroscopy<sup>(67)</sup> is the common spectroscopic techniques, which is the absorption measurement of different IR frequencies by a sample positioned in the path of an IR beam. The IR spectroscopic analysis is to determine the chemical functional groups of the sample for structural identification. Different functional groups absorb characteristic frequencies of IR radiation. A wide



range of sample types such as gases, liquids, and solids can be accepted to use in IR spectrometers. The mid-infrared, approximately  $4,000\text{--}400\text{ cm}^{-1}$  may be used to study the fundamental vibrations and associated rotational-vibrational structure (Figure 2.24).



**Figure 2.24** Example of IR spectrum of PPF-4.<sup>(58)</sup>

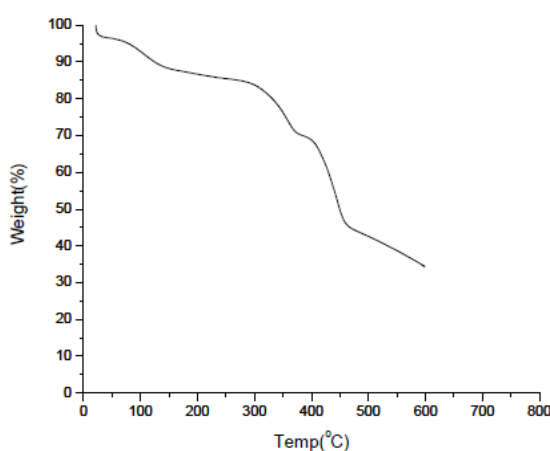
#### 2.1.2.2.5 CHNS/O Elemental analysis (EA)

CHNS/O Analyzer<sup>(68)</sup> is an elemental analyzer used to determine the amount of (%) of Carbon, Hydrogen, Nitrogen, Sulphur and Oxygen contained in organic, inorganic and polymeric materials. The sample weighed in milligrams housed in a tin capsule is dropped into a quartz tube at  $1020^{\circ}\text{C}$  with constant helium flow (carrier gas). A few seconds before the sample drops into the combustion tube, the stream is enriched with a measured amount of high purity oxygen to achieve a strong oxidizing environment which guarantees almost complete combustion/oxidation even of thermally resistant substances. The resulting four components of the combustion mixture are detected by a Thermal Conductivity Detector in the sequence  $\text{N}_2$ ,  $\text{CO}_2$ ,  $\text{H}_2\text{O}$  and  $\text{SO}_2$ . In case of oxygen which is analyzed separately, the sample undergoes immediate pyrolysis in a helium stream which ensures quantitative conversion of organic oxygen into carbon monoxide separated on a GC column packed with molecular sieves.

#### 2.1.2.2.6 Thermogravimetric Analysis (TGA)

Thermogravimetric Analysis (TGA)<sup>(69)</sup> measures the amount and rate of change in the weight of a material as a function of temperature or time in a controlled atmosphere for determining the composition of materials and to predict

their thermal stability at temperatures up to 1000°C. The technique can characterize materials that exhibit weight loss or gain due to decomposition, oxidation, or dehydration. The results from thermogravimetric analyses (Figure 2.25) are usually reported in the form of curves relating the mass lost from the sample against temperature. Thermogravimetric analysis data can also be presented in a differential form which is often more informative than the normal thermogravimetric analysis curve.



**Figure 2.25** Example of Thermogravimetric analysis curve (TGA) of PPF-4.<sup>(58)</sup>

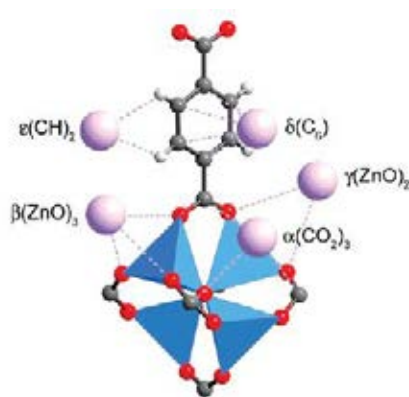
### 2.1.2.3 Application of MOFs

MOFs are highly porous materials with designable structures, which can be varied the synthesis parameters and modified to the desired MOFs that are used in a wide variety of applications such as, gas storage<sup>(70)</sup>, gas separation<sup>(17,88)</sup>, catalysis<sup>(18,90)</sup>, luminescence<sup>(19)</sup>, drug delivery<sup>(91)</sup> etc.

#### 2.1.2.3.1 Gas storage

In the past several years, metal-organic frameworks (MOFs) have been studied in the area of materials for gas storage, particularly for hydrogen storage,<sup>(70)</sup> due to their high specific surface areas. To compare with an empty gas cylinder, a MOF-filled gas cylinder can store more gas. Surface area and pore volume of MOFs can be determined by gas absorption isotherms. Most of porous MOFs are microporous having pore size of less than 2 nm and displaying type I absorption isotherm.

Hydrogen uptake mechanism has been theoretically studied by means of computation. In principle, two main sites for hydrogen adsorption in MOFs are recommended, one associates with inorganic metal clusters and another concerns organic linkers<sup>(71,72)</sup> (Figure 2.26). Many researches revealed that the metal cluster was primarily hydrogen adsorption, meanwhile the organic linker played as a secondary site. Nevertheless, hydrogen is preferentially adsorbed onto the organic linkers at higher pressure. This result may be due to the sites on the organic linker have lower binding energies but a much greater capacity to increase in hydrogen loading.<sup>(73)</sup> Moreover, the organic linkers may also alter the interaction of hydrogen with the metal cluster owing to differences in their electronic structures.



**Figure 2.26** Proposed five binding sites for adsorbed argon (purple spheres) in IRMOF-1, including three on the inorganic cluster and two on the phenylene link.<sup>(73)</sup>

#### 2.1.2.3.1.1 Adsorption force

In general, adsorption is divided into the two categories of physical adsorption (physisorption) and chemical adsorption (chemisorption)<sup>(3)</sup> The adsorption process can be determined whether chemical bonds are formed during the process. Physisorption refers to no chemical bond in adsorbate-adsorbent systems, whereas chemisorption occurs with making a chemical bond. Comparing of physisorption and chemisorption in porous adsorbent<sup>(74,75)</sup> is illustrated in Table 2.3.

**Table 2.3** Comparison of physisorption and chemisorption.<sup>(76)</sup>

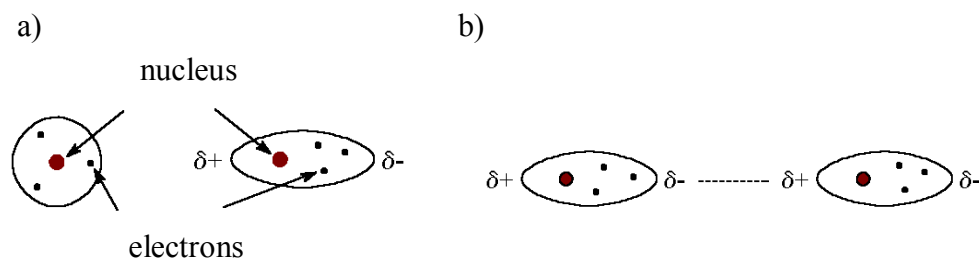
	Physisorption	Chemisorption
Chemical bond in adsorbate-adsorbent system	No chemical bond	Chemical bond
Gravimetric capacity	low	high
Heat of Adsorption / $\text{kJmol}^{-1}$	20 - 40	> 80
Rate of Adsorption (at 273K)	Fast	Slow
Temperature Dependence of Uptake (with Increasing T)	Decreases	Increases
Specificity	Non-specific	Very Specific
Monolayer Coverage	Mono or multilayer condition dependent	Monolayer
Desorption	Easy : reduced pressure or increased temperature	Difficult : high temperature required to break bonds
Desorbed Species	Adsorbate unchanged	May be different to original adsorbate
Reversibility	reversibility	Non-reversibility

No chemical bonds are formed during physisorption, thus the attraction between the adsorbate and adsorbent depends on the formation of intermolecular electrostatic, such as *Van der Waals* force from induced dipole interactions. These forces are the result of rapid fluctuations in the electronic density of one adsorbent molecule inducing an electrical moment in a second atom, therefore the rate of adsorption is faster than that of chemisorption. Physisorption has many advantages over chemisorptions, which concern about ease of desorption of gas molecule, unchanging in desorbed species and readily reversibility, while chemisorption requires for chemical reactions or high temperatures to release the stored gas, which consumes energy cost and desorbed species maybe different to

original gas adsorbate. However, the physisorption involves in weak interaction with gas, thus it may be not strong enough to store adequate gas amount. To solve this problem, the condition to store gas should be decreased temperature or increased pressure.<sup>(75)</sup>

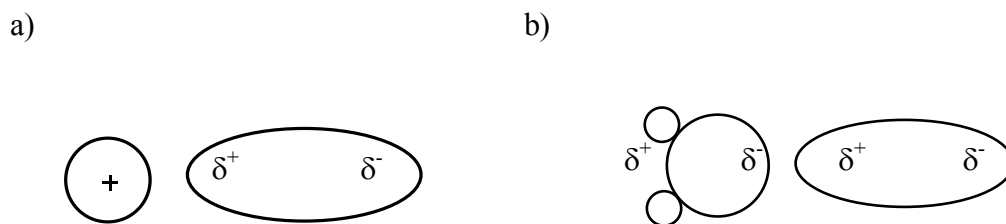
The principal forces involved in physisorption are the *Van der Waals* forces,<sup>(77)</sup> there are mainly two kinds of this forces, *London dispersion forces* (or induced dipole-induced dipole force) and *Debye force* (ion induced dipole force and dipole induced dipole).

The London dispersion force is a temporary attractive force (Figure 2.27). Because of the motion of the electrons, an atom or molecule can develop a temporary dipole when its electrons are distributed unsymmetrically. This force is sometimes called an *induced dipole-induced dipole attraction*. A second atom or molecule can be distorted by the appearance of the dipole in the first atom or molecule (because electrons repel one another) which leads to an *electrostatic attraction* between the two atoms or molecules.



**Figure 2.27** Schematic representation of a) temporary dipole in atom; and b) *electrostatic attraction* between two atoms.<sup>(78)</sup>

In the case of “ion induced dipole force” (Figure 2.28), it is a weak attraction that occurs when an ion induces a dipole in an atom or in a nonpolar molecule by disturbing the arrangement of electrons in the nonpolar species. While “dipole-induced dipole attraction” is a weak attraction, it results when a polar molecule induces a dipole in an atom or in a nonpolar molecule by disturbing the arrangement of electrons in the nonpolar species.



**Figure 2.28** Schematic representation of a) ion induced dipole force; and b) dipole-induced dipole force.<sup>(79)</sup>

The relationships between hydrogen gas and MOFs are physisorption. The interaction mechanism between hydrogen and MOFs is discussed. In compositions of MOFs, there are both metals part represented as positive charge and organic linker part represented as negative charge, which cause by aromatic rings. These parts result in the *Van der Waals* forces, both ion induced dipole force, dipole-induced dipole force and electrostatic attraction. The challenge in gas storage field is to obtain a high hydrogen capacity at ambient temperature.

#### 2.1.2.3.1.2 Factors influencing on H<sub>2</sub> storage in MOFs

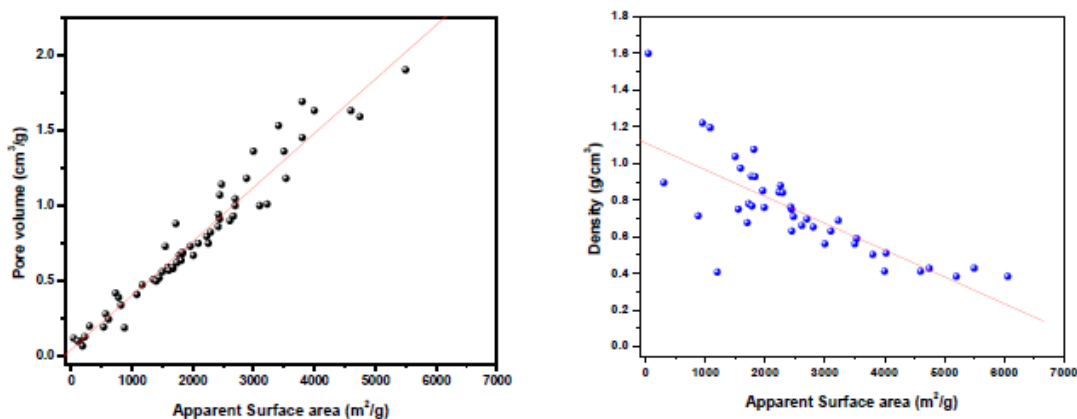
There are many factors influencing on hydrogen storage in MOFs such as, surface area and pore volume, pore size, accessible metal and polarizable ligand.

##### 2.1.2.3.1.2.1 Surface area and pore volume

Grand Canonical Monte Carlo simulations<sup>(80)</sup> were used to predict adsorption isotherms for hydrogen in a series of MOFs, which revealed that there were three adsorption regimes: at low pressure (loading), hydrogen uptake correlated with the heat of adsorption (the adsorbate-adsorbent binding energy); at intermediate pressure, uptake correlated with the surface area; and at the highest pressure, uptake correlated with the free volume. The surface area and free volume, which were calculated from the crystal structure, were used to estimate the potential of these materials for hydrogen storage in MOFs.

In Figure 2.29 a), it displays a positive correlation for MOFs between surface area (m<sup>2</sup>/g) and pore volume(cm<sup>3</sup>/g), while the

negative correlation between surface area ( $\text{m}^2/\text{g}$ ) and density ( $\text{g}/\text{cm}^3$ ) is shown in Figure 2.29 b). It implies that materials with high surface area and high pore volume have lower density.

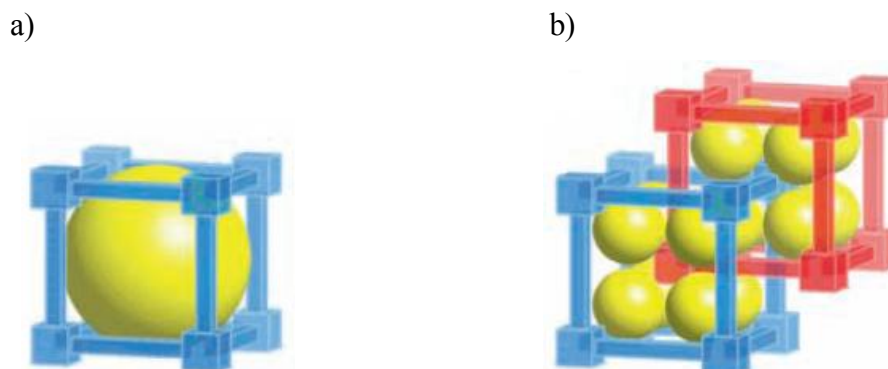


**Figure 2.29** Correlation of MOFs between surface area and a) pore volume; b) density (d), calculated from completely degassed materials i.e. free of solvent in the cavities or coordinated.<sup>(80)</sup>

#### 2.1.2.3.1.2.2 Pore size

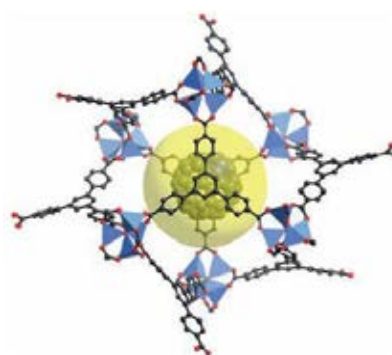
MOFs with large pores size will produce empty space, away from the walls, that will little interact to the hydrogen. In order to maximize the hydrogen-MOF interactions, which increase the uptake capacity, MOFs with smaller pore sizes are essential. Different ways have been pursued to produce MOFs with reduced pore sizes.

The most predominant strategy called “*catenation*”, (Figure 2.30) which the interpenetration of two or more frameworks occurred.<sup>(81)</sup> The very long ligands often results in catenated networks, if the pores of the network are large enough to accommodate the metal-carboxylate clusters, a second network is built inside the first one, which generate reduced pore sizes and free volume materials more than the corresponding non-catenated structure.<sup>(82)</sup> However, controlling interpenetration is very challenging, how to construct materials with small pore sizes that still maintain high surface area and not too high density.



**Figure 2.30** a) Schematic representation of the repeat unit of a MOF with secondary building units (SBUs) shown as cubes and linkers as rods. The yellow sphere represents the large pore within the framework; b) interpenetration of two identical frameworks.<sup>(83)</sup>

Another strategy to improve hydrogen uptake is *impregnation*, which a non-volatile well-anchored guest is inserted to provide additional hydrogen absorptive sites.<sup>(83)</sup> For example, Impregnated MOF-177 with  $C_{60}$  molecules encapsulated can provide additional surface absorption sites as presented in Figure 2.31.

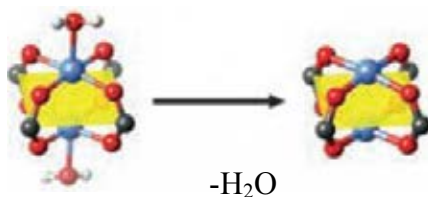


**Figure 2.31** Impregnated MOF-177 with  $C_{60}$  molecules.<sup>(83)</sup>

#### 2.1.2.3.1.2.3 Accessible metal site

In fact, the axial coordination position of the metal ion can be occupied by a water ligand, which can be easily removed by heating. The *open metal site* with coordinatively unsaturated metal ions could act as strong polarizing centers for adsorbed molecules<sup>(83,84)</sup> (Figure 2.32).





**Figure 2.32** Schematic representation of removing water ligand at the axial coordination position.<sup>(83)</sup>

#### 2.1.2.3.1.2.4 Polarizable ligand

Another approach to enhance the hydrogen-MOF interaction is using polarizable ligands. It should induce a dipole in the hydrogen molecule and increase the binding affinities, which increase the hydrogen uptake capacity.

The amount of gas adsorbed on a solid called “hydrogen storage capacity” can be expressed in several forms. The commonly applied definitions in hydrogen storage are the *weight percent (wt%) storage capacity* and the *volumetric storage capacity (vol)*. The *wt%* storage capacity is defined as the mass of hydrogen adsorbed ( $m_{H_2}$ ) over the total mass, including adsorbent ( $m_s$ ) and adsorbate, as shown in the following equation:

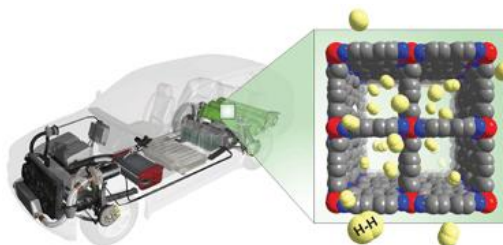
$$wt\% = \frac{m_{H_2}}{m_{H_2} + m_s} * 100$$

The volumetric uptake is defined as the amount of hydrogen adsorbed ( $m_{H_2}$ ) divided by the volume of the solid adsorbent ( $V_s$ ), while  $\rho_s$  is the packing density of the material, as shown in the following equation:

$$vol = \frac{m_{H_2}}{V_s} = \frac{m_{H_2}}{m_s} \cdot \rho_s$$

The US Department Of Energy (DOE) has set capacity targets based on a storage system that would contain 5-13 kg of hydrogen, which are necessary hydrogen amounts for driving range around 300 miles (480 km).<sup>(85)</sup> For hydrogen storage materials, the On-Board Hydrogen Storage System Targets of DOE is required to achieve system-level capacities of 1.8 kWh/kg system (5.5 wt.% hydrogen) and 1.3 kWh/L (0.040 kg hydrogen/L) in 2015 and the ultimate

targets of 2.5 kWh/kg system (7.5 wt.% hydrogen) and 2.3 kWh/L (0.070 kg hydrogen /L).<sup>(86)</sup> The complete system may include material, tank, regulators, valves, piping, mounting brackets, insulation and cooling system.



**Figure 2.33** Model of car using MOFs as hydrogen storage material.<sup>(87)</sup>

#### 2.1.2.3.2 Gas separation

MOFs have great potential in the selective adsorption characterizations including separation and purification of gas or vapor mixtures. MOFs possess gas adsorption selectivity owing to the molecular sieving effect.<sup>(17)</sup> The petroleum industry concerning about the separation of linear from branched alkanes in gasoline, MOFs can be useful for this purposes due to their selectivity and high thermal stability.

For example, MOF-508 has been demonstrated to be practical in the gas-chromatographic (GC) separation of alkane mixtures,<sup>(88)</sup> which suggests that the matching of the size and shape of the alkanes with the MOF-508 leads to different *van der Waals* interactions, resulting in the separation of alkanes in the MOF-508 column (Figure 2.34).

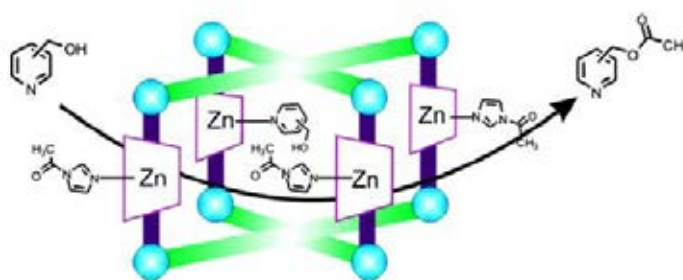


**Figure 2.34** Schematic representation of the GC separation of alkanes with MOF-508; *n*-hexane (1); *n*-pentane (2); 2-methylpentane (3); 2-methylbutane (4); and 2,2-dimethylbutane (5).<sup>(88)</sup>

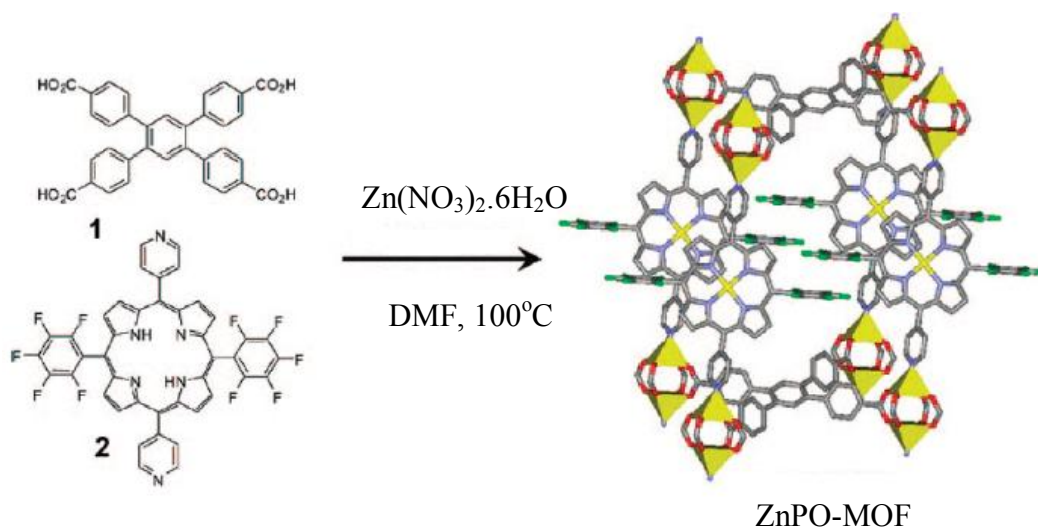
### 2.1.2.3.3 Catalysis

The role of metal-organic frameworks (MOFs) in the field of catalysis is discussed.<sup>(18)</sup> Their structural features with accessible reactive functional groups are presented in term of catalytic function. MOFs can be synthesized in chemical varieties over the other porous materials and also good thermal stability. Like other heterogeneous catalysts, post-reaction separation of MOFs is easy and recyclable.<sup>(89)</sup>

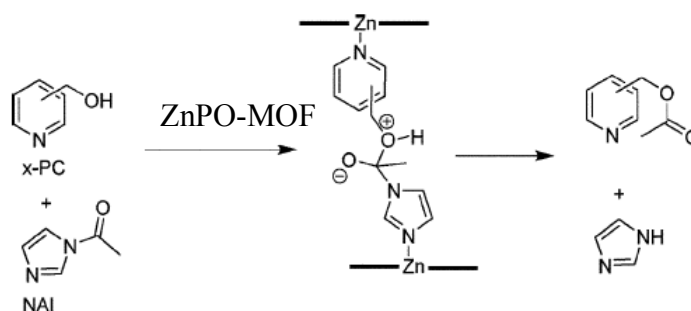
For example, ZnPO-MOF, a pillared porphyrin based MOF, was used for the catalysis of an intermolecular acyl-transfer reaction between *N*-acetylimidazole (NAI) and various pyridylcarbinols (PCs) as shown in Scheme 2.2-2.4.<sup>(90)</sup>



**Scheme 2.2** A scheme showing a unit cell of ZnPO-MOF, acted as catalyst in catalytic acyl transfer to pyridylcarbinol reaction.<sup>(90)</sup>



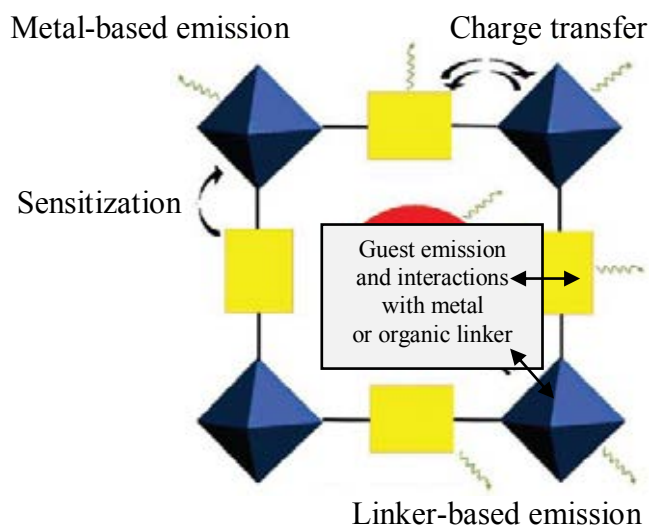
**Scheme 2.3** Synthetic reaction of **ZnPO-MOF**. The unit cell is shown. Color scheme: Zn polyhedra, yellow; O, red; F, green; N, blue; and C, grey.<sup>(90)</sup>



**Scheme 2.4** Mechanism of acyl transfer using ZnPO-MOF as catalyst.<sup>(90)</sup>

#### 2.1.2.3.4 Luminescence

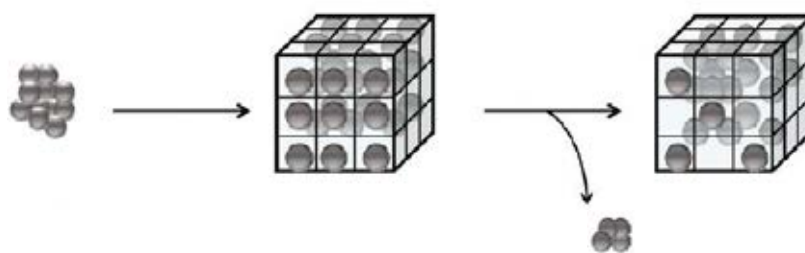
Metal–organic frameworks (MOFs) exhibited a wide range of luminescence (Scheme 2.5). Both the metal cluster and the linker can be used to create luminescence. Conjugated organic linker absorbed in the UV and visible region, thus emission can be directly from the linker, or can involve a charge transfer with the coordinated metal ions or clusters. Transition-metal ions with unpaired electrons can be efficient quenchers.<sup>(19)</sup>



**Scheme 2.5** Scheme of emission possibilities in a porous MOF, where metal clusters (blue octahedral) are linked by organic linkers (yellow rectangles) with an incorporated guest (grey rectangle).<sup>(19)</sup>

### 2.1.2.3.5 Drug delivery

MOFs can be regarded in biomedical applications due to the possibility in adjusting the framework's functional groups, tuning of the pore size, high drug loading capacity and biodegradability. One of the most important challenges in drug delivery research (Scheme 2.6) is the efficient delivery of drugs in the body using nontoxic nanocarriers. Some requirements for an efficient therapy are to (1) control the released drug and avoid the “burst effect”; (2) control matrix degradation; (3) be detectable by imaging techniques and; (4) high drug loading capacity. Beside, toxicity and biocompatibility are the two significant criteria related to a potential drug carrier.<sup>(91)</sup>

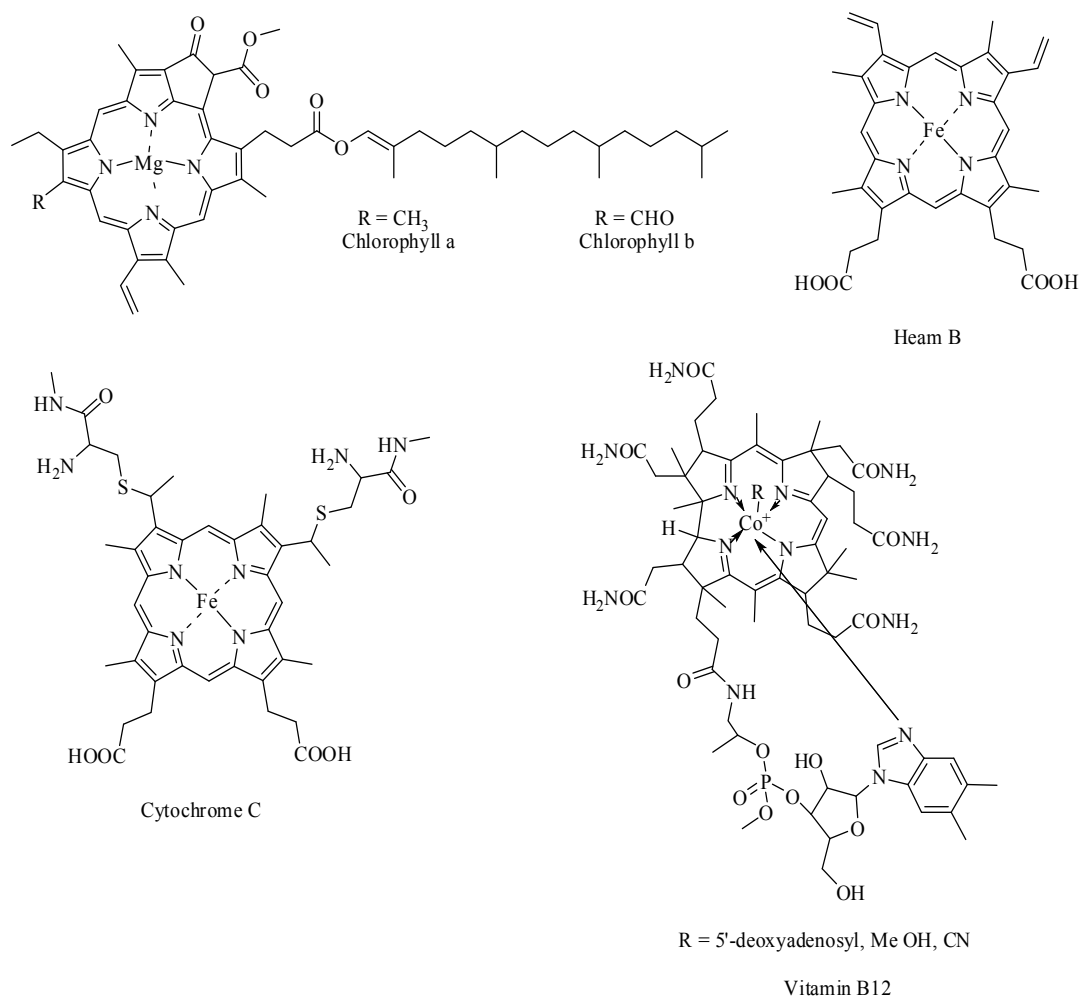


**Scheme 2.6** General scheme for using MOFs as drug delivery vehicles.<sup>(91)</sup>

MOFs exhibited high surface areas, as well as tunable pore size and functionalities, with applications ranging from gas storage to drug delivery. It represented as very interesting porous materials, which is ongoing challenge to study the new topology materials.

## 2.2 Porphyrin

The porphyrins are a class of naturally occurring macrocyclic aromatic compounds. The word “porphyrin” is derived from the Greek “porphura” meaning purple.<sup>(92)</sup> Because of their large  $\pi$ -conjugated systems, all porphyrins are intensely colored. They have been called the pigments and the colors of life. It relies on the full range of biological processes that are performed or catalyzed by porphyrin-containing substances. Variety of metalloporphyrins play an important role in biological activities such as, iron complexes in the haemoprotein and cytochrome C, magnesium complexes in the chlorophylls, and a cobalt complex in Vitamin B<sub>12</sub> as shown in Figure 2.35.

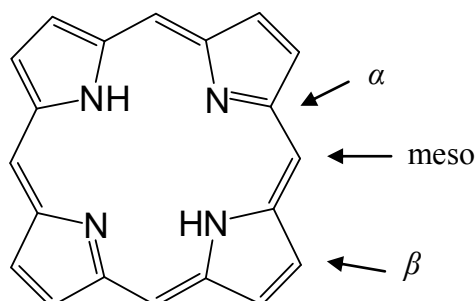


**Figure 2.35** Structures of some naturally porphyrin derivatives.

### 2.2.1 Structure and nomenclature of porphyrins

The porphyrin macrocycle consists of four pyrrole rings joined by four interpyrrolic methine bridges to give a highly conjugated macrocycle as illustrated in Figure 2.36. The aromaticity of porphyrin has been well established both by its chemical and physical properties. These tetrapyrrolic systems have a closed loop of edgewise overlapping  $p$ -orbitals. The 22  $\pi$  electrons available porphyrins make up six different 18e-delocalization pathway which follows Hückel's  $4n+2$  rule for aromaticity. Different positions on the porphyrin periphery are referred by specific names which are eight  $\alpha$ , eight  $\beta$ , and four *meso* positions. The  $\beta$  and *meso* positions are susceptible for substitution by functional groups. In addition to substitute on the periphery of the core, porphyrins can be metallated at the center of the core that

different metal atoms affect different electronic and binding properties than the free-base form.



**Figure 2.36** Porphyrin macrocycle.

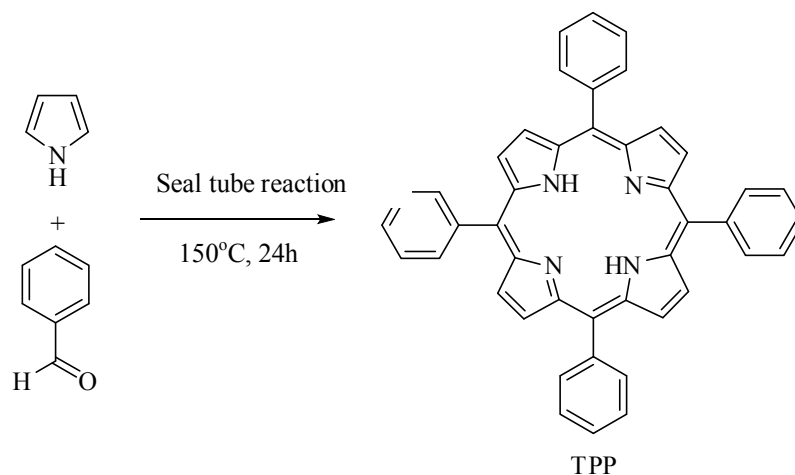
### 2.2.2 Synthetic approach of Porphyrin

Porphyrins have been synthesized by various routes depending on the different substituents on the porphyrin ring. All of the synthetic routes of porphyrins can be divided in four methods based on the number of pyrrolic subunits in starting materials: monopyrrolic, dipyrrolic, tripyrrolic and tetrapyrrolic intermediates. In this thesis, it focused only on monopyrrolic and dipyrrolic.

#### 2.2.2.1 Synthesis of porphyrins via monopyrrole tetramerization

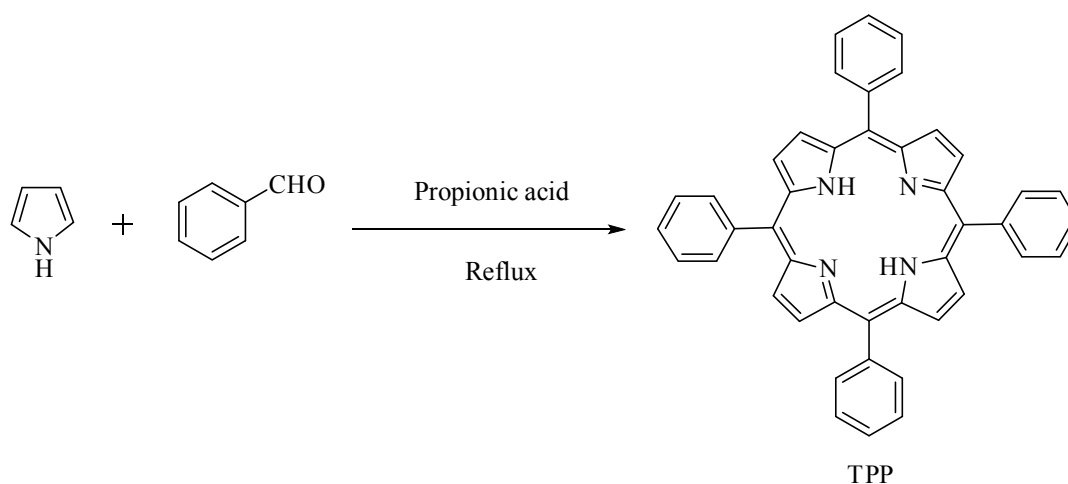
Monopyrrole tetramerization is the simplest synthetic approach to porphyrins which can produce a structurally unique product, if 3- and 4-substituents in the monopyrrole are identical.

One of the simplest porphyrins is tetraphenylporphyrin (TPP) obtained from the condensation of pyrrole and benzaldehyde under an acidic condition (Scheme 2.7). The first route was reported by Rothmund, P. who synthesized the porphyrin in a sealed glass tube at high temperature.<sup>(93)</sup> However, the yields were low and the strong conditions that only a limited number of aromatic aldehydes survived by the procedure.



**Scheme 2.7** Formation of TPP under Rothmund condition.

About three decades later, Adler, Longo and their colleagues described the use of refluxed propionic acid instead of sealed tubes to reproducibly obtain TPP and derivatives in 20–25% yield as shown in Scheme 2.8.<sup>(94)</sup> This procedure has been widely used when large amounts of porphyrins are needed and the corresponding aldehydes are able to survive under the condition of refluxing propionic acid.

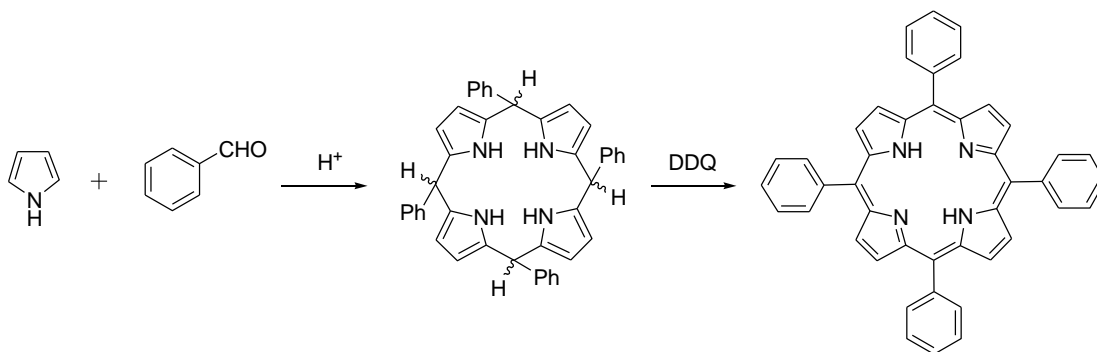


**Scheme 2.8** Synthesis of TPP using Adler-Longo's procedure.

Another porphyrin synthesis was developed by Lindsey's group who used mild reaction condition and obtained in high yields of a wide variety of *meso* tetraarylporphyrins.<sup>(95)</sup> The porphyrins were formed from two-steps reaction of arylaldehydes and pyrrole in the presence of mild acid. In the first step, the acid-



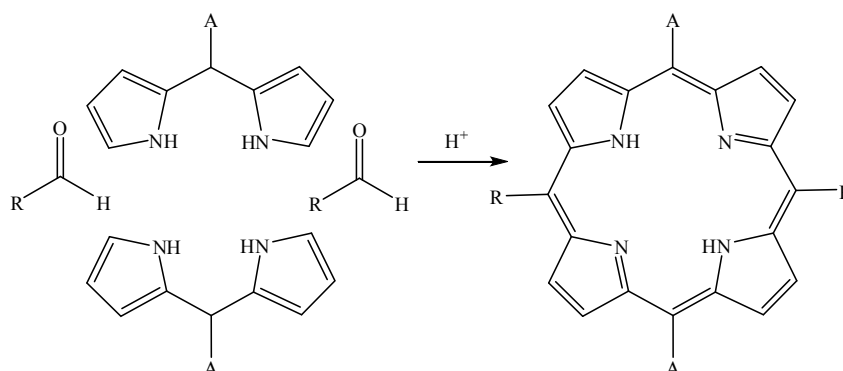
catalyzed condensation reaction is carried out in the presence of trace acid catalyst, usually  $\text{BF}_3 \cdot \text{OEt}_2$  or TFA, yielding tetraarylporphyrinogen. In the second step, the porphyrinogen intermediate is irreversibly oxidized by a quinone derivative, such as 2,3-dichloro-5,6-dicyanobenzoquinone (DDQ), to afford the desired tetraarylporphyrin as illustrated in Scheme 2.9.



**Scheme 2.9** Synthesis of TPP using Lindsey's procedure.

#### 2.2.2.2 Synthesis of porphyrins via dipyrromethanes

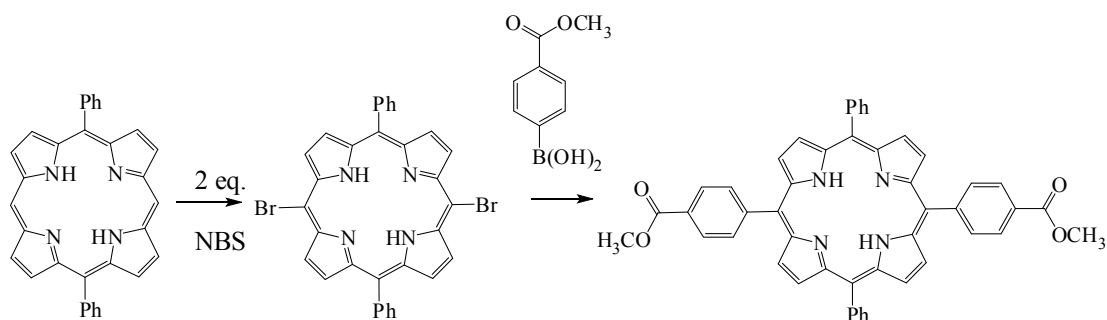
Another approach for the synthesis of substituted porphyrins has been devised in which dipyrrolic starting materials are combined to form tetrapyrrolic compounds. Dipyrromethanes are the intermediates in this approach, involving symmetrically or unsymmetrically substituted dipyrromethanes condensed with aldehydes to acquire the different porphyrin derivatives.<sup>(96)</sup>



**Scheme 2.10** Synthesis of porphyrin from dipyrromethane and aldehyde.

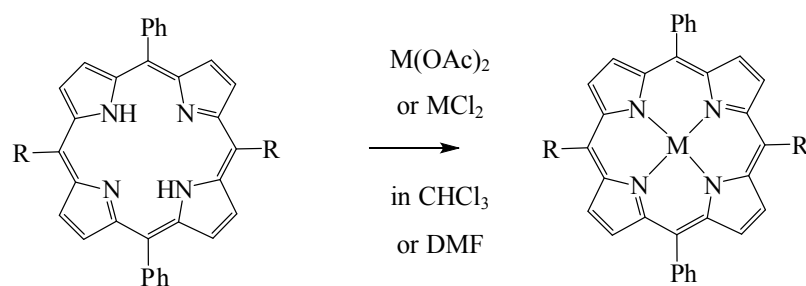
### 2.2.3 Reactions of porphyrins

There are many reactions of porphyrins and their derivatives, which are electrophilic substitutions, nucleophilic substitution, reduction, oxidation, metallation etc. Generally, the most reactive site at the periphery of porphyrins is the *meso*-position. Among the halogenation reactions of aromatic compounds, chlorination and bromination<sup>(97,98)</sup> take place quite easily, while the *meso*-positions have higher reactivity. It was found that some of the bromine-substituted porphyrins can be used as intermediates which were widely used in cross coupling reaction<sup>(99)</sup> catalyzed by compounds of palladium or other transition metals such as, Heck reaction, Sonogashira coupling, and Suzuki coupling to produce the desired product. In this thesis, we used a bromination and, then, Suzuki coupling to synthesize one of porphyrin linker (Scheme 2.11).



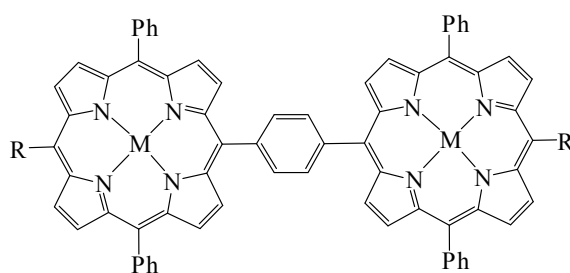
**Scheme 2.11** Bromination and Suzuki coupling reaction of porphyrin, respectively.

The porphyrin nucleus is a tetradentate ligand in which the space available for a coordinated metal. When the metal insertion occurs, two inner pyrrolic protons are removed resulting in a neutral charge metalloporphyrin. The porphyrin complexes with transition metals, such as Zn(II), Cd(II), Cu(II), Ni(II), Fe(II) and Co(II) called *metalloporphyrins*, are very stable.<sup>(100)</sup> The metal insertion into the core of porphyrins can be prepared in different solvent in which chloroform/methanol and dimethylformamide (DMF) are the most popular solvents (Scheme 2.12). Using the solvent should be based on good solubility of porphyrin in that solvent. The metal acetate, as metal salt, is usually used in chloroform/methanol method, while metal chloride is usually employed in DMF.<sup>(101)</sup>

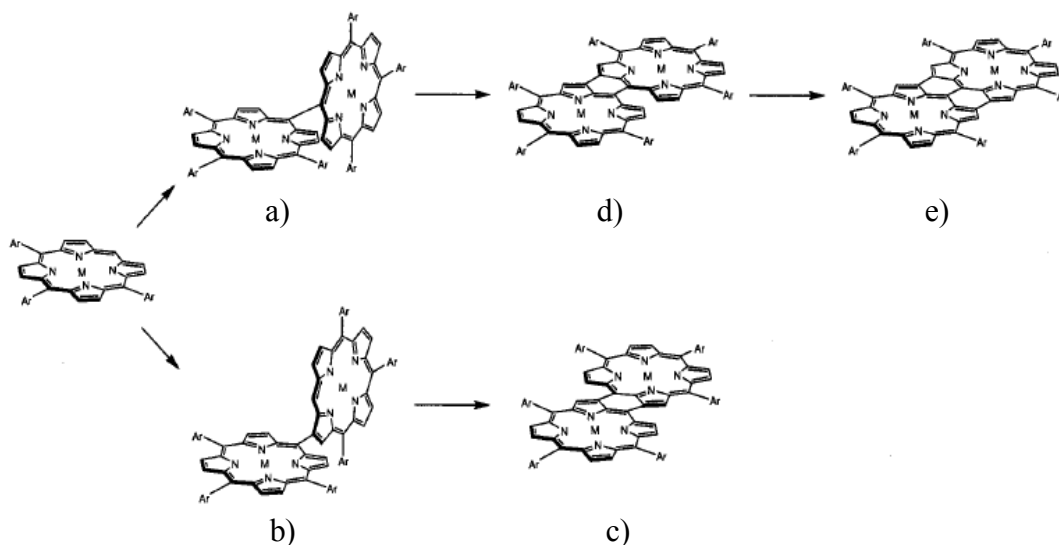


**Scheme 2.12** Metallation of porphyrin.

In order to develop a new organic functional material, the extended  $\pi$ -electronic conjugated system of porphyrin has been studied.<sup>(102)</sup> This system was linked at the *meso*- or  $\beta$ - positions (Scheme 2.13). The nature and position of conjugated system influenced on the properties of porphyrins. A variety of directly linked and fused porphyrin arrays have been synthesized, including 1,4-phenylene-bridged *meso*–*meso* linked diporphyrins<sup>(103)</sup>, *meso*–*meso* singly linked diporphyrins (a), *meso*– $\beta$  singly linked diporphyrins (b), *meso*– $\beta$  doubly linked (fused) diporphyrins (c) and *meso*–*meso*  $\beta$ – $\beta$  doubly linked (fused) diporphyrins (d), and *meso*–*meso*  $\beta$ – $\beta$ – $\beta$  triply linked (fused) diporphyrins (e).<sup>(104)</sup>



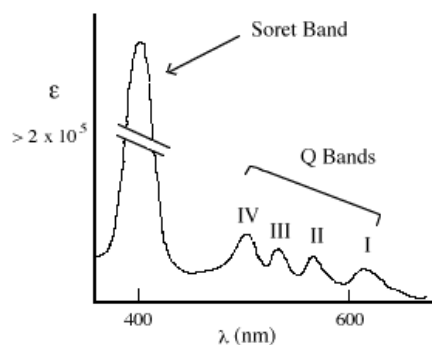
1,4-phenylene-bridged *meso*–*meso* linked diporphyrins



**Scheme 2.13** Schematic representation of extended  $\pi$ -electronic conjugated systems.<sup>(104)</sup>

#### 2.2.4 Spectroscopic properties of porphyrins and their derivatives

Characteristic of porphyrin and their derivatives are highly colored absorbing strongly in the visible region near 400 nm (molar extinction coefficients are about  $10^5 \text{ L}\cdot\text{cm}^{-1}\cdot\text{mol}^{-1}$ ). The main intense absorption band is known as Soret band or B band around 420 nm and four weaker absorption bands between 450–700 nm is recognized as Q bands. Normally, metallated porphyrins show only two Q-bands as presented in Figure 2.37.<sup>(105)</sup> A variation in the peripheral substituents of the porphyrin ring normally results in a slight change in the intensity and wavelength of the absorption bands. However, as long as a cyclic 18  $\pi$  electron-path exists, the intense Soret band is really a major characteristic of their optical spectra.



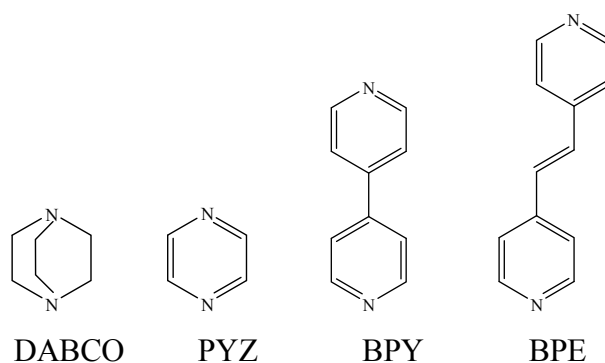
**Figure 2.37** Typical UV-visible absorption spectrum of porphyrins.

The porphyrin macrocycle and its derivatives are amphoteric. Pyrrolic nitrogen atoms at the center of the porphyrin are responsible for its characteristic. The NHs can be deprotonated with strong bases, while the two-imine nitrogen atoms can be protonated with acid. However, metallated porphyrins lack this amphoteric quality because the nitrogen atoms are chelated to the metal with covalent bonds. The NMR spectrum of the aromatic tetrapyrrole shows anisotropic effect. The ring current generated by the applied field induces a local magnetic field similar to that in benzene. The NH protons inside the porphyrin ring system are shifted upfield to as high as  $-5$  ppm in porphyrins, whereas the deshielded *meso*-protons appear at very low field ( $\delta \sim 10$  ppm). The pyrrolic protons are also deshielded and tend to resonate at  $\delta$  8 to 9 ppm, versus  $\delta \sim 6$  ppm in pyrrole. These porphyrin systems make their challenge NMR spectra.

### 2.2.5 Complexation of porphyrin derivatives

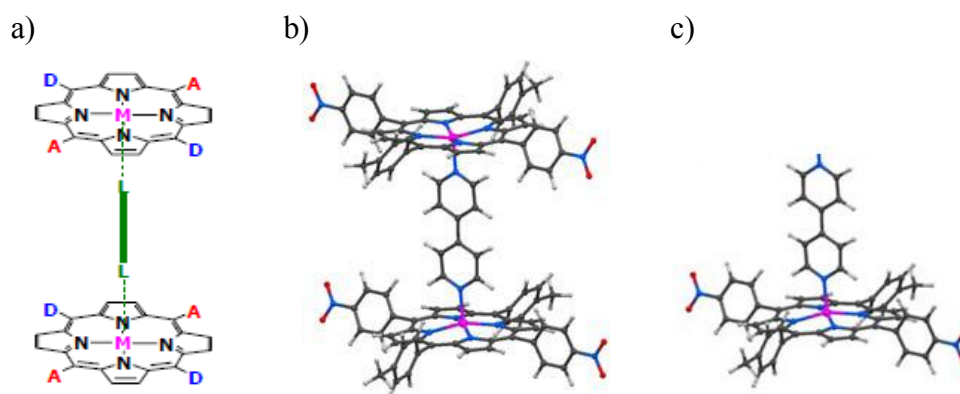
The  $\text{Zn}^{2+}$  has the right size to fit well inside the porphyrin core and to keep the core in a planar conformation, generating metalloporphyrin. Metal-ligand coordination may be employed in metalloporphyrin through either exocyclic ligands or through axial chelation of metal ion at the core, frequently form one or two additional bonds. Penta-coordinated geometry around  $\text{Zn}^{2+}$  ion is more stable than the hexa-coordination geometry.<sup>(106)</sup>

In addition, these ligands also allow the varied distance between the two porphyrin rings in a dimer (Figure 2.38).



**Figure 2.38** Examples of bidentate ligands, acted as pillar, used to coordinate with metalloporphyrin.

Zinc metallated porphyrin and ligands can give three possible structural dimers: (i) sandwich dimer (trimolecular complex, 1:2 ligand-porphyrin ratio), (ii) bimolecular complex, 1:1 ligand-porphyrin ratio, (iii) trimolecular complex, 2:1 ligand-porphyrin ratio, as shown in Figure 2.39.<sup>(107)</sup>



**Figure 2.39** Schematic representation of metalloporphyrin-ligand coordinations; a) and b) represent sandwich dimers; c) represents bimolecular complex.<sup>(107)</sup>

## 2.2.6 Uses and Applications of Porphyrin Derivatives

There are a lot of interesting applications of porphyrins in chemical and biomedical research, for example optoelectronic devices, especially solar cells,<sup>(108)</sup> organic light emitting diodes,<sup>(109)</sup> dyes for food, cloth and printing,<sup>(110)</sup> electrochemical and photocatalysts,<sup>(111)</sup> Photodynamic Therapy (PDT),<sup>(112)</sup> optical sensors<sup>(113)</sup> and organic semiconductors.<sup>(114)</sup>

## 2.2.7 Characterization of porphyrin derivatives

Porphyrinic compounds require many techniques to characterize the structures:

- (a) Nuclear magnetic resonance spectroscopy (NMR)
- (b) Mass spectrometry (MS)
- (c) Ultraviolet-visible spectrophotometry (UV-vis)

### 2.2.7.1 Nuclear Magnetic Resonance Spectroscopy (NMR)

Nuclear magnetic resonance spectroscopy<sup>(115,116)</sup> is a research technique that concerns about the magnetic properties of certain atomic nuclei to determine

physical and chemical properties of atoms or the molecules. NMR spectroscopy relies on the phenomenon of nuclear magnetic resonance and can provide detailed information about the organic structure, dynamics, reaction state, and chemical environment of molecules. This can range from small compounds analyzed with 1-dimensional proton or carbon-13 NMR to large proteins or nucleic acids using 3 or 4-dimensional techniques. The impact of NMR spectroscopy on the natural sciences has been substantial, and can be applied to a wide variety of samples in solution and solid state.

### **2.2.7.2 Mass spectrometry (MS)**

Mass spectrometry<sup>(117,118)</sup> is used to measure the mass-to-charge ratio of charged particles. It is used to determine masses of particles, the elemental composition of a sample, and to elucidate the chemical structures of molecules, such as peptides and other chemical compounds. The MS principle consists of ionizing chemical compounds to generate charged molecules or molecule fragments and measuring their mass-to-charge ratios. Other types of mass spectrometry data are represented as a three-dimensional map. In this form, the mass-to-charge,  $m/z$  is on the  $x$ -axis, intensity on the  $y$ -axis, and an additional experimental parameter, such as time, is recorded on the  $z$ -axis.

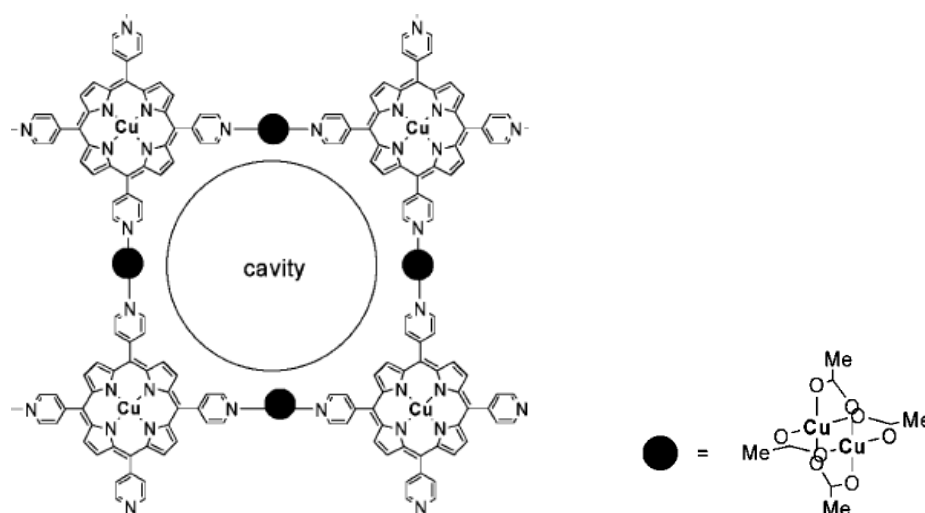
### **2.2.7.3 Ultraviolet-visible Spectrophotometry (UV-vis)**

UV-vis spectrophotometry<sup>(119,120)</sup> is used to determine the absorption or transmission of UV-vis light (180 to 820 nm) by a sample. It can be used to measure concentration of absorbing material based on developed calibration curve of the material. A sample is placed in the UV-vis beam and a graph of the transmittance or absorbance versus the wavelength is acquired. Most spectrometers show absorbance on the vertical axis, and the commonly observed range is from 0 (100% transmittance) to 2 (1% transmittance). The wavelength of maximum absorbance is a characteristic value as  $\lambda_{\text{max}}$ . The absorption or reflectance in the visible range directly affects the color of the chemical involved. In the region of the electromagnetic spectrum, molecules undergo electronic transitions. This technique is complementary to fluorescence spectroscopy, in which fluorescence deals with transitions from the

excited state to the ground state, while absorption measures transitions from the ground state to the excited state.

## LITERATURE REVIEWS

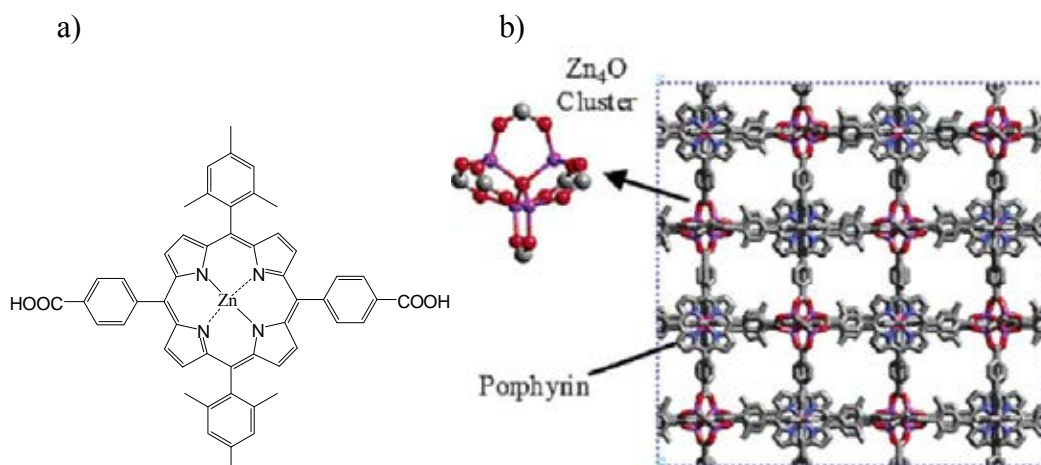
Tetsushi *et. al.*<sup>(121)</sup> reported 2D coordination networks, which were constructed from a dicopper(II) tetraacetate ( $\text{Cu}_2(\text{OAc})_4$ ) and 5,10,15,20-tetra-4-pyridyl-21H,23H-porphine ( $\text{H}_2\text{TPyP}$ ) as a four-connected linker as shown in Figure 2.40. The adsorption of  $\text{N}_2$  presented a type I isotherm with a BET surface area of  $812.08 \text{ m}^2/\text{g}$ .



**Figure 2.40** Construction of 2D coordination network.<sup>(121)</sup>

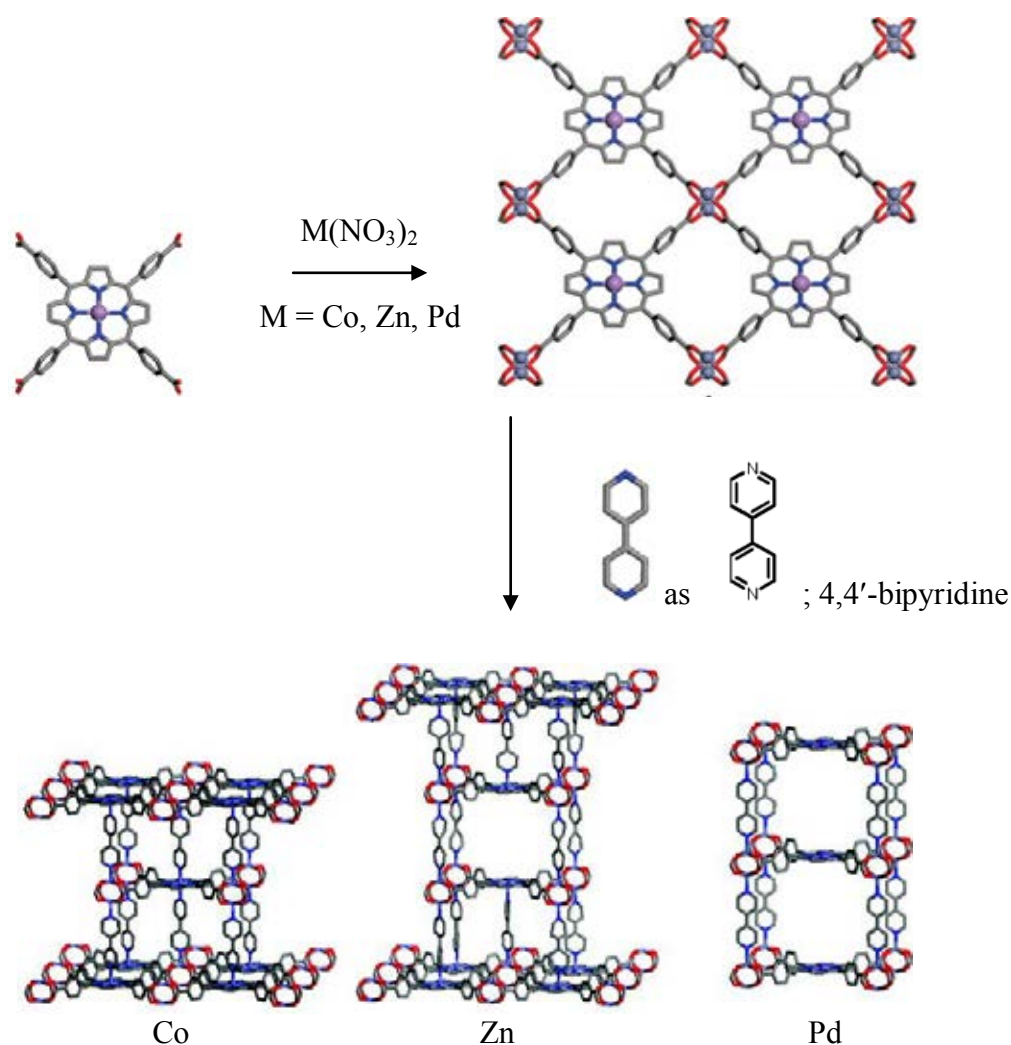
Dennis *et. al.*<sup>(122)</sup> synthesized the robust microporous zinc(II) metalloporphyrin framework solid named PIZA-4 (Figure 2.41) that obtained by slow triethylamine vapor diffusion into a solution of zinc-(II) 5,15-di(*p*-carboxyphenyl)-10,20-di(2',4',6'-trimethylphenyl) porphyrin and  $\text{Zn}(\text{NO}_3)_2$  in 50/50 %vol DMF/chlorobenzene. The obtained MOFs displayed a type I isotherm of nitrogen adsorption with a surface area of  $800 \text{ m}^2/\text{g}$ . His group has been interested in preparing porous metalloporphyrin frameworks as heterogeneous catalysts, such as for the hydroxylation and epoxidation of alkanes and alkenes in which metal in the porphyrin may create a catalytically active solid.





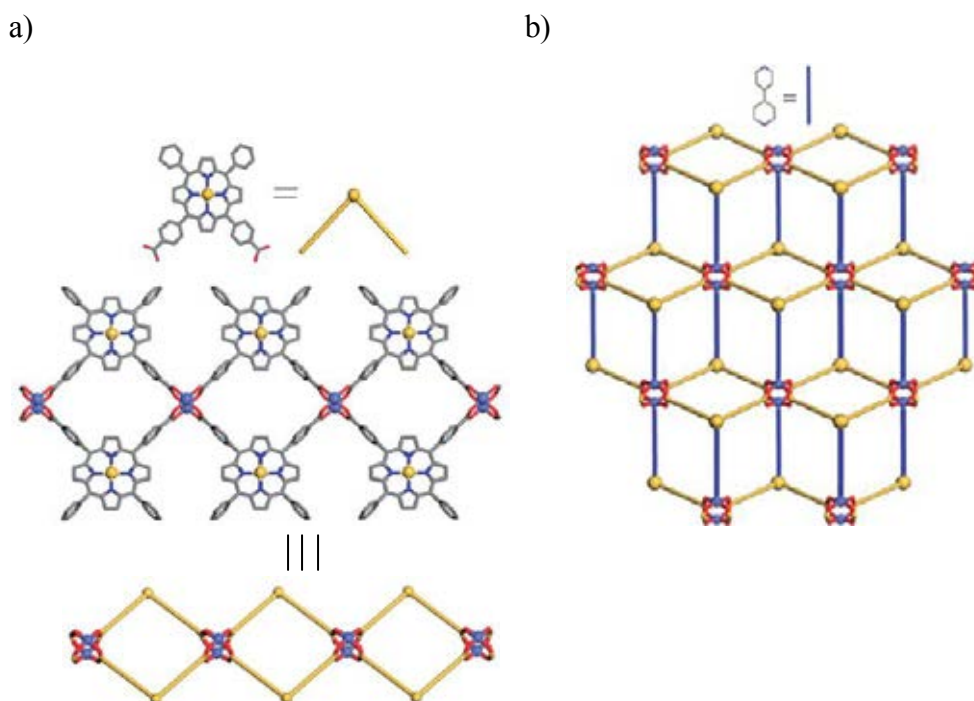
**Figure 2.41** a) Zinc(II) 5,15-di(*p*-carboxyphenyl)-10,20-di(2',4',6'-trimethylphenyl)porphyrin; and b) crystal structure of PIZA-4<sup>(122)</sup>.

Choi *et. al.*<sup>(123)</sup> reported the Porphyrin Paddle-wheel Frameworks(PPFs) series, displaying 3D metal-organic frameworks, while using bipyridine as pillar. These assembled from tetrakis(4-carboxyphenyl)porphine and metal(II) nitrate, such as Co, Zn and Pd with 4,4'-bipyridine via solvothermal reactions in which the resulting solids were PPF-3, PPF-4 and PPF-5 with representing six-(octahedral), five-(square-pyramidal), and four-(square-planar) coordination environments, respectively (Figure 2.42). The different packing structures were presented; PPF-3 possessed stacking pattern as AB, while the stacking in PPF-4 illustrated as ABBA and the AA stacking pattern observed in PPF-5. Besides, the frameworks with coordinatively unsaturated metal centers were important to increase hydrogen adsorption at ambient temperature or to be active sites in catalytic reactions.



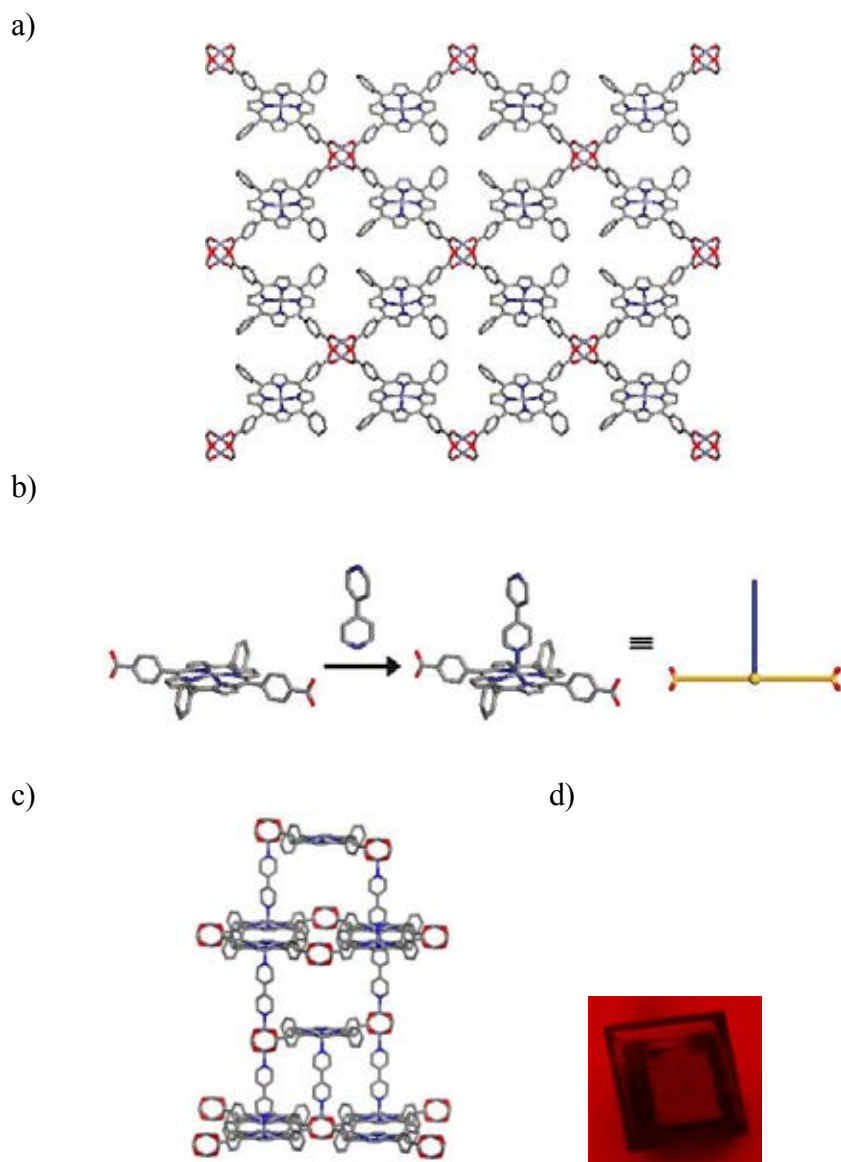
**Figure 2.42** Scheme of PPF-3, PPF-4 and PPF-5, respectively.<sup>(123)</sup>

Choi *et. al.*<sup>(124)</sup> synthesized a pillared porphyrin framework structure, called PPF-6, which constructed from paddle-wheel building units,  $\text{Co}_2(\text{COO})_4$ , and zinc-5,10-di(4-carboxyphenyl)-15,20-diphenylporphyrin (*cis*-ZnDCPP) with 4,4'-bipyridine linker as shown in Figure 2.43. Although zinc ions within the porphyrin core can have coordination numbers, ranging from four (square planar), five (square pyramidal), to six (octahedral), five-coordinated Zn is favored and noticed in PPF-6.



**Figure 2.43** a) Paddle-wheel building units,  $\text{Co}_2(\text{COO})_4$  with *cis*-ZnDCPP and b) 2D layer of PPF-6<sup>(124)</sup>.

Jennifer *et. al.*<sup>(125)</sup> reported a new porphyrin paddle-wheel framework (PPF-25), assembled from a zinc paddle-wheel cluster ( $\text{Zn}_2(\text{COO})_4$ ) and zinc 5,15-di(4-carboxyphenyl)-10,20-diphenylporphyrin( *trans*-DCPP) with 4,4'-bipyridine (Figure 2.44). The T-shaped organometallic structure possessed two carboxylate groups and one pyridyl group to the zinc paddle-wheel SBU. In contrast, the zinc paddle-wheel SBU accepted four carboxylate and two pyridyl groups. The pyridyl group bound to the axial coordination site in the zinc paddle-wheel, while the carboxylate sites connected to equatorial zinc paddle-wheel.



**Figure 2.44** a) 2D porphyrinic assembled from *trans*-DCPP(PPF-25) and zinc paddle-wheel cluster; b) formation of a T-Shaped organometallic structure using *trans*-ZnDCPP and bpy; c) PPF-25 in an *ABCD* stacking mode; and d) PPF-25 crystal<sup>(125)</sup>.

## CHAPTER III

### EXPERIMENTAL

#### 3.1 Chemicals

1. Pyrrole : TCI
2. Benzaldehyde : Fluka
3. 4-Bromobenzaldehyde : TCI
4. 4-Carboxybenzaldehyde : Fluka
5. Terephthalaldehyde : Fluka
6. Paraformaldehyde : Merck
7. Methyl-4-formylbenzoate : Merck
8. N-bromosuccinimide : Fluka
9. 4-ethoxycarbonylphenylboronic acid : TCI
10. 4-methoxycarbonylphenylboronic acid : TCI
11. 4,4'-bipyridine : Merck
12. Palladium tetrakisphosphine : TCI
13. [Bis(trifluoroacetoxy)iodo]benzene : TCI
14. Propionic acid : Merck
15. Trifluoroacetic acid : Sigma-Aldrich
16. Acetic acid : Lab Scan
17. Hydrochloric acid : Merck
18. Potassium bromide : Merck
19. Sodium borohydride : Fluka
20. Potassium carbonate : Sigma-Aldrich
21. Sodium hydrogen carbonate : Riedel-de Haen
22. Potassium hydroxide : Carlo Erba
23. Sodium hydroxide : Lab Scan
24. Bromine solution : Merck
25. Triethylamine : Merck
26. Zinc acetate dihydrate : Fluka

27. Copper acetate monohydrate	: TCI
28. Zinc nitrate hexahydrate	: Fluka
29. Copper nitrate hemi-pentahydrate	: Sigma-Aldrich
30. Chloroform, AR grade	: Lab Scan
31. Ethanol, AR grade	: Lab Scan
32. Dimethylformamide, AR grade	: Lab Scan
33. Methylene Chloride, commercial grade	: Lab Scan
34. Hexanes, commercial grade	: Lab Scan
35. Ethyl acetate, commercial grade	: Lab Scan
36. Tetrahydrofuran	: Lab Scan
37. Methanol, commercial grade	: Lab Scan
38. Acetone, commercial grade	: Lab Scan
39. Toluene	: Lab Scan
40. Deuterated chloroform	: Merck
41. Deuterated methanol	: CIL
42. Hexadeuterated dimethylsulfoxide	: CIL
43. Sodium sulfate (anhydrous)	: Riedel-de Haen
44. Magnesium sulfate (anhydrous)	: Riedel-de Haen
45. Thin layer chromatography (TLC) ;silica gel plates (Kieselgel 60, F <sub>254</sub> , 1 mm)	: Merck
46. Silica gel 60 (0.063-0.200 mm, 70-230 mesh ASTM)	: Merck
47. Nitrogen gas	: TIG
48. Liquid nitrogen	: TIG

### 3.2 Analytical Instruments

All reagents as analytical grade were used as received without further purification. Commercial grade solvent were purified by distillation. Anhydrous solvent were dried over CaH<sub>2</sub> and freshly distillation under nitrogen atmosphere. Column chromatography was carried out on silica gel (Kieselgel 60, 0.063-0.200 mm,

Merck). Thin layer chromatography (TLC) was performed on silica gel plates (Kieselgel 60, F<sub>254</sub>, 1 mm).

<sup>1</sup>H NMR and <sup>13</sup>C NMR spectra were obtained in deuterated chloroform (CDCl<sub>3</sub>), deuterated methanol (MeOD) and hexadeuterated dimethylsulfoxide (DMSO-*d*<sub>6</sub>) using Varian Mercury and Bruker NMR spectrometers operated at 400 MHz for <sup>1</sup>H and 100 MHz for <sup>13</sup>C nuclei (Varian Company, CA, USA and Bruker company, Germany). Chemical shifts ( $\delta$ ) are reported in parts per million (ppm) relative to the residual CHCl<sub>3</sub> peak (7.26 ppm for <sup>1</sup>H NMR and 77.16 ppm for <sup>13</sup>C NMR), MeOD peak (3.31 ppm for <sup>1</sup>H NMR and 49.00 ppm for <sup>13</sup>C NMR) and DMSO-*d*<sub>6</sub> peak (2.50 ppm for <sup>1</sup>H NMR and 39.52 ppm for <sup>13</sup>C NMR). Coupling constants (*J*) are reported in Hertz (Hz).

Mass spectra were obtained using a matrix-assisted laser desorption ionization mass spectrometry (MALDI-MS) technique by using 2-cyano-4-hydroxycinnamic acid (CCA) and dithranol as a matrix.

Absorption spectra were measured in CHCl<sub>3</sub> and DMSO by a Varian Cary 50 UV-vis spectrophotometer at 25°C with a Julabo F33 temperature controller. The samples were scan over range 200-800 nm.

The X-ray powder diffractometer was used for investigation of the phase purity and structure of samples. The XRD patterns were collected on a Rigaku, Dmax 2200/ultima plus X-ray powder diffractometer with a monochromater and Cu K $\alpha$  radiation (40kv, 30mA). The 2-theta angle was ranged from 5 to 50 degree with scan speed of 3 degree/min and sampling width of 0.02 degree. The scattering slit, divergent slit and receiving slit were fixed at 0.5 degree, 0.5 degree and 0.3 mm, respectively. The measured diffractograms were analyzed using MDI software (Jade 6.5)

JEOL JSM-6480LV scanning electron microscope (SEM) was used to identify the morphology and particle size of samples. The samples were dispersed on the carbon tape, depositing on the target, and coated with sputtering gold under vacuum prior to the SEM measurement to provide an electrically conductive surface.

Nitrogen adsorption-desorption isotherms of materials were performed in a BELSORP-II instrument. The materials were pretreated at 250 °C for 3 hours before the surface area measurement. Surface area and micropore volume of the material

were calculated by the BET equation. The external surface areas were obtained from the analysis of adsorption branch of the isotherm by the t-plot method.

Infrared (IR) spectra were performed on a Nicolet Impact 412 FT-IR spectrophotometer (Thermo Fisher Scientific Company, USA) using KBr disk method. The samples were scanned over a range of 500-4000  $\text{cm}^{-1}$  at a resolution of 4  $\text{cm}^{-1}$  and a number of scan was 32. The measurement was controlled by OMNIC software.

Elemental analysis was obtained by CHNS/O Analyzer, Perkin Elmer PE2400 Series II.

Thermogravimetric analysis (TGA) was performed by using Netzsch STA 409C thermogravimetric analyzer that was heated from 25 °C to 1000 °C at heating rate of 10 °C/min under nitrogen gas. The result of thermal stability was reported in percentage weight residue of sample.

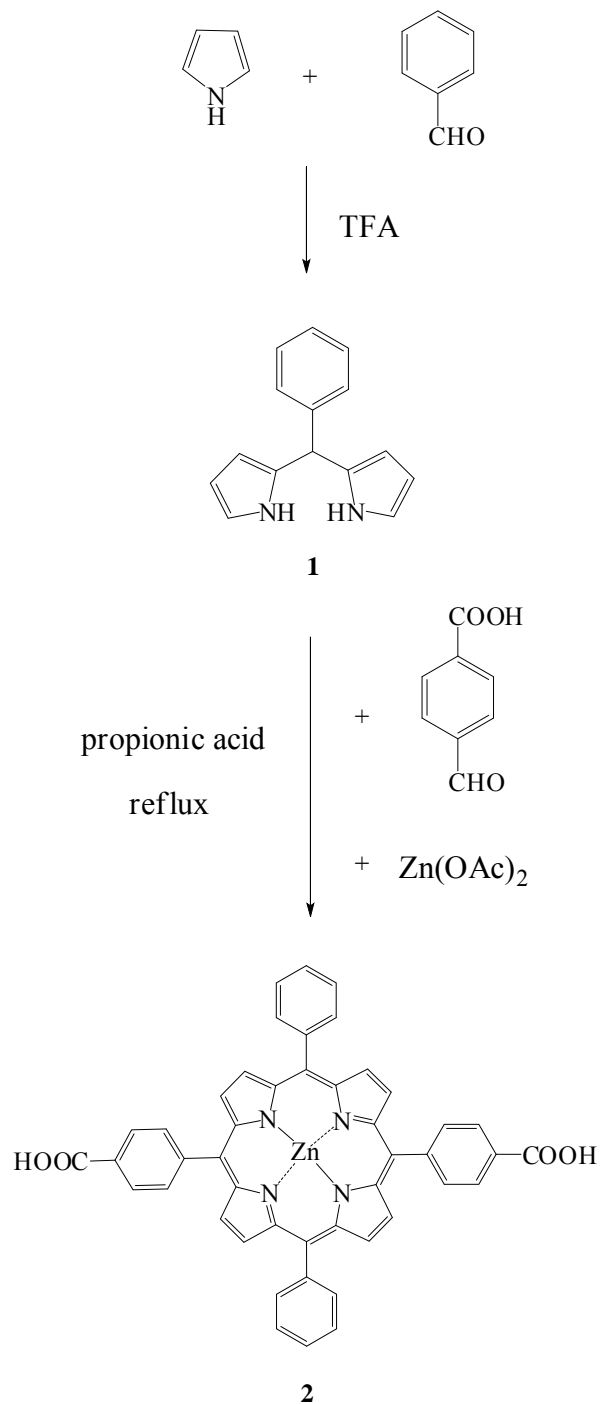
Crystal Data was obtained by Bruker Smart CCD diffractometer.

### 3.3 Experimental Procedure

There were four porphyrin derivatives which were synthesized in this thesis, including the first, dicarboxyphenylporphyrin (part1); the second, 1,4-phenylene-bridged *meso-meso* linked diporphyrin (part2); the third, *meso-meso*  $\beta$ - $\beta$   $\beta$ - $\beta$  triply linked (fused) diporphyrin (part3); and the fourth, tetracarboxybiphenylporphyrin (part4). However, only the last porphyrin derivative was used as organic linker in MOFs construction (part5).

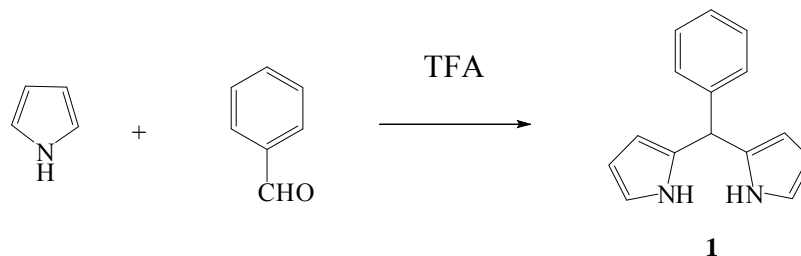


**3.3.1 Part 1: Synthesis of Zinc(II)-5,15-di(4-carboxyphenyl)-10,20-diphenylporphyrin (Zn-DCPP)**



**Scheme 3.1** Synthesis of Zinc porphyrin derivative (**2**).

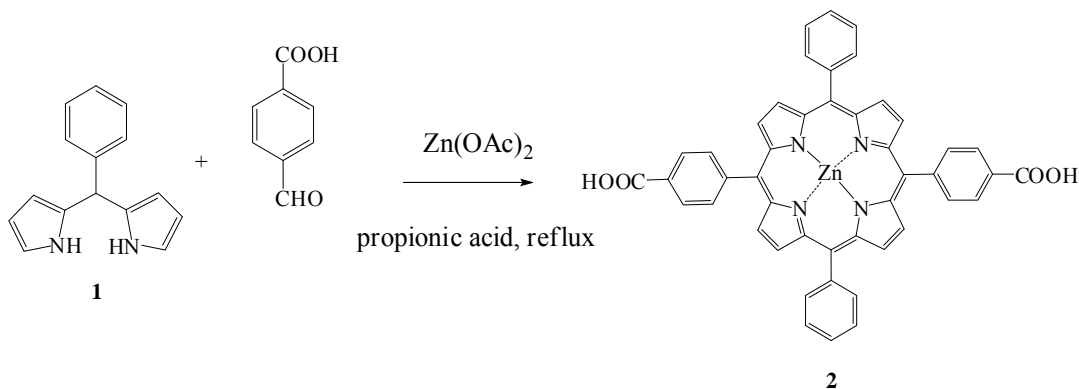
### 3.3.1.1 Synthesis of 5-phenyldipyrromethane (**1**)



A solution of freshly distilled pyrrole (10 mL, 144 mmol) and benzaldehyde (0.55 mL, 5.4 mmol) was stirred with nitrogen bubbling for 15 minutes, then trifluoroacetic acid (0.1 mL, 1.3 mmol) was added. The solution was stirred for 25 minutes at room temperature, at which point no starting aldehyde was evident by TLC analysis (cyclohexane/ EtOAc/ triethylamine; 80:20:1). The mixture was diluted with CH<sub>2</sub>Cl<sub>2</sub> (30 mL), washed with aqueous 0.1 M NaOH (2 × 25 mL) and then washed with water (2 × 25 mL). The organic layer was dried over anhydrous Na<sub>2</sub>SO<sub>4</sub>. The solvent and unreacted pyrrole were removed by rotary evaporation to yield a dark brown oil. Column chromatography (silica gel, cyclohexane/ EtOAc/ triethylamine; 80:20:1) yielded a brown oil (600 mg, 50 %) of the pure dipyrromethane **1**. TLC (silica gel; R<sub>f</sub> = 0.46) was monitored with visualization using bromine vapor. Compound **1** turned bright pink, and the higher oligomers were spots with lower R<sub>f</sub>.

<sup>1</sup>H NMR (400 MHz, CDCl<sub>3</sub>) δ: 7.88 (s (br), 2H, pyrrole-NH), 7.13-7.26 (m, 5H, Ar-H), 6.62 (dd, *J* = 1.6, 2.4 Hz, 2H, pyrrole-H), 6.08 (dd, *J* = 2.8, 3.2 Hz, 2H, pyrrole-H), 5.84 (s, 2H, pyrrole-H), 5.40 (s, 1H, *meso*-H) (Figure A-1).

### 3.3.1.2 Synthesis of Zinc(II)-5,15-di(4-carboxyphenyl)-10,20-diphenylporphyrin (Zn-DCPP, **2**)

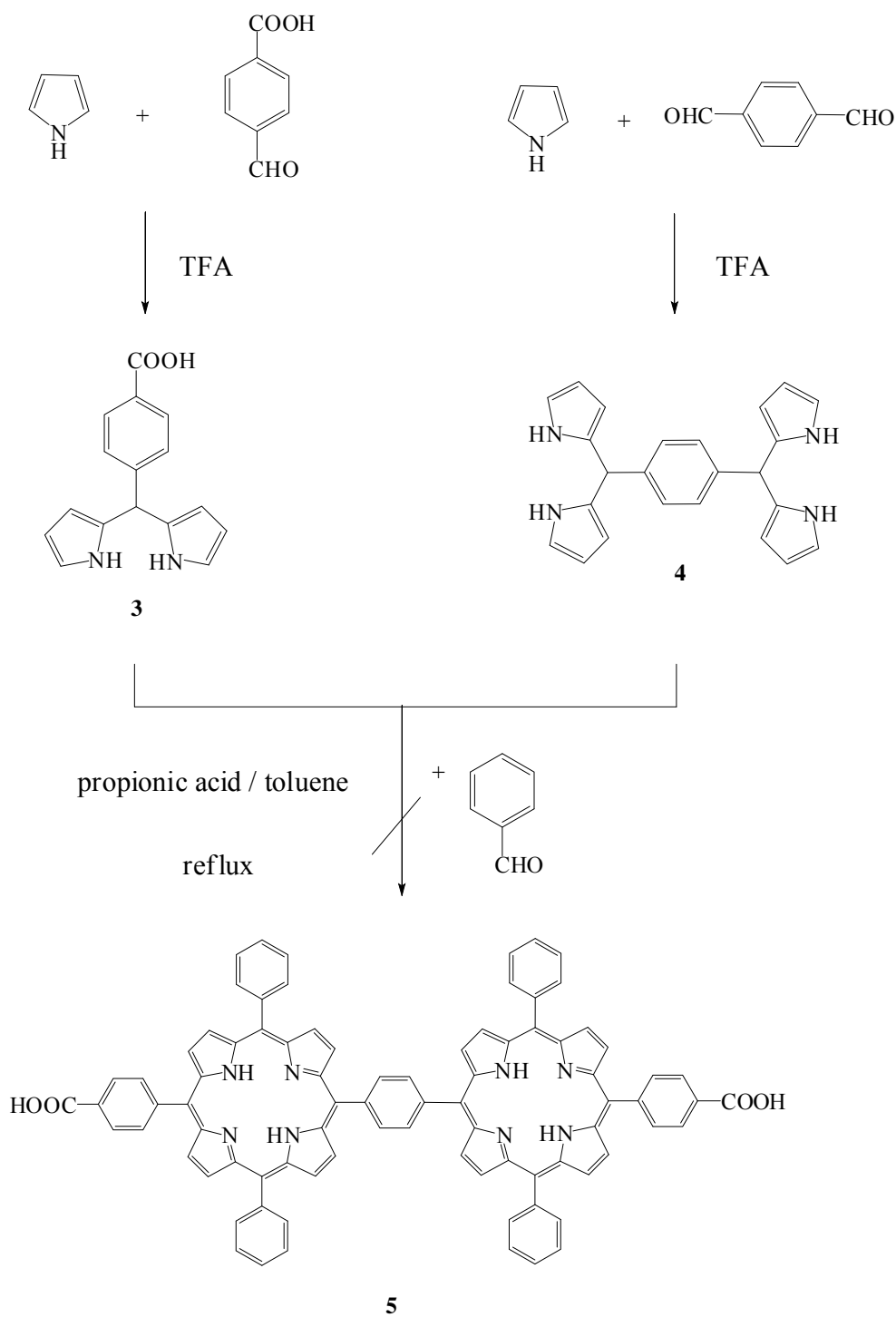


5-phenyldipyrromethane (**1**) (600 mg, 2.7 mmol) and Zn(OAc)<sub>2</sub>·2H<sub>2</sub>O (296 mg, 1.35 mmol) were charged into a 250 mL two-necked round-bottomed flask containing 50 mL of toluene and stirred under nitrogen. It turned to a dark brown solution. In another flask, 4-carboxybenzaldehyde (405 mg, 2.7 mmol) was dissolved in 50 mL of propionic acid and stirred until a clear solution was obtained. The solution was poured into prior prepared solution to provide a dark mixture. The reaction mixture was refluxed for 8 hours in the open air. The solvent was removed under reduced pressure (70°C) and the obtained crude was rinsed with CH<sub>2</sub>Cl<sub>2</sub> (3 × 30 mL). The residual propionic acid was extracted by NaHCO<sub>3</sub> solution (2 × 30 mL) and then washed with water (3 × 30 mL). The organic layer was dried over anhydrous Na<sub>2</sub>SO<sub>4</sub>. Column chromatography (silica gel, MeOH/ CH<sub>2</sub>Cl<sub>2</sub>/ TEA; 20:80:1) yielded a dark purple solid of porphyrin derivative **2** (413 mg, 20%).

<sup>1</sup>H NMR (400 MHz, MeOD) δ: 8.82 (m, 8H, Ar-**H**), 8.37 (d, *J* = 8.4 Hz, 4H, β-**H**), 8.27 (d, *J* = 7.6 Hz, 4H, β-**H**), 8.18 (d, *J* = 7.6 Hz, 4H, Ar-**H**), 7.75 (d, *J* = 6 Hz, 6H, Ar-**H**) (Figure A-2); <sup>13</sup>C NMR (100 MHz, MeOD) δ: 172.74, 151.54, 151.45, 151.08, 148.43, 144.81, 135.64, 135.47, 134.34, 132.75, 132.51, 132.35, 128.60, 128.46, 127.49, 122.10, 121.12 (Figure A-3); MS (MALDI-TOF) calcd for [C<sub>46</sub>H<sub>28</sub>N<sub>4</sub>O<sub>4</sub>Zn]<sup>+</sup> *m/z* 764.140, found 763.435 (Figure A-4); IR (KBr, cm<sup>-1</sup>): 3422 (br s, O-H stretching), 2924 (w, C-H stretching), 1693 (s, C=O stretching), 1600 (w, C=C stretching), 1273 (s, C-O stretching) (Figure A-5); Crystallographic data; Empirical formula: C<sub>27.50</sub> H<sub>24.50</sub> N<sub>3.50</sub> O<sub>3.25</sub> Zn<sub>0.50</sub>; Formula weight : 488.69; Temperature : 296(2) K; Wavelength : 0.71073 Å ; Crystal system, space group: triclinic, P(-1) ; Unit cell

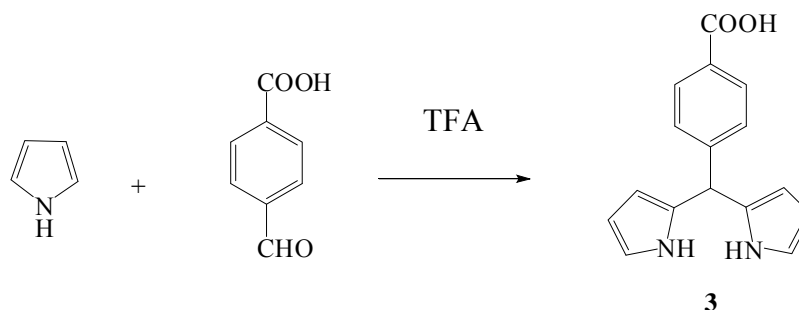
dimensions:  $a = 9.9591(2) \text{ \AA}$   $\alpha = 73.5700(10) \text{ deg.}$ ,  $b = 13.3337(4) \text{ \AA}$ ,  $\beta = 78.7150(10) \text{ deg.}$ ,  $c = 19.4373(5) \text{ \AA}$   $\gamma = 84.0310(10) \text{ deg.}$ ; Volume :  $2424.60(11) \text{ \AA}^3$ ;  $Z$ , Calculated density: 4,  $1.339 \text{ mg/m}^3$ ; Absorption coefficient:  $0.567 \text{ mm}^{-1}$ ; Crystal size:  $0.46 \times 0.30 \times 0.05 \text{ mm}$ ; R indices (all data):  $R1 = 0.0665$ ,  $wR2 = 0.1429$  (Figure A-6).

**3.3.2 Part 2: Synthesis of 1,4-phenylene-bridged *meso-meso* linked di-5-(4-methoxycarbonylphenyl)-10,20-diphenylporphyrin**



**Scheme 3.2** Synthesis of 1,4-phenylene-bridged *meso-meso* linked diporphyrin (5).

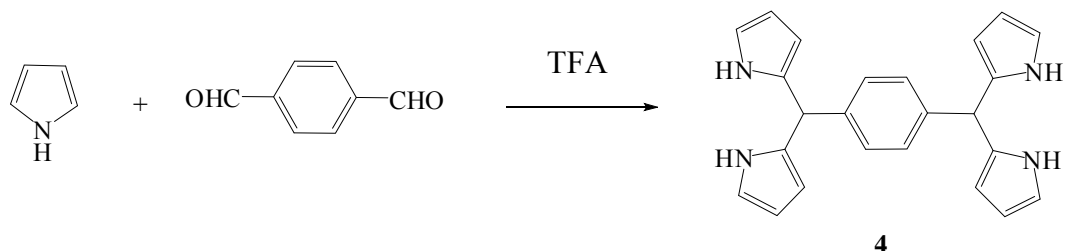
### 3.3.2.1 Synthesis of 5-(4-carboxyphenyl)dipyrromethane (**3**)



A mixture of freshly distilled pyrrole (10 mL, 144 mmol) and 4-carboxybenzaldehyde (0.81 g, 5.4 mmol) was stirred and bubbled with nitrogen gas for 15 minutes in a round bottom flask, then, trifluoroacetic acid (0.1 mL, 1.3 mmol) was added. The solution was stirred at room temperature for 25 minutes. At which point, no starting aldehyde was evident by TLC analysis (cyclohexane/ EtOAc/ triethylamine; 60:40:1). The mixture was diluted with CH<sub>2</sub>Cl<sub>2</sub> (20 mL), washed with aqueous 0.1 M NaOH (2 × 25 mL) and then washed with water (2 × 25 mL). The organic layer was dried over anhydrous Na<sub>2</sub>SO<sub>4</sub>. The solvent and unreacted pyrrole were removed by rotary evaporator to yield dark brown oil. Column chromatography (silica gel, cyclohexane/ EtOAc/ triethylamine; 60:40:1) yielded a brown oil (402 mg, 27%) of pure dipyrromethane **3**. TLC (silica gel; R<sub>f</sub> = 0.37) was visualized using bromine vapor. Compound **3** turned bright pink, and the higher oligomers were spots with lower R<sub>f</sub>.

<sup>1</sup>H NMR (400 MHz, CDCl<sub>3</sub>) δ: 8.05 (d, *J* = 8.4 Hz, 2H, Ar-**H**), 8.02 (s, 2H, pyrrole-N**H**), 7.32 (d, *J* = 8 Hz, 2H, Ar-**H**), 6.72 (dd, *J* = 2.4, 1.6 Hz, 2H, pyrrole-**H**), 6.17 (dd, *J* = 2.8, 3.2 Hz, 2H, pyrrole-**H**), 5.90 (s, 2H, pyrrole-**H**), 5.54 (s, 1H, *meso*-**H**) (Figure A-7).

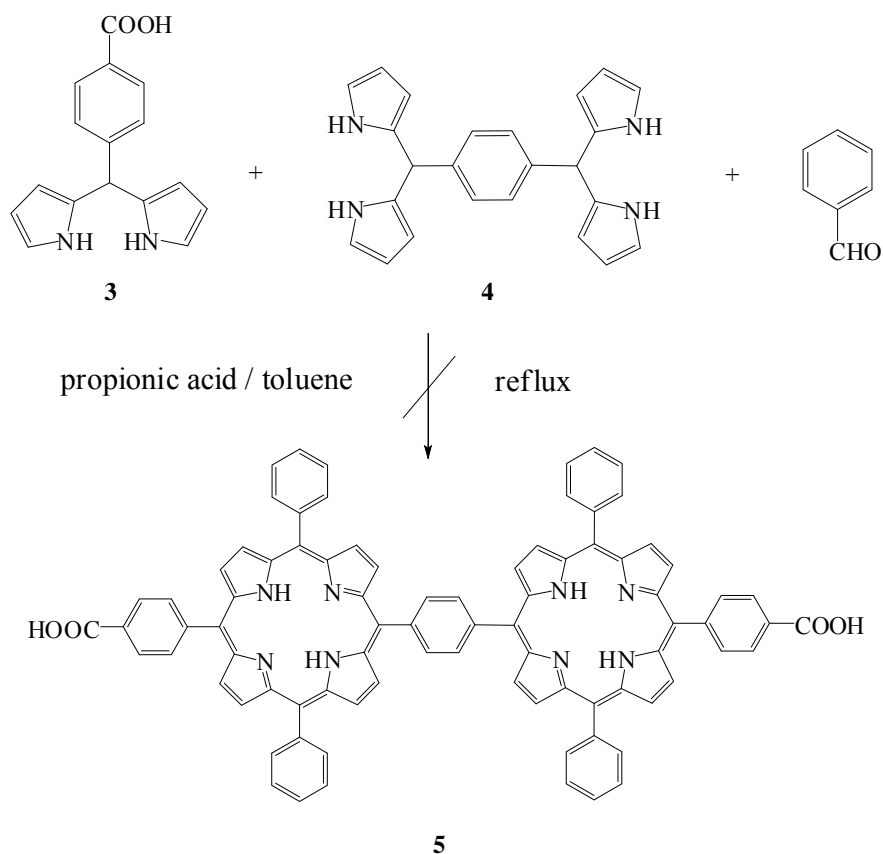
### 3.3.2.2 Synthesis of 1,4-bis(dipyrromethyl)benzene (**4**)



A mixture of freshly distilled pyrrole (5.2 mL, 75 mmol) and terephthalaldehyde (0.4 g, 3 mmol) was introduced and stirred in a round bottom flask with nitrogen bubbling for 15 minutes, then, trifluoroacetic acid (0.07 mL, 0.75 mmol) was added. The solution was stirred at room temperature for 25 minutes. At which point, no starting aldehyde was detected by TLC analysis (cyclohexane/ EtOAc/ triethylamine; 70:30:1). The mixture was diluted with CH<sub>2</sub>Cl<sub>2</sub> (20 mL), washed with aqueous 0.1 M NaOH (2 × 25 mL) and then washed with water (2 × 25 mL). The organic layer was dried over anhydrous Na<sub>2</sub>SO<sub>4</sub>. The solvent and unreacted pyrrole were removed in vacuum to yield dark brown oil. Column chromatography (silica gel, cyclohexane/ EtOAc/ triethylamine; 70:30:1) yielded a light yellow solid (297 mg, 28 %) of the pure dipyrromethane **4**. TLC (silica gel) was visualized by using bromine vapor by which compound **4** turned bright pink, and the higher oligomers had lower R<sub>f</sub>.

<sup>1</sup>H NMR (400 MHz, CDCl<sub>3</sub>) δ: 7.96 (br s, 4H, pyrrole-NH), 7.17 (s, 4H, Ar-H), 6.70 (dd, *J* = 1.6, 2.4 Hz, 4H, pyrrole-H), 6.15 (m, 4H, pyrrole-H), 5.91 (s, 4H, pyrrole-H), 5.46 (s, 2H, *meso*-H) (Figure A-8).

### 3.3.2.3 Synthesis of 1,4-phenylene-bridged *meso-meso* linked di-5-(4-methoxycarbonylphenyl)-10,20-diphenylporphyrin (**5**)

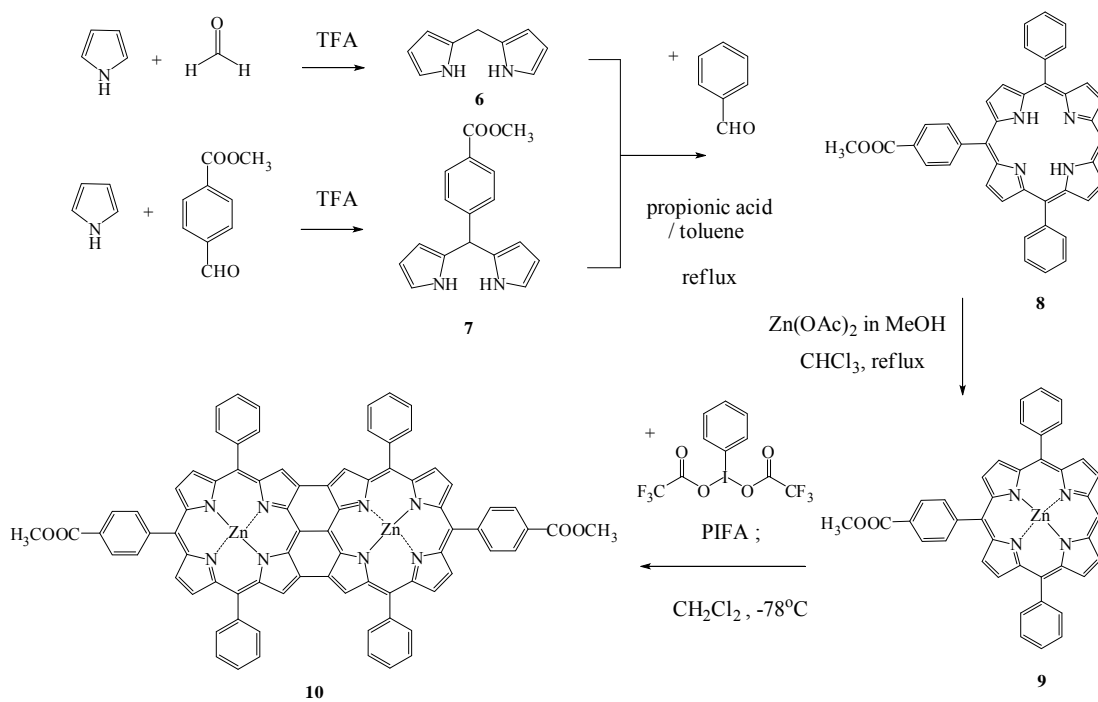


1,4-bis(dipyrromethyl)benzene (**4**) (280 mg, 0.76 mmol) was dissolved with toluene (20 mL) in a two-necked round-bottomed flask under nitrogen atmosphere. The solution was heated at 60 °C and charged with solutions of 5-(4-carboxyphenyl) dipyrromethane (**3**) (400 mg, 1.5 mmol) in toluene (20 mL) and benzaldehyde (0.32 mL, 3.1 mmol). Propionic acid (70 mL) was added into the solution which turned the solution to dark color. The reaction was heated at reflux for 3 hours in the open air. The solvents were removed under reduce pressure and the crude obtained was rinsed with CH<sub>2</sub>Cl<sub>2</sub> (3 × 30 mL). The residual propionic acid was removed by saturated NaHCO<sub>3</sub> solution (2 × 30 mL) and then washed with water (3 × 30 mL). The organic layer was separated, dried over anhydrous Na<sub>2</sub>SO<sub>4</sub>. After column chromatography (silica gel, MeOH/ CH<sub>2</sub>Cl<sub>2</sub>/ TEA; 20:80:1), the desired porphyrin product (**5**) was not obtained.



### 3.3.3 Part3: Synthesis of *meso-meso* $\beta$ - $\beta$ $\beta$ - $\beta$ triply linked (fused) diporphyrin

#### 3.3.3.1 Synthesis of *meso-meso* $\beta$ - $\beta$ $\beta$ - $\beta$ triply linked (fused) diporphyrin pathway I:



**Scheme 3.3** Synthesis of *meso-meso*  $\beta$ - $\beta$   $\beta$ - $\beta$  triply linked (fused) diporphyrin (**10**)

### 3.3.3.1.1 Synthesis of dipyrromethane (**6**)

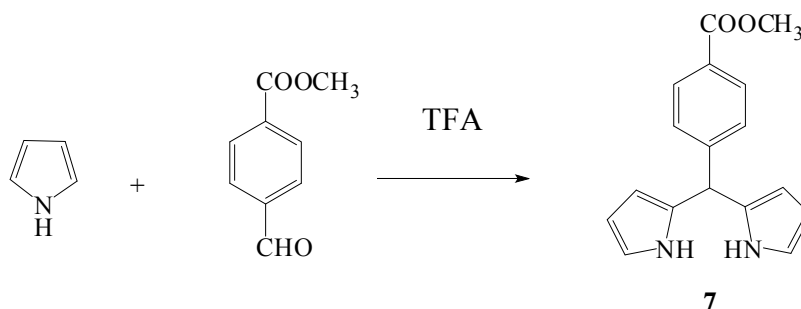


A mixture of freshly distilled pyrrole (14 mL, 202 mmol) and paraformaldehyde (0.3 g, 10 mmol) was stirred in a round bottom flask and bubbled with nitrogen gas for 15 minutes. The mixture was heated at 55°C to obtain a clear solution, and then trifluoroacetic acid (0.15 mL, 2 mmol) was added. The solution was kept stirring for additional until starting aldehyde disappeared monitored by TLC analysis (cyclohexane/ EtOAc/ triethylamine; 80:20:1). The reaction mixture was diluted with CH<sub>2</sub>Cl<sub>2</sub> (30 mL), washed with aqueous 0.1 M NaOH (2 × 25 mL) and then washed with water (2 × 25 mL). The organic layer was dried over anhydrous Na<sub>2</sub>SO<sub>4</sub>. The solvent and unreacted pyrrole were removed by rotary evaporator to yield a dark brown oil. Column chromatography (silica gel, cyclohexane /EtOAc /triethylamine; 80:20:1) provided a white solid (440 mg, 30%) of the pure dipyrromethane (**6**). TLC (silica gel) was monitored by using bromine vapor which compound **6** turned bright pink, and the higher oligomers had different colors and lower R<sub>f</sub>.

<sup>1</sup>H NMR (400 MHz, CDCl<sub>3</sub>) δ: 7.64 (s (br), 2 H, pyrrole-NH), 6.61 (s, 2 H, pyrrole-H), 6.18-6.20 (q, *J*=2.8 Hz, 2H, pyrrole-H), 6.06 (s, 2H, pyrrole-H), 3.93 (s, 2H, CH<sub>2</sub>) (Figure A-9)

### 3.3.3.1.2 Synthesis of 5-(4-methoxycarbonylphenyl)

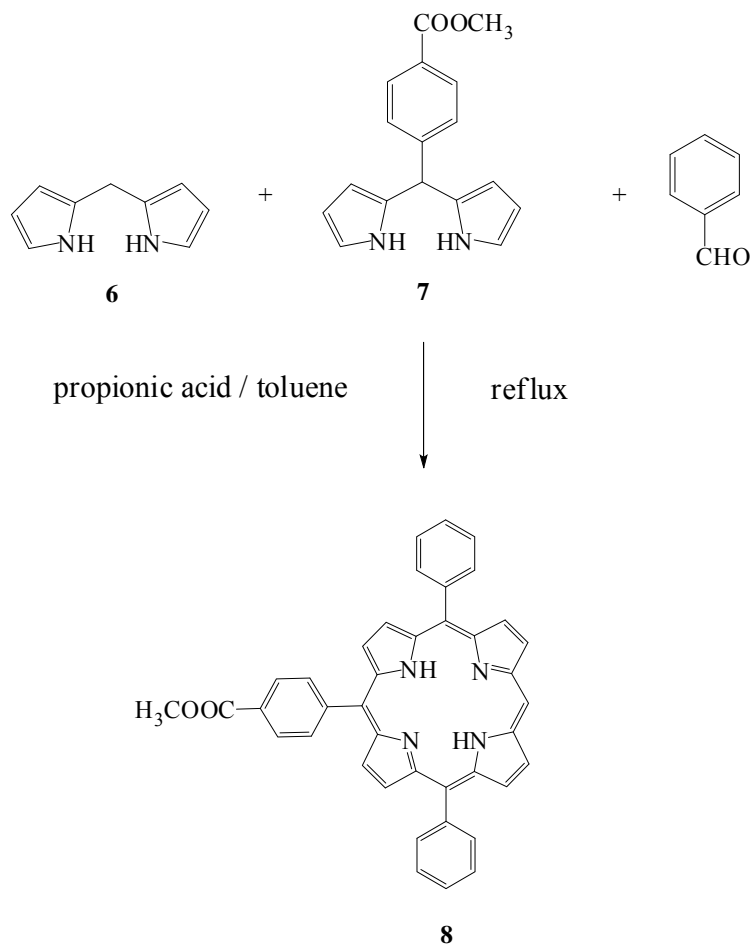
#### dipyrromethane (**7**)



A mixture of freshly distilled pyrrole (15 mL, 216 mmol) and methyl 4-formylbenzoate (1.77 g, 10.8 mmol) was stirred in a round bottom flask with nitrogen gas bubbling for 15 minutes, then trifluoroacetic acid (0.17 mL, 2.2 mmol) was added. The solution was stirred at room temperature until no starting aldehyde was noticed by TLC analysis (cyclohexane/ EtOAc/ triethylamine; 80:20:1). The mixture was diluted with CH<sub>2</sub>Cl<sub>2</sub> (30 mL), washed with aqueous 0.1 M NaOH (2 × 25 mL) and then washed with water (2 × 25 mL). The organic layer was dried over anhydrous Na<sub>2</sub>SO<sub>4</sub>. The reaction mixture was dried under reduced pressure to yield dark brown oil. Column chromatography (silica gel, cyclohexane/ EtOAc/ triethylamine; 80:20:1) gave a pale yellow solid (1,260 mg, 42%) of the pure dipyrromethane (**7**). TLC (silica gel) was used to monitor compound **7** which provided a bright pink spot while the higher oligomers had darker colors with lower R<sub>f</sub> under bromine vapor.

<sup>1</sup>H NMR (400 MHz, CDCl<sub>3</sub>) δ: 7.98 (d (br), *J*=8 Hz, 4H, pyrrole-NH and Ar-H), 7.29 (d, *J*=8 Hz, 2H, Ar-H), 6.72 (d, *J*=1.2 Hz, 2H, pyrrole-H), 6.17 (q, *J*=2.8 Hz, 2H, pyrrole-H), 5.89 (s, 2H, pyrrole-H), 5.52 (s, 1H, *meso*-H), 3.91 (s, 3H, -OCH<sub>3</sub>) (Figure A-10).

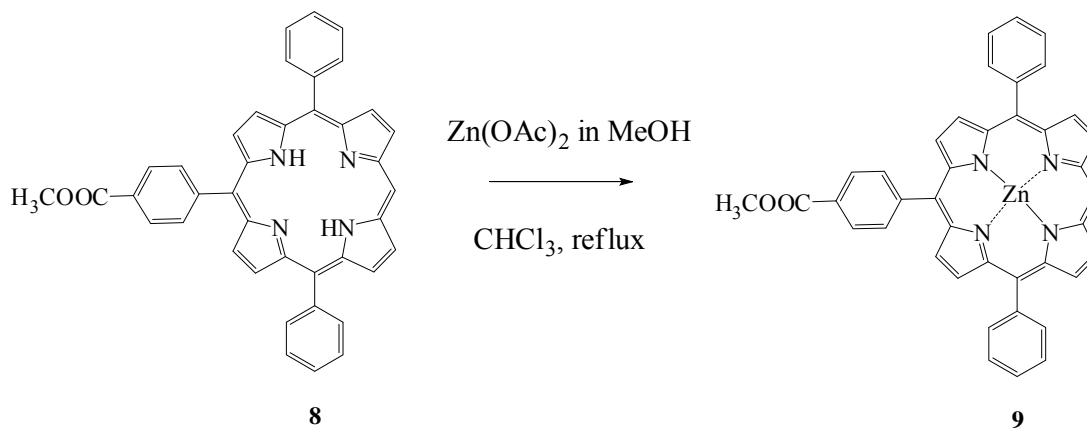
### 3.3.3.1.3 Synthesis of 5-(4-methoxycarbonylphenyl)-10,20-diphenylporphyrin (**8**)



5-(4-methoxycarbonylphenyl) dipyrromethane (**7**) (840 mg, 3 mmol) was dissolved with toluene (30 mL) in a two-necked round-bottomed flask under nitrogen atmosphere. The solution was heated at 60°C to obtain a clear solution and charged with solutions of dipyrromethane (**6**) (440 mg, 3 mmol) in toluene (20 mL) and benzaldehyde (0.6 mL, 6 mmol) in toluene (20 mL). Propionic acid (70 mL) was added into the solution which turned the solution to dark color. The reaction was heated at reflux for 3 hours in the open air. The solvents were removed under reduce pressure and the crude obtained was rinsed with CH<sub>2</sub>Cl<sub>2</sub> (3 × 30 mL). The residual propionic acid was removed by saturated NaHCO<sub>3</sub> solution (2 × 30 mL) and then washed with water (3 × 30 mL). The organic layer was separated, combined and dried over anhydrous Na<sub>2</sub>SO<sub>4</sub>. Column chromatography (silica gel, cyclohexane/ CH<sub>2</sub>Cl<sub>2</sub>; 80:20) yielded a purple solid (40 mg, 2.2 %) of the porphyrin derivative (**8**).

$^1\text{H}$  NMR (400 MHz,  $\text{CDCl}_3$ )  $\delta$ : 10.25 (s, 1H, *meso*-**H**), 9.36 (d,  $J=4.4$  Hz, 2H,  $\beta$ -**H**), 9.04 (d,  $J=4$  Hz, 2H,  $\beta$ -**H**), 8.93 (d,  $J=4.8$  Hz, 2H,  $\beta$ -**H**), 8.83 (d,  $J=4.8$  Hz, 2H,  $\beta$ -**H**), 8.45 (d,  $J=4$  Hz, 2H, Ar-**H**), 8.30 (d,  $J=8$  Hz, 2H, Ar-**H**), 8.25 (d,  $J=7.2$  Hz, 4H, Ar-**H**), 7.80 (d,  $J=6.4$  Hz, 6H, Ar-**H**), 4.11 (s, 3H,  $-\text{OCH}_3$ ),  $-3.02$  (s, 2H, **NH**) (Figure A-11); MS (MALDI-TOF) calcd for  $[\text{C}_{40}\text{H}_{28}\text{N}_4\text{O}_2]^+$   $m/z$  596.221, found 597.252  $[\text{M}+\text{H}]^+$  (Figure A-12).

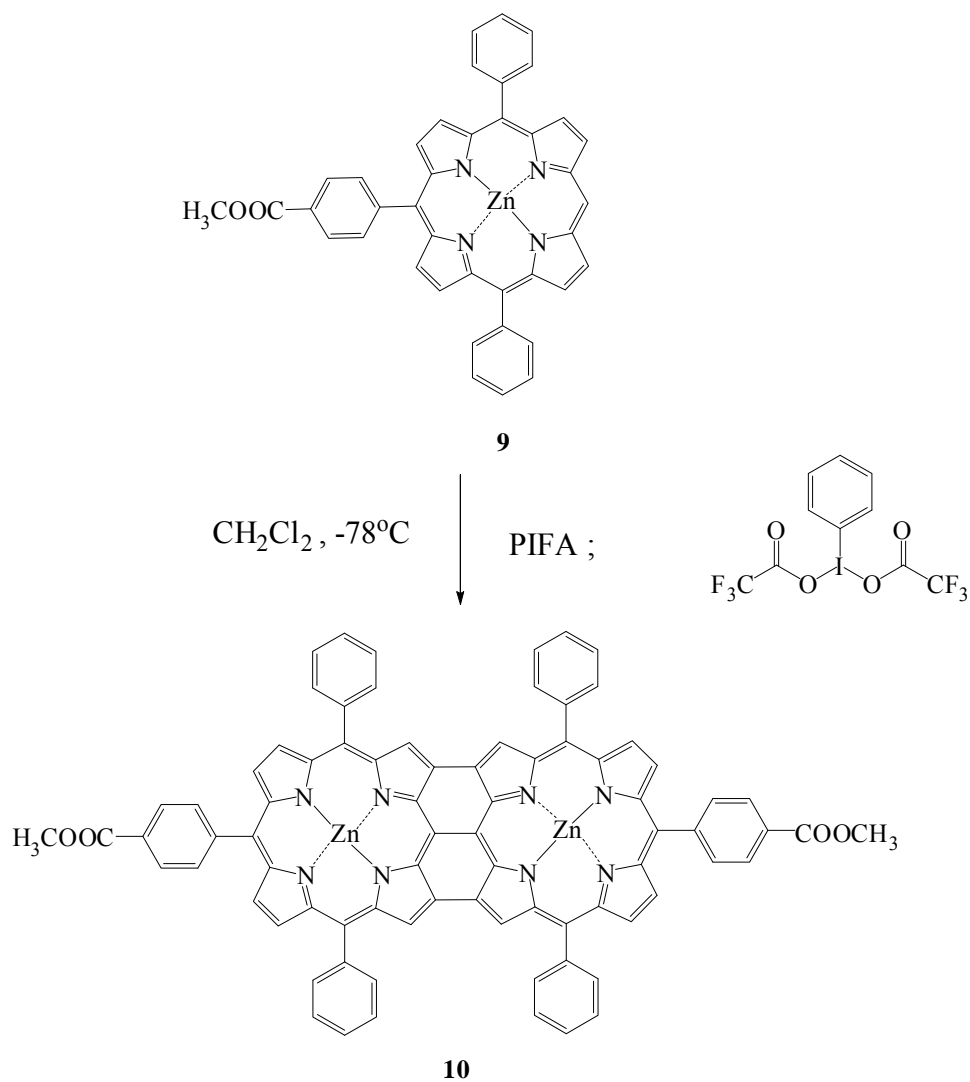
### 3.3.3.1.4 Synthesis of Zinc(II)-5-(4-methoxycarbonylphenyl)-10,20-diphenylporphyrin (**9**)



A saturated solution of  $\text{Zn}(\text{OAc})_2 \cdot 2\text{H}_2\text{O}$  (147 mg, 0.67 mmol) in MeOH (20 mL) was added to a solution of free-base porphyrin derivative (**8**) (40 mg, 0.067 mmol) in  $\text{CHCl}_3$  (40 mL), and the mixture was heated at reflux for 10 hours. After the complete metallation confirmed by TLC, the mixture was washed with water ( $3 \times 30$  mL) and the organic layer was dried over anhydrous  $\text{Na}_2\text{SO}_4$  to yield a reddish purple solid of Zinc porphyrin complex (**9**) (43 mg, quantitative yield).

$^1\text{H}$  NMR (400 MHz,  $\text{CDCl}_3$ )  $\delta$ : 10.20 (s, 1H, *meso*-**H**), 9.36 (d,  $J=4.4$  Hz, 2H,  $\beta$ -**H**), 9.07 (d,  $J=4.4$  Hz, 2H,  $\beta$ -**H**), 9.00 (d,  $J=4.8$  Hz, 2H,  $\beta$ -**H**), 8.91 (d,  $J=4.8$  Hz, 2H,  $\beta$ -**H**), 8.39 (d,  $J=8.4$  Hz, 2H, Ar-**H**), 8.29 (d,  $J=8$  Hz, 2H, Ar-**H**), 8.23 (d,  $J=7.2$  Hz, 4H, Ar-**H**), 7.76-7.81 (m, 6H, Ar-**H**), 4.11 (s, 3H,  $-\text{OCH}_3$ ) (Figure A-13); MS (MALDI-TOF) calcd for  $[\text{C}_{40}\text{H}_{26}\text{N}_4\text{O}_2\text{Zn}]^+$   $m/z$  658.135, found 659.293  $[\text{M}+\text{H}]^+$  (Figure A-14); UV-vis  $\lambda_{\text{abs}}$ : 414, 544 nm. (Figure 4.2).

**3.3.3.1.5 Synthesis of *meso-meso*  $\beta\text{-}\beta\text{-}\beta\text{-}\beta$  triply linked (fused) di-Zinc(II)-5-(4-methoxycarbonylphenyl)-10,20-diphenylporphyrin (**10**)**

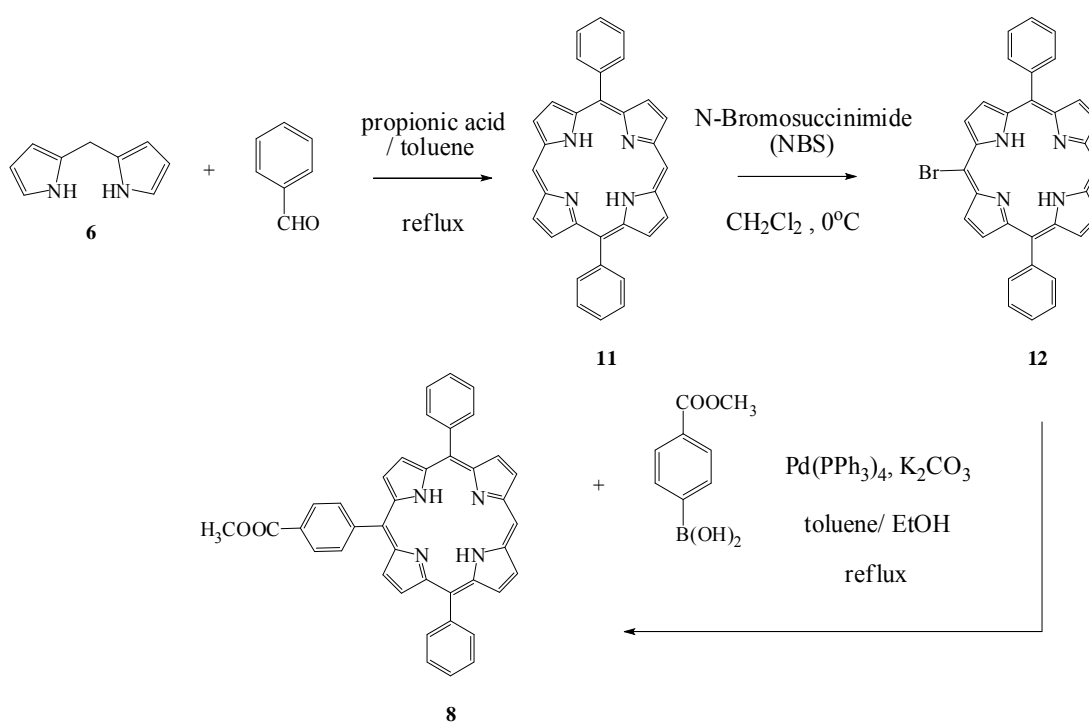


Zinc Porphyrin complex (**9**) (20 mg, 0.03 mmol) was dissolved in dry  $\text{CH}_2\text{Cl}_2$  (30 mL) in a round-bottomed flask. The solution was cooled to  $-78^\circ\text{C}$  by a dry ice-acetone bath, and PIFA ([bis(trifluoroacetoxy)iodo]benzene) (32 mg, 0.074 mmol) was added. Then, the cooling bath was removed, and the mixture was stirred at ambient temperature for 2 hours. A suspension of  $\text{NaBH}_4$  (11.4 mg, 0.3 mmol) in methanol (5 mL) was added, and stirred for 0.5 hour. The reaction mixture was poured into water and extracted with  $\text{CH}_2\text{Cl}_2$  ( $3 \times 30$  mL). The organic layer was washed with saturated  $\text{NaHCO}_3$  solution ( $2 \times 30$  mL) and water ( $3 \times 30$  mL) and dried

over anhydrous  $\text{Na}_2\text{SO}_4$ . Column chromatography (silica gel,  $\text{MeOH}/\text{CH}_2\text{Cl}_2$ ; 1:99) yielded a blue-violet solid (9 mg, 30%) of the triply-fused diporphyrin derivative (**10**).

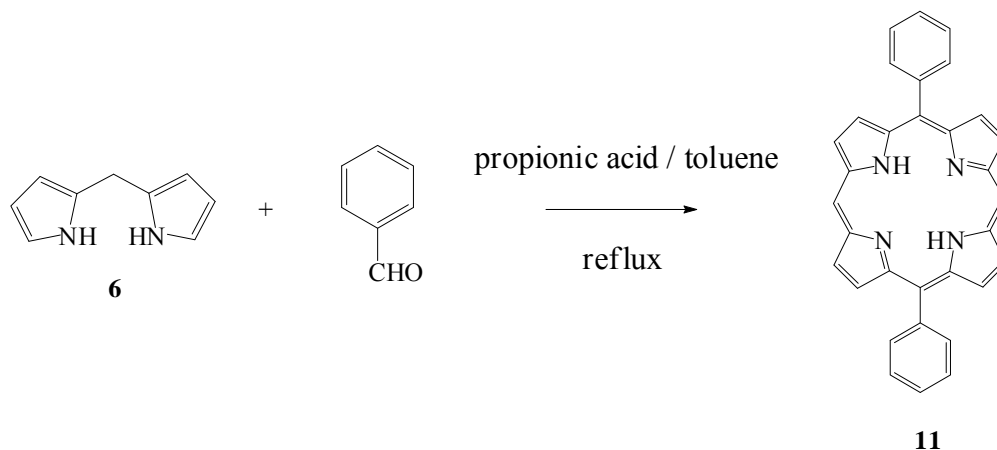
$^1\text{H}$  NMR (400 MHz,  $\text{CDCl}_3$ )  $\delta$ : 7.16 (s, 12H,  $\beta\text{-H}$ ), 7.18 (s, 20H, Ar-H), 7.23 (s, 8H,  $\beta\text{-H}$ ), 4.10 (s, 6H,  $-\text{OCH}_3$ ) (Figure A-15); MS(MALDI-TOF) calcd for  $[\text{C}_{80}\text{H}_{46}\text{N}_8\text{O}_2\text{Zn}_2]^+$  1314.092 m/z, found 1314.392 (Figure A-16);  $\lambda_{\text{abs}}$ : 418, 561-579 nm. (Figure 4.2).

### 3.3.3.2 Synthesis of *meso-meso* $\beta\text{-}\beta$ $\beta\text{-}\beta$ triply linked (fused) diporphyrin pathway II :



**Scheme 3.4** Synthesis of porphyrin derivative (**8**)

### 3.3.3.2.1 Synthesis of 10,20-diphenylporphyrin (**H<sub>2</sub>DPP**, **11**)

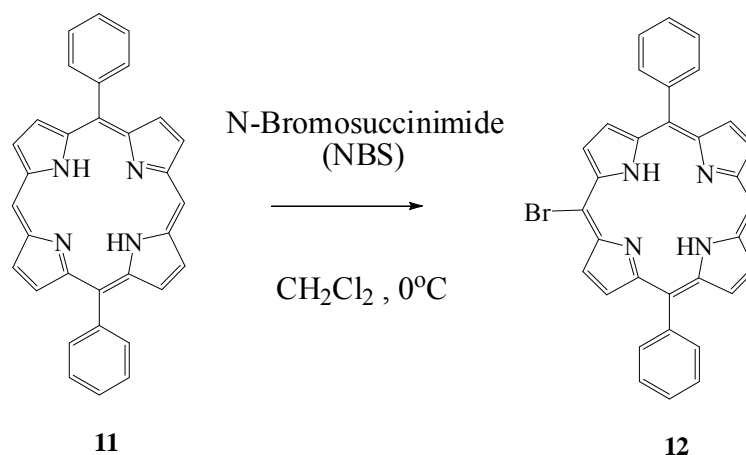


Dipyrromethane (**6**) (380 mg, 2.6 mmol) was dissolved in toluene (20 mL) in a two-necked round-bottomed flask and charged with solutions of benzaldehyde (0.27 mL, 2.6 mmol) in toluene (20 mL). Propionic acid (50 mL) was added into the solution which turned the solution to dark color. The reaction was heated at reflux for 3 hours in the open air. The reaction mixture was dried under reduce pressure and the crude obtained was dissolved in  $\text{CH}_2\text{Cl}_2$  ( $3 \times 30$  mL). The residual propionic acid was removed by saturated  $\text{NaHCO}_3$  solution ( $2 \times 30$  mL) and then washed with water ( $3 \times 30$  mL). The organic phase was separated and dried over anhydrous  $\text{Na}_2\text{SO}_4$ . Column chromatography (silica gel, EtOAc/ Hexane ; 10:70) yielded a purple solid (98 mg, 16%) of the porphyrin derivative (**11**).

$^1\text{H}$  NMR (400 MHz,  $\text{CDCl}_3$ )  $\delta$ : 10.34 (s, 2H, *meso*-**H**), 9.42 (d,  $J=4.8$  Hz, 4H,  $\beta$ -**H**), 9.10 (d,  $J=4.4$  Hz, 4H,  $\beta$ -**H**), 8.27-8.30 (m, 4H, Ar-**H**), 7.81-7.82 (m, 6H, Ar-**H**), -3.13 (s, 2H, **NH**) (Figure A-17).



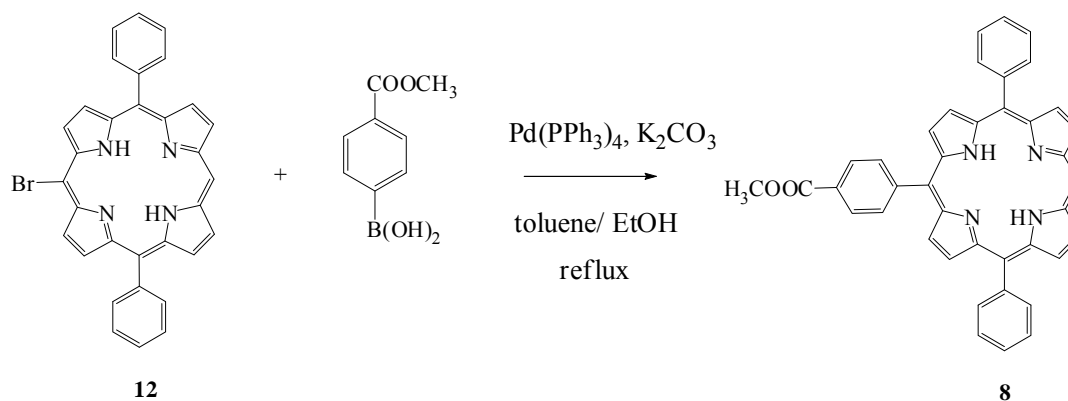
### 3.3.3.2.2 Synthesis of 5-bromo-10,20-diphenylporphyrin ( $H_2DPP(Br)$ , **12**)



10,20-diphenylporphyrin (**10**) (80 mg, 0.17 mmol) was dissolved in 40 mL of dry  $CH_2Cl_2$  and the solution was cooled to  $0^\circ C$  by an ice bath. To neutralize the acid formed, pyridine (0.16 mL) was added and then solution of *N*-bromosuccinimide (NBS) (31 mg, 0.17 mmol) in dry  $CH_2Cl_2$  (5 mL) was introduced dropwise *via* syringe. The solution was stirred for 10 minutes and washed with water ( $3 \times 30$  mL). The organic layer was separated and dried over anhydrous  $Na_2SO_4$ . Column chromatography (silica gel,  $CH_2Cl_2$ / Hexane; 10:90) yielded a purple solid (13 mg, 14%) of the porphyrin derivative (**12**).

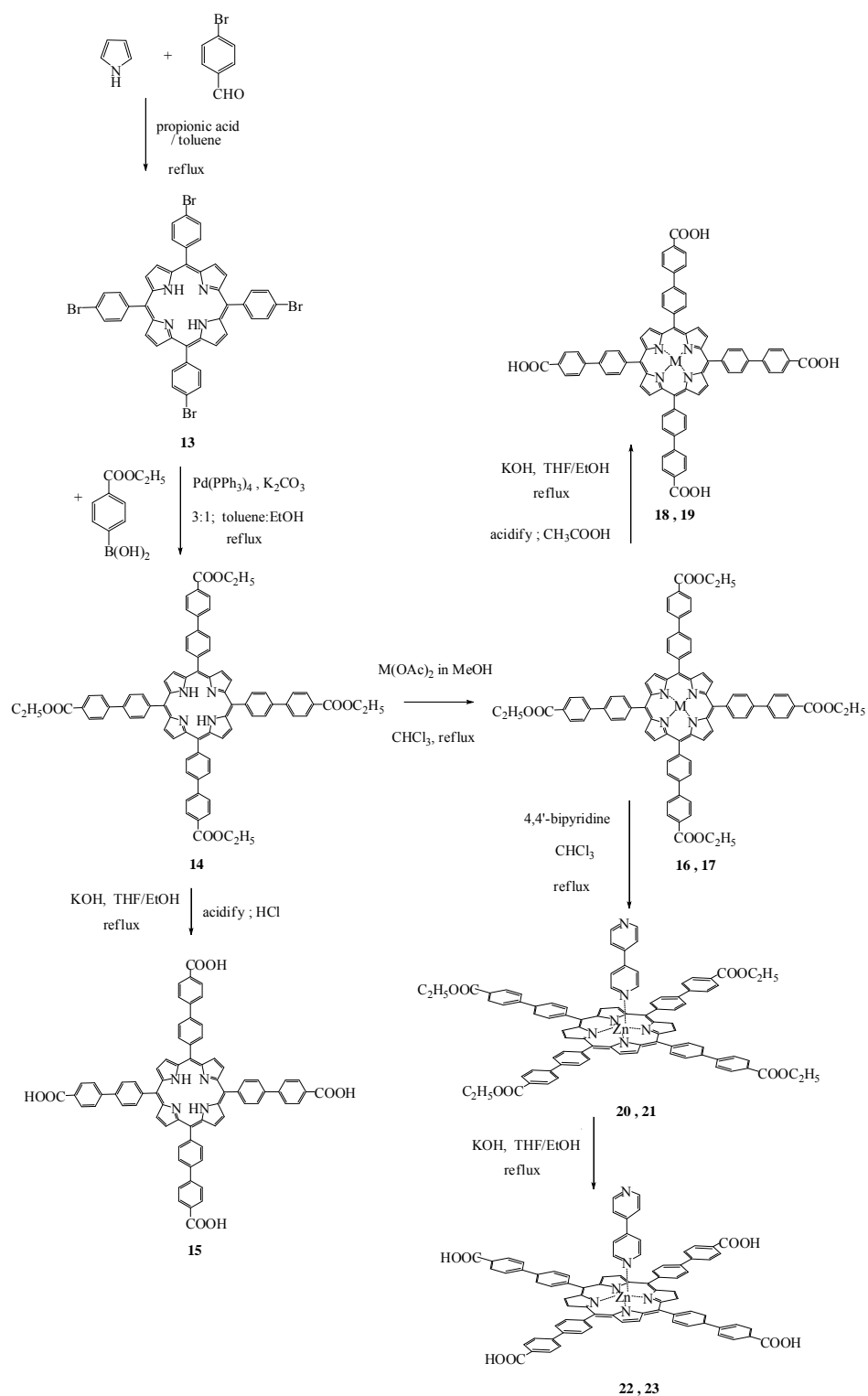
$^1H$  NMR (400 MHz,  $CDCl_3$ )  $\delta$ : 10.19 (s, 1H, *meso-H*), 9.76 (d,  $J=4.8$  Hz, 2H,  $\beta-H$ ), 9.31 (d,  $J=4.8$  Hz, 2H,  $\beta-H$ ), 8.98 (t,  $J=4.4$  Hz, 4H,  $\beta-H$ ), 8.23-8.21 (m, 4H, Ar-H), 7.82-7.78 (m, 6H, Ar-H), -3.00 (s, 2H, NH) (Figure A-18); MS (MALDI-TOF) calcd for  $[C_{32}H_{21}BrN_4]^+$  540.095 m/z, found 542.955 (Figure A-19).

### 3.3.3.2.3 Synthesis of 5-(4-methoxycarbonylphenyl)-10,20-diphenylporphyrin (**8**)



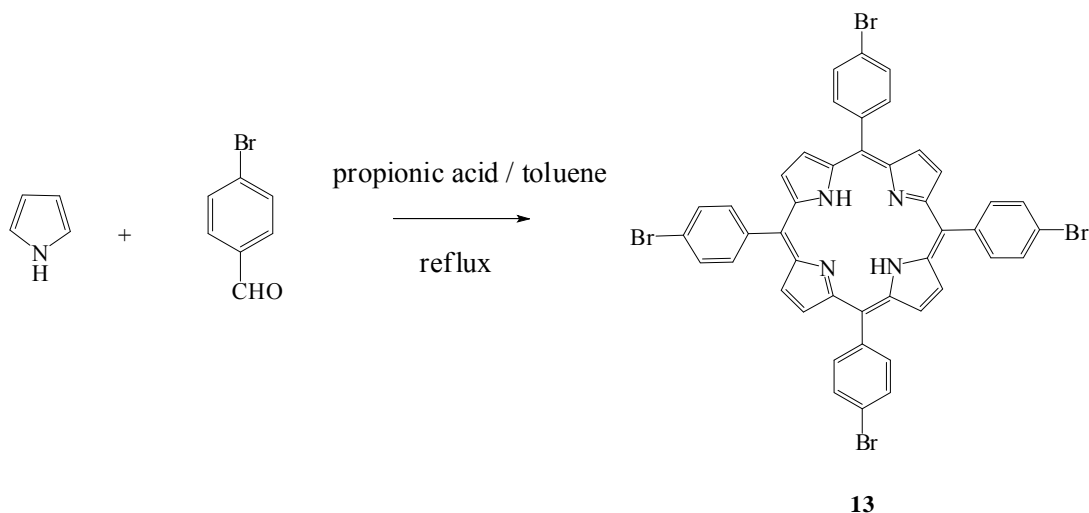
5-bromo-10,20-diphenylporphyrin (**12**) (30 mg, 0.055 mmol), 4-methoxycarbonylphenylboronic acid (20 mg, 0.11 mmol) and K<sub>2</sub>CO<sub>3</sub> (31 mg, 0.22 mmol) were stirred in dry solvent mixture (toluene/ EtOH; 36 mL:2mL) in a 250 mL two-necked round-bottomed flask under nitrogen atmosphere for 20 minutes, and then Pd(PPh<sub>3</sub>)<sub>4</sub> (13 mg, 0.011 mmol) was added. The reaction was heated at reflux for 20 hours. The reaction mixture was dried by rotary evaporator. The crude obtained was redissolved in CH<sub>2</sub>Cl<sub>2</sub> (30 mL) and washed with water (3 × 30 mL). The organic layer was separated and dried over anhydrous Na<sub>2</sub>SO<sub>4</sub>. Column chromatography (silica gel, CH<sub>2</sub>Cl<sub>2</sub>/ Hexane; 50:50) provided a purple solid (25 mg, 76 %) of the porphyrin derivative (**8**).

### 3.3.4 Part 4: Synthesis of tetracarboxybiphenylporphyrin derivative



**Scheme 3.5** Synthesis of tetracarboxybiphenylporphyrin derivatives

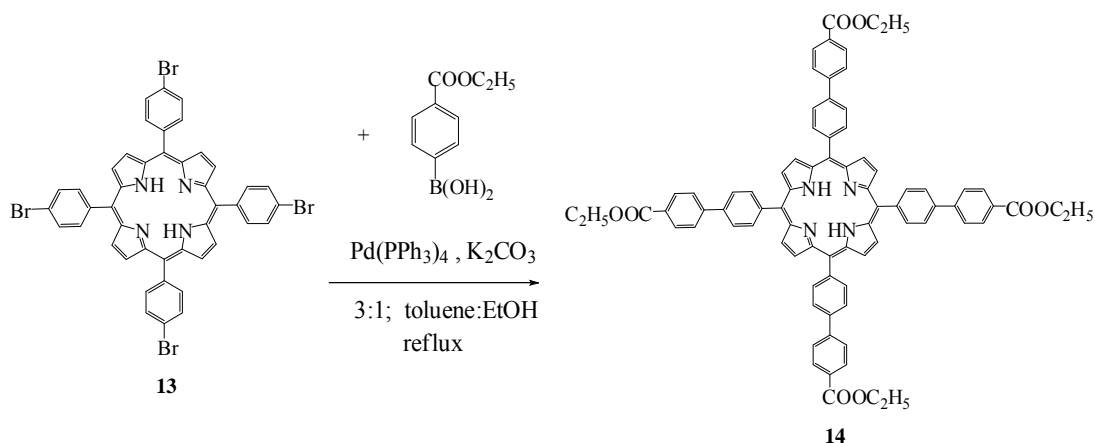
### 3.3.4.1 Synthesis of 5,10,15,20-Tetra(4-bromophenyl)porphyrin (TPPBr, **13**)



4-bromobenzaldehyde (800 mg, 4.32 mmol) was dissolved with toluene (30 mL) in a two-necked round-bottomed flask, then pyrrole was added (0.3 mL, 4.32 mmol). Propionic acid (30 mL) was added into the solution which turned the solution to dark color. The reaction was heated at reflux for 3 hours in the open air. The reaction mixture was dried under reduce pressure and the crude obtained was dissolved in  $\text{CH}_2\text{Cl}_2$  (30 mL). The residual propionic acid was removed by saturated  $\text{NaHCO}_3$  solution ( $3 \times 30$  mL) and then washed with water ( $3 \times 30$  mL). The organic layer was separated and dried over anhydrous  $\text{Na}_2\text{SO}_4$ . Column chromatography (silica gel,  $\text{CH}_2\text{Cl}_2$ ) gave a purple solid (210 mg, 21 %) of the porphyrin derivative (**13**).

$^1\text{H}$  NMR (400 MHz,  $\text{CDCl}_3$ )  $\delta$ : 8.84 (s, 8H,  $\beta$ -**H**), 8.08 (d,  $J=8$  Hz, 8H, Ar-**H**), 7.91 (d,  $J=8$  Hz, 16H, Ar-**H**), -2.89 (s, 2H, **NH**) (Figure A-20);  $^{13}\text{C}$  NMR (100 MHz,  $\text{CDCl}_3$ )  $\delta$ : 140.85, 135.82, 130.00, 122.66, 119.00, 29.71, 26.72 (Figure A-21); MS(MALDI-TOF) calcd for  $[\text{C}_{44}\text{H}_{26}\text{Br}_4\text{N}_4]^+$  930.320 m/z, found 930.756 (Figure A-22).

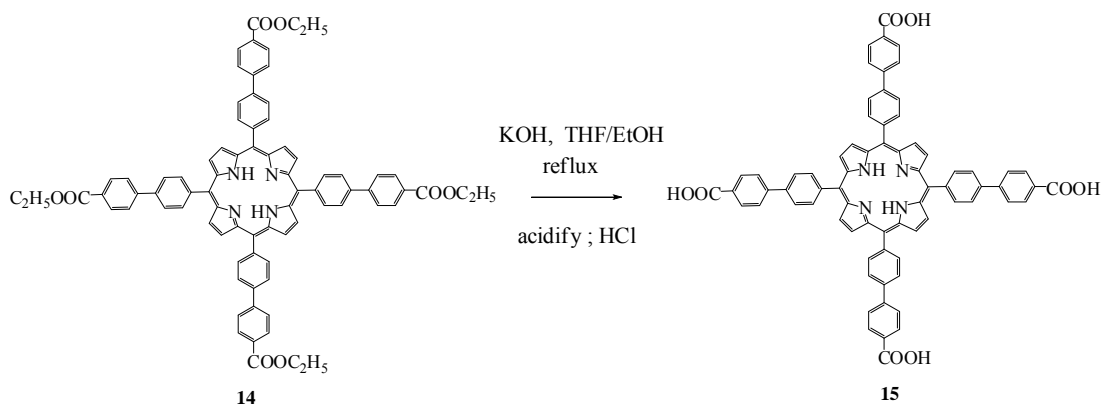
### 3.3.4.2 Synthesis of 5,10,15,20-Tetra(4-ethoxycarbonylbiphenyl) porphyrin (**14**)



5,10,15,20-Tetra(4-bromophenyl)porphyrin (**13**) ( 200 mg, 0.22 mmol), 4-ethoxycarbonylphenyl boronic acid (417 mg, 2.15mmol) and  $\text{K}_2\text{CO}_3$  (446 mg, 3.22 mmol) were stirred with dry solvent mixture (toluene/ EtOH; 120 mL:40 mL) in a 250 mL two-necked round-bottomed flask under nitrogen atmosphere for 20 minutes, then  $\text{Pd}(\text{PPh}_3)_4$  (50 mg, 0.043 mmol) was added. The reaction was heated at reflux for 20 hours. The solvents were removed by rotary evaporator. The crude obtained was dissolved in  $\text{CH}_2\text{Cl}_2$  (40 mL) and washed with water ( $3 \times 30$  mL). The organic layer was separated and dried over anhydrous  $\text{Na}_2\text{SO}_4$ . Column chromatography (silica gel,  $\text{CH}_2\text{Cl}_2$ ) yielded a purple solid (115 mg, 44.3%) of the porphyrin derivative (**14**).

$^1\text{H}$  NMR (400 MHz,  $\text{CDCl}_3$ )  $\delta$ : 8.92 (s, 8H,  $\beta\text{-H}$ ), 8.25 (d,  $J=4.4$  Hz, 16H, Ar-**H**), 7.95 (d,  $J=6.4$  Hz, 16H, Ar-**H**), 4.49 (q,  $J=7.2$  Hz, 8H,  $-\text{OCH}_2\text{CH}_3$ ), 1.49 (t,  $J=7.2$  Hz, 12H,  $-\text{OCH}_2\text{CH}_3$ ), -2.67 (s, 2H, **NH**) (Figure A-23);  $^{13}\text{C}$  NMR (100 MHz,  $\text{CDCl}_3$ )  $\delta$ : 166.58, 145.09, 142.02, 139.39, 135.18, 130.33, 129.66, 127.47, 127.23, 125.61, 119.75, 61.09, 14.42 (Figure A-24); MS (MALDI-TOF) calcd for  $[\text{C}_{80}\text{H}_{62}\text{N}_4\text{O}_8]^+$  1207.370 m/z, found 1208.813[M+H] $^+$  (Figure A-25); IR (KBr,  $\text{cm}^{-1}$ ): 1712 (s, C=O stretching), 1606 (m, C=C stretching), 1268 (s, C-O stretching) (Figure 4.11).

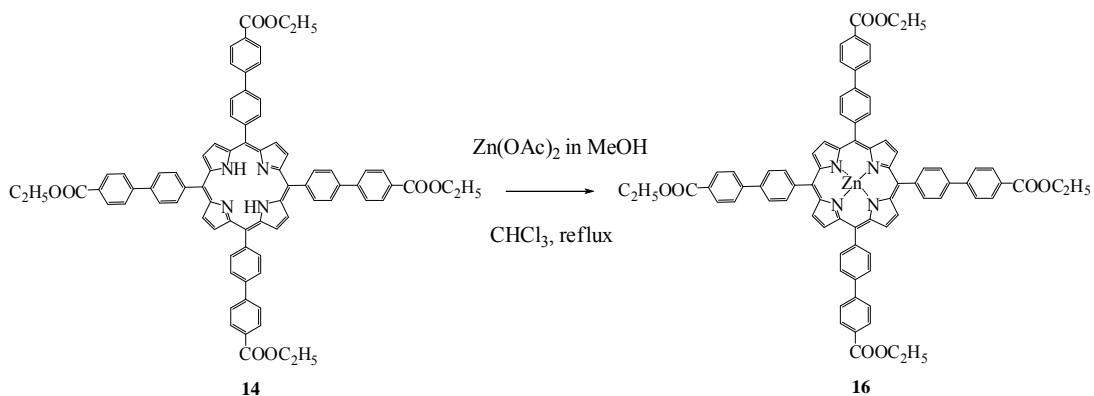
### 3.3.4.3 Synthesis of 5,10,15,20-Tetra(4-carboxybiphenyl)porphyrin (TCBPP, **15**)



5,10,15,20-Tetra(4-ethoxycarbonylbiphenyl)porphyrin (**14**) (100 mg, 0.083 mmol) was dissolved with solvent mixture (THF/ EtOH; 80 mL:20 mL) in a 250 mL two-necked round-bottomed flask, then added aqueous KOH 1 M (8mL, 8 mmol) and heated at reflux for 20 hours. The solvents were removed by rotary evaporator and dissolved with water (20 mL), then acidified with aqueous HCl 3 M. The precipitate was filtered and washed with water (3 × 30 mL) to yield a purple solid (85 mg, 93.8%) of the porphyrin derivative (**15**).

$^1\text{H}$  NMR (400 MHz, DMSO- $d_6$ )  $\delta$ : 13.01 (s, 4H, -COOH), 8.82 (s, 8H,  $\beta$ -H), 8.24 (d,  $J=8$  Hz, 8H, Ar-H), 8.10 (d,  $J=8$  Hz, 24H, Ar-H), -2.89 (s, 2H, NH) (Figure A-26);  $^{13}\text{C}$  NMR (100 MHz, DMSO- $d_6$ )  $\delta$ : 167.20, 149.28, 143.91, 142.67, 137.85, 134.88, 131.75, 130.11, 129.85, 126.99, 125.10, 119.88 (Figure A-27); MS(MALDI-TOF) calcd for  $[\text{C}_{72}\text{H}_{46}\text{N}_4\text{O}_8]^+$  1094.332 m/z, found 1095.940[M+H] $^+$  (Figure A-28); IR (KBr,  $\text{cm}^{-1}$ ): 3458 (br s, O-H stretching), 1719 (s, C=O stretching), 1603 (m, C=C stretching), 1273 (s, C-O stretching) (Figure 4.11).

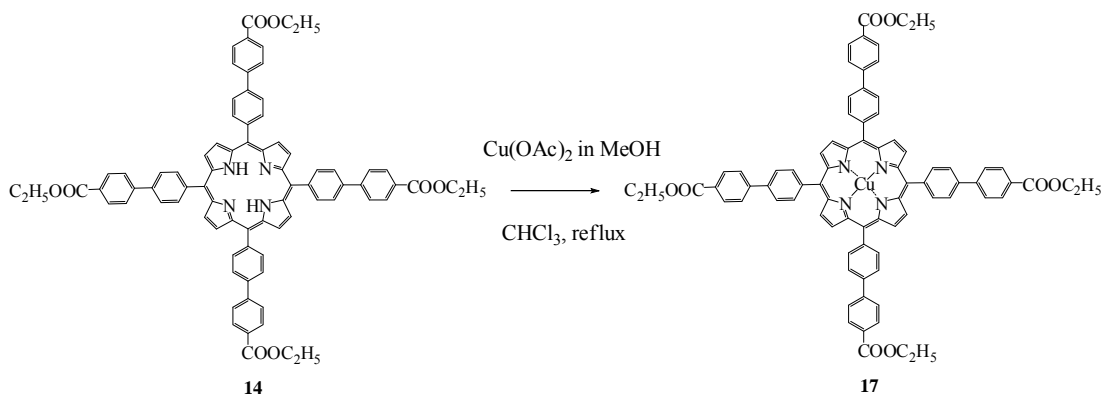
### 3.3.4.4 Synthesis of Zinc(II)-5,10,15,20-Tetra(4-ethoxycarbonylbiphenyl)porphyrin (Zn-TEBPP, **16**)



A saturated solution of Zn(OAc)<sub>2</sub> · 2H<sub>2</sub>O (727 mg, 3.3 mmol) in MeOH (20 mL) was added to a solution of free-base 5,10,15,20-Tetra(4-ethoxycarbonylbiphenyl) porphyrin (**14**) (400 mg, 0.33 mmol) in CHCl<sub>3</sub> (40 mL), and the mixture was heated at reflux under nitrogen for 10 hours. After the complete metallation confirmed by TLC, the mixture was washed with water (3 × 30 mL). The organic layer was separated and dried over anhydrous Na<sub>2</sub>SO<sub>4</sub>. Column chromatography (silica gel, CH<sub>2</sub>Cl<sub>2</sub>) yielded a purple solid (395 mg, 94%) of the porphyrin derivative (**16**).

<sup>1</sup>H NMR (400 MHz, CDCl<sub>3</sub>) δ: 9.05 (s, 8H, β-**H**), 8.35 (d, *J*=8 Hz, 8H, Ar-**H**), 8.28 (d, *J*=8.4 Hz, 8H, Ar-**H**), 8.04 (dd, *J*=4.4, 8.4 Hz, 16H, Ar-**H**), 4.48 (q, *J*=8 Hz, 8H, -OCH<sub>2</sub>CH<sub>3</sub>), 1.48 (t, *J*=7.2 Hz, 12H, -OCH<sub>2</sub>CH<sub>3</sub>) (Figure A-29); MS(MALDI-TOF) calcd for [C<sub>80</sub>H<sub>60</sub>N<sub>4</sub>O<sub>8</sub>Zn]<sup>+</sup> 1268.370 m/z, found 1269.155[M+H]<sup>+</sup> (Figure A-30); IR (KBr, cm<sup>-1</sup>): 1717 (s, C=O stretching), 1606 (m, C=C stretching), 1273 (s, C-O stretching) (Figure 4.7).

### 3.3.4.5 Synthesis of Copper(II)-5,10,15,20-Tetra(4-ethoxycarbonylbiphenyl)porphyrin (Cu-TEBPP,17)

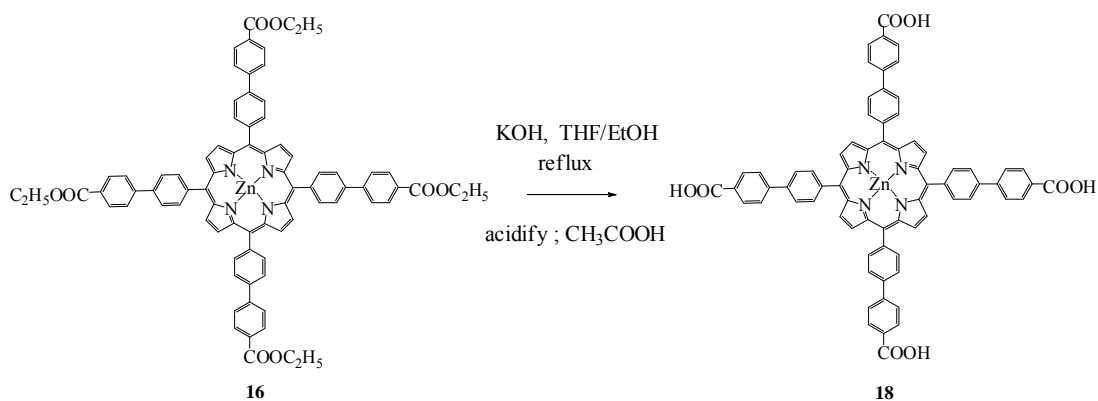


A saturated solution of  $\text{Cu(OAc)}_2 \cdot 1\text{H}_2\text{O}$  (602 mg, 3.3 mmol) in MeOH (20 mL) was added to a solution of free-base 5,10,15,20-Tetra(4-ethoxycarbonylbiphenyl) porphyrin (**14**) (400 mg, 0.33 mmol) in  $\text{CHCl}_3$  (40 mL), then the mixture was heated at reflux under nitrogen for 10 hours. After the complete metallation confirmed by TLC, the mixture was washed with water ( $3 \times 30$  mL). The organic layer was separated and dried over anhydrous  $\text{Na}_2\text{SO}_4$ . Column chromatography (silica gel,  $\text{CH}_2\text{Cl}_2$ ) yielded a reddish purple solid (384 mg, 91%) of the porphyrin derivative (**17**).

MS(MALDI-TOF) calcd for  $[\text{C}_{80}\text{H}_{60}\text{N}_4\text{O}_8\text{Cu}]^+$  1267.371 m/z, found 1267.807 (Figure A-31); IR (KBr,  $\text{cm}^{-1}$ ): 1712 (s, C=O stretching), 1606 (w, C=C stretching), 1273 (s, C-O stretching) (Figure 4.8)



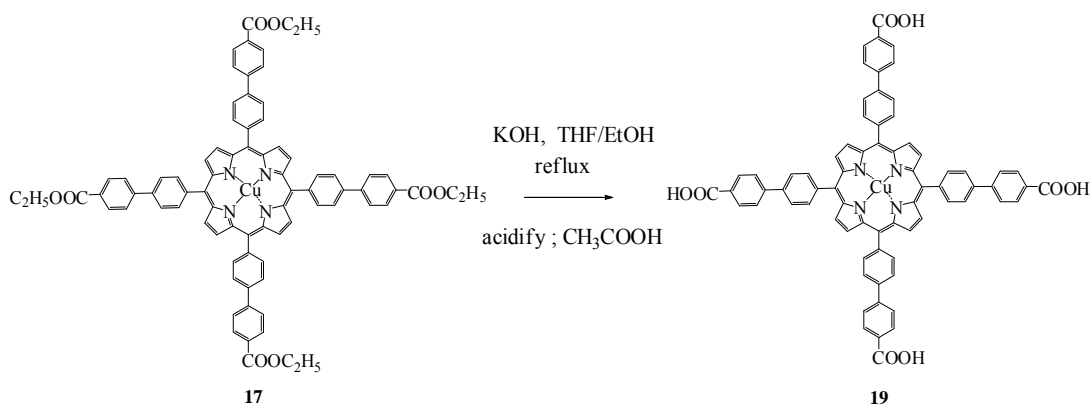
### 3.3.4.6 Synthesis of Zinc(II)-5,10,15,20-Tetra(4-carboxybiphenyl)porphyrin (Zn-TCBPP, **18**)



Zinc(II)-5,10,15,20-Tetra(4-ethoxycarbonylbiphenyl)porphyrin (**16**) (200 mg, 0.157 mmol) was dissolved with solvent mixture (THF/EtOH; 120 mL:30 mL) in a 250 mL two-necked round-bottomed flask, then added aqueous KOH 1 M (16 mL) and heated at reflux for 20 hours. The solvent was removed by rotary evaporator and dissolved with water (30 mL), then acidified with aqueous CH<sub>3</sub>COOH 3 M. The precipitate was filtered and washed with water (3 × 30 mL), then yielded a purple solid (163 mg, 90%) of the porphyrin derivative (**18**).

<sup>1</sup>H NMR (400 MHz, DMSO-*d*<sub>6</sub>) δ: 8.88 (s, 8H, β-**H**), 8.29 (d, *J*=7.2 Hz, 8H, Ar-**H**), 8.16 (d, *J*=8.4 Hz, 24H, Ar-**H**) (Figure A-32); <sup>13</sup>C NMR (100 MHz, DMSO-*d*<sub>6</sub>) δ: 167.22, 149.28, 143.33, 134.92, 131.74, 130.12, 127.02, 125.14, 119.89 (Figure A-33); MS(MALDI-TOF) calcd for [C<sub>72</sub>H<sub>44</sub>N<sub>4</sub>O<sub>8</sub>Zn]<sup>+</sup> 1156.245 m/z, found 1156.705 (Figure A-34); IR (KBr, cm<sup>-1</sup>): 3445 (br s, O-H stretching), 1689 (s, C=O stretching), 1601 (s, C=C stretching), 1388 (s), 1264 (w, C-O stretching) (Figure 4.9); Job plot analysis of Zn-TCBPP(**18**) : 4,4'-bipyridine = 2:1 (Figure 4.13)

### 3.3.4.7 Synthesis of Copper(II)-5,10,15,20-Tetra(4-carboxybiphenyl)porphyrin (Cu-TCBPP, 19)

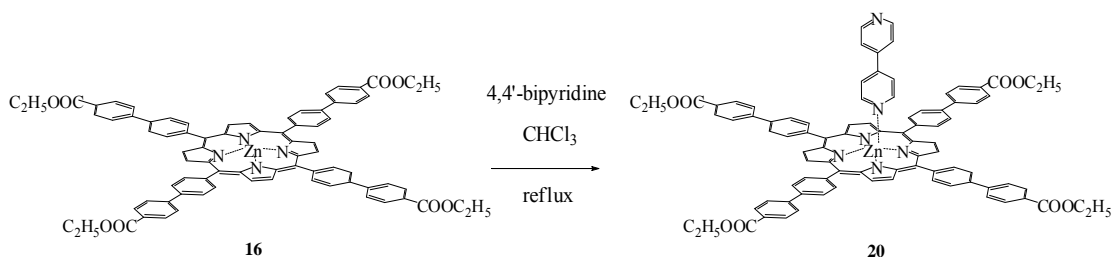


#### Copper(II)-5,10,15,20-Tetra(4-ethoxycarbonylbiphenyl)

porphyrin (**17**) (200 mg, 0.157 mmol) was dissolved with solvent mixture (THF/EtOH; 120mL: 30mL) in a 250 mL two-necked round-bottomed flask, then added aqueous KOH 1 M (16 mL) and heated at reflux for 20 hours. The solvent was removed by rotary evaporator and dissolved with water (30 mL), then acidified with aqueous CH<sub>3</sub>COOH 3 M. The precipitate was filtered and washed with water (3 × 30 mL), then yielded a reddish purple solid (151 mg, 76%) of the porphyrin derivative (**19**).

MS(MALDI-TOF) calcd for [C<sub>72</sub>H<sub>44</sub>N<sub>4</sub>O<sub>8</sub>Cu]<sup>+</sup> 1155.246 m/z, found 1155.809 (Figure A-35); IR (KBr, cm<sup>-1</sup>): 3422 (br s, O-H stretching), 1703 (s, C=O stretching), 1601 (s, C=C stretching), 1222 (s, C-O stretching) (Figure 4.10); Job plot analysis of Cu-TCBPP(**19**) : 4,4'-bipyridine = 2:1 (Figure 4.13)

### 3.3.4.8 Synthesis of Complex of Zinc(II)-5,10,15,20-Tetra(4-ethoxycarbonylbiphenyl)porphyrin with 4,4'-bipyridine ([Zn-TEBPP]-bpy, **20**)

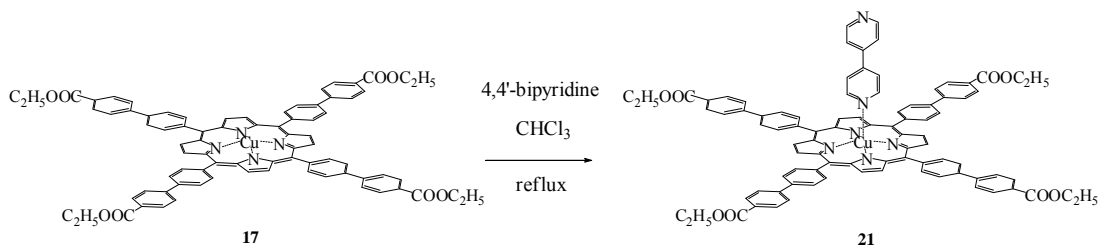


Zinc(II)-5,10,15,20-Tetra(4-ethoxycarbonylbiphenyl)porphyrin (**16**) (200 mg, 0.157 mmol) was dissolved with  $\text{CHCl}_3$  (80 mL) and charged with solutions of 4,4'-bipyridine (24.5 mg, 0.157 mmol) in  $\text{CHCl}_3$  (40 mL), then the mixture was heated at reflux under nitrogen for 10 hours. The solvent was removed by rotary evaporator. The obtained porphyrin derivative (**20**) was a blue-purple solid (221 mg, 94%).

$^1\text{H}$  NMR (400 MHz,  $\text{CDCl}_3$ )  $\delta$ : 8.98 (s, 8H,  $\beta\text{-H}$ ), 8.30 (m, 16H, Ar-H), 8.02 (m, 16H, Ar-H), 7.74 (br s, 8H, pyridyl-H), 7.13 (s, 8H, pyridyl-H), 4.48 (q,  $J=7.2$  Hz, 8H,  $-\text{OCH}_2\text{CH}_3$ ), 1.47 (t,  $J=7.6$  Hz, 12H,  $-\text{OCH}_2\text{CH}_3$ ) (Figure A-36);  $^1\text{H}$  NMR (400 MHz, DMSO)  $\delta$ : 8.88 (s, 8H,  $\beta\text{-H}$ ), 8.72 (d,  $J=5.6$  Hz, 16H, pyridyl-H), 8.33 (d,  $J=8$  Hz, 8H, Ar-H), 8.18 (s, 24H, Ar-H), 7.83 (d,  $J=6$  Hz, 16H, pyridyl-H), 4.41 (q,  $J=6.8$  Hz, 8H,  $-\text{OCH}_2\text{CH}_3$ ), 1.40 (t,  $J=7.2$  Hz, 12H,  $-\text{OCH}_2\text{CH}_3$ ) (Figure A-38);  $^{13}\text{C}$  NMR (100 MHz,  $\text{CDCl}_3$ )  $\delta$ : 166.61, 150.01, 143.86, 145.33, 145.23, 145.05, 143.32, 138.79, 138.73, 135.17, 131.80, 130.34, 130.30, 129.52, 127.21, 127.17, 125.20, 120.91, 120.19, 115.23, 61.09, 29.43, 14.43 (Figure A-37); MS(MALDI-TOF) calcd for  $[\text{C}_{90}\text{H}_{68}\text{N}_6\text{O}_8\text{Zn}]^+$  1424.439 m/z, found 1269.319 (Figure A-39); IR (KBr,  $\text{cm}^{-1}$ ): 1707 (s, C=O stretching), 1601 (m, C=C stretching), 1268 (s, C-O stretching) (Figure 4.7) ; Job plot analysis of Zn-TEBPP(**16**) : 4,4'-bipyridine = 1:1 (Figure 4.12)

$^1\text{H}$  NMR (400 MHz,  $\text{CDCl}_3$ ) of 4,4'-bipyridine  $\delta$ : 8.75 (d,  $J=6$  Hz 4H, pyridyl-H), 7.55 (d,  $J=6$  Hz 4H, pyridyl-H) (Figure A-45);  $^{13}\text{C}$  NMR (100 MHz,  $\text{CDCl}_3$ )  $\delta$ : 150.53, 144.29, 121.24, 120.95 (Figure A-46)

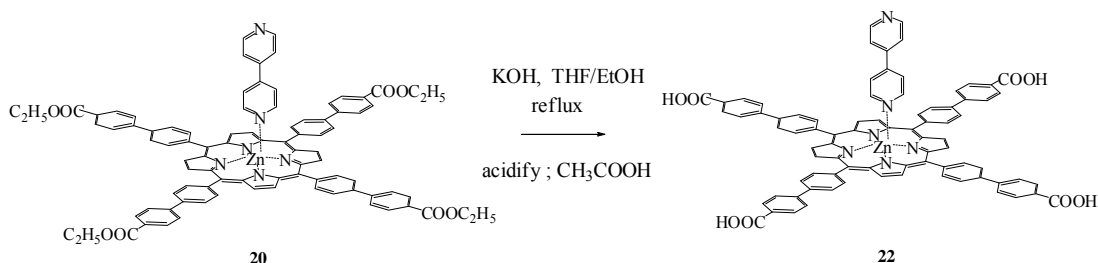
### 3.3.4.9 Synthesis of Complex of Copper(II)-5,10,15,20-Tetra(4-methoxycarbonylbiphenyl) porphyrin with 4,4'-bipyridine ([Cu-TEBPP]-bpy, **21**)



Copper(II)-5,10,15,20-Tetra(4-ethoxycarbonylbiphenyl) porphyrin (**17**) (200 mg, 0.157 mmol) was dissolved with  $\text{CHCl}_3$  (80 mL) and charged with solutions of 4,4'-bipyridine (24.5 mg, 0.157 mmol) in  $\text{CHCl}_3$  (40 mL), then the mixture was heated at reflux under nitrogen for 10 hours. The solvent was removed by rotary evaporator. The obtained porphyrin derivative (**21**) was a blue-purple solid (218 mg, 97%).

MS(MALDI-TOF) calcd for  $[\text{C}_{90}\text{H}_{68}\text{N}_6\text{O}_8\text{Cu}]^+$  1423.439 m/z, found 1268.692 (Figure A-40); IR (KBr,  $\text{cm}^{-1}$ ): 1717 (s, C=O stretching), 1606 (m, C=C stretching), 1587 (m), 1278 (s, C-O stretching) (Figure 4.8); Job plot analysis of Cu-TEBPP(**17**) : 4,4'-bipyridine = 1:1 (Figure 4.12)

### 3.3.4.10 Synthesis of Complex of Zinc(II)-5,10,15,20-Tetra(4-carboxybiphenyl)porphyrin with 4,4'-bipyridine ([Zn-TCBPP]-bpy, **22**)

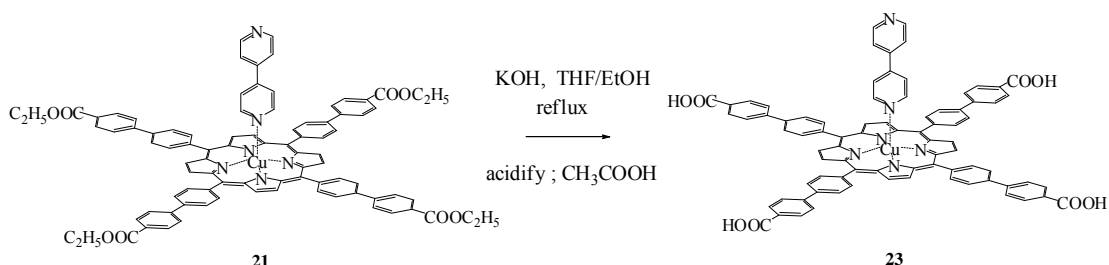


Complex of Zinc(II)-5,10,15,20-Tetra(4-ethoxycarbonyl biphenyl) porphyrin with 4,4'-bipyridine (**20**) (200 mg, 0.140 mmol) was dissolved with solvent mixture (THF/EtOH; 120 mL:30 mL) in a 250 mL two-necked round-bottomed flask, then added aqueous KOH 1 M (14 mL) and heated at reflux for 20 hours. The solvent was removed by rotary evaporator and dissolved with water (30 mL), then acidified with aqueous CH<sub>3</sub>COOH 3 M. The precipitate was filtered and washed with water (3 × 30 mL), then yielded a blue-purple solid (183 mg, 93 %) of the porphyrin derivative (**22**).

<sup>1</sup>H NMR (400 MHz, DMSO-*d*<sub>6</sub>) δ: 8.89 (s, 8H, β-**H**), 8.71 (d, *J*=5.2 Hz, 16H, pyridyl-**H**), 8.32 (d, *J*=7.2 Hz, 8H, Ar-**H**), 8.19 (d, *J*=12 Hz, 24H, Ar-**H**), 7.82 (d, *J*=4.4 Hz, 16H, pyridyl-**H**) (Figure A-41); <sup>13</sup>C NMR (100 MHz, DMSO-*d*<sub>6</sub>) δ: 150.52, 149.28, 144.29, 134.94, 131.30, 130.11, 126.97, 125.12, 121.24, 115.27 (Figure A-42); MS(MALDI-TOF) calcd for [C<sub>82</sub>H<sub>52</sub>N<sub>6</sub>O<sub>8</sub>Zn]<sup>+</sup> 1312.314 m/z, found 1157.818 (Figure A-43); IR (KBr, cm<sup>-1</sup>): 3454 (br w, O-H stretching), 1893 (s, C=O stretching), 1601 (s, C=C stretching), 1398 (m), 1268 (m, C-O stretching) (Figure 4.9)

<sup>1</sup>H NMR (400 MHz, DMSO-*d*<sub>6</sub>) of 4,4'-bipyridine δ: 8.69 (d, *J*=4.8 Hz, 4H, pyridyl-**H**), 7.80 (d, *J*=4.8 Hz, 4H, pyridyl-**H**) (Figure A-47); <sup>13</sup>C NMR (100 MHz, CDCl<sub>3</sub>) δ: 150.67, 145.56, 121.41 (Figure A-48)

### 3.3.4.11 Synthesis of Complex of Copper(II)-5,10,15,20-Tetra(4-carboxybiphenyl)porphyrin with 4,4'-bipyridine ([Cu-TCBPP]-bpy, **23**)



Complex of Copper(II)-5,10,15,20-Tetra(4-ethoxycarbonylbiphenyl)porphyrin with 4,4'-bipyridine (**21**) (200 mg, 0.140 mmol) was dissolved with solvent mixture (THF/EtOH; 120 mL:30 mL) in a 250 mL two-necked round-bottomed flask, then added aqueous KOH 1 M (14 mL) and heated at reflux for 20 hours. The solvent was removed by rotary evaporator and dissolved with water (30 mL), then acidified with aqueous  $\text{CH}_3\text{COOH}$  3 M. The precipitate was filtered and washed with water ( $3 \times 30$  mL), then yielded a reddish-purple solid (179 mg, 91 %) of the porphyrin derivative (**23**).

MS(MALDI-TOF) calcd for  $[\text{C}_{82}\text{H}_{52}\text{N}_6\text{O}_8\text{Cu}]^+$  1311.314 m/z, found 1155.828 (Figure A-44); IR (KBr,  $\text{cm}^{-1}$ ): 3024 (m, C-H stretching), 1601 (s, C=C stretching and C=N stretching), 1402 (s, C=C stretching), 1222 (m) (Figure 4.10)

### **3.3.5 Part 5 : Synthesis of Porphyrin- based MOFs using tetracarboxybiphenylporphyrin derivatives as organic linkers**

#### **3.3.5.1 Synthesis of Porphyrin- based MOFs Pathway A: Using free-base porphyrin (TCBPP) as organic linker (TCBPP + M(NO<sub>3</sub>)<sub>2</sub>.nH<sub>2</sub>O +/- bpy)**

<b>Code of MOF</b>	<b>TCBPP + M(NO<sub>3</sub>)<sub>2</sub> +/- bpy</b>
2A	TCBPP+Zn(NO <sub>3</sub> ) <sub>2</sub>
6A	TCBPP+Cu(NO <sub>3</sub> ) <sub>2</sub>
3A	TCBPP+Zn(NO <sub>3</sub> ) <sub>2</sub> +bpy
7A	TCBPP+Cu(NO <sub>3</sub> ) <sub>2</sub> +bpy
5A	TCBPP+Zn(NO <sub>3</sub> ) <sub>2</sub> add bpy
8A	TCBPP+Cu(NO <sub>3</sub> ) <sub>2</sub> add bpy

**Table 3.1** Code of Porphyrin-based MOFs via pathway A

##### **3.3.5.1.1 Synthesis of MOF 2A and MOF 6A**

5,10,15,20-Tetra(4-carboxybiphenyl) porphyrin (TCBPP, **15**)(200 mg, 0.183 mmol) was dissolved in anhydrous DMF (30 mL) in a 100 mL two-necked round-bottomed flask, then charged with a solution of Zn(NO<sub>3</sub>)<sub>2</sub>.6H<sub>2</sub>O (109 mg, 0.366 mmol) in anhydrous DMF (10 mL) and stirred for 30 minutes. The solution was heated at 140°C without stirring for 48 hours. The precipitate was filtered and washed with anhydrous DMF (4 × 20 mL), then yielded a purple solid (175 mg, 88% based on TCBPP) of the MOF **2A**.

IR (KBr, cm<sup>-1</sup>): 3454 (br s, O-H stretching), 1657 (s, C=O stretching), 1601 (s, C=C stretching), 1393 (s, C-O stretching) (Figure 4.14); XRD pattern: 2θ of 6.92°, 19.40° (Figure 4.20)

In the case of MOF 6A, using the same amount of TCBPP in the same method as upper condition but the reaction was charged with Cu(NO<sub>3</sub>)<sub>2</sub>.2.5H<sub>2</sub>O (88 mg, 0.366 mmol) instead of Zn(NO<sub>3</sub>)<sub>2</sub>. The precipitate was filtered and washed with anhydrous DMF (4 × 20 mL), then yielded a reddish-purple solid (186 mg, 93% based on TCBPP) of the MOF **6A**.

IR (KBr, cm<sup>-1</sup>): 3445 (br s, O-H stretching), 1652 (s, C=O stretching), 1601 (s, C=C stretching), 1388 (s, C-O stretching) (Figure 4.15);

XRD pattern:  $2\theta$  of  $6.74^\circ$ ,  $9.04^\circ$ ,  $10.22^\circ$ ,  $11.18^\circ$ ,  $11.96^\circ$ ,  $13.56^\circ$ ,  $16.30^\circ$ ,  $17.84^\circ$ ,  $19.26^\circ$ ,  $22.42^\circ$  (Figure 4.20)

### 3.3.5.1.2 Synthesis of MOF 3A and MOF 7A

5,10,15,20-Tetra(4-carboxyphenyl) porphyrin (TCBPP, **15** (200 mg, 0.183 mmol) was dissolved in anhydrous DMF (30 mL) in a 100 mL two-necked round-bottomed flask, then charged with the mixture solutions of  $\text{Zn}(\text{NO}_3)_2 \cdot 6\text{H}_2\text{O}$  (109 mg, 0.366 mmol) and 4,4'-bipyridine (57 mg, 0.366 mmol) in anhydrous DMF (10 mL). The solution was stirred for 30 minutes and then heated at  $140^\circ\text{C}$  without stirring for 48 hours. The precipitate was filtered and washed with anhydrous DMF ( $4 \times 20$  mL), then yielded a blue-purple solid (164. mg, 82% based on TCBPP) of the MOF **3A**.

IR (KBr,  $\text{cm}^{-1}$ ): 3445 (br s, O-H stretching), 1652 (s, C=O stretching), 1601 (s, C=C stretching), 1388 (s, C-O stretching) (Figure 4.14); XRD pattern:  $2\theta$  of  $6.90^\circ$ ,  $8.96^\circ$ ,  $10.32^\circ$ ,  $11.10^\circ$ ,  $17.76^\circ$ ,  $19.22^\circ$ ,  $22.15^\circ$  (Figure 4.20)

In the case of MOF **7A**, using the same amount of TCBPP in the same method as upper condition but the reaction was charged with  $\text{Cu}(\text{NO}_3)_2 \cdot 2.5\text{H}_2\text{O}$  (88mg, 0.366 mmol) instead of  $\text{Zn}(\text{NO}_3)_2$  and 4,4'-bipyridine (57 mg, 0.366 mmol). The precipitate was filtered and washed with anhydrous DMF ( $4 \times 20$  mL), then yielded a reddish-purple solid (171 mg, 86% based on TCBPP) of the MOF **7A**.

IR (KBr,  $\text{cm}^{-1}$ ): 3426 (br s, O-H stretching), 1657 (s, C=O stretching), 1606 (s, C=C stretching), 1398 (s, C-O stretching) (Figure 4.15); XRD pattern:  $2\theta$  of  $6.72^\circ$ ,  $9.06^\circ$ ,  $10.20^\circ$ ,  $11.18^\circ$ ,  $11.94^\circ$ ,  $13.50^\circ$ ,  $16.30^\circ$ ,  $17.84^\circ$ ,  $19.28^\circ$ ,  $22.06^\circ$  (Figure 4.20)

### 3.3.5.1.3 Synthesis of MOF 5A and MOF 8A

5,10,15,20-Tetra(4-carboxyphenyl) porphyrin (TCBPP, **15**) (200 mg, 0.183 mmol) was dissolved in anhydrous DMF (30 mL) in a 100 mL two-necked round-bottomed flask, then charged with a solution of  $\text{Zn}(\text{NO}_3)_2 \cdot 6\text{H}_2\text{O}$  (109 mg, 0.366 mmol) in anhydrous DMF (5 mL). The solution was



stirred for 30 minutes and then heated at 140°C without stirring for 10 hours. A solution of 4,4'-bipyridine (57 mg, 0.366 mmol) in anhydrous DMF (5 mL) was added in that reaction and stirred for 20 minutes, then heated at 140°C without stirring for 38 hours. The precipitate was filtered and washed with anhydrous DMF (4 × 20 mL), then yielded a blue-purple solid (195 mg, 98% based on TCBPP) of the MOF **5A**.

IR (KBr,  $\text{cm}^{-1}$ ): 3445 (br m, O-H stretching), 1652 (s, C=O stretching), 1601 (s, C=C stretching), 1393 (s, C-O stretching) (Figure 4.14); XRD pattern:  $2\theta$  of 6.93°, 7.30°, 8.35°, 9.03°, 10.02°, 10.50°, 13.98°, 15.36°, 18.34°, 19.45°, 21.12°, 22.20° (Figure 4.20)

In the case of MOF **8A**, using the same amount of TCBPP in the same method as upper condition but the reaction was charged with  $\text{Cu}(\text{NO}_3)_2 \cdot 2.5\text{H}_2\text{O}$  (88mg, 0.366 mmol) instead of  $\text{Zn}(\text{NO}_3)_2$  and 4,4'-bipyridine (57 mg, 0.366 mmol). The precipitate was filtered and washed with anhydrous DMF (4 × 20 mL), then yielded a reddish-purple solid (152 mg, 76% based on TCBPP) of the MOF **8A**.

IR (KBr,  $\text{cm}^{-1}$ ): 3426 (br m, O-H stretching), 1657 (m, C=O stretching), 1601 (m, C=C stretching), 1388 (m, C-O stretching) (Figure 4.15); XRD pattern:  $2\theta$  of 6.78°, 7.91°, 9.04°, 10.24°, 11.17°, 11.88°, 13.62°, 17.90°, 19.26°, 22.34°, 35.46°, 36.40°, 38.66°, 48.72° (Figure 4.20)

### 3.3.5.2 Synthesis of Porphyrin- based MOFs Pathway B: Using metalloporphyrin (Zn-TCBPP and Cu-TCBPP) as organic linker (M-TCBPP + $\text{M}(\text{NO}_3)_2 \cdot n\text{H}_2\text{O}$ + bpy)

Code of MOF	M-TCBPP + $\text{M}(\text{NO}_3)_2$ + bpy
10B	Zn-TCBPP + $\text{Zn}(\text{NO}_3)_2$ add bpy
11B	Zn-TCBPP + bpy add $\text{Zn}(\text{NO}_3)_2$
12B	Zn-TCBPP + $\text{Zn}(\text{NO}_3)_2$ + bpy
13B	Cu-TCBPP + $\text{Cu}(\text{NO}_3)_2$ add bpy
14B	Cu-TCBPP + bpy add $\text{Cu}(\text{NO}_3)_2$
15B	Cu-TCBPP + $\text{Cu}(\text{NO}_3)_2$ + bpy

**Table 3.2** Code of Porphyrin-based MOFs via pathway B

### 3.3.5.2.1 Synthesis of 10B and MOF 13B

As the same condition as synthesis of MOF 5A, zinc(II)-5,10,15,20-Tetra(4-carboxybiphenyl)porphyrin (Zn-TCBPP, **18**) (200 mg, 0.173 mmol),  $\text{Zn}(\text{NO}_3)_2 \cdot 6\text{H}_2\text{O}$  (102 mg, 0.346 mmol) and 4,4'-bipyridine (54 mg, 0.346 mmol) were used. The precipitate was filtered and washed with anhydrous DMF ( $4 \times 20$  mL), then yielded a blue-purple solid (195 mg, 98% based on Zn-TCBPP) of the MOF **10B**.

IR (KBr,  $\text{cm}^{-1}$ ): 3450 (br m, O-H stretching), 1657 (s, C=O stretching), 1601 (m, and C=C stretching), 1388 (s, C-O stretching) (Figure 4.16); XRD pattern:  $2\theta$  of  $6.90^\circ$ ,  $8.94^\circ$ ,  $10.40^\circ$ ,  $11.06^\circ$ ,  $17.66^\circ$ ,  $19.36^\circ$ ,  $22.16^\circ$  (Figure 4.21)

In the case of MOF 13B, using the same condition as synthesis of MOF 5A, copper(II)-5,10,15,20-Tetra(4-carboxybiphenyl)porphyrin (Cu-TCBPP, **19**) (200 mg, 0.173 mmol),  $\text{Cu}(\text{NO}_3)_2 \cdot 2.5\text{H}_2\text{O}$  (84mg, 0.346 mmol) and 4,4'-bipyridine (54 mg, 0.346 mmol) were used. The precipitate was filtered and washed with anhydrous DMF ( $4 \times 20$  mL), then yielded a reddish-purple solid (124 mg, 62% based on Cu-TCBPP) of the MOF **13B**.

IR (KBr,  $\text{cm}^{-1}$ ): 3436 (br s, O-H stretching), 1657 (s, C=O stretching), 1601 (s, and C=C stretching), 1398 (s, C-O stretching) (Figure 4.17); XRD pattern:  $2\theta$  of  $6.78^\circ$ ,  $9.04^\circ$ ,  $10.24^\circ$ ,  $11.16^\circ$ ,  $11.98^\circ$ ,  $13.58^\circ$ ,  $14.72^\circ$ ,  $16.38^\circ$ ,  $17.84^\circ$ ,  $19.44^\circ$ ,  $20.56^\circ$ ,  $22.42^\circ$  (Figure 4.20)

### 3.3.5.2.2 Synthesis of MOF 11B and MOF 14B

Zinc(II)-5,10,15,20-Tetra(4-carboxybiphenyl)porphyrin (Zn-TCBPP, **18**) (200 mg, 0.173 mmol) was dissolved in anhydrous DMF (30 mL) in a 100 mL two-necked round-bottomed flask, then charged with a solution of 4,4'-bipyridine (54 mg, 0.346 mmol) in anhydrous DMF (5 mL). The solution was stirred for 30 minutes and then heated at  $140^\circ\text{C}$  without stirring for 10 hours. A solution of  $\text{Zn}(\text{NO}_3)_2 \cdot 6\text{H}_2\text{O}$  (102 mg, 0.346 mmol) in anhydrous DMF (5 mL) was added in that reaction and stirred for 20 minutes, then heated at  $140^\circ\text{C}$  without stirring for 38 hours.

The precipitate was filtered and washed with anhydrous DMF ( $4 \times 20$  mL), then yielded a blue-purple solid (188 mg, 94% based on Zn-TCBPP) of the MOF **11B**.

IR (KBr,  $\text{cm}^{-1}$ ): 3436 (br m, O-H stretching), 1652 (s, C=O stretching), 1610 (m, and C=C stretching), 1388 (s, C-O stretching) (Figure 4.16); XRD pattern:  $2\theta$  of  $6.94^\circ$ ,  $8.92^\circ$ ,  $10.42^\circ$ ,  $11.10^\circ$ ,  $18.08^\circ$ ,  $19.46^\circ$ ,  $22.14^\circ$  (Figure 4.21)

In the case of MOF 14B, using the same condition as synthesis of MOF 11B, copper(II)-5,10,15,20-Tetra(4-carboxybiphenyl)porphyrin (Cu-TCBPP, **19**) (200 mg, 0.173 mmol), 4,4'-bipyridine (54 mg, 0.346 mmol) and  $\text{Cu}(\text{NO}_3)_2 \cdot 2.5\text{H}_2\text{O}$  (84 mg, 0.346 mmol) were used. The precipitate was filtered and washed with anhydrous DMF ( $4 \times 20$  mL), then yielded a reddish-purple solid (134 mg, 67% based on Cu-TCBPP) of the MOF **14B**.

IR (KBr,  $\text{cm}^{-1}$ ): 3440 (br s, O-H stretching), 1657 (s, C=O stretching), 1606 (s, and C=C stretching), 1388 (s, C-O stretching) (Figure 4.17); XRD pattern:  $2\theta$  of  $5.46^\circ$ ,  $6.40^\circ$  (Figure 4.21)

### 3.3.5.2.3 Synthesis of MOF 12B and MOF 15B

As the same condition as synthesis of MOF 3A, zinc(II)-5,10,15,20-Tetra(4-carboxybiphenyl)porphyrin (Zn-TCBPP, **18**) (200 mg, 0.173 mmol),  $\text{Zn}(\text{NO}_3)_2 \cdot 6\text{H}_2\text{O}$  (102 mg, 0.346 mmol) and 4,4'-bipyridine (54 mg, 0.346 mmol) were used. The precipitate was filtered and washed with anhydrous DMF ( $4 \times 20$  mL), then yielded a blue-purple solid (187 mg, 94% based on Zn-TCBPP) of the MOF **12B**.

IR (KBr,  $\text{cm}^{-1}$ ): 3445 (br s, O-H stretching), 1657 (s, C=O stretching), 1606 (m, and C=C stretching), 1398 (s, C-O stretching) (Figure 4.16); XRD pattern:  $2\theta$  of  $6.94^\circ$ ,  $8.94^\circ$ ,  $10.46^\circ$ ,  $11.06^\circ$ ,  $18.06^\circ$ ,  $19.40^\circ$ ,  $22.16^\circ$  (Figure 4.21)

In the case of MOF 15B, using the same condition as synthesis of MOF 3A, copper(II)-5,10,15,20-Tetra(4-carboxybiphenyl)porphyrin (Cu-TCBPP, **19**) (200 mg, 0.173 mmol), 4,4'-bipyridine (54 mg, 0.346 mmol) and

$\text{Cu}(\text{NO}_3)_2 \cdot 2.5\text{H}_2\text{O}$  (84 mg, 0.346 mmol) were used. The precipitate was filtered and washed with anhydrous DMF ( $4 \times 20$  mL), then yielded a reddish-purple solid (157 mg, 79% based on Cu-TCBPP) of the MOF **15B**.

IR (KBr,  $\text{cm}^{-1}$ ): 3431 (br m, O-H stretching), 1670 (s, C=O stretching), 1606 (m, and C=C stretching), 1402 (s, C-O stretching) (Figure 4.17); XRD pattern:  $2\theta$  of  $5.50^\circ$ ,  $6.16^\circ$ ,  $6.80^\circ$ ,  $11.16^\circ$ ,  $35.40^\circ$ ,  $38.66^\circ$  (Figure 4.21)

### 3.3.5.3 Synthesis of Porphyrin- based MOFs Pathway C: Using Complex of metalloporphyrin with 4,4'-bipyridine ( [Zn-TCBPP]-bpy and [Cu-TCBPP]-bpy) as organic linker ([M-TCBPP]-bpy + $\text{M}(\text{NO}_3)_2 \cdot n\text{H}_2\text{O}$ +/- bpy)

Code of MOF	M-TCBPP + $\text{M}(\text{NO}_3)_2$ + bpy
16C	[Zn-TCBPP]-bpy + $\text{Zn}(\text{NO}_3)_2$
19C	[Zn-TCBPP]-bpy + $\text{Zn}(\text{NO}_3)_2$ add bpy
20C	[Zn-TCBPP]-bpy + $\text{Cu}(\text{NO}_3)_2$
21C	[Cu-TCBPP]-bpy + $\text{Cu}(\text{NO}_3)_2$
22C	[Cu-TCBPP]-bpy + $\text{Cu}(\text{NO}_3)_2$ add bpy
23C	[Cu-TCBPP]-bpy + $\text{Zn}(\text{NO}_3)_2$

**Table 3.3** Code of Porphyrin-based MOFs via pathway C

#### 3.3.5.3.1 Synthesis of MOF 16C, MOF 20C, MOF 21C and MOF 23C

As the same condition as synthesis of MOF 2A, complex of Zinc(II)-5,10,15,20-Tetra(4-carboxybiphenyl)porphyrin with 4,4'-bipyridine ([Zn-TCBPP]-bpy, **22**) (200 mg, 0.152 mmol) and  $\text{Zn}(\text{NO}_3)_2 \cdot 6\text{H}_2\text{O}$  (91 mg, 0.304 mmol) were used. The precipitate was filtered and washed with anhydrous DMF ( $4 \times 20$  mL), then yielded a blue-purple solid (186 mg, 93% based on [Zn-TCBPP]-bpy) of the MOF **16C**.

IR (KBr,  $\text{cm}^{-1}$ ): 3426 (br s, O-H stretching), 1657 (s, C=O stretching), 1601 (s, and C=C stretching), 1393 (s, C-O stretching) (Figure 4.18); XRD pattern:  $2\theta$  of  $6.96^\circ$ ,  $7.24^\circ$ ,  $8.38^\circ$ ,  $9.00^\circ$ ,  $10.00^\circ$ ,  $10.48^\circ$ ,  $11.08^\circ$ ,  $11.80^\circ$ ,  $12.66^\circ$ ,  $15.36^\circ$ ,  $18.38^\circ$ ,  $19.48^\circ$ ,  $22.20^\circ$ ,  $31.72^\circ$ ,  $34.38^\circ$ ,  $36.22^\circ$  (Figure 4.22)

In the case of MOF 20C, using the same condition as synthesis of MOF 2A, complex of Zinc(II)-5,10,15,20-Tetra(4-carboxybiphenyl) porphyrin with 4,4'-bipyridine ([Zn-TCBPP]-bpy, **22**) (200 mg, 0.152 mmol) and  $\text{Cu}(\text{NO}_3)_2 \cdot 2.5\text{H}_2\text{O}$  (74 mg, 0.304 mmol) were used. The precipitate was filtered and washed with anhydrous DMF ( $4 \times 20$  mL), then yielded a reddish-purple solid (157 mg, 79% based on [Zn-TCBPP]-bpy) of the MOF **20C**.

IR (KBr,  $\text{cm}^{-1}$ ): 3440 (br s, O-H stretching), 1652 (s, C=O stretching), 1615 (m, and C=C stretching), 1388 (s, C-O stretching) (Figure 4.18); XRD pattern:  $2\theta$  of  $6.90^\circ$ ,  $9.00^\circ$ ,  $10.32^\circ$ ,  $11.12^\circ$ ,  $18.00^\circ$ ,  $19.46^\circ$ ,  $22.30^\circ$ ,  $35.34^\circ$ ,  $36.38^\circ$ ,  $38.74^\circ$  (Figure 4.22)

In the case of MOF 21C, using the same condition as synthesis of MOF 2A, complex of copper(II)-5,10,15,20-Tetra(4-carboxybiphenyl) porphyrin with 4,4'-bipyridine ([Cu-TCBPP]-bpy, **23**) (200 mg, 0.153 mmol) and  $\text{Cu}(\text{NO}_3)_2 \cdot 2.5\text{H}_2\text{O}$  (74 mg, 0.305 mmol) were used. The precipitate was filtered and washed with anhydrous DMF ( $4 \times 20$  mL), then yielded a reddish-purple solid (177 mg, 89% based on [Cu-TCBPP]-bpy) of the MOF **21C**.

IR (KBr,  $\text{cm}^{-1}$ ): 3445 (br s, O-H stretching), 1610 (m, C=C stretching), 1416 (m, and C-O stretching), 1217 (m) (Figure 4.19); XRD pattern:  $2\theta$  of  $10.72^\circ$ ,  $14.60^\circ$ ,  $15.92^\circ$ ,  $23.62^\circ$ ,  $27.92^\circ$  (Figure 4.22)

In the case of MOF 23C, using the same condition as synthesis of MOF 2A, complex of copper(II)-5,10,15,20-Tetra(4-carboxybiphenyl) porphyrin with 4,4'-bipyridine ([Cu-TCBPP]-bpy, **23**) (200 mg, 0.153 mmol) and  $\text{Zn}(\text{NO}_3)_2 \cdot 6\text{H}_2\text{O}$  (91 mg, 0.305 mmol) were used. The precipitate was filtered and washed with anhydrous DMF ( $4 \times 20$  mL), then yielded a reddish-purple solid (173 mg, 87% based on [Cu-TCBPP]-bpy) of the MOF **23C**.

IR (KBr,  $\text{cm}^{-1}$ ): 3445 (br s, O-H stretching), 1657 (s, C=O stretching), 1610 (m, and C=C stretching), 1388 (s, C-O stretching) (Figure 4.19); XRD pattern:  $2\theta$  of  $6.76^\circ$ ,  $9.02^\circ$ ,  $10.28^\circ$ ,  $11.16^\circ$ ,  $13.60^\circ$ ,  $16.32^\circ$ ,  $17.84^\circ$ ,  $19.44^\circ$ ,  $20.50^\circ$ ,  $22.30^\circ$  (Figure 4.22)

### 3.3.5.3.2 Synthesis of MOF 19C and MOF 22C

As the same condition as synthesis of MOF 5A, complex of Zinc(II)-5,10,15,20-Tetra(4-carboxybiphenyl)porphyrin with 4,4'-bipyridine ([Zn-TCBPP]-bpy, **22**) (200 mg, 0.152 mmol),  $\text{Zn}(\text{NO}_3)_2 \cdot 6\text{H}_2\text{O}$  (91 mg, 0.304 mmol) and 4,4'-bipyridine (48 mg, 0.305 mmol) were used. The precipitate was filtered and washed with anhydrous DMF ( $4 \times 20$  mL), then yielded a blue-purple solid (182 mg, 91% based on [Zn-TCBPP]-bpy) of the MOF **19C**.

IR (KBr,  $\text{cm}^{-1}$ ): 3422 (br m, O-H stretching), 1652 (s, C=O stretching), 1610 (s, and C=C stretching), 1388 (s, C-O stretching) (Figure 4.18); XRD pattern:  $2\theta$  of  $6.98^\circ$ ,  $7.26^\circ$ ,  $8.34^\circ$ ,  $8.98^\circ$ ,  $10.02^\circ$ ,  $10.48^\circ$ ,  $11.10^\circ$ ,  $11.86^\circ$ ,  $12.74^\circ$ ,  $15.42^\circ$ ,  $18.40^\circ$ ,  $19.56^\circ$ ,  $22.18^\circ$ ,  $31.74^\circ$ ,  $34.30^\circ$ ,  $36.20^\circ$  (Figure 4.22)

In the case of MOF 22C, using the same condition as synthesis of MOF 5A, complex of copper(II)-5,10,15,20-Tetra(4-carboxybiphenyl)porphyrin with 4,4'-bipyridine ([Cu-TCBPP]-bpy, **23**) (200 mg, 0.153 mmol),  $\text{Cu}(\text{NO}_3)_2 \cdot 2.5\text{H}_2\text{O}$  (74 mg, 0.305 mmol) and 4,4'-bipyridine (48 mg, 0.305 mmol) were used. The precipitate was filtered and washed with anhydrous DMF ( $4 \times 20$  mL), then yielded a reddish-purple solid (142 mg, 71% based on [Cu-TCBPP]-bpy) of the MOF **22C**.

IR (KBr,  $\text{cm}^{-1}$ ): 3417 (br m, O-H stretching), 1657 (s, C=O stretching), 1610 (m, and C=C stretching), 1393 (m, C-O stretching) (Figure 4.19); XRD pattern:  $2\theta$  of  $6.74^\circ$ ,  $9.02^\circ$ ,  $10.26^\circ$ ,  $11.14^\circ$ ,  $13.48^\circ$ ,  $14.62^\circ$ ,  $17.92^\circ$ ,  $19.48^\circ$ ,  $22.40^\circ$  (Figure 4.22)

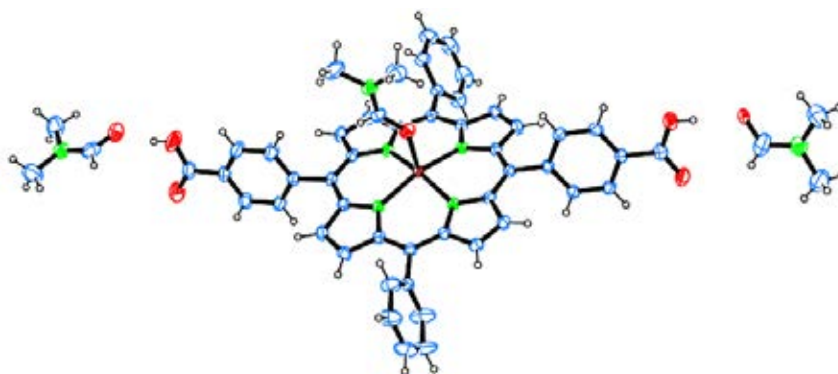
## CHAPTER IV

### RESULTS AND DISCUSSION

In this research, there were two parts of the results which concerned about synthesis of porphyrin derivatives and porphyrin-based MOFs construction. For the first one, it focused on four porphyrin derivatives, including dicarboxyphenylporphyrin, 1,4-phenylene-bridged *meso-meso* linked diporphyrin, *meso-meso*  $\beta$ - $\beta$   $\beta$ - $\beta$  triply linked (fused) diporphyrin and tetracarboxybiphenylporphyrin. Nevertheless, only the last porphyrin derivatives were used as organic linker in metal-organic frameworks formation that were investigated their gas adsorption properties and morphology for the potential use in gas storage.

#### 4.1 Part 1: Synthesis of Zinc(II)-5,15-di(4-carboxyphenyl)-10,20-diphenyl porphyrin (Zn-DCPP, **2**)

Synthesis of zinc porphyrin derivative **2** was illustrated in Scheme 3.1. The prior step was the preparation of dipyrromethane **1**, following with Adler-Longo method via reflux with propionic acid to generate the desired product **2** with moderate yield. Surprisingly, the single crystal of zinc porphyrin derivative **2** was obtained as shown in **Figure 4.1**.

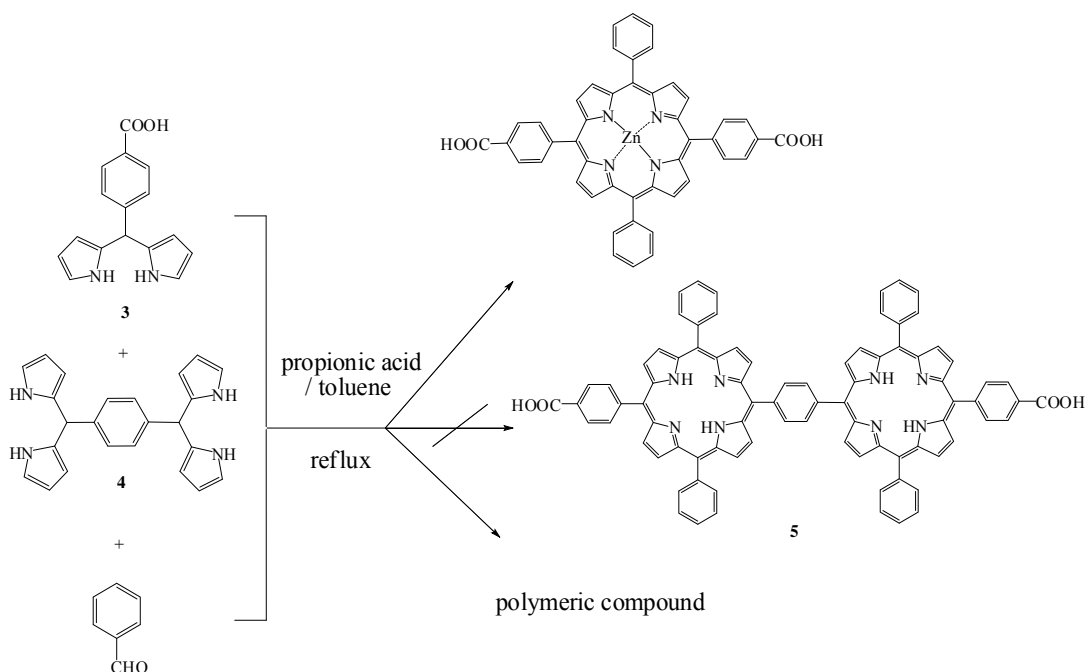


**Figure 4.1** Crystal structure of Zinc(II)-5,15-di(4-carboxyphenyl)-10,20-diphenyl porphyrin(**Zn-DCPP**), coordinated with DMF ; Color scheme: Zn, violet; C, blue; O, red; N, green and H, white

According to crystallographic data, DMF not only coordinated to zinc porphyrin derivative **2** at zinc ion within the inner core of porphyrin ring, but also carboxylic groups of **2**. Unfortunately, this porphyrin derivative **2** has been already used as organic linker in MOFs preparation.<sup>(105)</sup>

#### 4.2 Part 2: Synthesis of 1,4-phenylene-bridged *meso-meso* linked di-5-(4-methoxycarbonylphenyl)-10,20-diphenylporphyrin (**5**)

1,4-phenylene-bridged *meso-meso* linked diporphyrin (**5**) was synthesized by condensation of 5-(4-carboxyphenyl)dipyrromethane (**3**), 1,4-bis(dipyrromethyl) (**4**) and benzaldehyde but the desired porphyrin product (**5**) was not acquired. This may be due to the low solubility of 1,4-bis(dipyrromethyl) (**4**) in toluene and propionic acid or its condensation reactivity, thus 5-(4-carboxyphenyl)dipyrromethane (**3**) and benzaldehyde condensed, giving undesired products, 5,15-di(4-carboxyphenyl)-10,20-diphenyl porphyrin (**DCPP**) and polymeric compounds, as shown in Scheme 4.1.



**Scheme 4.1** Undesired products from synthesis of 1,4-phenylene-bridged *meso-meso* linked diporphyrin

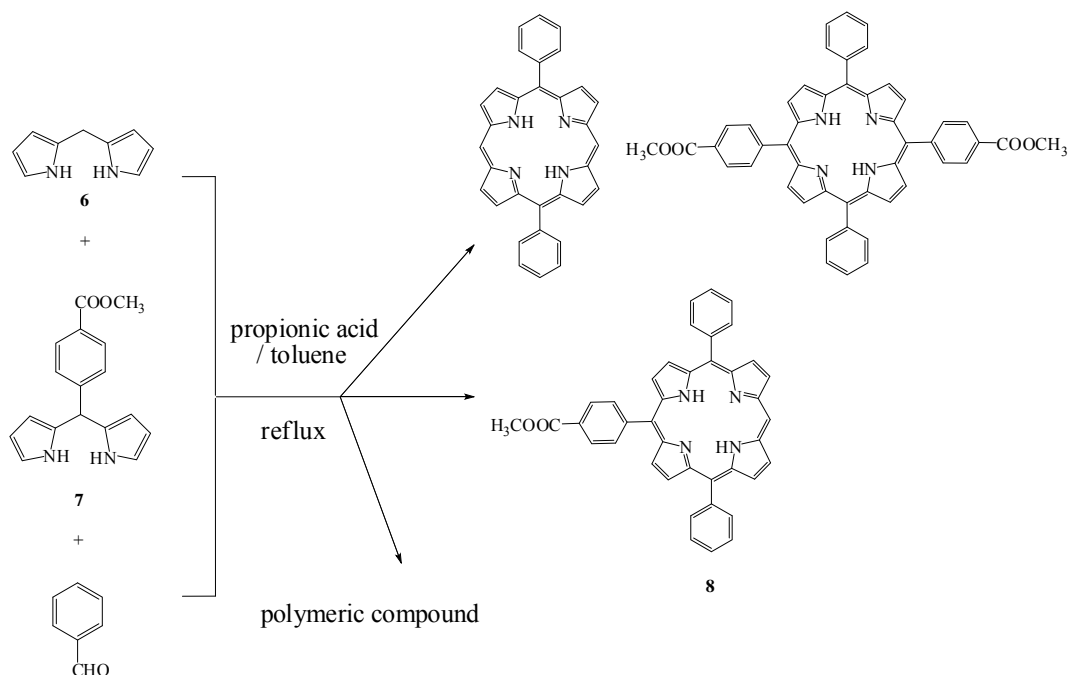


### 4.3 Part3: Synthesis of *meso-meso* $\beta$ - $\beta$ $\beta$ - $\beta$ triply linked (fused) diporphyrin (10)

#### 4.3.1 Synthesis of *meso-meso* $\beta$ - $\beta$ $\beta$ - $\beta$ triply linked (fused) diporphyrin pathway I:

Generally, dipyrromethane (**6**) was synthesized by condensation of excess pyrrole and paraformaldehyde in the presence of an acid catalyst without solvent.<sup>(96)</sup> Paraformaldehyde was insoluble in pyrrole at room temperature, thus it was necessary to heat the reaction mixture to 55°C to increase the solubility.

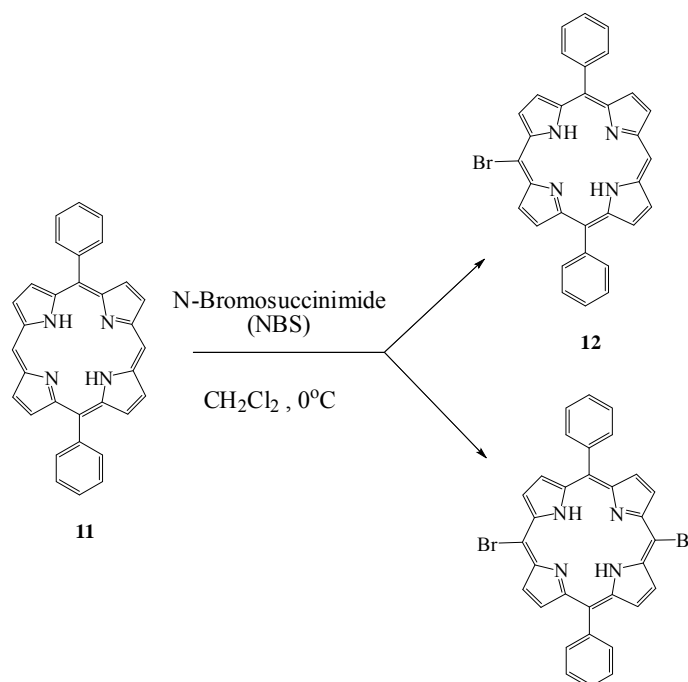
5-(4-methoxycarbonylphenyl)-10,20-diphenylporphyrin (**8**) was synthesized by condensation of dipyrromethane (**6**), 5-(4-methoxycarbonylphenyl)dipyrromethane (**7**) and benzaldehyde. There was different reactivity between two dipyrromethane (**6** and **7**) to compete reaction in the porphyrin formation. 5-(4-Methoxycarbonylphenyl)dipyrromethane (**7**) was a better nucleophile than dipyrromethane (**6**) due to aromatic substituent, thus it attacked aldehyde (benzaldehyde) easier than **6** to obtain other statistically possible porphyrin by-products such as 5,15-(4-methoxycarbonylphenyl)-10,20-diphenyl porphyrin and 5,15-diphenylporphyrin which were major and minor by-products, respectively. Consequently, the desired porphyrin product (**8**) was obtained in trace amount (2% yields) as illustrated in Scheme 4.2.



**Scheme 4.2** Synthesis of 5-(4-methoxycarbonylphenyl)-10,20-diphenylporphyrin (8).

#### 4.3.2 Synthesis of *meso-meso* $\beta$ - $\beta$ $\beta$ - $\beta$ triply linked (fused) diporphyrin pathway II:

Another pathway for synthesis porphyrin derivative (8) was a bromination at the *meso* position of 5,15-diphenylporphyrin (11) using *N*-bromosuccinimide (NBS) to obtain mono-brominated porphyrin, then followed by Suzuki coupling reaction using boronic acid and palladium catalyst. The mechanism of this reaction concerned about radicals, so cooling the reaction was required to stabilize the radicals. The gradually addition of NBS into a diluted *reactant* solution was necessary to obtain the desired product. However, the *mono*-brominated porphyrin (12) was obtained at a low percent yield (14%) but undesired product, di-brominated porphyrin, was gotten at 80% yield as shown in Scheme 4.3.



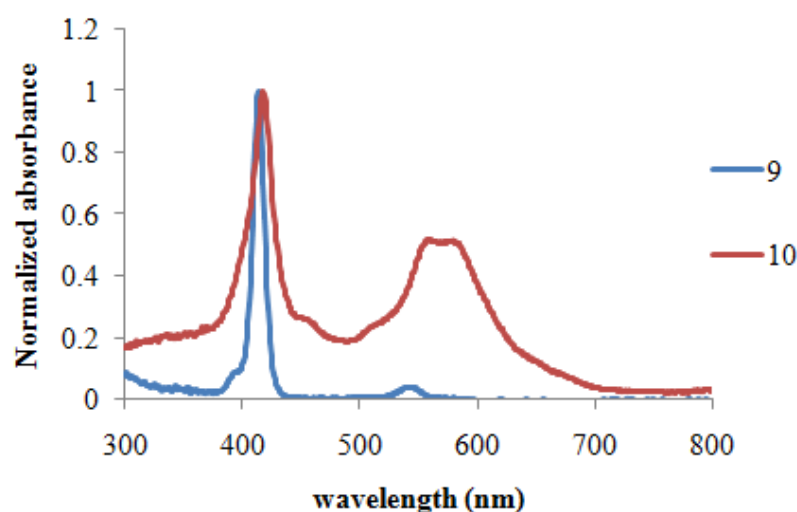
**Scheme 4.3** Products obtained from bromination of 5,15-diphenylporphyrin (**11**).

For the preparation of Zinc(II)-5-(4-methoxycarbonylphenyl)-10,20-diphenyl porphyrin (**9**), Zinc(II) ion was easily inserted into the core of free base 5-(4-methoxycarbonylphenyl)-10,20-diphenylporphyrin (**8**) as indication by a color change of the solution of **8** from purple to bright reddish purple. The  $^1\text{H}$  NMR spectrum of zinc porphyrin derivative (**9**) displayed relatively similar signal to the free base porphyrin (**8**) with slightly shifted peaks. From  $^1\text{H}$ -NMR spectrum, a characteristic a singlet at  $\delta -3.02$  ppm of inner protons of a free base porphyrin (**8**) disappeared which indicated the complete metallation of the porphyrin **8**.

The synthesis of triply-fused diporphyrin derivative (**10**) relied on the synthesis procedure and the center metal of porphyrin due to radical mechanism. Cooling the reaction was required to stabilize the radical of catalyst (PIFA) and porphyrin that could reduce the polymeric residue. Free base porphyrin could not be promoted triply-fused diporphyrin because the phenyl iodide radical of catalyst would combine with a inner  $-\text{NH}$  proton of porphyrin which was a weaker bond than

–CH proton of *meso*- and  $\beta$ -position.<sup>(104)</sup> That would result in the porphyrin (**8**) reactant not the desired triply-fused diporphyrin (**10**).

#### 4.3.3 UV-Vis study of *meso-meso* $\beta$ - $\beta$ $\beta$ - $\beta$ triply linked (fused) diporphyrin (**10**)



**Figure 4.2** UV-vis absorption spectra of zinc porphyrin **9** and triply-fused diporphyrin **10** in  $\text{CH}_2\text{Cl}_2$

Figure 4.2 displays the UV-vis absorption spectra of zinc porphyrin **9** and triply-fused diporphyrin **10** in  $\text{CH}_2\text{Cl}_2$ . The absorption spectrum of porphyrin **9** shows a Soret band at 414 nm and a Q-band at 544 nm, while the triply-fused diporphyrin **10** exhibits a Soret band at 418 nm and Q-bands at 561 and 579 nm. Comparison of absorption bands of single core (**9**) and fused-core (**10**) porphyrins, broadness and red-shift of Soret and Q-bands as well as number of Q-bands were often discovered which may be ascribed to the increased conjugation of porphyrin core that allowed increasing of electron delocalization.

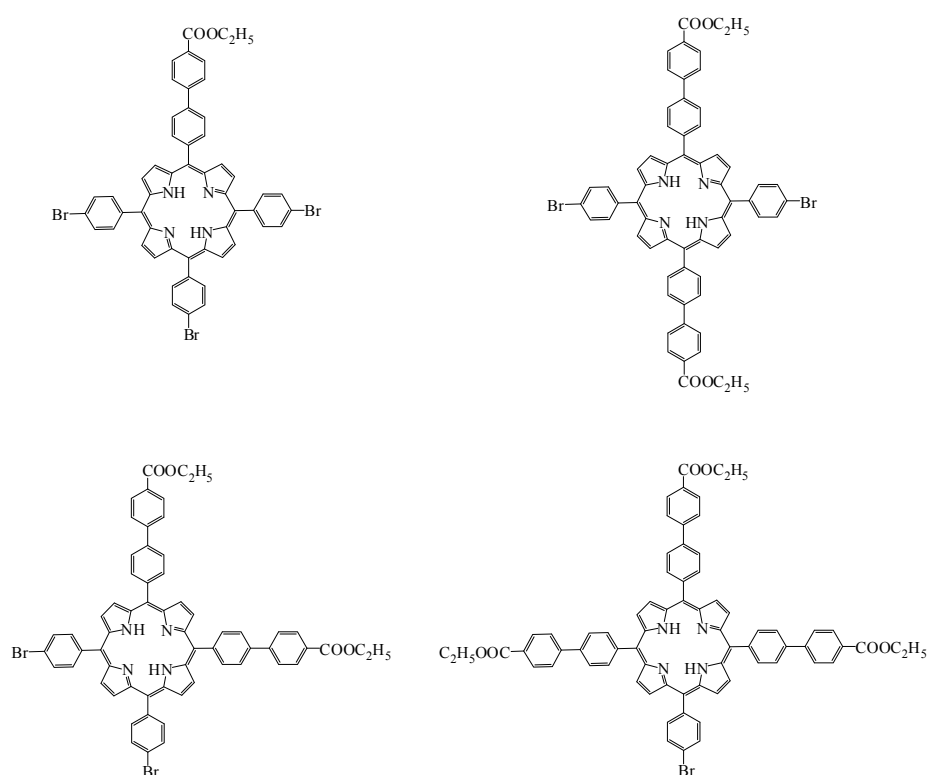
$^1\text{H}$  NMR spectrum of triply-fused diporphyrin **10** was so confused, it should have more peaks than as shown in Figure A-15. This may be due to the extensively delocalized electron. However, the desired porphyrin product (**10**) was trace amount which was not suitable to use as organic linker for MOF synthesis.

#### 4.4 Part 4: Synthesis of tetracarboxybiphenylporphyrin derivatives

To discuss about synthesis and characterization of tetracarboxybiphenyl porphyrin derivatives, it should be focused on Suzuki coupling reaction, metallation, hydrolysis and complexation studies of metalloporphyrins with 4,4'-bipyridine.

##### 4.4.1 Synthesis of 5,10,15,20-tetra(4-ethoxycarbonylbiphenyl) porphyrin (TEBPP, **14**)

Suzuki coupling reaction of 5,10,15,20-tetra(4-bromophenyl) porphyrin (TPPBr, **13**) with 4-ethoxycarbonylphenyl boronic acid generated the desired product, 5,10,15,20-tetra(4-ethoxycarbonylbiphenyl) porphyrin (TEBPP, **14**), which was a major product and the other porphyrin derivatives as presented in Figure 4.3.



**Figure 4.3** By products obtained from Suzuki coupling reaction of TPPBr **13** and boronic acid derivative.

#### **4.4.2 Metallation of 5,10,15,20-tetra(4-ethoxycarbonylbiphenyl) porphyrin (TEBPP, 14)**

Metallations of TEBPP (**14**) with  $\text{Zn}(\text{OAc})_2$  and  $\text{Cu}(\text{OAc})_2$  were successful with high yields (over 90% yield) and the presence of zinc metallated porphyrin (Zn-TEBPP, **16**) (Figure A-29) was confirmed by disappearance of inner proton peak of a free base porphyrin (TEBPP, **14**) at  $\delta$  -2.67 ppm (Figure A-23). In the case of copper metallated porphyrin (Cu-TEBPP, **17**), it could not be characterized by  $^1\text{H}$  NMR because copper was paramagnetic metal ion, which affected the NMR measurement, presenting as very broad peaks of proton resonance thus it was not shown.

#### **4.4.3 Hydrolysis of TEBPP (14), Zn-TEBPP (16) and Cu-TEBPP (17)**

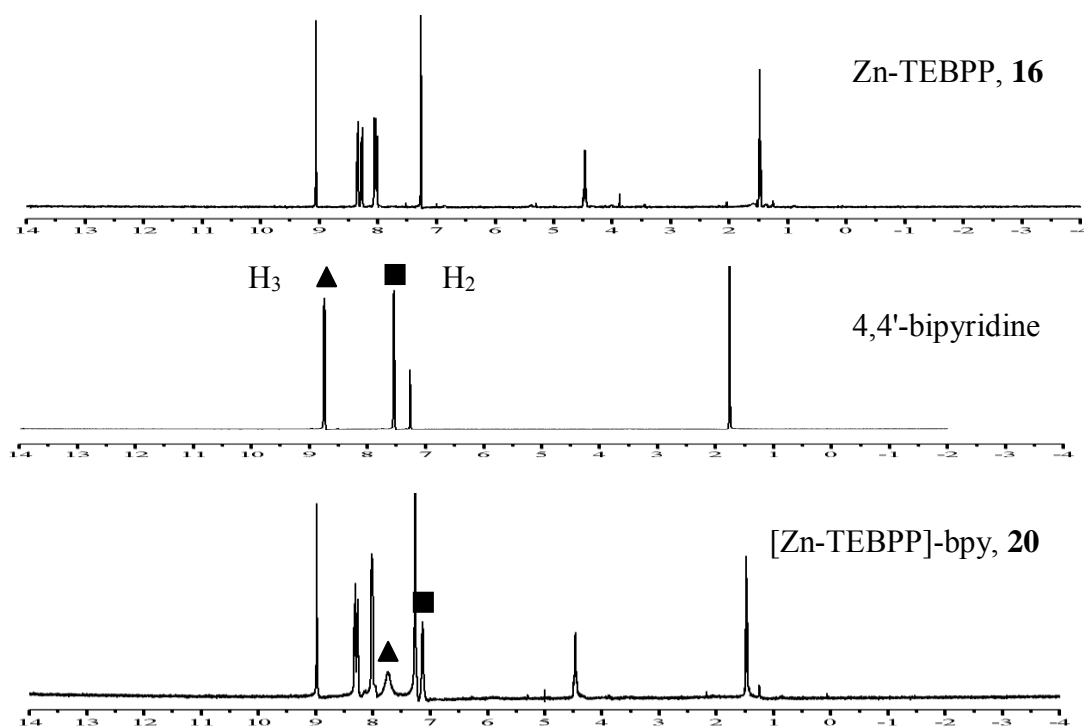
The 5,10,15,20-Tetra(4-ethoxycarbonylbiphenyl)porphyrin (**14**) was hydrolysed to 5,10,15,20-tetra(4-carboxybiphenyl)porphyrin (TCBPP, **15**) by using KOH solution and following by acidification with HCl. The desired product was obtained in a good yield (94%). In the cases of hydrolysis of metallated porphyrin (Zn-TEBPP, **16** and Cu-TEBPP, **17**),  $\text{CH}_3\text{COOH}$  was used instead of HCl to acidify and the desired products (Zn-TCBPP, **18** and Cu-TCBPP, **19**) also got in good yields (94 and 90 %, respectively). Otherwise, using HCl to acidify in these cases may demetallate the porphyrin and generated porphyrin **15**.

#### **4.4.4 Complexation studies of Zn-TEBPP (16), Cu-TEBPP(17), Zn-TCBPP (18) and Cu-TCBPP(19) with 4,4'-bipyridine**

##### **4.4.4.1 $^1\text{H}$ NMR Spectroscopic study**

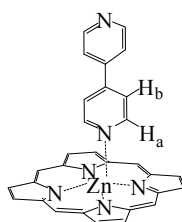
From the  $^1\text{H}$  NMR spectra, complex of Zinc(II)-5,10,15,20-tetra(4-ethoxycarbonylbiphenyl)porphyrin with 4,4'-bipyridine ( $[\text{Zn-TEBPP}]\text{-bpy}$ , **20**) (Figure A-36) was noticed. The coordination of nitrogen atom of 4,4'-bipyridine to Zn(II)ion at the core of porphyrin (**16**) could be confirmed by the upfield shifts of doublets of  $\text{H}_2$  and  $\text{H}_3$  of 4,4'-bipyridine in  $\text{CDCl}_3$  (7.13 and 7.74 ppm, respectively)

compared to free 4,4'-bipyridine (7.35 and 8.75 ppm) (Figure A-45) as shown in Figure 4.4.



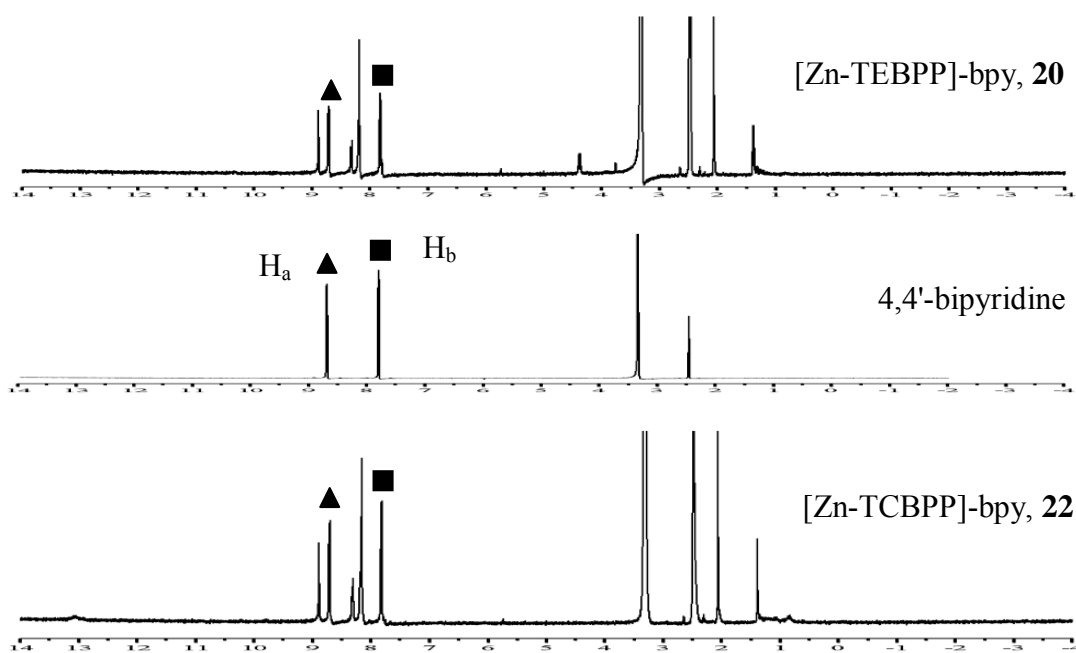
**Figure 4.4** Compared  $^1\text{H}$  NMR spectra of Zn-TEBPP (**16**), 4,4'-bipyridine and [Zn-TEBPP]-bpy (**20**) in  $\text{CDCl}_3$ .

Particularly, the signal of  $\text{H}_3$  of 4,4'-bipyridine displayed the large change since these protons were closed to the core of porphyrin ring, which could be affected by the ring current of porphyrin as displayed in Figure 4.5.



**Figure 4.5** Complex of zinc porphyrin with 4,4'-bipyridine.

The coordination of nitrogen atom of 4,4'-bipyridine to Zn(II)ion at the core of porphyrin in the complex of Zinc(II)-5,10,15,20-Tetra(4-carboxybiphenyl) porphyrin ([Zn-TCBPP]-bpy, **22**) (Figure A-41) could not be confirmed by the upfield shifts of H<sub>2</sub> and H<sub>3</sub> signals of 4,4'-bipyridine in DMSO (7.82 and 8.71 ppm; respectively) compared to free 4,4'-bipyridine (7.80 and 8.69 ppm) (Figure A-47) as shown in Figure 4.6. This may be due to DMSO, which was polar solvent, could coordinate to zinc ion at the core of porphyrin *via* oxygen linkage with zinc as Figure 4.1. Nitrogen atom of 4,4'-bipyridine could not bind to zinc, thus 4,4'-bipyridine may be free the complex and its <sup>1</sup>H NMR was similar to that of pure 4,4'-bipyridine.



**Figure 4.6** Compared <sup>1</sup>H NMR spectra of [Zn-TEBPP]-bpy (**20**), 4,4'-bipyridine and [Zn-TCBPP]-bpy (**22**) in DMSO.

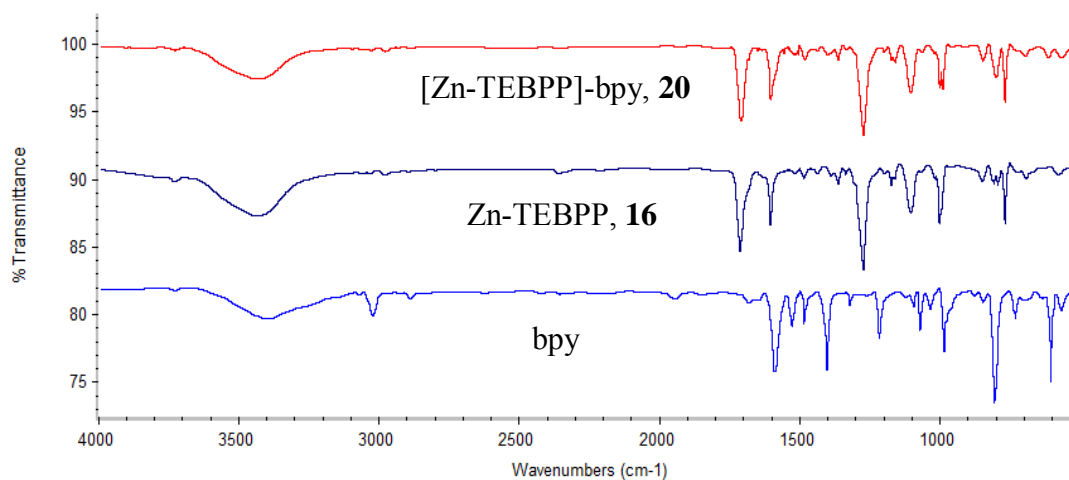
In case of complex of copper(II)-5,10,15,20-tetra(4-ethoxy carbonylbiphenyl)porphyrin with 4,4'-bipyridine ([Cu-TEBPP]-bpy, **21**) and complex of Copper(II)-5,10,15,20-tetra(4-carboxybiphenyl)porphyrin with 4,4'-bipyridine



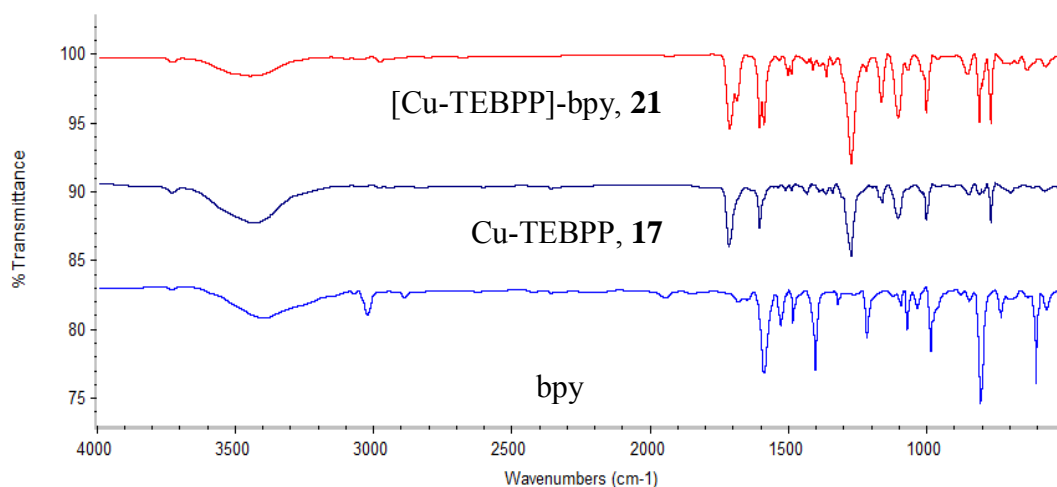
([Cu-TCBPP]-bpy, **23**),  $^1\text{H}$  NMR spectra were not acquired because of their paramagnetic properties.

#### 4.4.4.2 IR spectroscopic study

Another technique which is suitable to prove complexation between 4,4'-bipyridine and Zn-TEBPP(**16**) is IR spectroscopy. Comparing IR spectra of 4,4'-bipyridine, Zn-TEBPP(**16**) and [Zn-TEBPP]-bpy(**20**) (Figure 4.7), it is revealed that spectra of Zn-TEBPP(**16**) and [Zn-TEBPP]-bpy(**20**) had similar peaks at  $1,717\text{ cm}^{-1}$  (C=O stretching),  $1,606\text{ cm}^{-1}$  (C=C stretching) and  $1,273\text{ cm}^{-1}$  (C-O stretching) but the ratio of peak intensity between  $1,717\text{ cm}^{-1}$  and  $1,606\text{ cm}^{-1}$  increased indicating that 4,4'-bipyridine presented in complex **20**. In case of Cu-TEBPP(**17**) and [Cu-TEBPP]-bpy(**21**), they presented the same result as zinc complex as shown in Figure 4.8.

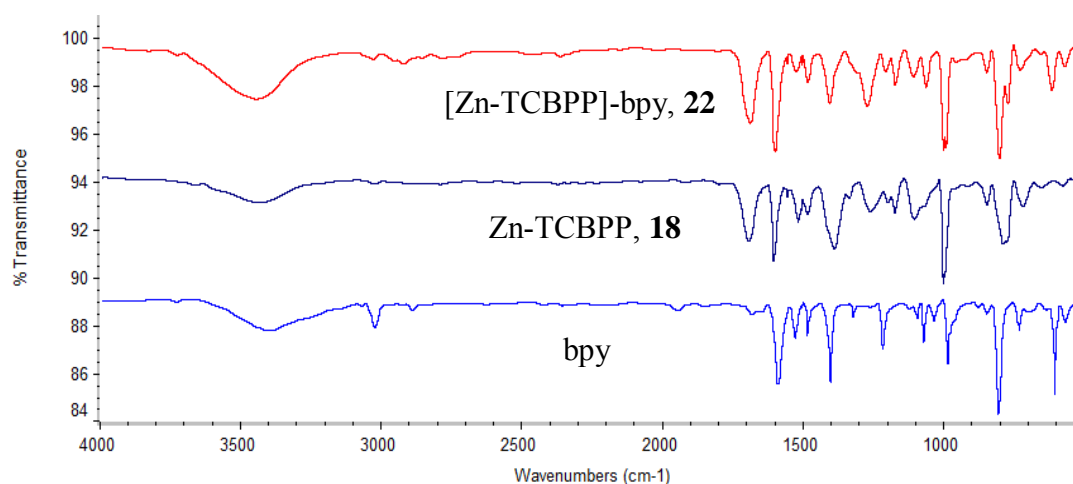


**Figure 4.7** Compared IR spectra of 4,4'-bipyridine, Zn-TEBPP(**16**) and [Zn-TEBPP]-bpy (**20**).

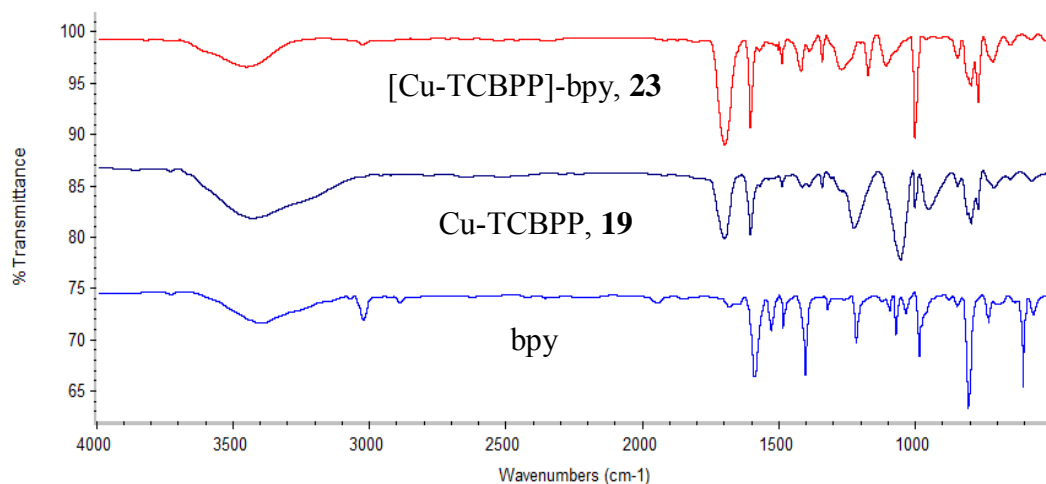


**Figure 4.8** Compared IR spectra of 4,4'-bipyridine, Cu-TEBPP(**17**) and [Cu-TEBPP]-bpy (**21**).

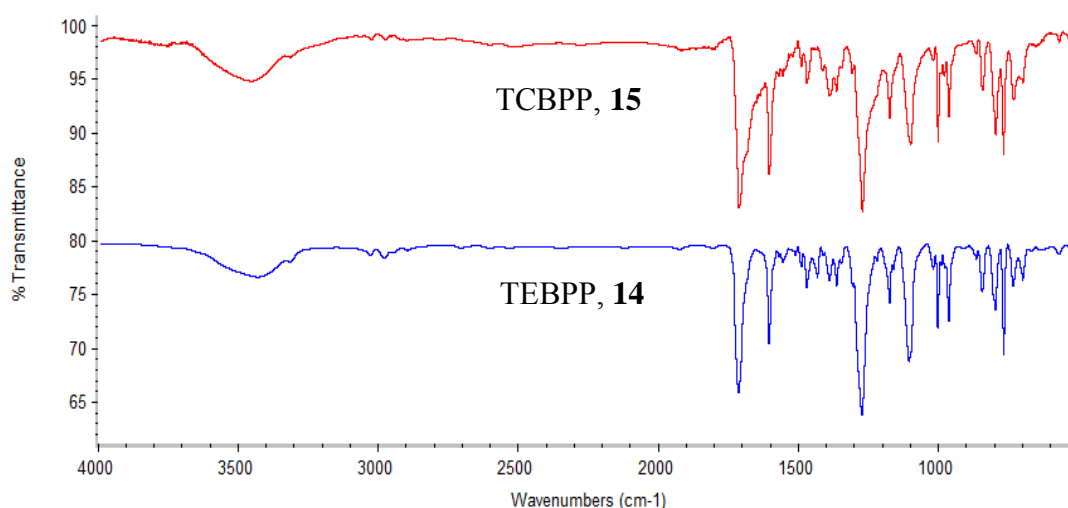
Similarly to the complexation of 4,4'-bipyridine to Zn-TEBPP(**16**), IR spectra of Zn-TCBPP(**18**) and [Zn-TCBPP]-bpy(**22**) or Cu-TCBPP(**19**) and [Cu-TEBPP]-bpy(**23**) showed the same results as in case of Zn-TEBPP(**16**) and [Zn-TEBPP]-bpy(**20**) as illustrated in Figure 4.9 and Figure 4.10, respectively. They contained similar peaks at  $3,445\text{ cm}^{-1}$  (O-H stretching),  $1,689\text{ cm}^{-1}$  (C=O stretching),  $1,601\text{ cm}^{-1}$  (C=C stretching) and  $1,264\text{ cm}^{-1}$  (C-O stretching) but the peak intensity ratio between  $1,689$  and  $1,601\text{ cm}^{-1}$  increased which implied a presence of 4,4'-bipyridine in the compounds.



**Figure 4.9** Compared IR spectra of 4,4'-bipyridine, Zn-TCBPP(**18**) and [Zn-TCBPP]-bpy (**22**).



**Figure 4.10** Compared IR spectra of 4,4'-bipyridine, Cu-TCBPP(**19**) and [Cu-TCBPP]-bpy(**23**).



**Figure 4.11** Compared IR spectra of TEBPP(**14**) and TCBPP(**15**)

#### 4.4.4.3 Mass spectrometric study

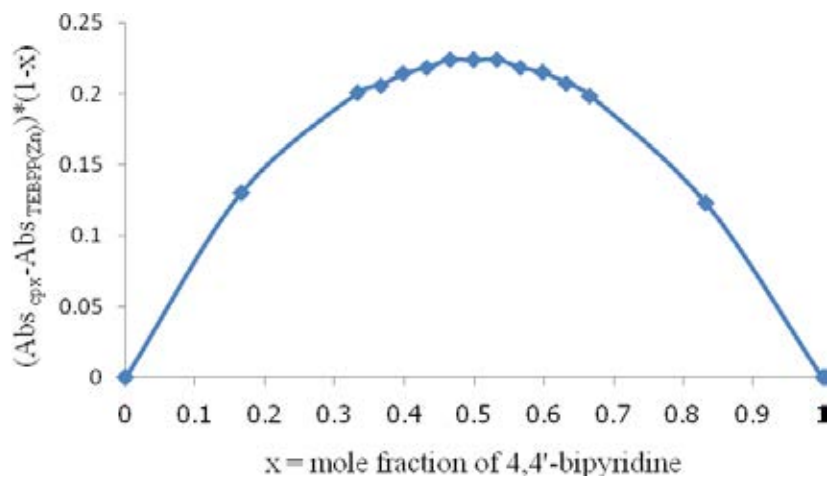
MALDI-TOF mass spectrometry was also used to examine for all complexes of metallated porphyrins with 4,4'-bipyridine (**20**, **21**, **22**, **23**). Unfortunately, only the molecular ion peaks of porphyrins were observed, meanwhile the porphyrin-4,4'-bipyridine complexes could not be detected. This may be due to the complexations of porphyrins with 4,4'-bipyridine were not strong enough to survive under this ionization conditions.

#### 4.4.4.4 UV-vis spectrophotometric study

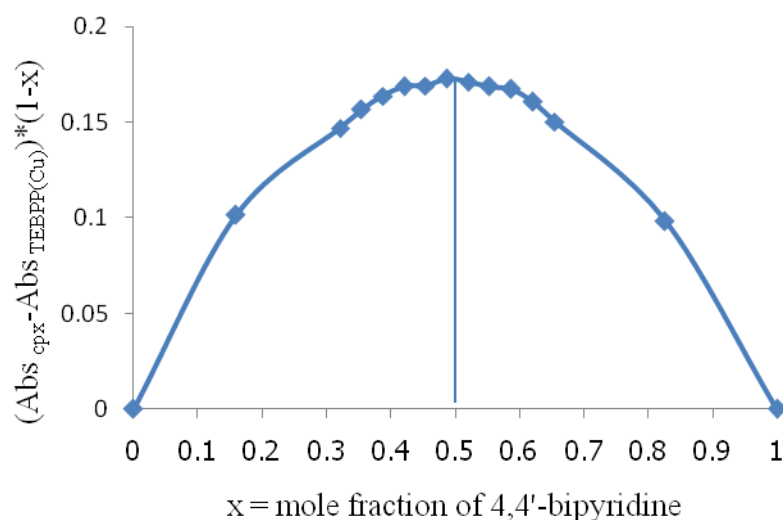
Moreover, complexation study of metallated porphyrins with 4,4'-bipyridine (bpy) in  $\text{CHCl}_3$  and DMSO by UV-visible spectrophotometry were also investigated. The UV-visible absorption spectra of all porphyrins were measured at a concentration of  $10^{-6}$  M. The job's plot between absorption and the mole fraction of 4,4'-bipyridine was used to determine the binding stoichiometry of the complexes using the absorption at 429 nm for **16**, 420 nm for **17**, 433 nm for **18** and 424 nm for **19**. The job's plot was plotted between the mole fraction of 4,4'-bipyridine in the mixture (x) and  $\Delta A (1-x)$  calculated from the maximum absorption changes ( $\Delta A$ ) multiplied by their inverse mole fraction (1-x).

The plots afforded the maximum points at 0.5 for Zn-TEBPP (**16**) and Cu-TEBPP (**17**), indicating that the complex stoichiometry with 4,4'-bipyridine was 1:1 as illustrated in Figure 4.12.

a)

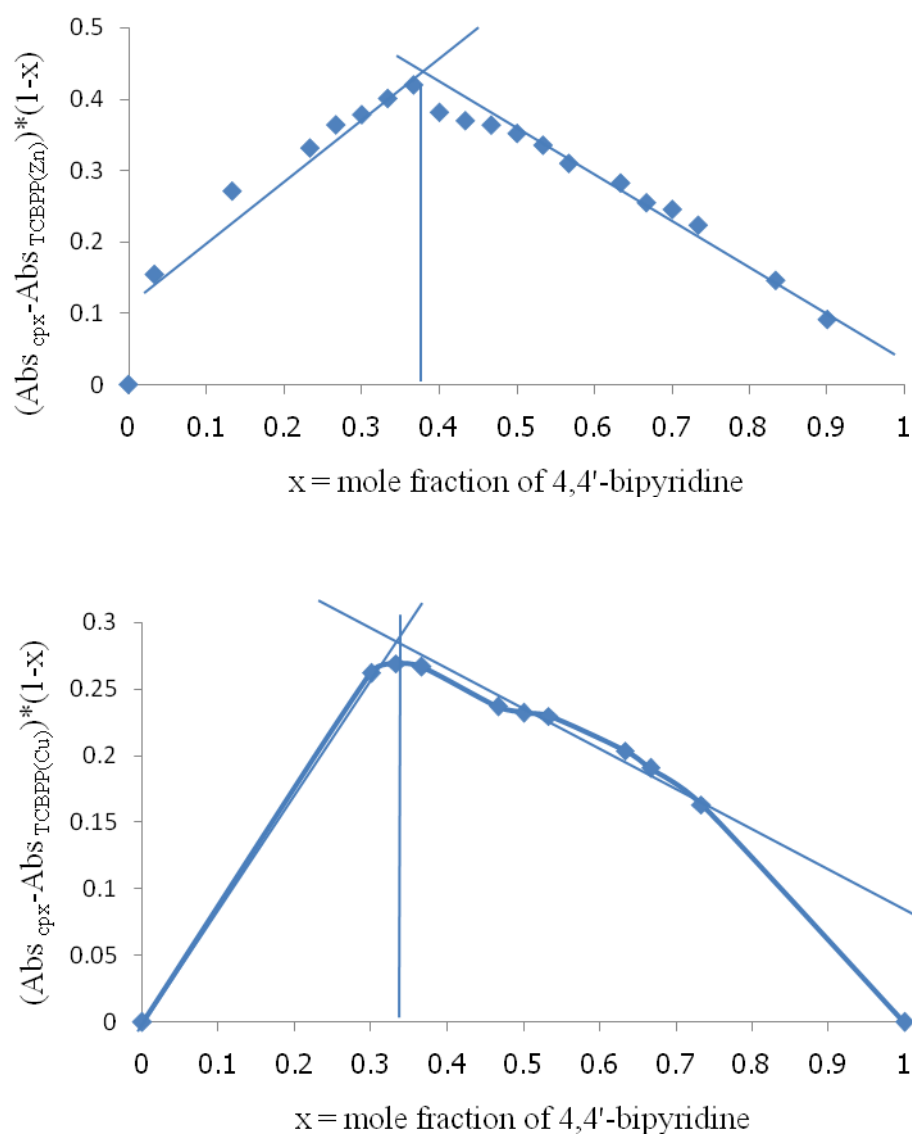


b)



**Figure 4.12** The job's plots of the complexations of metallated porphyrins with 4,4'-bipyridine in  $\text{CHCl}_3$ : a) Zn-TEBPP (**16**) and b) Cu-TEBPP(**17**).

For 4,4'-bipyridine complexation of Zn-TCBPP (**18**) and Cu-TCBPP (**19**), the Job's plots afforded the maximum points at 0.33 indicating that the complex stoichiometry with 4,4'-bipyridine were 2:1 (metallated porphyrins: 4,4'-bipyridine) as displayed in Figure 4.13.

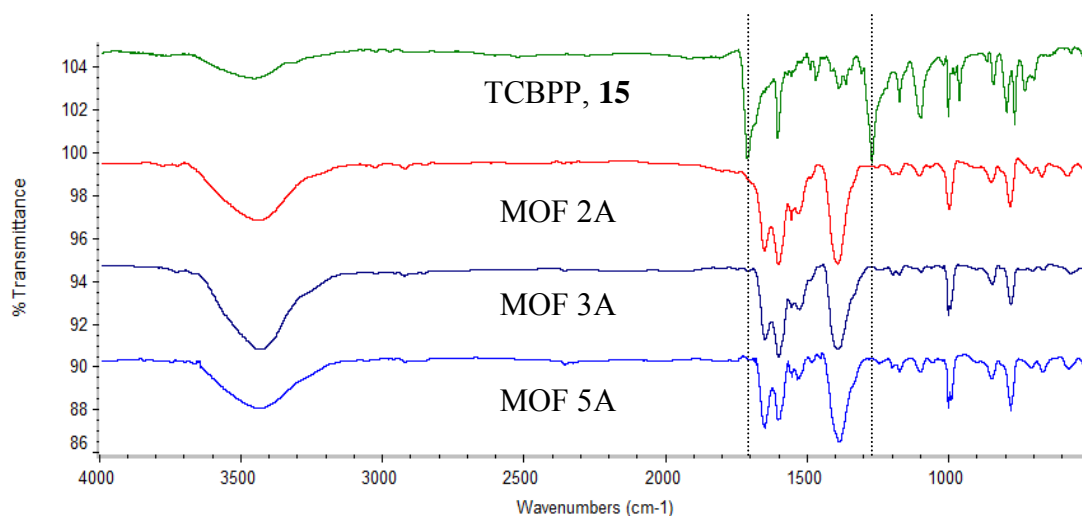


**Figure 4.13** The job's plots of the complexations of metallated porphyrins with 4,4'-bipyridine in DMSO: a) Zn-TCBPP (**18**) and b) Cu-TCBPP(**19**).

## 4.5 Part 5: Synthesis of Porphyrin-based MOFs using tetracarboxybiphenyl porphyrin derivatives as organic linkers

### 4.5.1 IR spectroscopic study

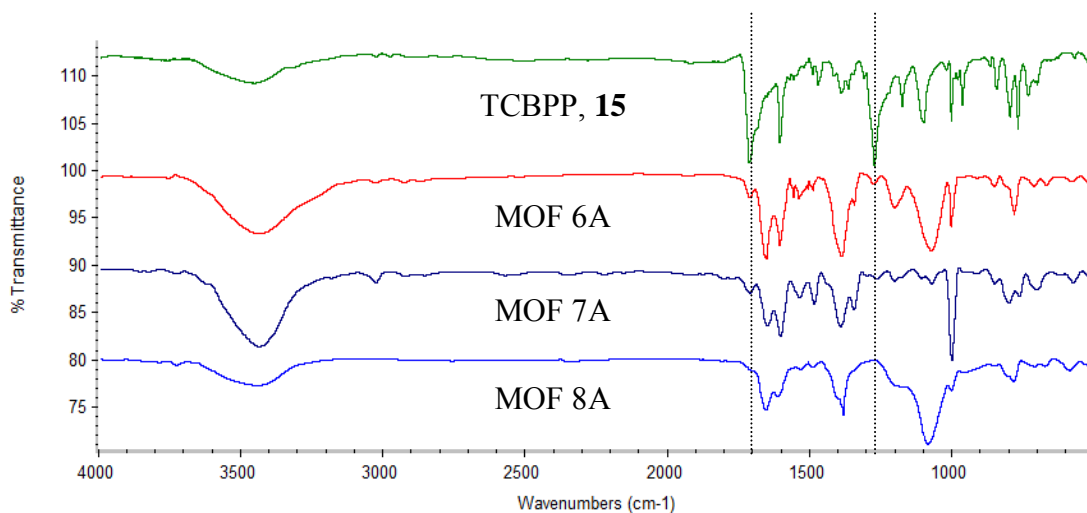
For all porphyrin-based MOFs, the peaks of all IR spectra of MOFs were shifted comparing with the porphyrin organic linkers. In cases of MOFs **2A**, **3A** and **5A** which had zinc as metal and TCBPP (**15**) as organic linker with or without 4,4'-bipyridine as pillar, their IR spectra presented at  $3,454\text{ cm}^{-1}$  (br s, O-H stretching),  $1,657\text{ cm}^{-1}$  (s, C=O stretching),  $1,601\text{ cm}^{-1}$  (s, C=C stretching) and  $1,393\text{ cm}^{-1}$  (s, C-O stretching), while IR spectra of TCBPP **15** using as organic linker showed at  $3,458\text{ cm}^{-1}$  (br s, O-H stretching),  $1,719\text{ cm}^{-1}$  (s, C=O stretching),  $1,603\text{ cm}^{-1}$  (m, C=C stretching) and  $1,273\text{ cm}^{-1}$  (s, C-O stretching) as exhibited in Figure 4.14. The shift of C=O and C-O stretching peaks may suggest that the carboxylate group may coordinate to metal and the frameworks could be generated.



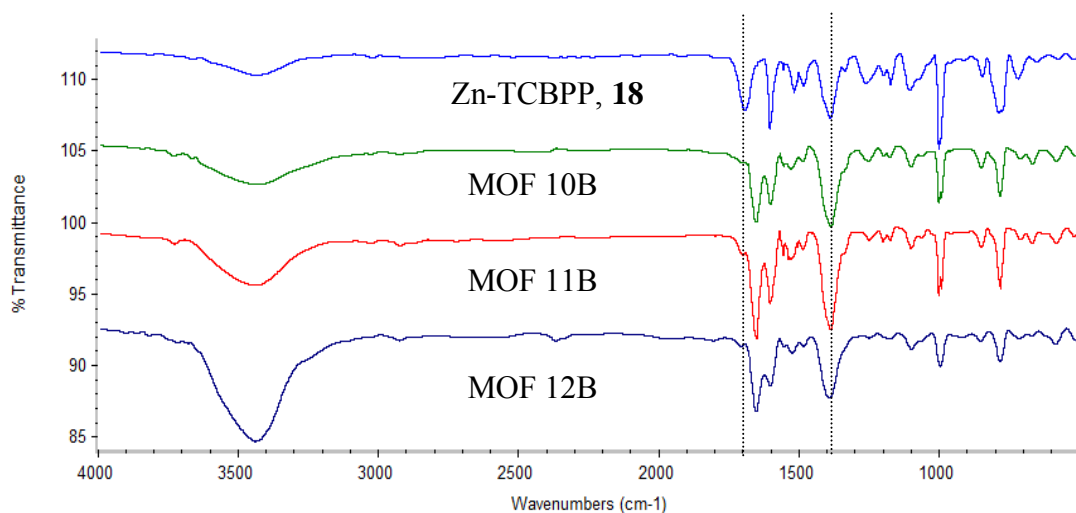
**Figure 4.14** Compared IR spectra of TCBPP (**15**) and MOFs **2A** (**15**+Zn(NO<sub>3</sub>)<sub>2</sub>), **3A** (**15**+Zn(NO<sub>3</sub>)<sub>2</sub>+bpy), and **5A** (**15**+Zn(NO<sub>3</sub>)<sub>2</sub> added bpy).

For other MOFs, the comparison of IR spectra of porphyrin organic linkers and each MOFs are presented in Figure 4.15-4.19 which show similar results to that of TCBPP (**15**). However, IR spectrum of MOF 21C (Figure 4.19) showed asymmetrical and symmetrical stretchings ( $\nu_a(\text{COO}) \sim 1600\text{ cm}^{-1}$  and  $\nu_s(\text{COO}) \sim 1400$

$\text{cm}^{-1}$  for  $\text{COO}^-$ , respectively) which implied that  $\text{Cu}_2(\text{COO})_4$  paddle-wheel units formed.

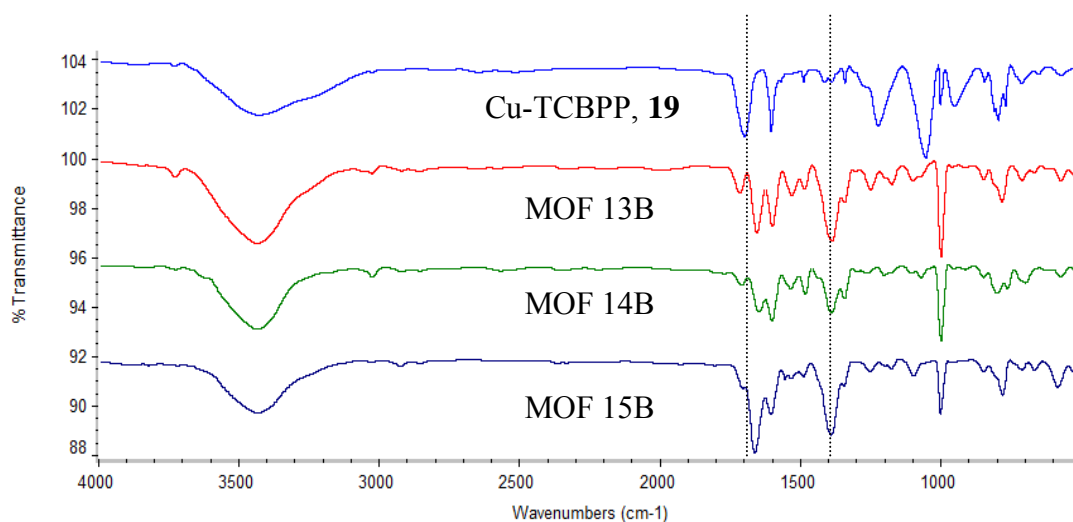


**Figure 4.15** Compared IR spectra of TCBPP (**15**) and MOFs **6A** (**15**+ $\text{Cu}(\text{NO}_3)_2$ ), **7A** (**15**+ $\text{Cu}(\text{NO}_3)_2$ +bpy) and **8A** (**15**+ $\text{Cu}(\text{NO}_3)_2$  added bpy).

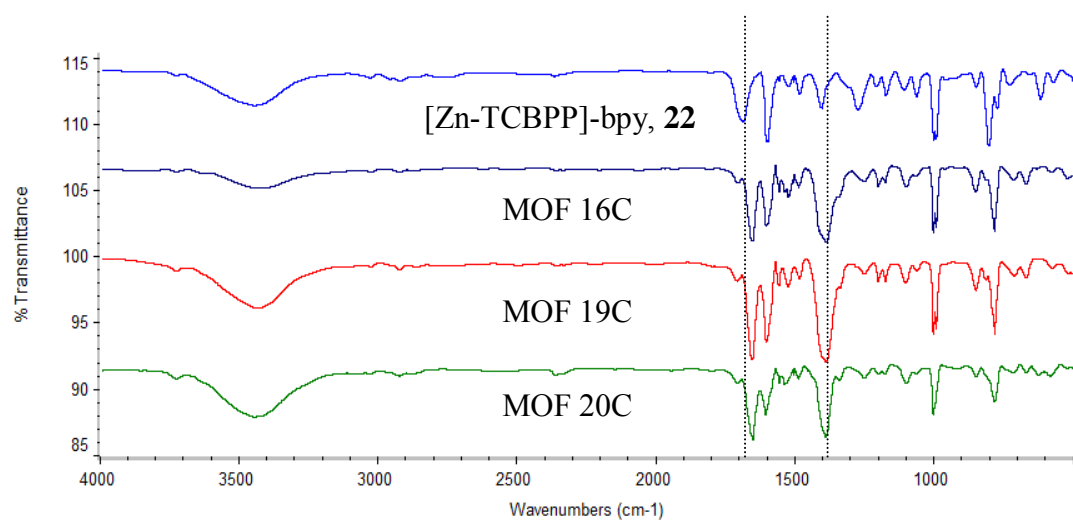


**Figure 4.16** Compared IR spectra of Zn-TCBPP(**18**), MOFs **10B** (**18**+ $\text{Zn}(\text{NO}_3)_2$  added bpy), **11B** (**18**+ bpy added  $\text{Zn}(\text{NO}_3)_2$ ) and **12B** (**18**+ bpy +  $\text{Zn}(\text{NO}_3)_2$ ).

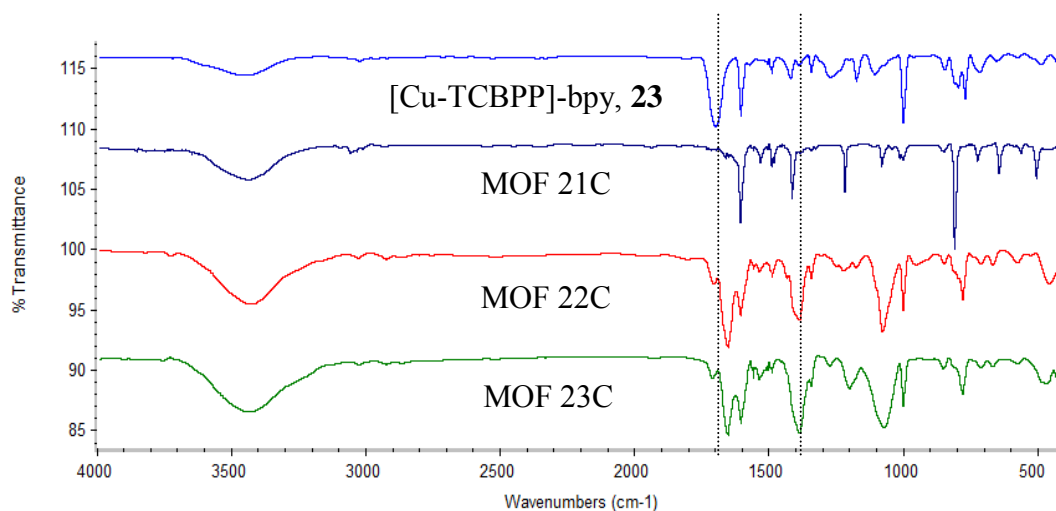




**Figure 4.17** Compared IR spectra of Cu-TCBPP(**19**), MOFs **13B** (**18**+Cu(NO<sub>3</sub>)<sub>2</sub> added bpy), **14B** (**18**+ bpy added Cu(NO<sub>3</sub>)<sub>2</sub>) and **15B** (**18**+ bpy + Cu(NO<sub>3</sub>)<sub>2</sub>).



**Figure 4.18** Compared IR spectra of [Zn-TCBPP]-bpy(**22**), MOFs **16C** (**22**+Zn(NO<sub>3</sub>)<sub>2</sub>), **19C** (**22**+Zn(NO<sub>3</sub>)<sub>2</sub> added bpy) and **20C** (**22**+Cu(NO<sub>3</sub>)<sub>2</sub>).

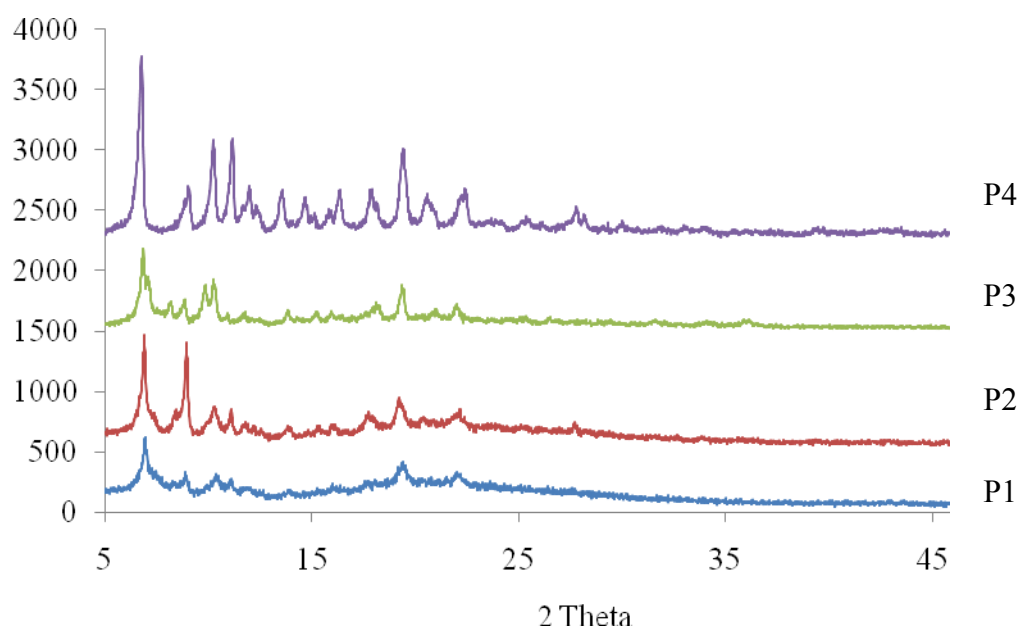


**Figure 4.19** Compared IR spectra of [Cu-TCBPP]-bpy(**23**), MOFs **21C** (**23**+Cu(NO<sub>3</sub>)<sub>2</sub>), **22C** (**23**+Cu(NO<sub>3</sub>)<sub>2</sub> added bpy) and **23C** (**23**+Zn(NO<sub>3</sub>)<sub>2</sub>)

#### 4.5.2 XRD study

For porphyrin-based MOFs synthesized *via* pathway A using TCBPP (**15**) as organic linker and different metal nodes (zinc or copper) presented the different XRD patterns (see Figure 4.20) because of different coordination modes of metals.

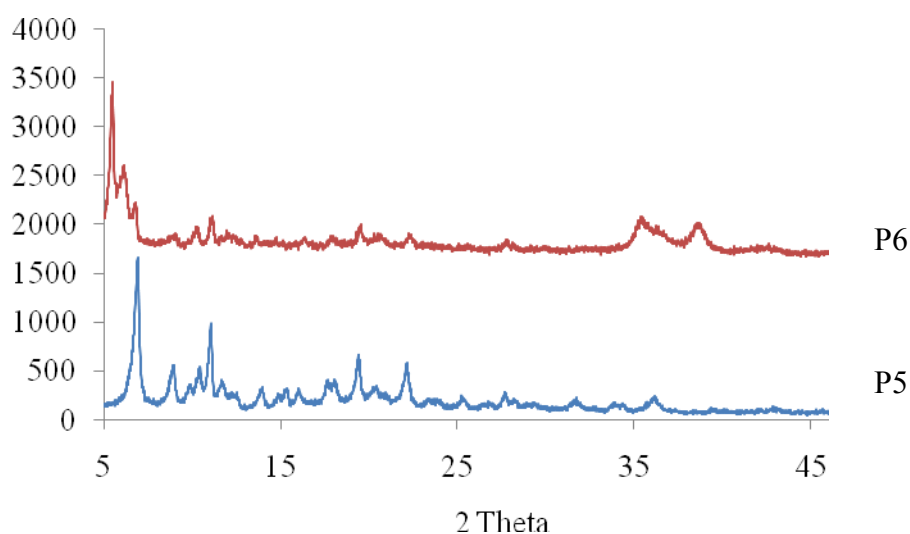
In free base TCBPP (**15**)-based MOFs (MOF **2A**, **3A** and **5A**), they showed the different XRD patterns with pattern 1 (**P1**), pattern 2 (**P2**) and pattern 3 (**P3**), respectively. These results may let us to conclude that the 4,4'-bipyridine addition and its addition sequence effected on geometry of MOFs. Opposite to copper series (MOF **6A**, **7A** and **8A**), they exhibited the same XRD pattern as pattern 4 (**P4**), it was predicted that the copper ion may firstly be bound by carboxylate group of porphyrin, followed by 4,4'-bipyridine.



**Figure 4.20** XRD patterns of the synthesized MOFs presented as **P1**, **P2**, **P3** and **P4**.

In the case of Zn-TCBPP (**18**)-based MOFs *via* pathway B (MOF **10B**, **11B** and **12B**), the XRD patterns were similar which were presented as pattern 5 (**P5**). The chronology of mixing 4,4'-bipyridine in the solution mixture was not affected to the geometry of MOFs, indicating that the kinetics of 4,4'-bipyridine to bind to zinc ion and zinc ion in the porphyrin core were alike.

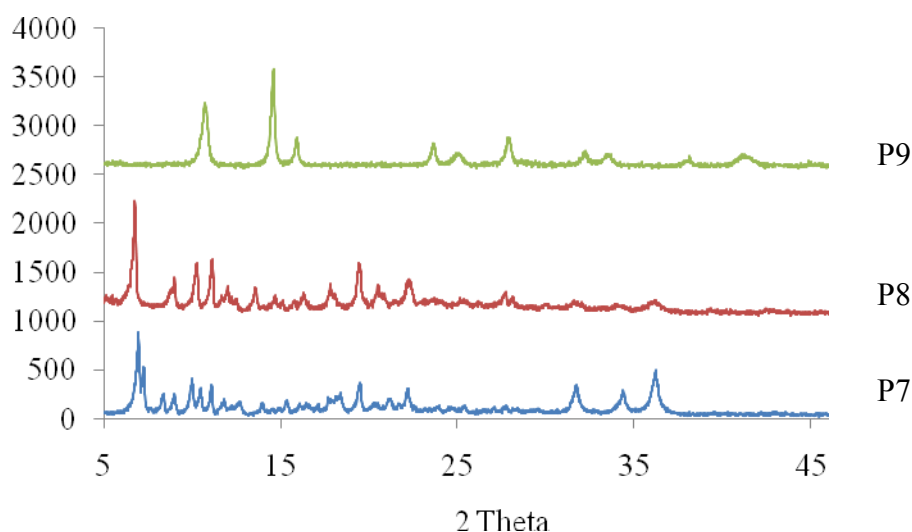
Contrastingly, in the case of Cu-TCBPP (**19**)-based MOFs (MOF **13B**, **14B** and **15B**), the different XRD patterns, **P2**, **P4** (Figure 4.20) and **P6** (Figure 4.21), were found because the kinetic of 4,4'-bipyridine binding to copper ion in the core of porphyrin ring was faster than copper ion. It was predicted that 4,4'-bipyridine bound firstly to copper ion in the core of porphyrin ring, followed by formation of secondary building unit (SBU) by chelation of carboxylate group of **19** to metal ion from copper nitrate.



**Figure 4.21** XRD patterns of the synthesized MOFs presented as **P5** and **P6**.

In the case of [Zn-TCBPP]-bpy (**22**)-based MOFs synthesized *via* pathway C, the zinc SBU series MOFs (**16C**, **19C**) showed the same XRD pattern as **P7**. It showed that added 4,4'-bipyridine to the mixture solution had no significant effect which was confirmed by both IR spectra and XRD pattern of MOFs **16C** and **19C**.

However, in the case of [Cu-TCBPP]-bpy (**23**)-based MOFs using copper ion to create SBU without or with addition of 4,4'-bipyridine (MOF **21C**, **22C**), the different XRD patterns, **P9** and **P8** (see Figure 4.22), were obtained respectively. According to their IR spectra (Figure 4.19), they indicated that 4,4'-bipyridine may uncoordinate from the complex **23** but when 4,4'-bipyridine was further added to the mixture solution, different structure MOF was obtained.



**Figure 4.22** XRD patterns of the synthesized MOFs presented as **P7**, **P8** and **P9**.

Intensities of three main characteristics peak of porphyrin-based MOFs structure at the Bragg angles,  $2\theta$  of  $6.9^\circ$ ,  $11.1^\circ$  and  $19.4^\circ$  were found which the first one was very intense peak and the others were medium. Some of XRD peaks indicated the amorphous phase as broad peaks with lower peak intensities, owing to the less ordered structure and the less crystallinity of porphyrin-based MOFs.

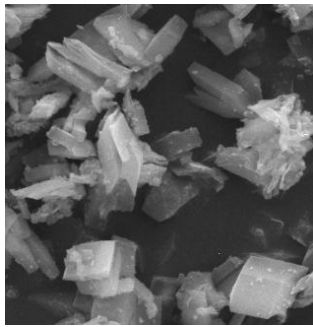
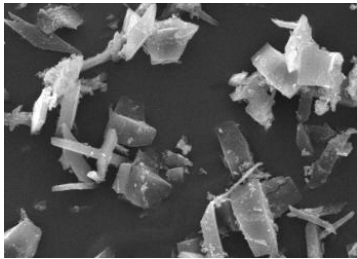
#### 4.5.3 SEM study

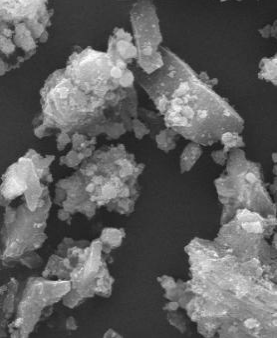
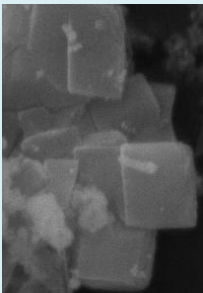
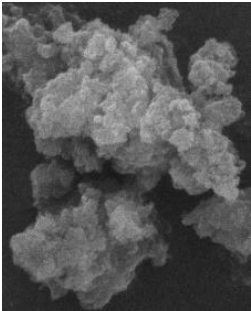
Morphology of MOFs were investigated by SEM image, which exhibited as micro-particle of MOFs in various uniform of cubic, rod and platelet shapes as displayed in Table 4.1. However, some of them exhibited as aggregated particles or chunky particles. The average size of MOFs particles was around 0.5 to 1.5  $\mu\text{m}$ . SEM images of MOFs were illustrated with different magnification, which displayed at the bottom of the images as shown in Appendix B (Figure B-1 to B-16).

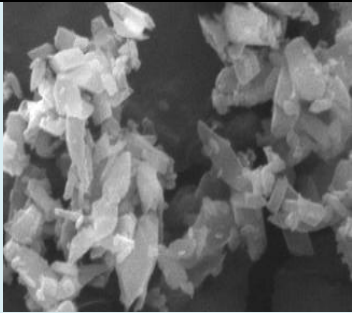
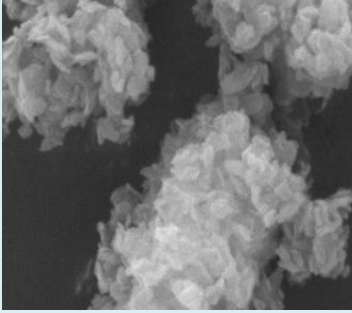
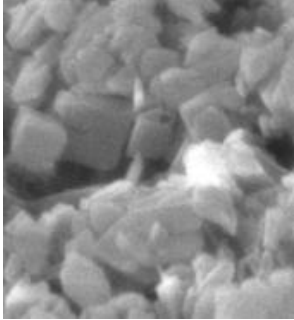
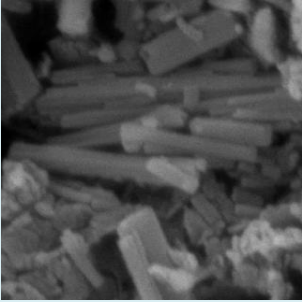
MOFs synthesized *via* pathway A were bigger and well-shaped than other pathways, while MOFs containing 4,4'-bipyridine were better than the absence ones. This may be due to TCBPP(**15**), which was used as organic linker in MOFs synthesis by pathway A, had no metal in the core of porphyrin so 4,4'-bipyridine could bind only to the metal node resulting in the unique structures of MOFs.

The morphology of MOFs obtained from pathway B and C, were displayed in various uniform. That may be due to M-TCBPP (**18** and **19**) and [M-TCBPP]-bpy (**22** and **23**) used as organic linkers in MOFs synthesis pathway B and C, respectively contained metal in the core of porphyrin thus 4,4'-bipyridine could bind not only to the core metal in porphyrin ring, but also the metal node resulting the non-unique structures of MOFs.

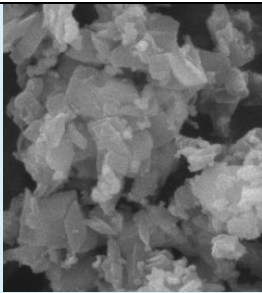
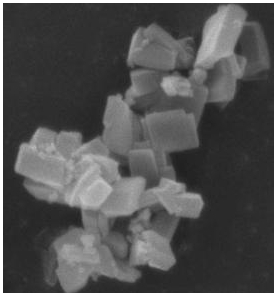

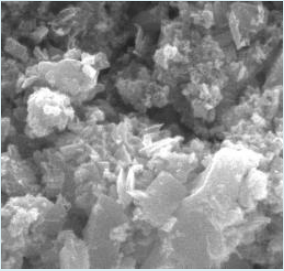
**Table 4.1** SEM images of synthesized MOFs and particle size, estimated from SEM image.

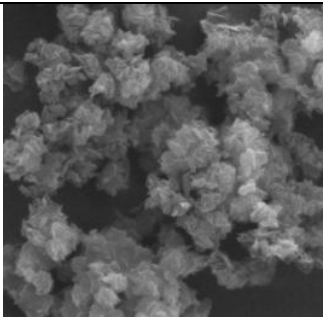

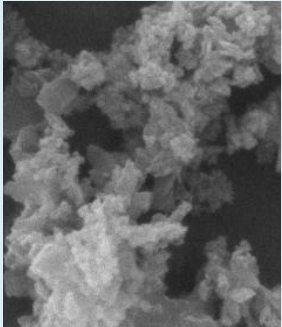
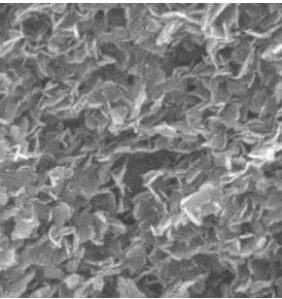
Code of MOFs	Condition	XRD pattern	SEM	
			Particle size( $\mu\text{m}$ )	image
2A	TCBPP +Zn(NO <sub>3</sub> ) <sub>2</sub>	P1	5 , 1×8	
3A	TCBPP +Zn(NO <sub>3</sub> ) <sub>2</sub> +bpy	P2	10 , 5×20	
5A	TCBPP +Zn(NO <sub>3</sub> ) <sub>2</sub> add bpy	P3	-	

				
6A	TCBPP +Cu(NO <sub>3</sub> ) <sub>2</sub>	P4	-	-
7A	TCBPP +Cu(NO <sub>3</sub> ) <sub>2</sub> +bpy	P4	-	-
8A	TCBPP +Cu(NO <sub>3</sub> ) <sub>2</sub> add bpy	P4 + CuO	1.5	
10B	Zn-TCBPP + Zn(NO <sub>3</sub> ) <sub>2</sub> add bpy	P5	-	
11B	Zn-TCBPP + bpy add Zn(NO <sub>3</sub> ) <sub>2</sub>	P5	1	

				
12B	Zn-TCBPP + Zn(NO <sub>3</sub> ) <sub>2</sub> + bpy	P5	0.5	
13B	Cu-TCBPP + Cu(NO <sub>3</sub> ) <sub>2</sub> add bpy	P2	0.5	
14B	Cu-TCBPP + bpy add Cu(NO <sub>3</sub> ) <sub>2</sub>	P6	0.2×1	
15B	Cu-TCBPP + Cu(NO <sub>3</sub> ) <sub>2</sub>	P6	1	

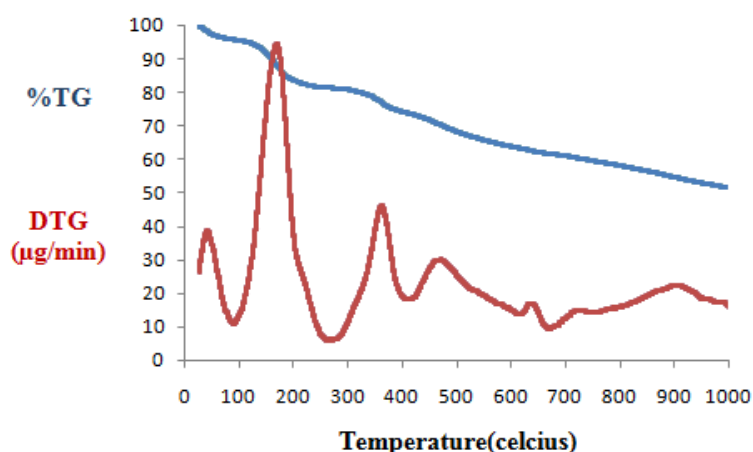


	+ bpy				
16C	[Zn-TCBPP]- bpy + Zn(NO <sub>3</sub> ) <sub>2</sub>	P7	1		 
17C	Same 16C; pretreat at T 250 °C	-	-	-	-
18C	Same 16C; pretreat at T 300 °C	-	-	-	-
19C	[Zn-TCBPP]- bpy + Zn(NO <sub>3</sub> ) <sub>2</sub> add bpy	P7	-		
20C	[Zn-TCBPP]- bpy	P8	0.5		

	+ Cu(NO <sub>3</sub> ) <sub>2</sub>			
21C	[Cu-TCBPP]- bpy + Cu(NO <sub>3</sub> ) <sub>2</sub>	P9	-	
22C	[Cu-TCBPP]- bpy + Cu(NO <sub>3</sub> ) <sub>2</sub> add bpy	P8	0.5	
23C	[Cu-TCBPP]- bpy + Zn(NO <sub>3</sub> ) <sub>2</sub>	P8	0.5	

#### 4.5.4 TGA study

In order to evaluate the robustness of MOFs and retention of solvent molecule in the framework, MOF **16C** was used as candidate. Due to the boiling point of the solvent used (DMF, 150°C), **16C** was heated at 80 °C to 260°C under vacuum. The weight loss of 15% was found at 180 °C as presented by TGA and DTG (Figure 4.23) which indicated that DMF might encapsulate inside the cavity and had interaction with the framework. Moreover, there were some molecules departed from MOF **16C** at the temperature over 300°C.



**Figure 4.23** TGA and DTG of MOF **16C**.

The information from TGA technique was used to pretreat MOFs before nitrogen adsorption-desorption study. Data from TGA study indicated that the pretreatment temperature should be 250°C, which was the temperature that solvent molecules were completely removed.

#### 4.5.5 Nitrogen Adsorption-Desorption study

The nitrogen adsorption-desorption isotherms of the most of porphyrin-based MOFs performed as type I adsorption isotherm of IUPAC classification<sup>(63)</sup> which was typical for microporous material as shown in Figure 4.24. Whereas filling of micropores was controlled by stronger interaction between the nitrogen as adsorbate molecules and pore walls of MOFs. This type of isotherm

displayed an initial steep increase, corresponding to progressive filling of the micropores, and then a plateau was reached at higher pressures, corresponding to monolayer coverage. Indeed, for microporous materials, the small pore dimensions of the adsorbent limit the adsorption only to one or a few molecular layers.

**Table 4.2** Textural properties of synthesized MOFs with pretreatment temperature at 250°C.

Code of MOFs	Condition	$S_{\text{BET}}^{\text{a}}$ (m <sup>2</sup> /g)	$d_{\text{p}}^{\text{b}}$ (nm)	$S_{\text{ext}}^{\text{c}}$ (m <sup>2</sup> /g)	Micropore volume <sup>c</sup> (cm <sup>3</sup> /g)
2A	TCBPP+Zn(NO <sub>3</sub> ) <sub>2</sub>	75.01	1.5	11.10	-0.003
6A	TCBPP+Cu(NO <sub>3</sub> ) <sub>2</sub>	67.33	1.8	43.40	0.014
3A	TCBPP+Zn(NO <sub>3</sub> ) <sub>2</sub> +bpy	34.07	0.8	15.66	0.006
7A	TCBPP+Cu(NO <sub>3</sub> ) <sub>2</sub> +bpy	322.87	0.6	65.05	0.136
5A	TCBPP+Zn(NO <sub>3</sub> ) <sub>2</sub> add bpy	242.11	0.7	15.01	0.117
8A	TCBPP+Cu(NO <sub>3</sub> ) <sub>2</sub> add bpy	404.7	0.6	108.85	0.116
10B	Zn-TCBPP + Zn(NO <sub>3</sub> ) <sub>2</sub> add bpy	407.64	0.7	156.06	0.092
11B	Zn-TCBPP + bpy add Zn(NO <sub>3</sub> ) <sub>2</sub>	451.13	0.6	95.09	0.165
12B	Zn-TCBPP + Zn(NO <sub>3</sub> ) <sub>2</sub> + bpy	536.10	0.6	155.43	0.157
13B	Cu-TCBPP + Cu(NO <sub>3</sub> ) <sub>2</sub> add bpy	26.747	1.8	26.801	-0.006
14B	Cu-TCBPP + bpy add Cu(NO <sub>3</sub> ) <sub>2</sub>	353.55	0.6	85.417	0.121

15B	Cu-TCBPP + Cu(NO <sub>3</sub> ) <sub>2</sub> + bpy	560.13	0.6	77.812	0.241
16C	[Zn-TCBPP]-bpy + Zn(NO <sub>3</sub> ) <sub>2</sub>	73.443	0.9	8.711	0.036
17C	Same 16 C; pretreat T 250 °C	547.47	0.6	14.197	0.286
18C	Same 16 C; pretreat T 300 °C	433.73	0.6	12.994	0.225
19C	[Zn-TCBPP]-bpy + Zn(NO <sub>3</sub> ) <sub>2</sub> add bpy	404.52	0.6	17.202	0.205
20C	[Zn-TCBPP]-bpy + Cu(NO <sub>3</sub> ) <sub>2</sub>	43.251	0.8	46.875	-0.015
21C	[Cu-TCBPP]-bpy + Cu(NO <sub>3</sub> ) <sub>2</sub>	25.886	1.8	76.203	-0.064
22C	[Cu-TCBPP]-bpy + Cu(NO <sub>3</sub> ) <sub>2</sub> add bpy	605.93	0.6	129.74	0.239
23C	[Cu-TCBPP]-bpy + Zn(NO <sub>3</sub> ) <sub>2</sub>	169.05	0.8	50.95	0.064

<sup>a</sup> specific surface area determined by application of the BET-plot method

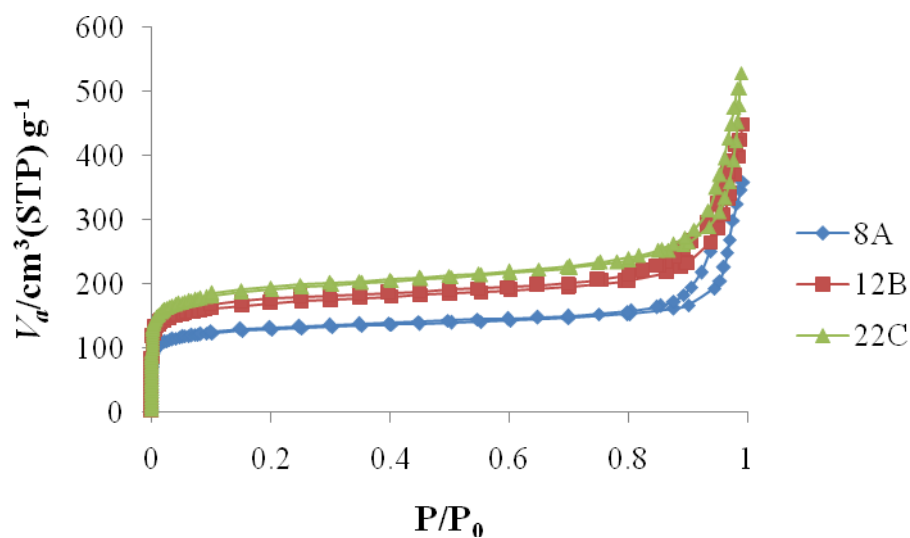
<sup>b</sup> particle size distribution determined by application of the MP-plot method

<sup>c</sup> external surface area and micropore volume determined by application of the t-plot method

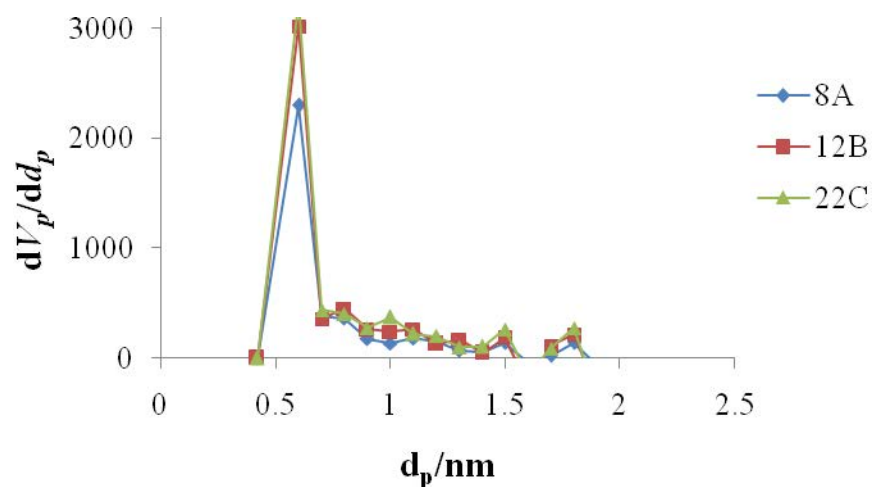
For porphyrin-based MOFs, the total specific surface area were calculated using Brunauer, Emmett and Teller (BET) equation which were in range of 400-600 m<sup>2</sup>/g. The pore size distribution of MOFs was obtained from the nitrogen adsorption data by means of MP method. In case of the good textural properties of MOFs, the quite narrow pore size distribution was found at the pore diameter of 0.6 nm. Moreover, the external surface area and micropore volume were in range of 10-150 m<sup>2</sup>/g and 0.1-0.3 cm<sup>3</sup>/g, respectively.

The textural properties of MOFs synthesized via pathway A were not be satisfied with low surface area because of low connection as described in 2.5.3. For most of MOFs obtained from pathway B and C, they displayed high surface area on account of high connection with various forms.

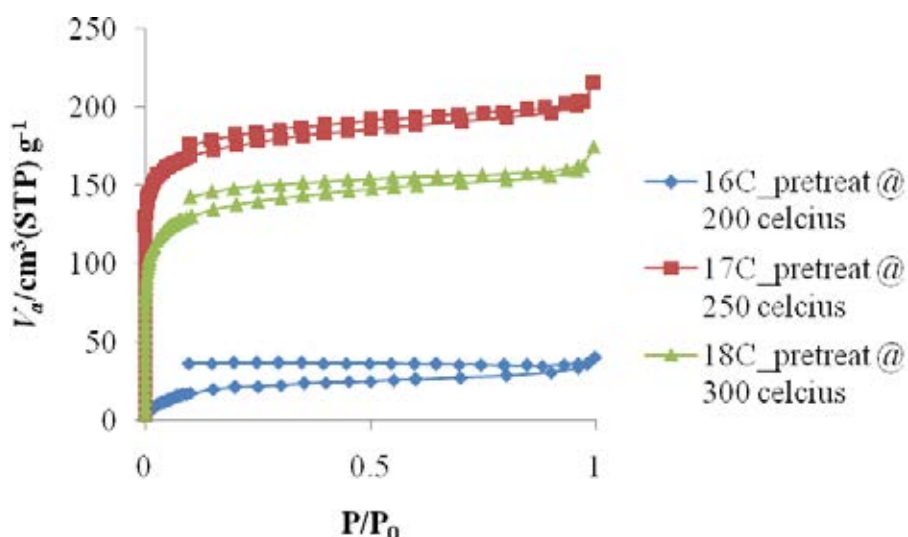
a) Nitrogen adsorption-desorption isotherm



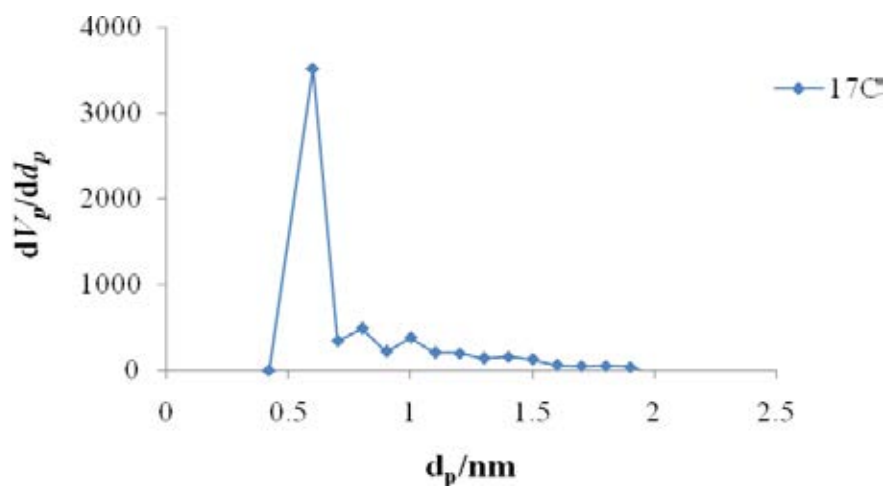
MP pore-size distribution



## b) Nitrogen adsorption-desorption isotherm



## MP pore-size distribution



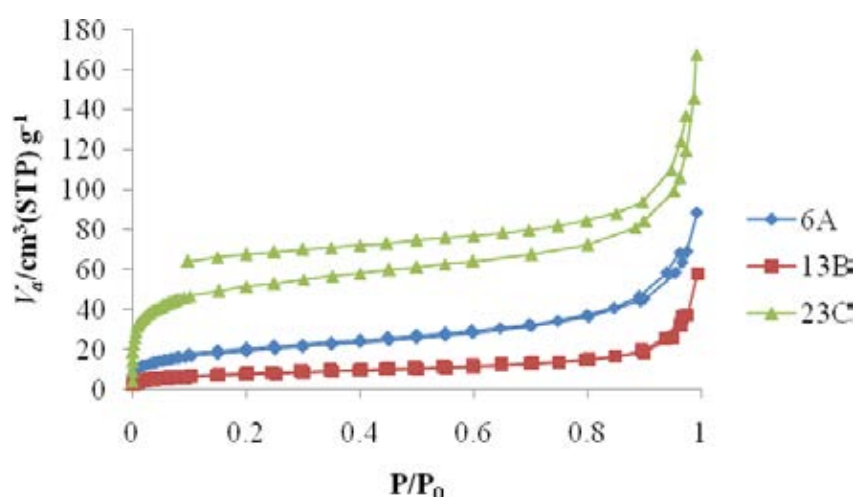
**Figure 4.24** Example of the nitrogen adsorption-desorption isotherms with high surface performed as type I adsorption isotherm and MP pore-size distribution of porphyrin-based MOFs a) **8A**; **12B**; and **22C**; b) **16C**, **17C** and **18C**.

According to the nitrogen adsorption-desorption isotherms, the pretreatment temperature of the prepared MOFs were so essential for adsorption properties. In Figure 4.24 b), the compared isotherms of MOF **16C**, **17C** and **18C**

with different pretreatment temperatures, 200°C, 250°C and 300°C respectively, demonstrated that **17C** showed the better isotherm than the others. This confirmed that 250°C was the suitable pretreatment temperature to eliminate the solvent molecules.

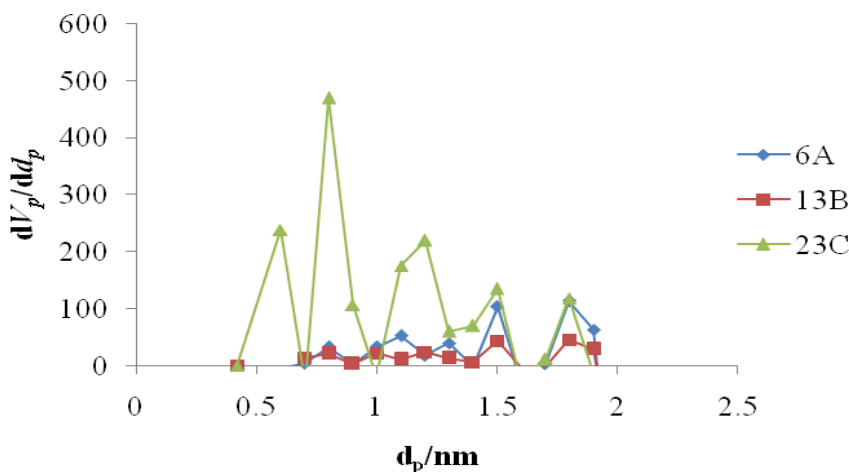
Some of the obtained MOFs showed the nitrogen adsorption-desorption isotherms with low surface area and confused MP pore-size distribution with many peaks as displayed in Figure 4.25, resulting from the various structures of MOFs with amorphous phase.

a) Nitrogen adsorption-desorption isotherm





MP pore-size distribution



**Figure 4.25** The nitrogen adsorption-desorption isotherms with low surface area and MP pore-size distribution of porphyrin-based MOFs **6A**; **13B**; and **23C**.

For the Nitrogen adsorption-desorption isotherm and MP pore-size distribution of the other porphyrin-based MOFs that were not presented in this chapter, they displayed in the appendix B (Figure B-17 to B-22) and categorized by pathway of synthesis.

According to the morphology and gas adsorption properties of porphyrin-based MOFs, it can be concluded that the synthesized MOFs *via* pathway B were the appropriated pathway to synthesize MOFs. The use of 4,4'-bipyridine as a pillar in the frameworks prevented the aggregation of the porphyrins ring owing to the conjugation system. The chronology of mixing 4,4'-bipyridine in the solution mixture may affect to the properties of MOFs, depending on the kinetic of metal ion and 4,4'-bipyridine to form the framework.

In case of MOFs synthesized *via* pathway A, they presented the well-shaped but low gas adsorption property. This may be due to the absence of metal in the core of porphyrin rings. While the MOFs synthesized *via* pathway C possessed in various morphology and gas adsorption properties, some MOFs were good but some MOFs were not. This may be due to the complex of metal and 4,4'-bipyridine (complex **20-23**) can occur in many modes. This supported the significant of 4,4'-bipyridine in the frameworks.

For the future research, ultrathin films of metal–organic frameworks (MOFs) were so interesting because of the well-controlled growth direction and film thickness using a layer by layer growth technique.

## CHAPTER V

### CONCLUSION

This research covered the synthesis of porphyrin-based MOFs containing 5,10,15,20-tetra(4-carboxybiphenyl)porphyrin derivatives as organic linkers via three synthetic pathways. A series of porphyrin-based MOFs has been investigated their morphologies and gas adsorption properties for the potential use in gas storage. Morphology of MOFs was investigated by SEM image, which exhibited as micro-particles of MOFs in various uniforms of cubic, rod and platelet shapes. Meanwhile the nitrogen adsorption-desorption isotherms performed as type I adsorption isotherm which was typical for microporous materials. Total specific surface areas were calculated using Brunauer, Emmett and Teller (BET) equation which were in range of 400-600 m<sup>2</sup>/g and a quite narrow pore size distribution was found with the average pore diameter of 0.6 nm. Furthermore, the external surface areas and micropore volumes were in range of 10-150 m<sup>2</sup>/g and 0.1-0.3 cm<sup>3</sup>/g, respectively.

According to the morphology and gas adsorption properties of porphyrin-based MOFs, it should be summarized that the suitable pathway for synthesis of porphyrin-based MOFs was the pathway B which used M-TCBPP (M=Zn and Cu) as organic linkers along with using 4,4'-bipyridine as a pillar in the frameworks to prevent the aggregation of porphyrins. Moreover, the stability of this framework was investigated by TGA with the temperature not over than 300°C. The control of MOF self-assembly is still a challenge in the construction of well-defined MOFs.

## REFERENCES

- [1] Dunn, S. The hydrogen experiment. World Watch (2000): 14-25.
- [2] Tollefson, J. Fuel of the future. Nature (2010): 1262-1264.
- [3] Zuttel, A. Hydrogen storage methods. Naturewissenschaften 91 (2004): 157-172.
- [4] Dillon, A. C., and Heben, M. J. Hydrogen storage using carbon adsorbents: past, present and future. Appl. Phys. 72 (2001): 133-142.
- [5] Logar, N. Z., and Kaucic, V. Nanoporous Materials: From Catalysis and Hydrogen Storage to Wastewater Treatment. Acta Chim. Slov. 53 (2006): 117-135.
- [6] Rosseinsky, M. J. Recent developments in metal-organic framework chemistry: design, discovery, permanent porosity and flexibility. Microporous and Mesoporous Mater. 73 (2004): 15-30.
- [7] Beletskaya, I., Tyurin, V. S., Tsivadze, A. Y., Guilard, R., and Stern, C. Supramolecular Chemistry of Metalloporphyrins. Chem. Rev. 109 (2009): 1659-1713.
- [8] Suh, M. P., Cheon, Y. E., and Lee, E. Y. Syntheses and functions of porous metallosupramolecular networks. Coordin. Chem. Rev. 252 (2008): 1007-1026.
- [9] Batten, S. R., Neville, S. M., and Turner, D. R. Coordination Polymers Design, Analysis and Application. The Royal Society of Chemistry: Cambridge, 2009.
- [10] Bailar, J. C. Jr. Coordination Polymers. Prep. Inorg. React. 1 (1964): 1-57.
- [11] Fujita, M., Kwon, Y. J., Washizu, S., and Ogura, K. J. Am. Chem. Soc. 116 (1994): 1151-1152.
- [12] Janiak, C., and Vieth, J. K. MOFs, MILs and more: concepts, properties and applications for porous coordination networks (PCNs). New J. Chem. 34 (2010): 2366-2388.

- [13] Yaghi, O. M., and Li, H. Hydrothermal Synthesis of a Metal-Organic Framework Containing Large Rectangular Channels. J. Am. Chem. Soc. 117 (1995): 10401-10402.
- [14] Biradha, K., Ramanan, A., and Vittal, J. J. Cryst. Growth Des. 9 (2008): 2969.
- [15] Mueller, U., Schubert, M., Teich, F., Puetter, H., Schierle-Arndt, K., and Pastre, J. Metal-Organic Frameworks-Prospective Industrial Applications. J. Mater. Chem. 16 (2006): 626-636.
- [16] Rosseinsky, M. J. Recent Developments in Metal Organic Framework Chemistry: Design, Discovery, Permanent Porosity and Flexibility. Microporous Mesoporous Mater. 73 (2004): 15-30.
- [17] Li, J. R., Kuppler, J. R., and Zhou, H. C. Selective gas adsorption and separation in metal-organic frameworks. Chem. Soc. Rev. 38 (2009): 1477-1504.
- [18] Farrusseng, D., Aguado, S., and Pinel, C. Metal-Organic Frameworks: Opportunities for Catalysis. Angew. Chem. Int. Ed. 48 (2009): 7502-7513.
- [19] Allendorf, M. D., Bauer, C. A., Bhaktaa, R. K., and Houka, R. J. T. Luminescent metal-organic frameworks. Chem. Soc. Rev. 38 (2009): 1330-1352.
- [20] McKinlay, A. C., Morris, R. E., Horcajada, P., Ferey, G., Gref, R., Couvreur, P., and Serre, C. BioMOFs: Metal-Organic Frameworks for Biological and Medical Applications. Angew. Chem. Int. Ed. 49 (2010): 6260-6266.
- [21] Zheng, C.-G., Li, S., Zhang, P.-P., Wang, W.-X., Hong, J.-H., Qian, Q.-L., and Chen, X.-Y. Synthesis and characterization of zinc(II), copper(II) and cadmium(II) coordination polymers with tetrachloroterephthalate-based ligands. Transition Met. Chem. 34 (2009): 815-820.
- [22] Coordination geometry [online]. 2012. Available from:[http://en.wikipedia.org/wiki/Coordination\\_geometry](http://en.wikipedia.org/wiki/Coordination_geometry) [2012, February 20]
- [23] Dinca, M., Yu, A. F., and Long, J. R. Microporous Metal-Organic Frameworks Incorporating 1,4-Benzeneditetrazolate: Syntheses,

- Structures, and Hydrogen Storage Properties. J. Am. Chem. Soc. 128 (2006): 8904-8913.
- [24] Duangthongyou, T., Jirakulpattana, S., Phakawatchai, C., Kurmoo, M., and Siripaisarnpipat, S. Comparison of crystal structures and magnetic properties of two Co(II) complexes containing different dicarboxylic acid ligands. Polyhedron 29 (2010): 1156-1162.
- [25] Eddaoudi, M., Kim, J., Rosi, N., Vodak, D., Wachter, J., O'Keeffe, M., and Yaghi, O. M. Systematic Design of Pore Size and Functionality in Isorecticular MOFs and Their Application in Methane Storage. Science 295 (2002): 469-472.
- [26] Chung, H., Barron, P. M., Novotny, R. W., Son, H.-T., Hu, C., and Choe, W. Structural Variation in Porphyrin Pillared Homologous Series: Influence of Distinct Coordination Centers for Pillars on Framework Topology Cryst. Growth Des. 9 (2009): 3327-3332.
- [27] Eddaoudi, M., Moler, D. B., Li, H., Chen, B., Reineke, T. M., O'Keeffe, M., and Yaghi, O. M. Modular Chemistry: Secondary Building Units as a Basis for the Design of Highly Porous and Robust Metal-Organic Carboxylate Frameworks. Acc. Chem. Res. 34 (2001): 319-330.
- [28] Zhao, D., Timmon, D. J., Yuan, D., and Zhou, A.-C. Tuning the and Functionality of Metal-Organic Frameworks by Ligand Design. Accounts Chem. Res. 44 (2011): 123-133.
- [29] Tranchemontagne, D. J., Mendoza-Cortes, J. L., O'Keeffe, M., and Yaghi, O. M. Secondary building units, nets and bonding in the chemistry of metal-organic frameworks. Chem. Soc. Rev. 38 (2009): 1257-1283.
- [30] Yaghi, O. M., O'Keeffe, M., Ockwig, N. W., Chae, H. K., Eddaoudi, M., and Kim, J. Reticular synthesis and the design of new materials. Nature. 423 (2003): 705-714.
- [31] Rowsell, J. L. C., Millward, A. R., Park, K. S., and Yaghi, O. M. Hydrogen Sorption in Functionalized Metal-Organic Frameworks. J. Am. Chem. Soc. 126 (2004): 5666-5667.
- [32] Biemmi, E., Christian, S., Stock, N., and Bein, T. High-throughput screening of synthesis parameters in the formation of the metal-organic

- frameworks MOF-5 and HKUST-1. Microporous Mesoporous Mater. 117 (2009): 111-117.
- [33] Gao, Q., Xie, Y.-B., Li, J.-R., Yuan, D.-Q., Yakovenko, A. A., Sun, J.-H., and Zhou, H.-C. Tuning the Formations of Metal-Organic Frameworks by Modification of Ratio of Reactant, Acidity of Reaction System, and Use of a Secondary Ligand. Cryst. Growth Des. 12 (2012): 281-288.
- [34] Suh, M. P., Cheon, Y. E., and Lee, E. Y. Reversible Transformation of Zn<sup>II</sup> Coordination Geometry in a Single Crystal of Porous Metal-Organic Framework [Zn<sub>3</sub>(ntb)<sub>2</sub>(EtOH)<sub>2</sub>].4EtOH. Chem. Eur. J. 13 (2007): 4208-4215.
- [35] Lee, E. Y., Jang, S. Y., and Suh, M. P. Multifunctionality and Crystal Dynamics of a Highly Stable, Porous Metal-Organic Framework [Zn<sub>4</sub>O(NTB)<sub>2</sub>]. J. Am. Chem. Soc. 127 (2005): 6374-6381.
- [36] Burrows, A. D., Cassar, K., Friend, R. M. W., Mahon, M. F., Rigby, S. P., and Warren, J. E. Solvent hydrolysis and templating effects in the synthesis of metal-organic frameworks. Cryst. Eng. Comm. 7 (2005): 548-550.
- [37] Zhang, J. J., Wojtas, L., Larsen, R. W., Eddaoudi, M., and Zaworotko, M. J. Temperature and Concentration Control over Interpenetration in a Metal-Organic Material. J. Am. Chem. Soc. 131 (2009): 17040-17041.
- [38] Khan, N. A., Kang, I. J., Seok, H. Y., and Jung, S. H. Facile synthesis of nano-sized metal-organic frameworks, chromium benzenedicarboxylate, MIL-101. Chem. Eng. J. 166 (2011): 1152-1157.
- [39] Tsuruoka, T., Furukawa, S., Takashima, Y., Yoshida, K., Isoda, S., and Kitagawa, S. Nanoporous Nanorods Fabricated by Coordination Modulation and Oriented Attachment Growth. Angew. Chem. Int. Ed. 48 (2009): 4739-4743.
- [40] Choi, J. S., Son, W. J., Kim, J., and Ahn, W. S. Metal-organic framework MOF-5 prepared by microwave heating: Factors to be considered, Microporous and Mesoporous Mater. 116 (2008): 727-731.
- [41] Seo, Y. K., Hundal, G., Jang, I. T., Hwang, Y. K., Jun, C.-H., and Chang, J. S. Microwave synthesis of hybrid inorganic-organic materials including

- porous  $\text{Cu}_3(\text{BTC})_2$  from Cu(II)-trimesate mixture Microporous and Mesoporous Mater. 119 (2009): 331-337.
- [42] Stock, N., and Biswas, S. Synthesis of Metal-Organic Frameworks (MOFs): Routes to Various MOF Topologies, Morphologies, and Composites. Chem. Rev. 112 (2012): 933-969.
- [43] Qiu, S., and Zhu, G. Molecular engineering for synthesizing novel structures of metal-organic frameworks with multifunctional properties. Coordin. Chem. Rev. 253 (2009): 2891–2911.
- [44] Staples, R. J. Growing and Mounting Crystals Your Instrument Will Treasure [online]. 2012. Available from: <http://www2.chemistry.msu.edu/facilities/crystallography/xtalgrow.pdf> [2012, April 28]
- [45] Fang, Q. R., Zhu, G. S., Jin, Z., Ji, Y. Y., Ye, J. W., Xue, M., Yang, H., Wang, Y., and Qiu, S. L. Mesoporous Metal-Organic Framework with Rare etb Topology for Hydrogen Storage and Dye Assembly. Angew. Chem. Int. Ed. 46 (2007): 6638-6642.
- [46] Smithenry, D. W., Wilson, S. R., and Suslick, K. S. A Robust Microporous Zinc Porphyrin Framework Solid. Inorg. Chem. 42 (2003): 7719-7721.
- [47] Growing crystals for x-ray structure determination [online]. 2012. Available from: <http://www.southampton.ac.uk/xray/links/crystalgrowth/grow1.htm#introd> [2012, April 28]
- [48] Lin, W., Wang, Z., and Ma, L. A Novel Octupolar Metal-Organic NLO Material Based on a Chiral 2D Coordination Network. J. Am. Chem. Soc. 121 (1999): 11249-11250.
- [49] Shi, X., Zhu, G. S., Qiu, S. L., Huang, K. L., Yu, J. H., and Xu, R. R.  $\text{Zn}_2[(\text{S})\text{-O}_3\text{PCH}_2\text{NHC}_4\text{H}_7\text{CO}_2]_2$ : A Homochiral 3D Zinc Phosphonate with Helical Channels. Angew. Chem. Int. Ed. 43(2004): 6482-6485.
- [50] Walton, R. I. Subcritical solvothermal synthesis of condensed inorganic materials. Chem. Soc. Rev. 31 (2002): 230-238.
- [51] Subramanian, M. Standard Operating Procedure (SOP): Use of Autoclaves for Hydrothermal Experiments [online]. 2012. Available from:



- [http://www.chemistry.oregonstate.edu/blakemore/safety/SOPs/SOP\\_hydrothermal/SOP\\_hydrothermal.html](http://www.chemistry.oregonstate.edu/blakemore/safety/SOPs/SOP_hydrothermal/SOP_hydrothermal.html) [2012, April 28]
- [52] Tompsett, G. A., Conner, W. C., and Yngvesson, K. S. Microwave Synthesis of Nanoporous Materials. *Chem. Phys. Chem.* 7 (2006): 296-319.
- [53] Zheng, Ni., and Richard I. M. Rapid production of metal-organic frameworks via microwave-assisted solvothermal synthesis. *J. Am. Chem. Soc.* 128 (2006) : 12394-12395.
- [54] Pichon, A., Lazuen-Garay, A., and James, S. L. Solvent-free synthesis of a microporous metal-organic framework. *Cryst. Eng. Comm.* 8 (2006): 211-214.
- [55] Pichon, A., and James, S. L. An array-based study of reactivity under solvent-free mechanochemical conditions-insights and trends. *Cryst. Eng. Comm.* 10 (2008): 1839.
- [56] Dutrow, B. L., and Clark, C. M. X-Ray Powder Diffraction [online]. 2012. Available from:[http://serc.carleton.edu/research\\_education/geochemsheets/techniques/XRD.html](http://serc.carleton.edu/research_education/geochemsheets/techniques/XRD.html) [2012, February 20]
- [57] X-ray powder diffraction [online]. 2012. Available from: <http://pubs.usgs.gov/of/2001/of01-041/htmldocs/xrpd.htm> [2012, April 28]
- [58] Choi, E.-Y., Barron, P. M., Novotny, R. W., Son, H.-T., Hu, C., and Choe, W. Pillared Porphyrin Homologous Series: Intergrowth in Metal-Organic Frameworks, *Inorg. Chem.* 48 (2009): 426-428.
- [59] Swapp, S. Scanning Electron Microscope [online]. 2012. Available from: [http://serc.carleton.edu/research\\_education/geochemsheets/techniques/SEM.html](http://serc.carleton.edu/research_education/geochemsheets/techniques/SEM.html) [2012, February 16]
- [60] SEM image of MOF-5 [online]. 2012. Available from: <http://yaghi.chem.ucla.edu/gallery/album> [2012, February 16]
- [61] Rouquerol, F., Rouquerol, J., and Sing, K. Adsorption by Powders and Porous Solids: Principles, Methodology and Applications. Academic Press: San Diego, 1999.
- [62] Adsorption isotherm [online]. 2012. Available from: <http://saf.chem.ox.ac.uk/Instruments/BET/sorptoptprin.html#ads> [2012, April 28]

- [63] Carmody, O., Frost, R., Xi, Y., and Kokot, S. Surface characterisation of selected sorbent materials for common hydrocarbon fuels. Surf. Sci. 601 (2007): 2066-2076.
- [64] Langmuir, I. The adsorption of gases on plane surfaces of glass, mica, and platinum. J. Am. Chem. Soc. 40 (1918): 1361-1402.
- [65] Brunauer, S., Emmett, P. H., and Teller, E. Adsorption of gases in multimolecular layers. J. Am. Chem. Soc. 60 (1938): 309-319.
- [66] Storck, S., Bretinger, H., and Maier, W. F. Characterization of micro- and mesoporous solids by physisorption methods and pore-size analysis. Appl. Catal. A-Gen. 174 (1998): 137-146.
- [67] Infrared [online]. 2012. Available from: <http://en.wikipedia.org/wiki/Infrared> [2012, February 21]
- [68] Elemental Analysis [online]. 2011. Available from: [http://en.wikipedia.org/wiki/Elemental\\_analysis](http://en.wikipedia.org/wiki/Elemental_analysis) [2011, December 15]
- [69] Thermogravimetric analysis [online]. 2012. Available from: [http://en.wikipedia.org/wiki/Thermogravimetric\\_Analysis](http://en.wikipedia.org/wiki/Thermogravimetric_Analysis) [2012, March 20]
- [70] Hu, Y. H., and Zhang, L. Hydrogen Storage in Metal–Organic Frameworks. Adv. Mater. 22 (2010): E117-E130.
- [71] Han, S. S., Deng, W. Q., and Goddard, W. A. Improved Designs of Metal–Organic Frameworks for Hydrogen Storage. Angew. Chem. Int. Ed. 46 (2007): 6289-6292.
- [72] Rosi, N.L., Eckert, J., Eddaoudi, M., Vodak, D.T., Kim, J., O’Keeffe, M., and Yaghi, O.M. Hydrogen Storage in Microporous Metal-Organic Frameworks. Science 300 (2003): 1127-1129.
- [73] Rowsell, J. L. C., Eckert, J., and Yaghi, O. M. Characterization of H<sub>2</sub> Binding Sites in Prototypical Metal-Organic Frameworks by Inelastic Neutron Scattering. J. Am. Chem. Soc. 127 (2005): 14904-14910.
- [74] Kelly, M. T. Perspective on the Storage of Hydrogen: Past and Future. Struct. Bond. 141 (2011): 169-201.

- [75] Adsorption behaviour [online]. 2012. Available from: <http://personal.strath.ac.uk/~ashleigh.fletcher/adsorption.htm> [2012, March 20]
- [76] Chemisorption and physisorption [online]. 2012. Available from: [http://old.iupac.org/reports/2001/colloid\\_2001/manual\\_of\\_s\\_and\\_t/node16.html](http://old.iupac.org/reports/2001/colloid_2001/manual_of_s_and_t/node16.html) [2012, April 28]
- [77] Stern, A. C., Belof, J. L., Eddaoudi, M., and Space, B. Understanding hydrogen sorption in a polar metal-organic framework with constricted channels. *J. Chem. Phys.* 136 (2012): 34705-34714.
- [78] London dispersion forces [online]. 2012. Available from: <http://www.chem.purdue.edu/gchelp/liquids/disperse2.html> [2012, April 28]
- [79] Induced-dipole forces [online]. 2012. Available from: <http://www.chem.purdue.edu/gchelp/liquids/inddip.html> [2012, April 28]
- [80] Frost, H., Düren, T., and Snurr, R. Q. Effects of Surface Area, Free Volume, and Heat of Adsorption on Hydrogen Uptake in Metal-Organic Frameworks. *J. Phys. Chem.* 110 (2006): 9565-9570.
- [81] Zhang, J., Wojtas, L., Larsen, R. W., Eddaoudi, M., and Zaworotko, M. Temperature and Concentration Control over Interpenetration in a Polymorphic Metal-Organic Material. *J. Am. Chem. Soc.* 131 (2009): 17040-17041.
- [82] Ma, S., Sun, D., Ambrogio, M., Fillinger, J. A., Parkin, S., and Zhou, H. C. Framework-Catenation Isomerism in MOFs and Its Impact on Hydrogen Uptake. *J. Am. Chem. Soc.* 129 (2007): 1858-1859.
- [83] Rowsell, J. L. C. and Yaghi, O. M. Strategies for Hydrogen Storage in Metal-Organic Frameworks. *Angew. Chem. Int. Ed.* 44 (2005): 4670-4679.
- [84] Chen, B. L., Eddaoudi, M., Reineke, T. M., Kampf, J. W., O'Keeffe M., and Yaghi, O. M. *J. Am. Chem. Soc.* 122 (2000): 11559-11560.
- [85] Hydrogen [online]. 2012. Available from: <http://www.hydrogen.energy.gov/> [2012, March 14]

- [86] Hydrogen storage [online]. 2011. Available from: [http://www.eere.energy.gov/hydrogenandfuelcells/storage/current\\_technology.html](http://www.eere.energy.gov/hydrogenandfuelcells/storage/current_technology.html) [2011, August 26]
- [87] Hydrogen storage technologies [online]. 2012. Available from: <http://www.mygreeneducation.com/doe-awards-more-than-7-million-for-innovative-hydrogen-storage-technologies/> [2012, April 28]
- [88] Chen, B., Liang, C., Yang, J., Contreras, D. S., Clancy, Y. L., Lobkovsky, E. B., Yaghi, O. M., and Dai, S. A Microporous Metal-Organic Framework for Gas-Chromatographic Separation of Alkanes. Angew. Chem. Int. Ed. 45 (2006): 1390-1393.
- [89] Lee, J. Y., Farha, O. K., Roberts, J., Scheidt, K. A., Nguyen, S. T., and Hupp, J. T. Metal-organic framework materials as catalysts. Chem. Soc. Rev. 38 (2009): 1450-1459.
- [90] Shultz, A. M., Farha, O. K., Hupp, J. T., and Nguyen, S. T. A Catalytically Active, Permanently Microporous MOF with Metalloporphyrin Struts. J. Am. Chem. Soc. 131 (2009): 4204-4205.
- [91] Keskin, S., and Kizilel, S. Biomedical Applications of Metal Organic Frameworks. Ind. Eng. Chem. Res. 50 (2011): 1799-1812.
- [92] Milgrom, L.R. The color of life: Introduction to the Chemistry of Porphyrins and Related Compounds. Oxford: OUP, 1975.
- [93] Rothermund, P. Formation of Porphyrins from Pyrrole and Aldehydes. J. Am. Chem. Soc. 57 (1935): 2010-2011.
- [94] Adler, A. D., Longo, F. R., Finarelli, J. D., Goldmacher, J., Assour, J., and Korsakoff, L. A Simplified Synthesis for *meso*-Tetraphenylporphine. J. Org. Chem. 32 (1967): 476.
- [95] Lindsey, J. S., Schreiman, I. C., Hsu, H. C., Kearney, P. C., and Marguerettaz, A. M. Rothermund and Adler-Longo Reactions Revisited: Synthesis of Tetraphenyl Porphyrins under Equilibrium Conditions. J. Org. Chem. 52 (1987): 827-836.
- [96] Burrell, A. K., Officer, D. L., Plieger, P. G., and Reid, D. C. W. Synthetic Routes to Multiporphyrin Arrays. Chem. Rev. 101(2001): 2751-2796.

- [97] Chumakov, D. E., Khoroshutin, A. V., Anisimov, A. V., and Kobrakov, K. I. Bromination of porphyrins (review). Chem. Heterocyc. Compd. 45 (2009): 259-283.
- [98] Liu, C., Shen, D.-M., and Chen, Q.-Y. Unexpected bromination ring-opening of tetraarylporphyrins. Chem. Commun. (2006): 770-772.
- [99] Capitosti, G. J., Guerrero, C. D., Binkley, D. E., Rajesh, C. S., and Modarelli, D. A. Efficient Synthesis of Porphyrin-Containing, Benzoquinone-Terminated, Rigid Polyphenylene Dendrimers. J. Org. Chem. 68 (2003): 247-261.
- [100] Falk, J.E. Porphyrins and metalloporphyrins. New York: Elsevier, 1975.
- [101] Plater, M. J., Aiken, S., and Bourhill, G. Metallated porphyrins containing lead(II), copper(II) or zinc(II). Tetrahedron 58 (2002): 2415-2422.
- [102] Aratani, N., and Osuka, A. Directly Linked Porphyrin Arrays. Chem. Rec. 3 (2003): 255-234.
- [103] Peng, X., Nakamura, Y., Aratani, N., Kimb, D., and Osuka, A. 1,4-Phenylene-bridged meso-meso linked diporphyrin array. Tetrahedron Lett. 45 (2004): 4981-4984.
- [104] Tsuda, A., Furuta, H., and Osuka, A. Syntheses, Structural Characterizations, and Optical and Electrochemical Properties of Directly Fused Diporphyrins. J. Am. Chem. Soc. 123 (2001): 10304-10321.
- [105] Prushan, M. Absorption and Fluorescence Spectroscopy of Tetrphenylporphyrin and Metallo-Tetrphenylporphyrin (2005)
- [106] Camara-Campos, A., Hunter, C. A., and Tomas, S. Cooperativity in the self-assembly of porphyrin ladders. PNAS 103 (2006): 3034-3038.
- [107] Synthesis of porphyrin cofacial dimmers [online]. 2012. Available from: <http://www.wpi.edu/Pubs/ETD/Available/etd-071608-180708/unrestricted/Salimgeray-Adilov-PhD-Thesis-July-2008.pdf> [2012, April 28]
- [108] Granstrom, M., Petritsch, K., Arias, A. C., Lux, A., Anderson, M. R., and Friend, R. H. Laminated Fabrication of Polymeric Photovoltaic Diodes. Nature 395 (1998): 257-260.

- [109] Friend, R. H., et al. Electroluminescence in Conjugated Polymers. Nature 397 (1999): 121–128.
- [110] Berezin, B. D., Berezin, M. B., Moryganov, A. P., Rumyantseva, S. V., and Dymnikova, N. S. Chlorophyll and Its Derivatives, Chlorins and Porphyrins, as a Promising Class of Environmentally Friendly Dyes. Russ. J. Appl. Chem. 76 (2003): 1958–1961.
- [111] Rahiman, A. K., Rajesh, K., Bharathi, K. S., Sreedaran, S., and Narayanan, V. Catalytic Oxidation of Alkenes by Manganese(III) Porphyrin-Encapsulated Al, V, Si-Mesoporous Molecular Sieves. Inorg. Chim. Acta. 362 (2009): 1491–1500.
- [112] Fukushima, K., Tabata, K., and Okura, I. Photochemical Properties of Water-Soluble Fluorinated Zinc Phthalocyanines and Their Photocytotoxicity Against HeLa cells. J. Porphyr. Phthalocya. 2 (1998): 219–222.
- [113] Fang, Z., and Liu, B. A Cationic Porphyrin-Based Self-assembled Film for Mercury Ion Detection. Tetrahedron Lett. 49 (2008): 2311–2315.
- [114] Kathiravan, A., Kumar, P. S., Renganathan, R., and Anandan, S. Photoinduced Electron Transfer Reactions Between *meso*-Tetrakis(4-sulfonatophenyl) porphyrin and Colloidal Metal-Semiconductor Nanoparticles Colloid and Surfaces A 333 (2002): 175–181.
- [115] Nuclear Magnetic Resonance [online]. 2012. Available from: [http://en.wikipedia.org/wiki/Nuclear\\_magnetic\\_resonance](http://en.wikipedia.org/wiki/Nuclear_magnetic_resonance) [2012, February 14]
- [116] Hornak, J. P. The basic of NMR [online]. 2012. Available from: <http://www.cis.rit.edu/htbooks/nmr/inside.htm> [2012, February 14]
- [117] Mass spectrometry [online]. 2012. Available from: [http://en.wikipedia.org/wiki/Mass\\_spectrometry](http://en.wikipedia.org/wiki/Mass_spectrometry) [2012, February 14]
- [118] Mass spectrometry [online]. 2012. Available from: <http://www2.chemistry.msu.edu/faculty/reusch/VirtTxtJml/Spectrpy/MassSpec/masspec1.htm> [2012, February 14]
- [119] Ultraviolet-visible spectroscopy [online]. 2012. Available from: [http://en.wikipedia.org/wiki/Ultraviolet%E2%80%93visible\\_spectroscopy](http://en.wikipedia.org/wiki/Ultraviolet%E2%80%93visible_spectroscopy) [2012, February 14]

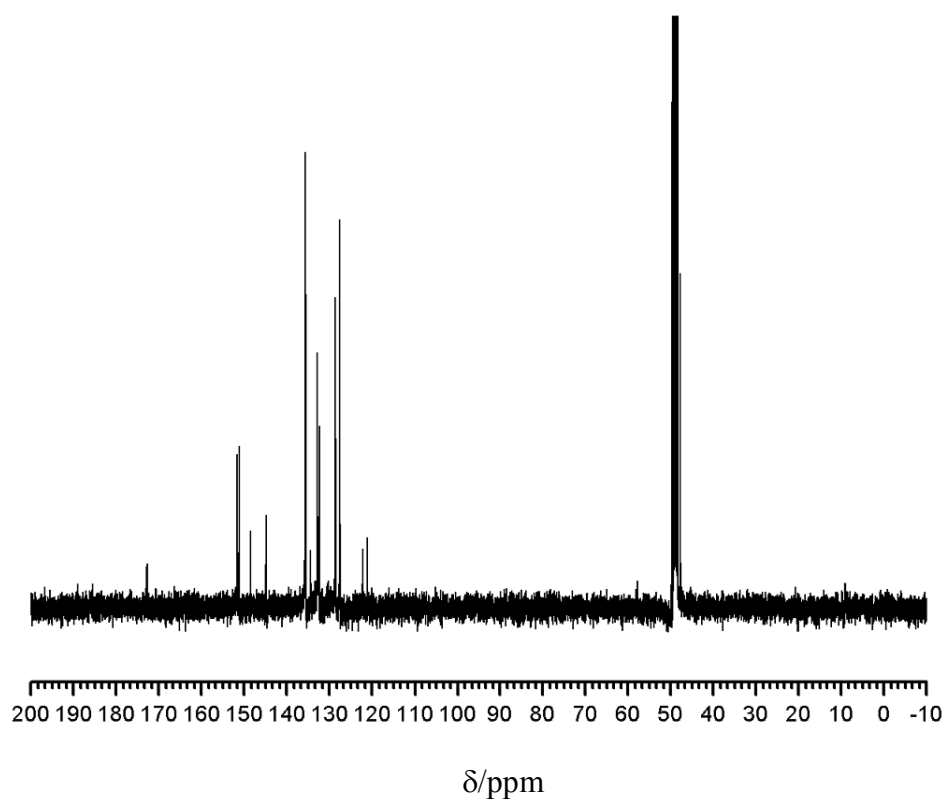
- [120] Ferenc, S. Ultraviolet and Visible (UV-Vis) Absorption Spectroscopy [online]. 2012 Available from: <http://www2.chemistry.msu.edu/faculty/reusch/VirtTxtJml/Spectrpy/UV-Vis/spectrum.htm> [2012, February 14]
- [121] Ohmura, T., Usuki, A., Fukumori, K., Ohta, T., Ito, M., and Tatsumi, K. New Porphyrin-Based Metal-Organic Framework with High Porosity: 2-D Infinite 22.2-Å Square-Grid Coordination Network. *Inorg. Chem.* 45 (2006): 7988-7990.
- [122] Dennis, W. S., Scott, R. W. and Kenneth, S. S. A Robust Microporous Zinc Porphyrin Framework Solid. *Inorg. Chem.* 42 (2003): 7719-7721.
- [123] Choi, E.-Y., Barron, P. M., Novotny, R. W., Son, H.-T., Hu, C., and Choe, W. Pillared Porphyrin Homologous Series: Intergrowth in Metal-Organic Frameworks. *Inorg. Chem.* 48 (2009): 426-428.
- [124] Choi, E.-Y., Barron, P. M., Novotny, R. W., Hu, C., Kwon, Y.-UK., and Choe, W. A mixed-linker porphyrin framework with CdI<sub>2</sub>-type topology. *Cryst. Eng. Comm.* 10 (2008): 824-826.
- [125] Verduzco, J. M., Chung, H., Hu, C., and Choe, W. Metal-Organic Framework Assembled from T-Shaped and Octahedral Nodes: A Mixed-Linker Strategy To Create a Rare Anatase TiO<sub>2</sub> Topology. *Inorg. Chem.* 48 (2009): 9060-9062.

## **APPENDICES**

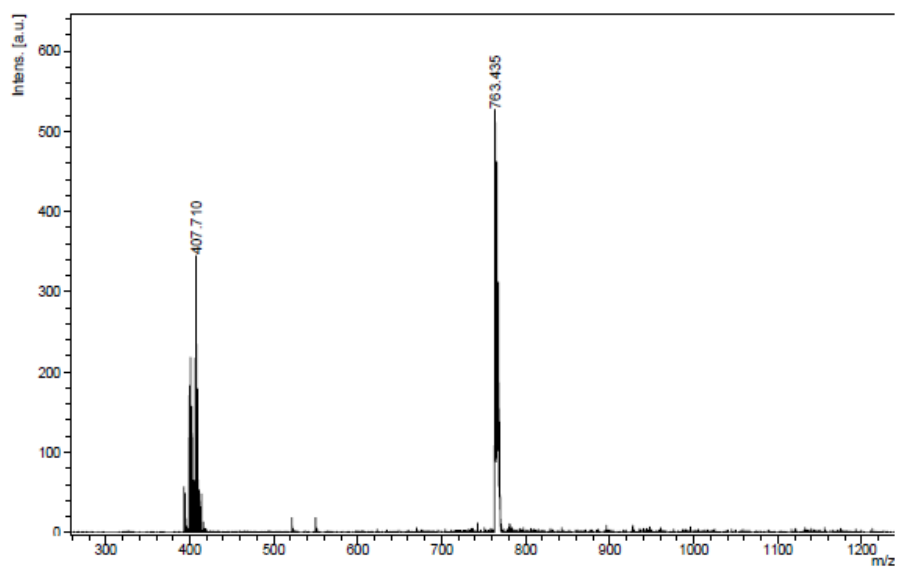


## **APPENDIX A**

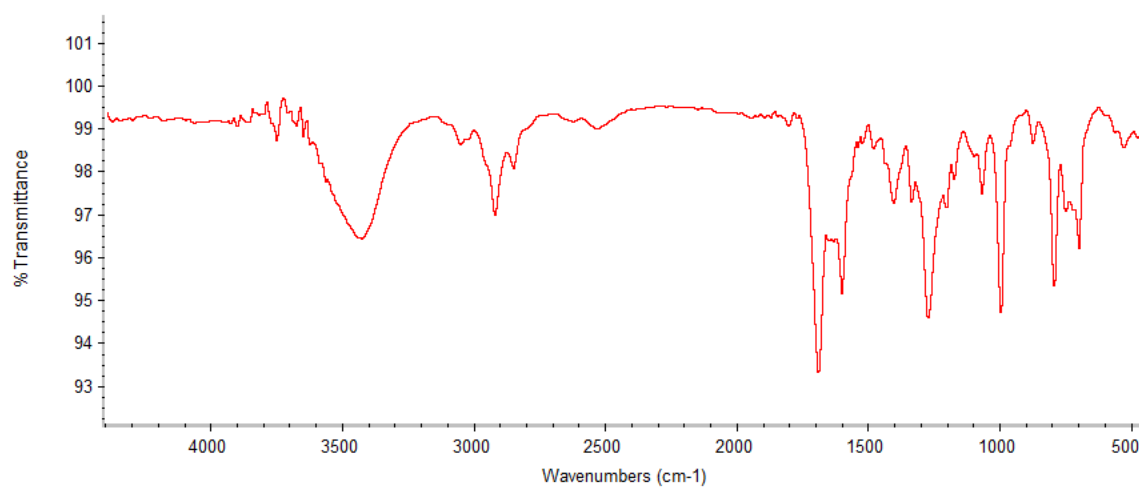




**Figure A-3.**  $^{13}\text{C}$  NMR of compound 2.



**Figure A-4.** Mass spectrum of compound 2.

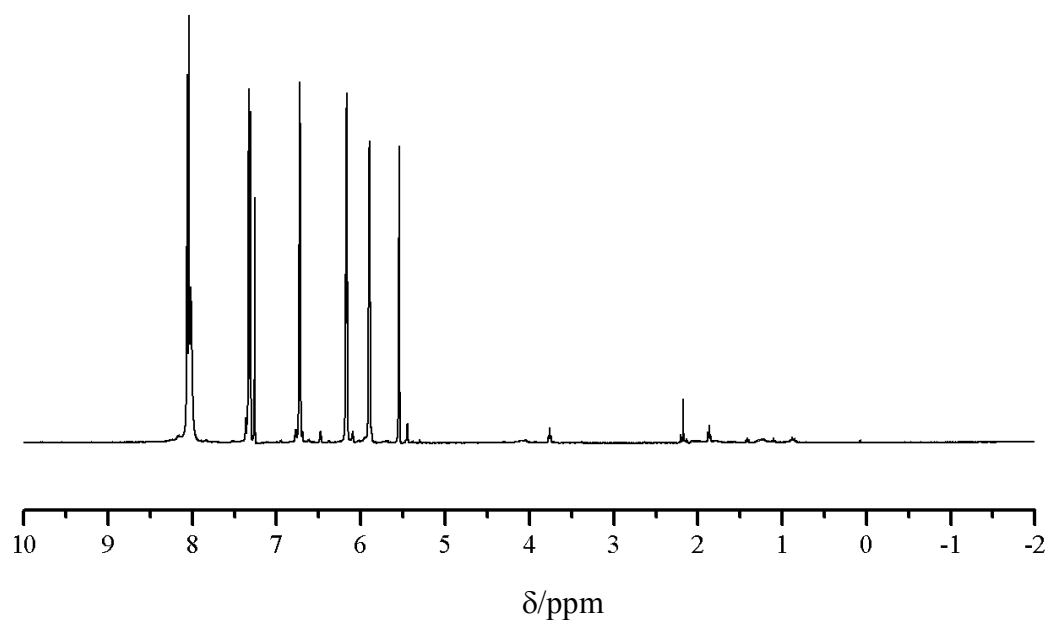


**Figure A-5.** IR spectrum of compound 2.

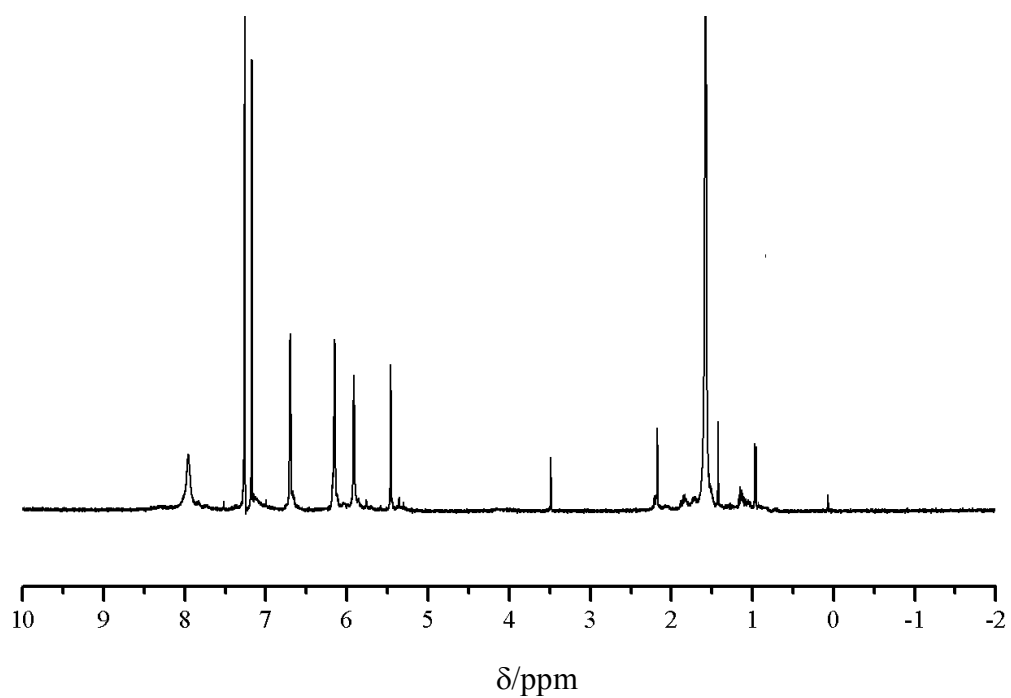


Empirical formula	$C_{27.50} H_{24.50} N_{3.50} O_{3.25} Zn_{0.50}$
Formula weight	488.69
Temperature	296(2) K
Wavelength	0.71073 Å
Crystal system, space group	triclinic, P(-1)
Unit cell dimensions	a = 9.9591(2) Å    alpha = 73.5700(10) deg. b = 13.3337(4) Å    beta = 78.7150(10) deg. c = 19.4373(5) Å    gamma = 84.0310(10) deg.
Volume	2424.60(11) Å <sup>3</sup>
Z, Calculated density	4, 1.339 Mg/m <sup>3</sup>
Absorption coefficient	0.567 mm <sup>-1</sup>
F(000)	1020
Crystal size	0.46 x 0.30 x 0.05 mm
Theta range for data collection	2.17 to 25.15 deg.
Limiting indices	-11 ≤ h ≤ 8, -15 ≤ k ≤ 15, -23 ≤ l ≤ 23
Reflections collected / unique	17303 / 8533 [R(int) = 0.0239]
Completeness to theta = 25.15	98.5 %
Max. and min. transmission	0.9722 and 0.7805
Refinement method	Full-matrix least-squares on F <sup>2</sup>
Data / restraints / parameters	8533 / 0 / 640
Goodness-of-fit on F <sup>2</sup>	1.027
Final R indices [I > 2σ(I)]	R1 = 0.0488, wR2 = 0.1304
R indices (all data)	R1 = 0.0665, wR2 = 0.1429
Largest diff. peak and hole	1.655 and -0.352 e.Å <sup>-3</sup>

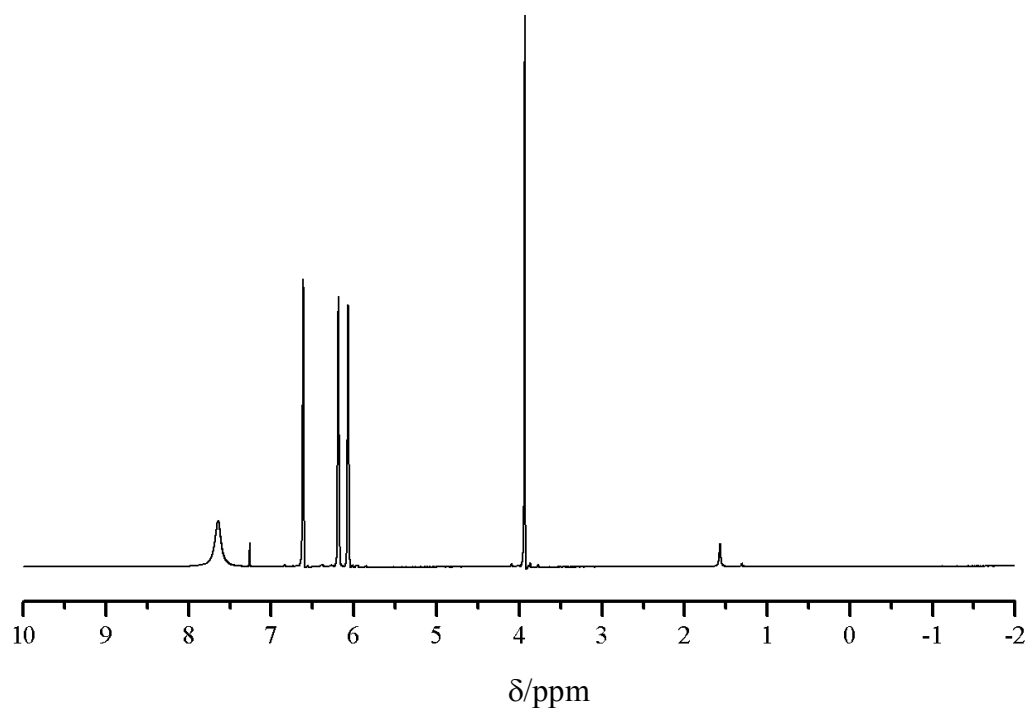
**Figure A-6.** Crystallographic data of compound **2**.



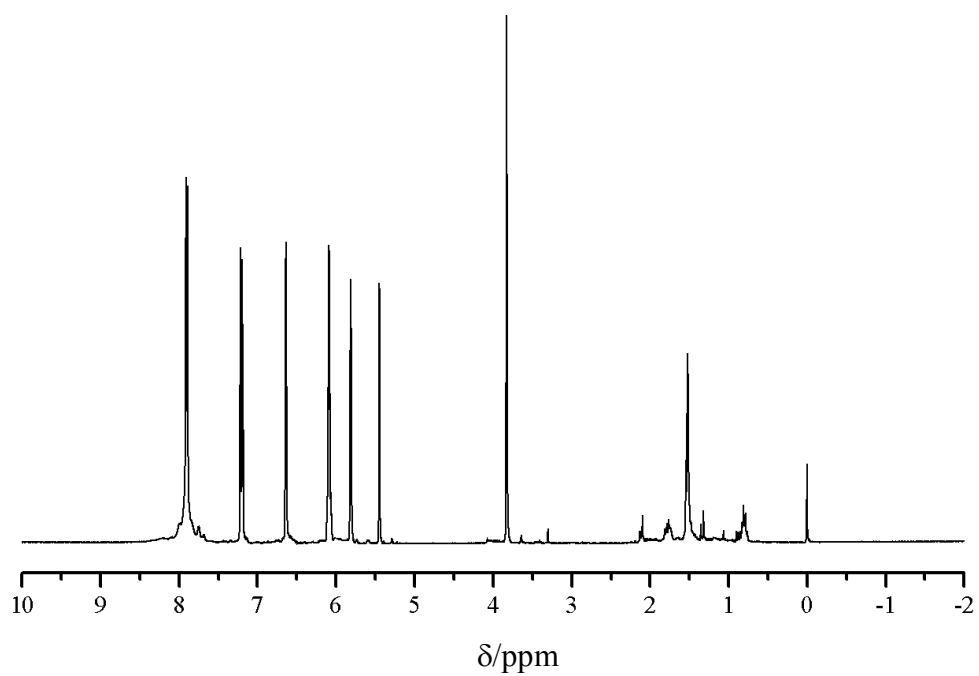
**Figure A-7.**  $^1\text{H}$  NMR spectrum of compound 3.



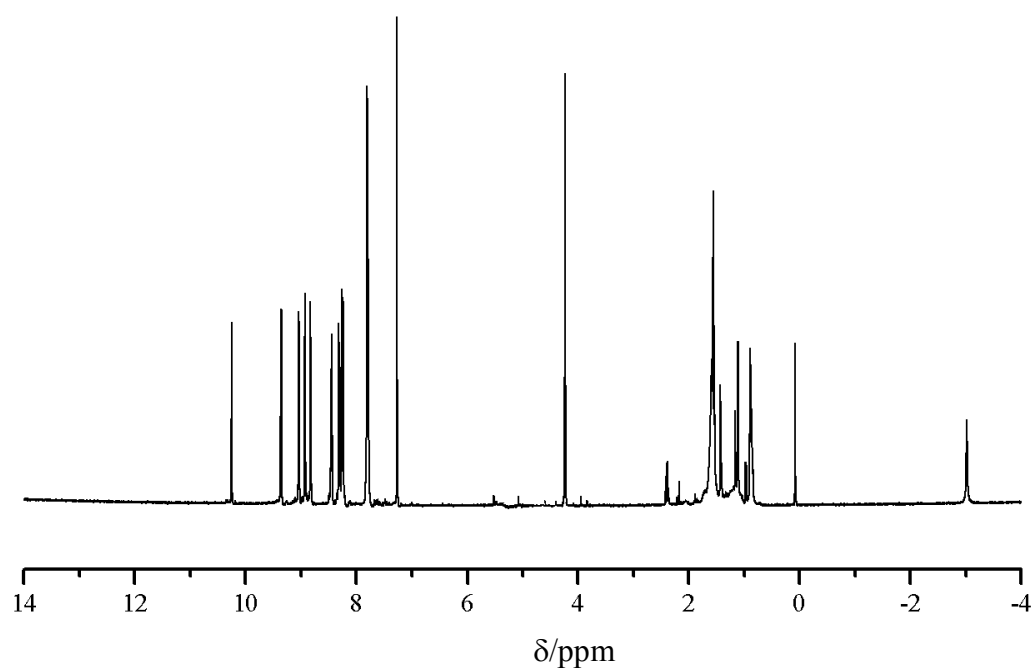
**Figure A-8.**  $^1\text{H}$  NMR spectrum of compound 4.



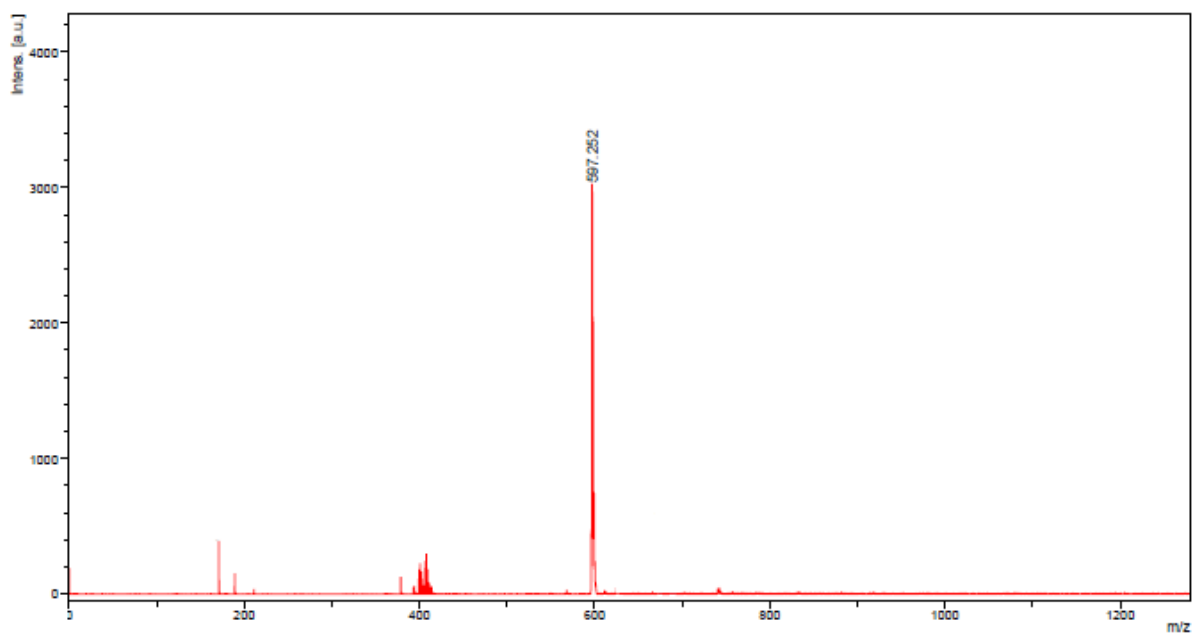
**Figure A-9.**  $^1\text{H}$  NMR spectrum of compound 6.



**Figure A-10.**  $^1\text{H}$  NMR spectrum of compound 7.

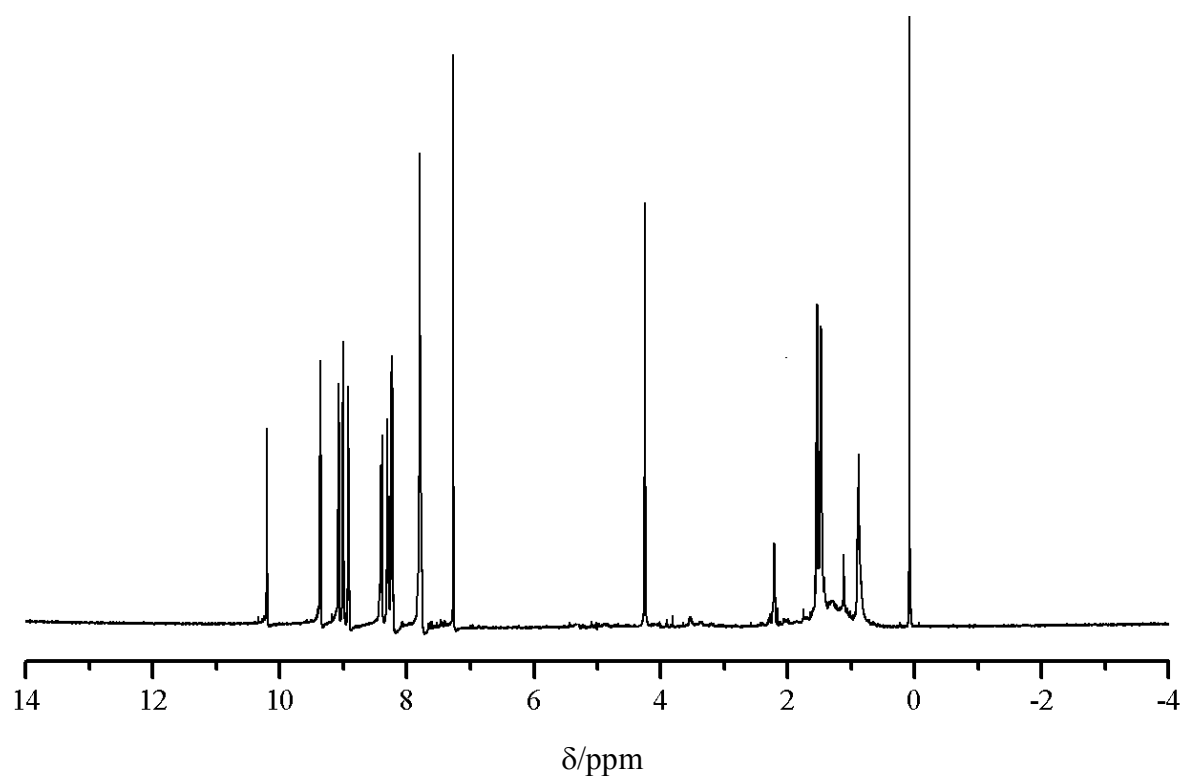


**Figure A-11.**  $^1\text{H}$  NMR spectrum of compound **8**.

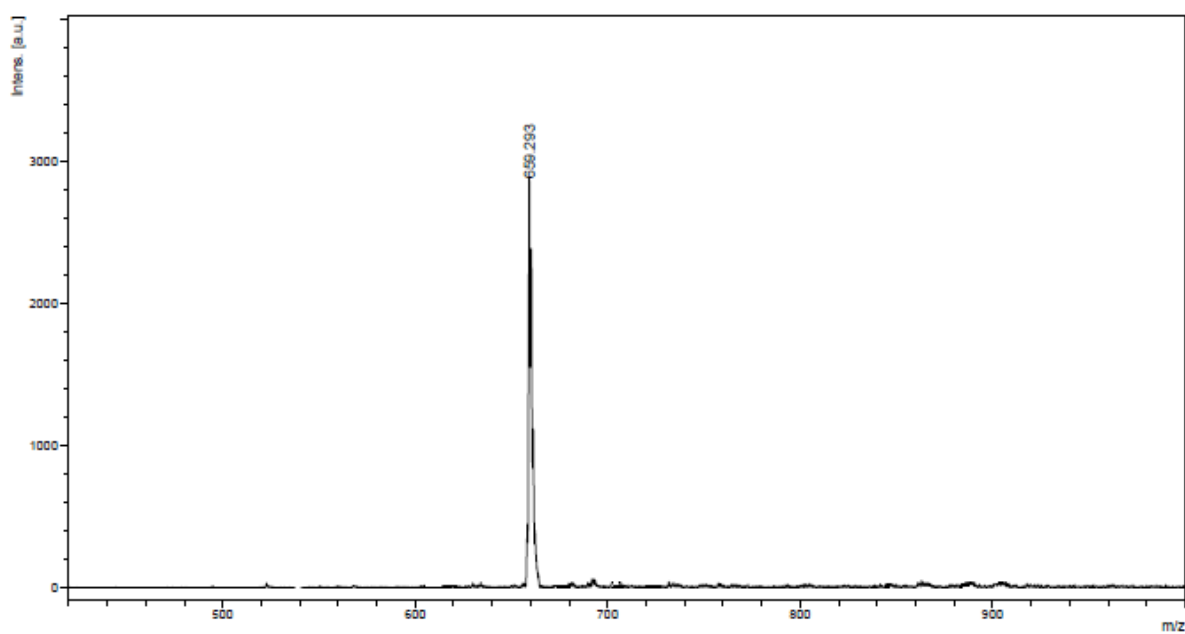


**Figure A-12.** Mass spectrum of compound **8**.

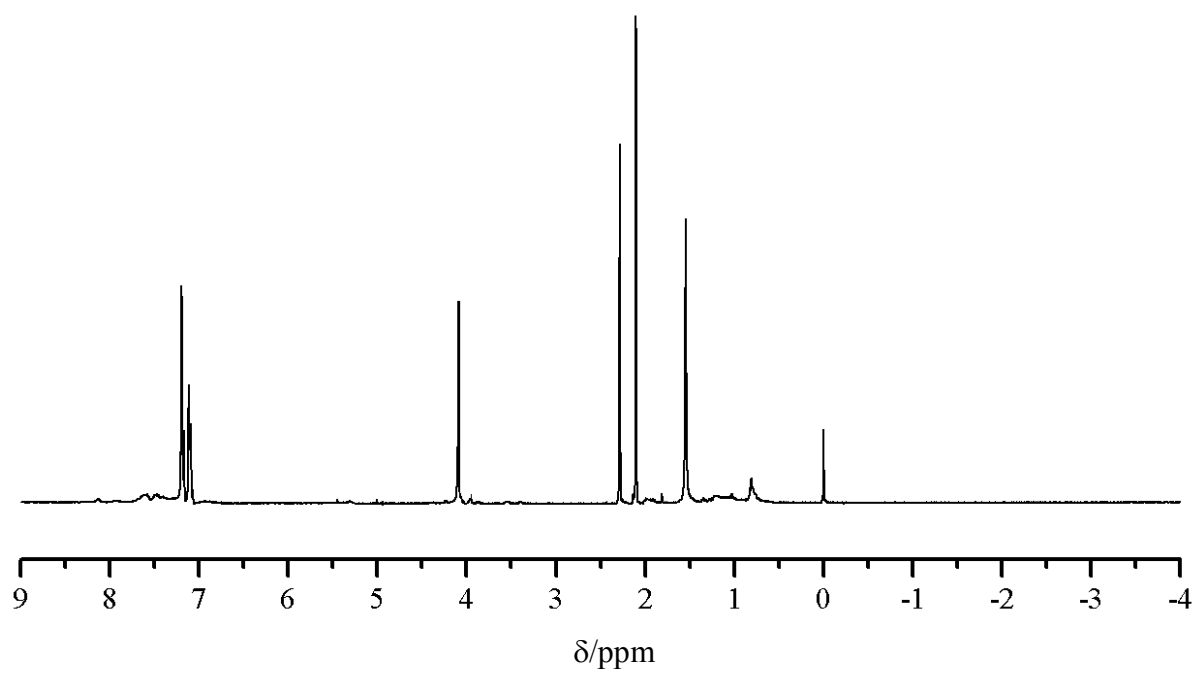




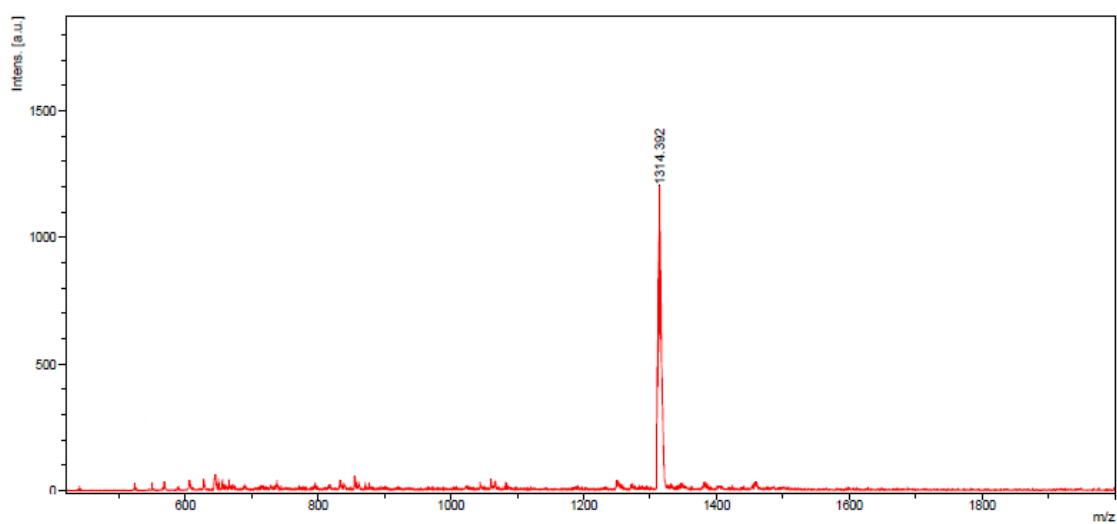
**Figure A-13.** <sup>1</sup>H NMR spectrum of compound **9**.



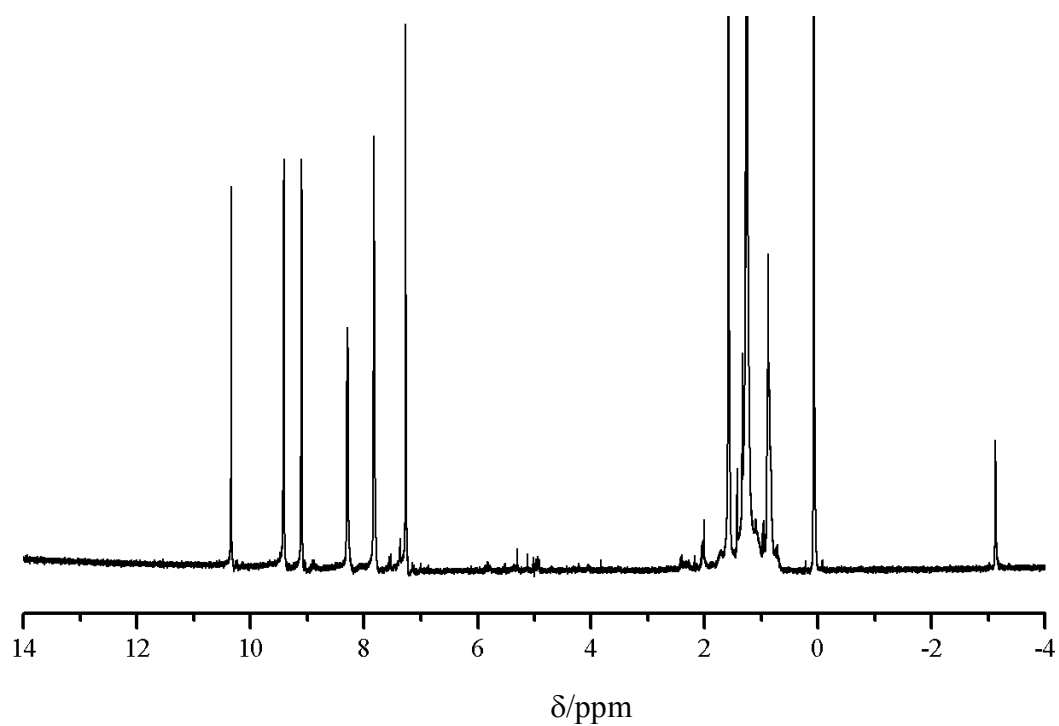
**Figure A-14.** Mass spectrum of compound **9**.



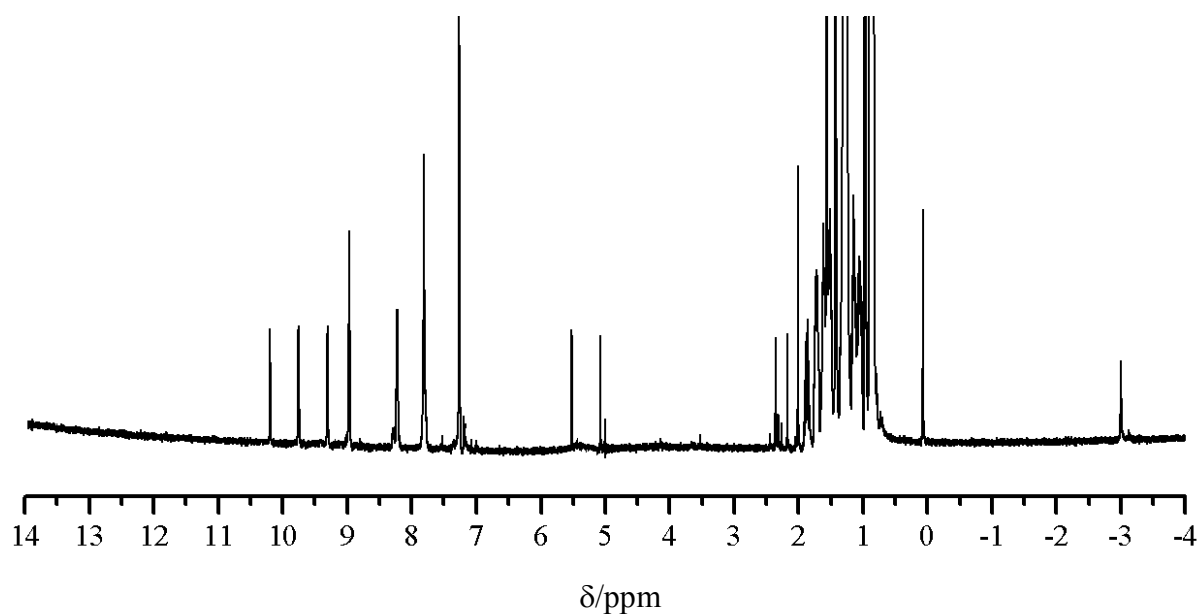
**Figure A-15.**  $^1\text{H}$  NMR spectrum of compound 10.



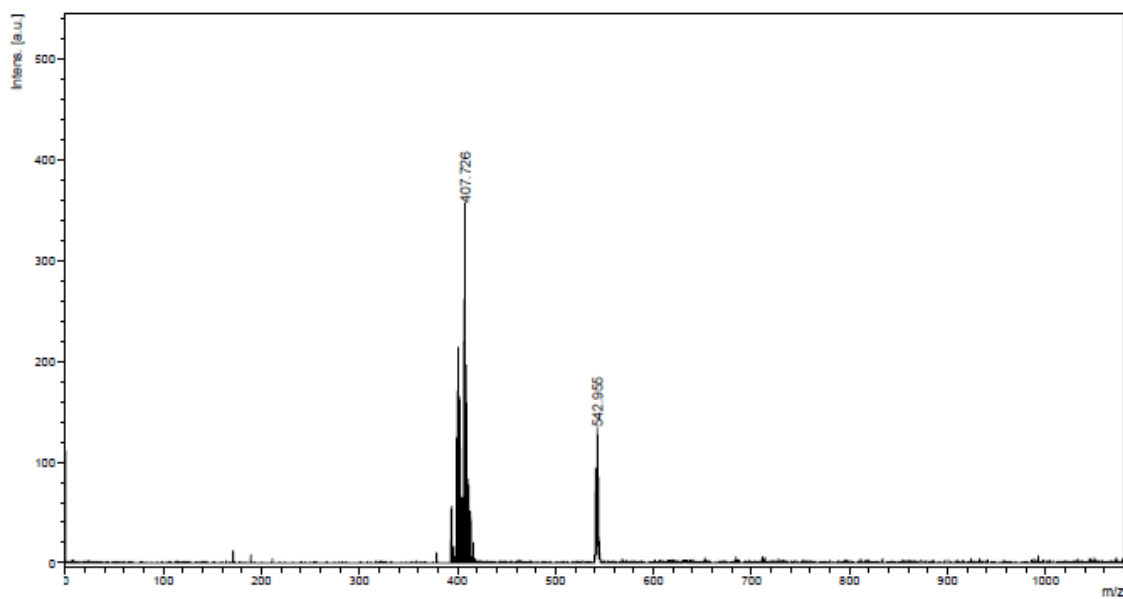
**Figure A-16.** Mass spectrum of compound 10.



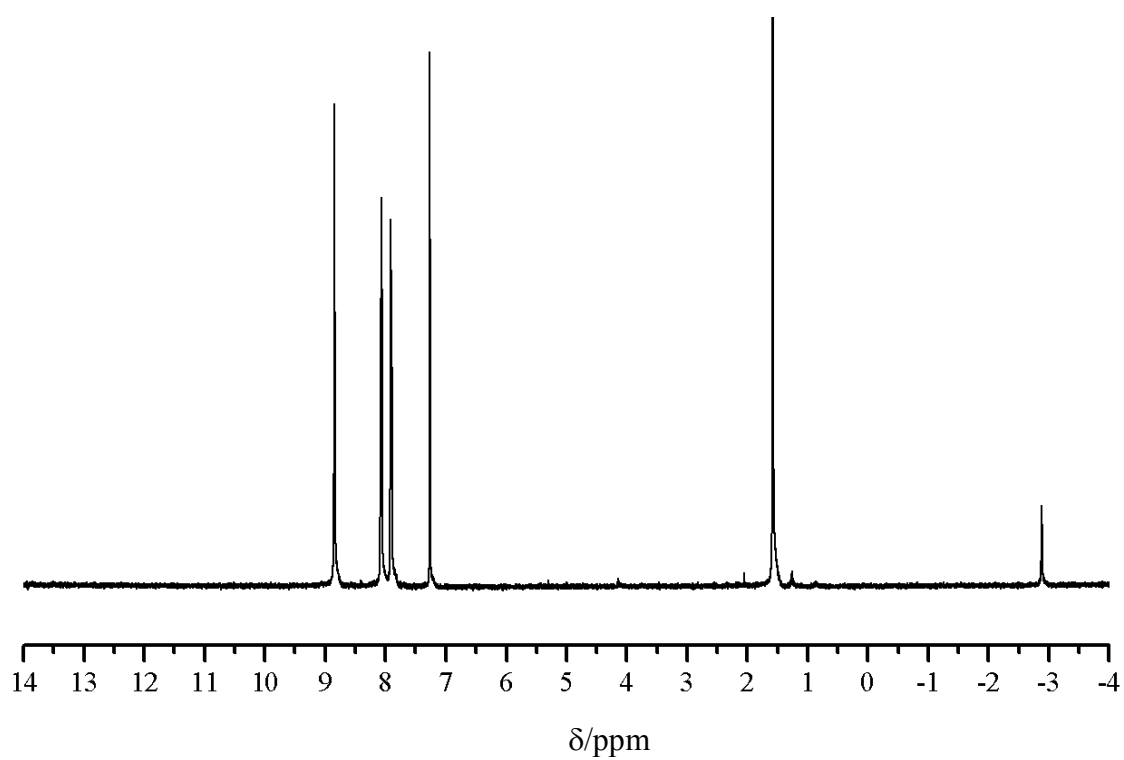
**Figure A-17.**  $^1\text{H}$  NMR spectrum of compound 11.



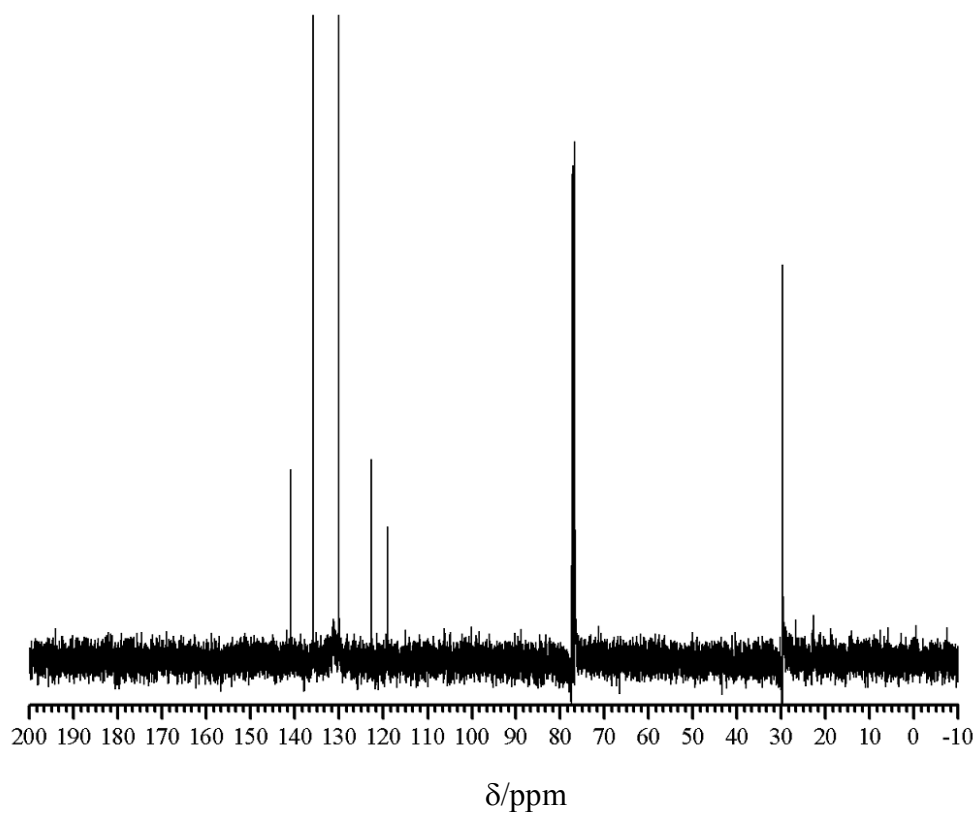
**Figure A-18.**  $^1\text{H}$  NMR spectrum of compound 12.



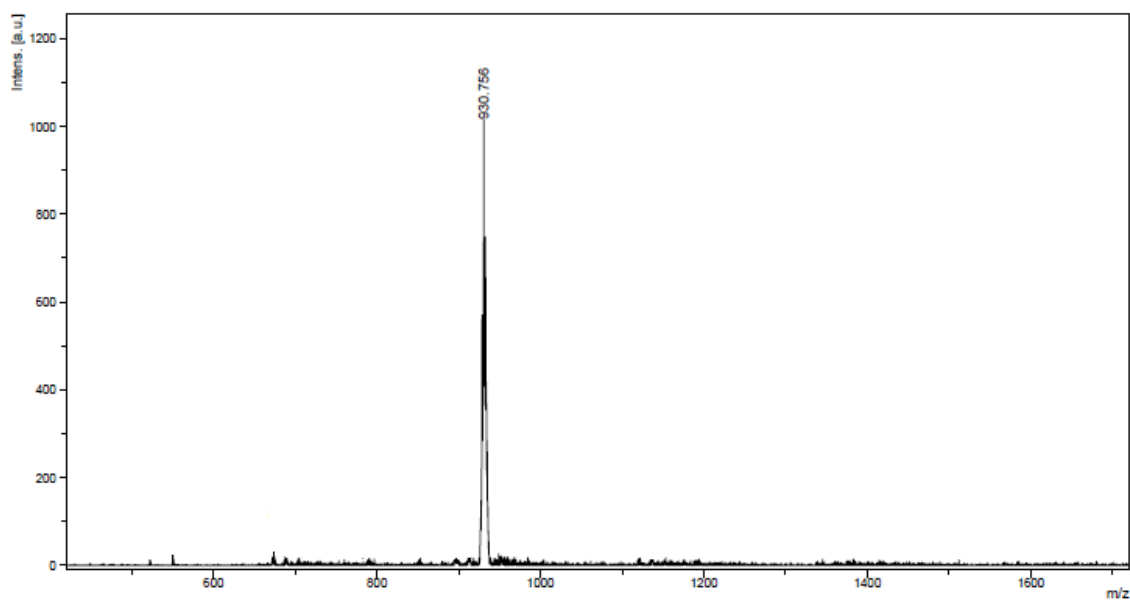
**Figure A-19.** Mass spectrum of compound 12.



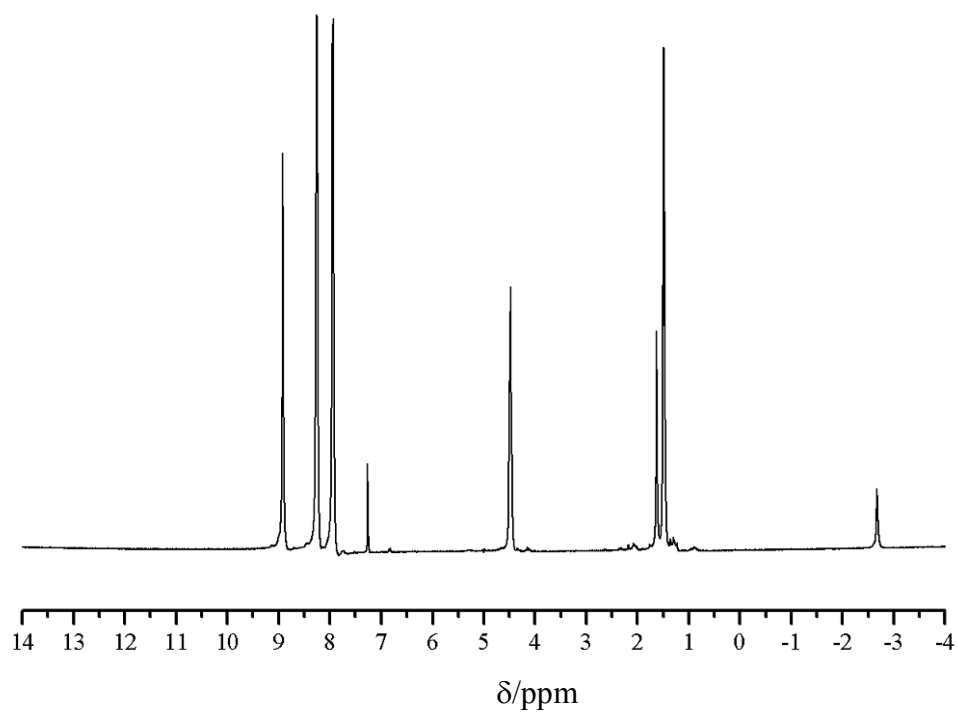
**Figure A-20** <sup>1</sup>H NMR spectrum of compound 13.



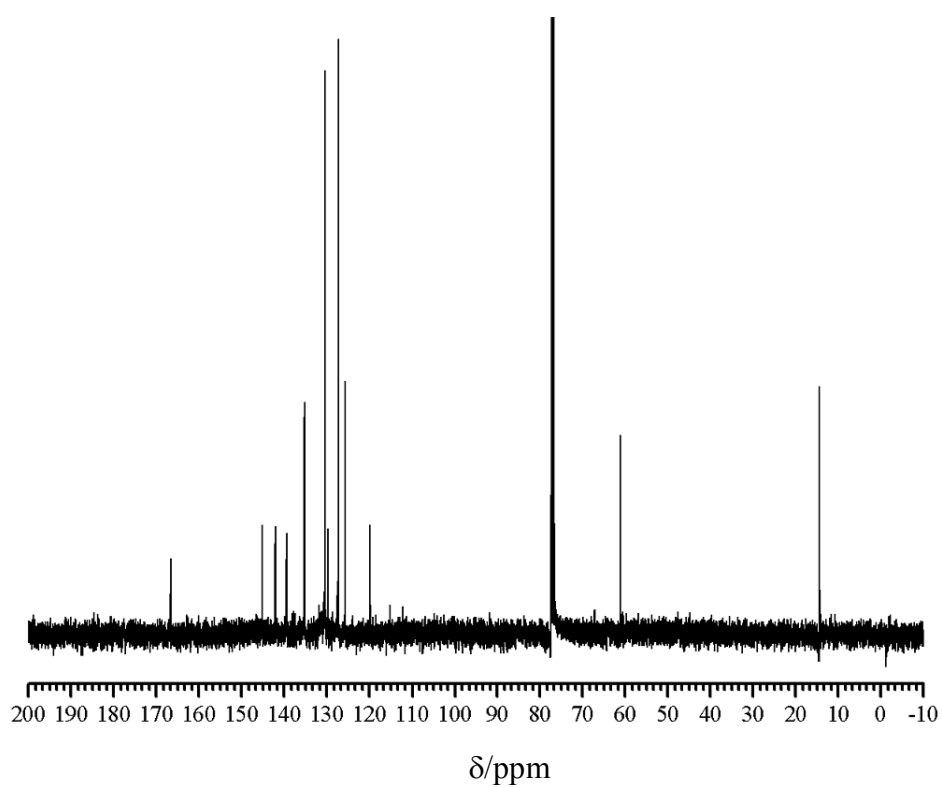
**Figure A-21.**  $^{13}\text{C}$  NMR spectrum of compound **13**.



**Figure A-22.** Mass spectrum of compound **13**.



**Figure A-23.**  $^1\text{H}$  NMR spectrum of compound 14.



**Figure A-24.**  $^{13}\text{C}$  NMR spectrum of compound 14.

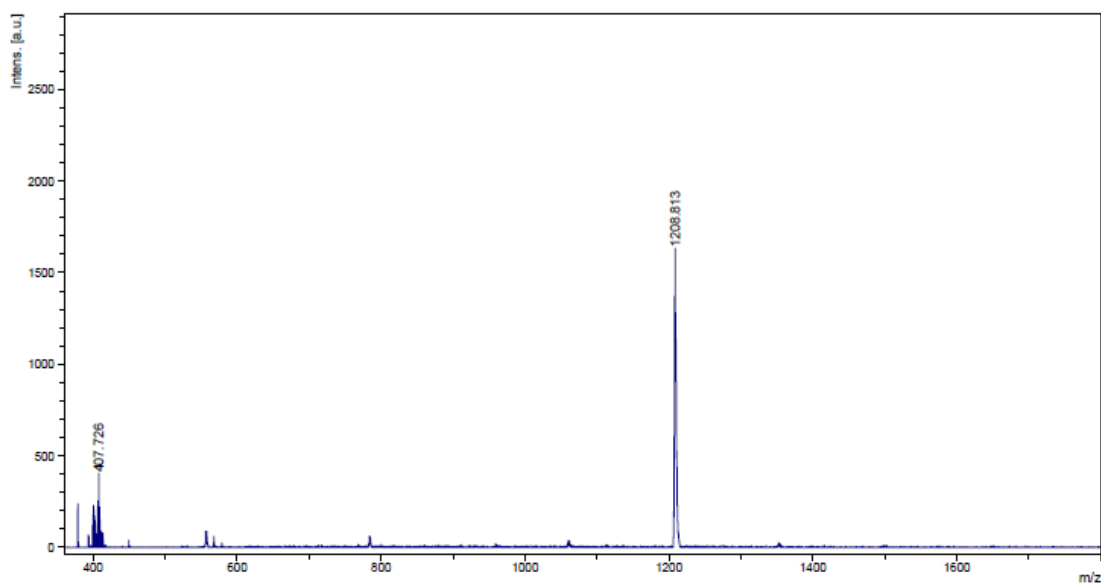


Figure A-25. Mass spectrum of compound 14.

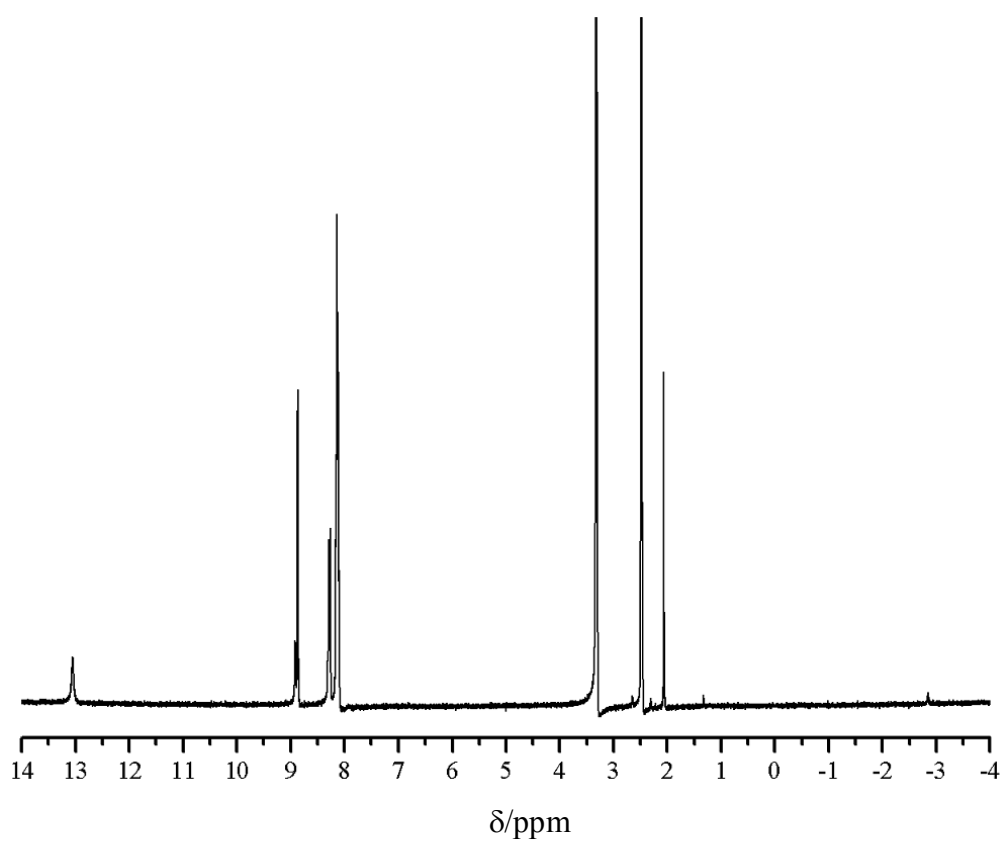
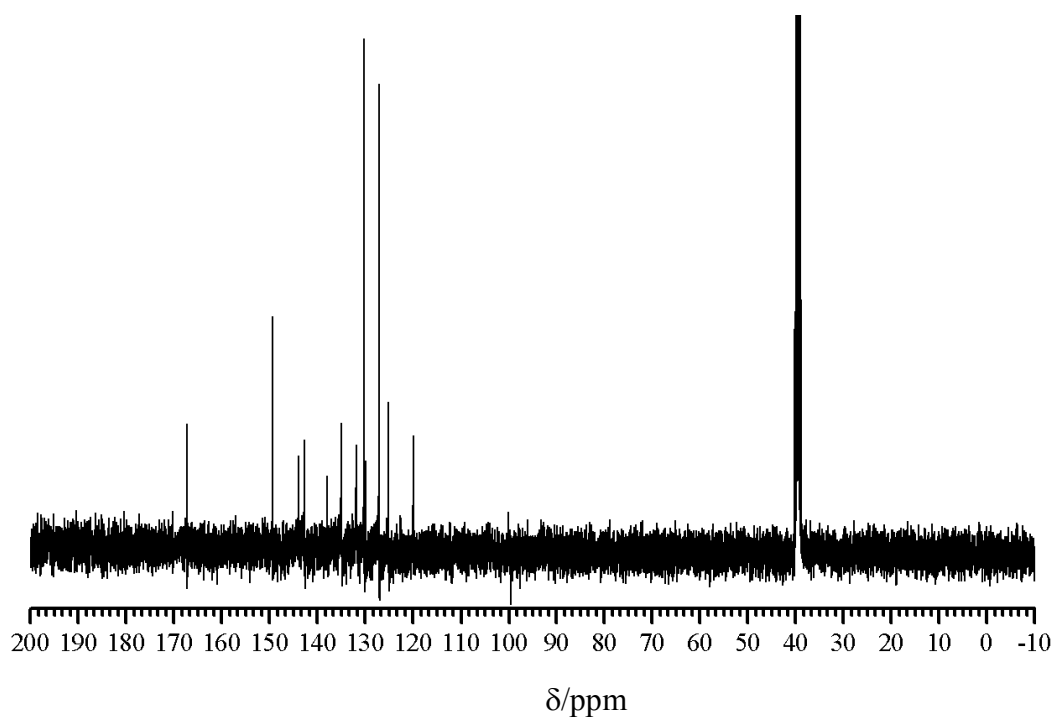
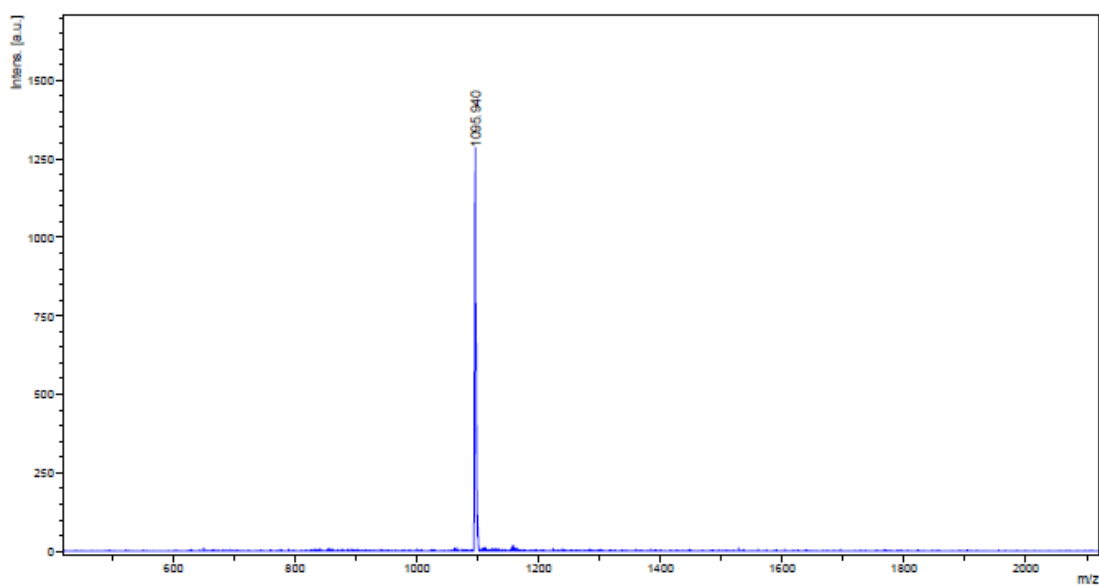


Figure A-26. <sup>1</sup>H NMR spectrum of compound 15.

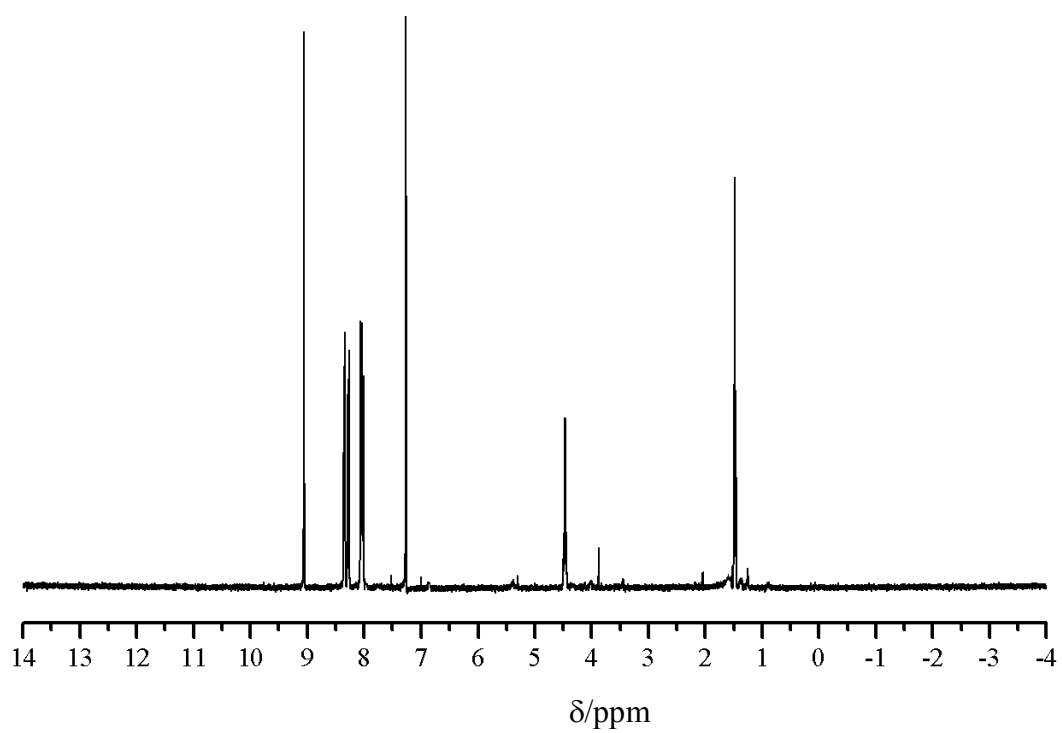


**Figure A-27.**  $^{13}\text{C}$  NMR spectrum of compound **15**.

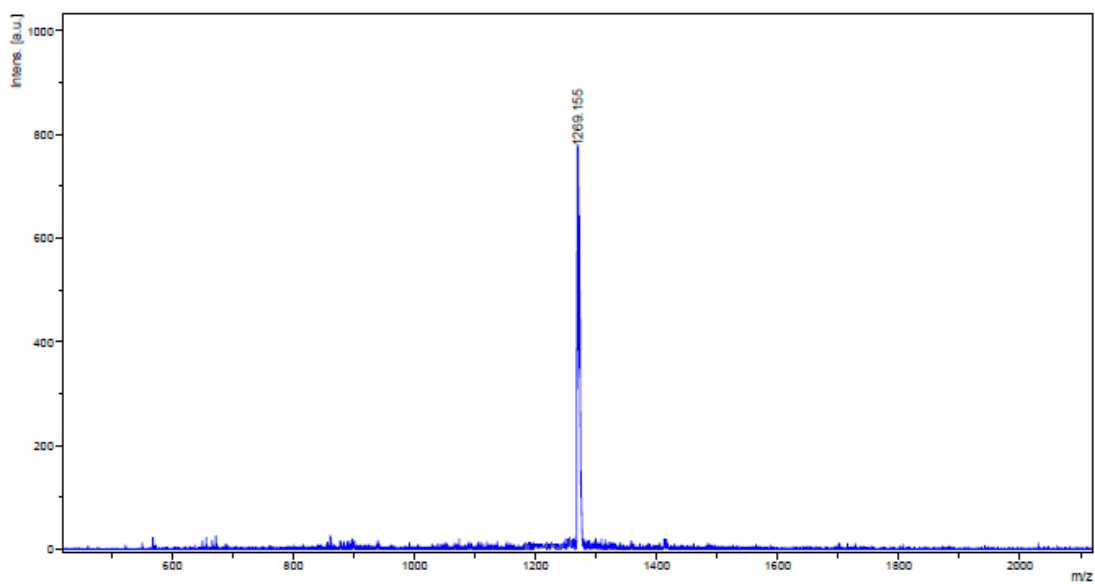


**Figure A-28.** Mass spectrum of compound **15**.

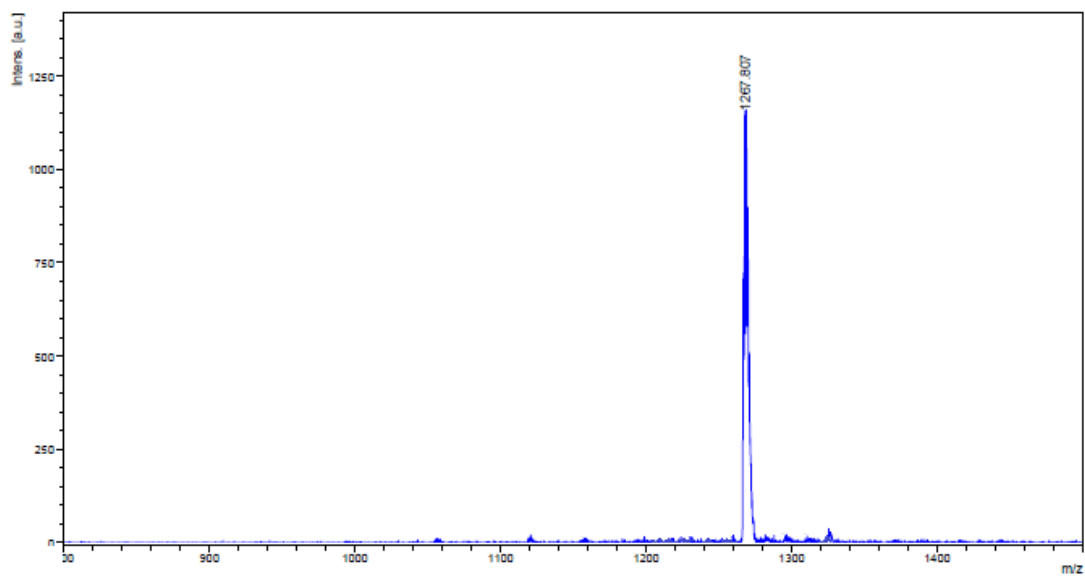




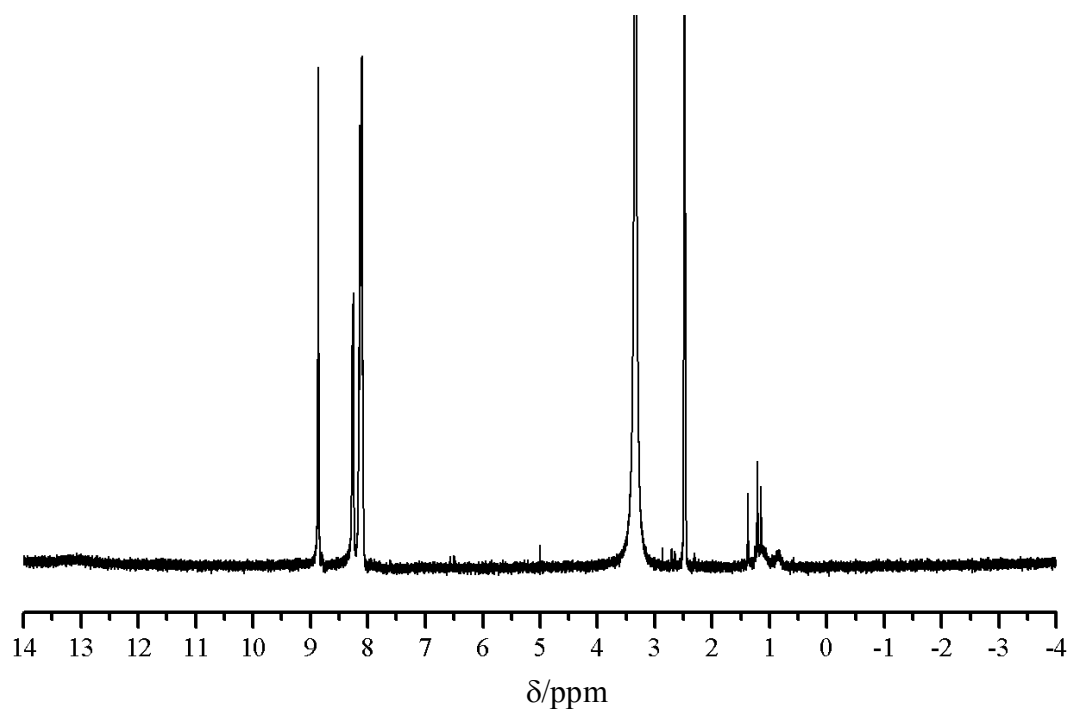
**Figure A-29.**  $^1\text{H}$  NMR spectrum of compound **16**.



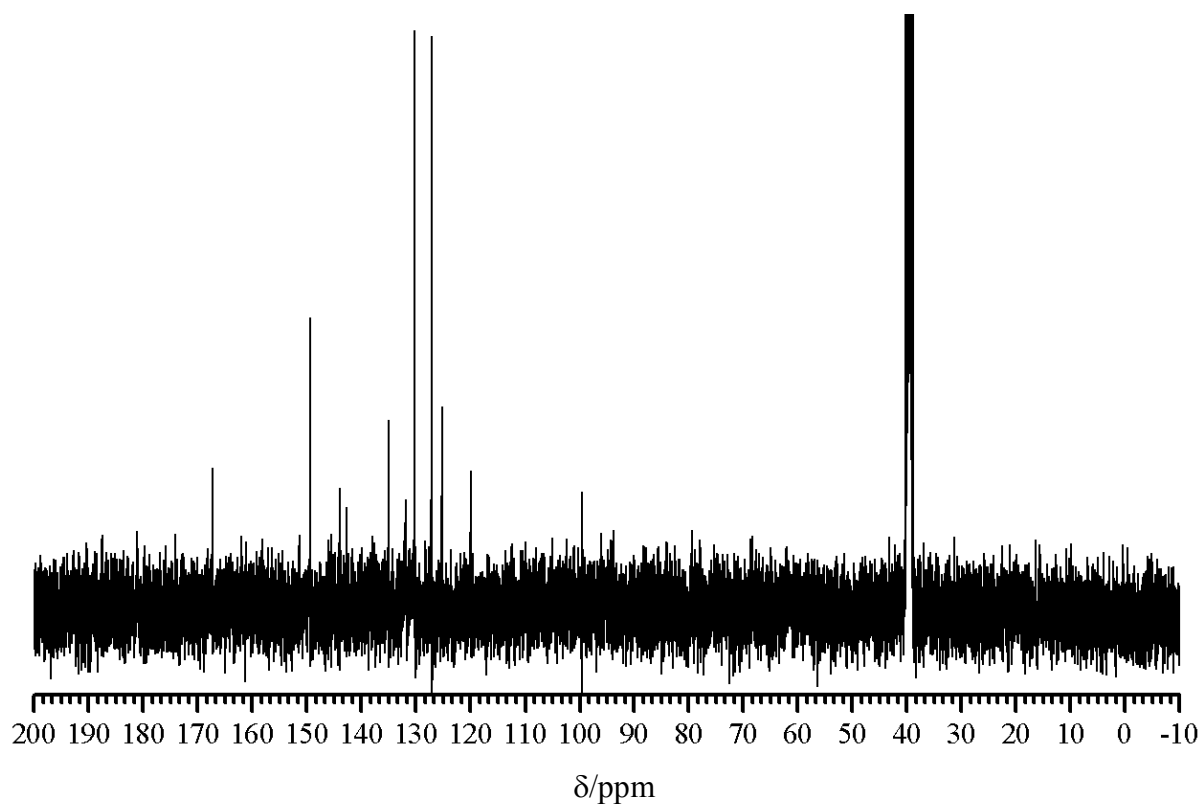
**Figure A-30.** Mass spectrum of compound **16**.



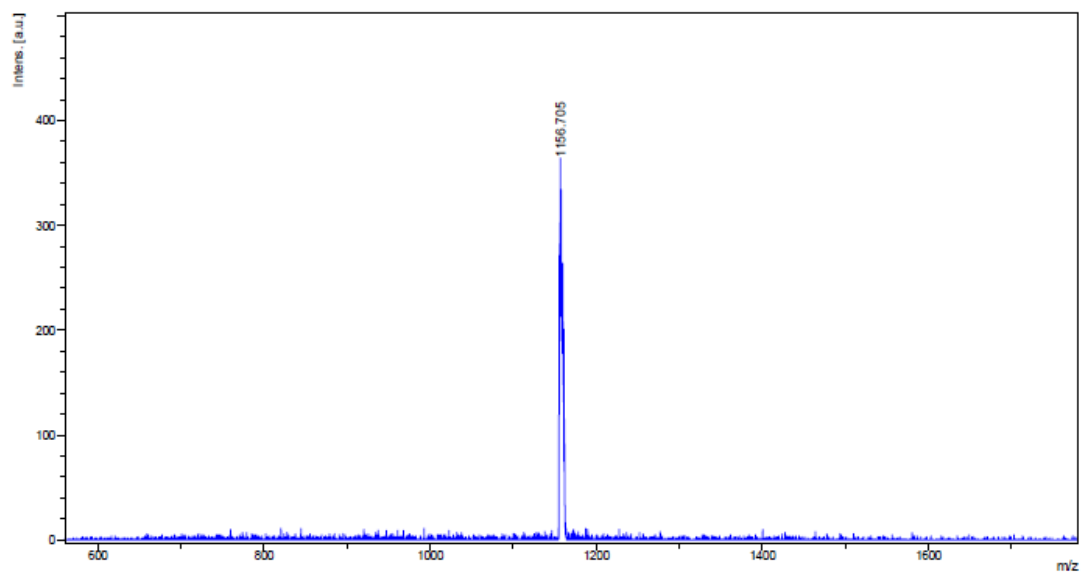
**Figure A-31.** Mass spectrum of compound **17**.



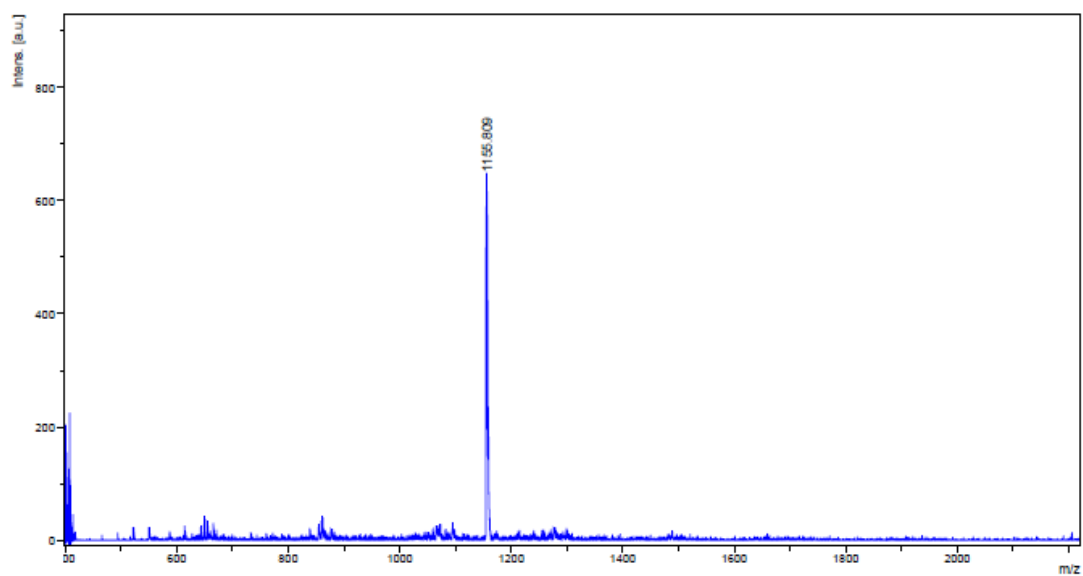
**Figure A-32.** <sup>1</sup>H NMR spectrum of compound **18**.



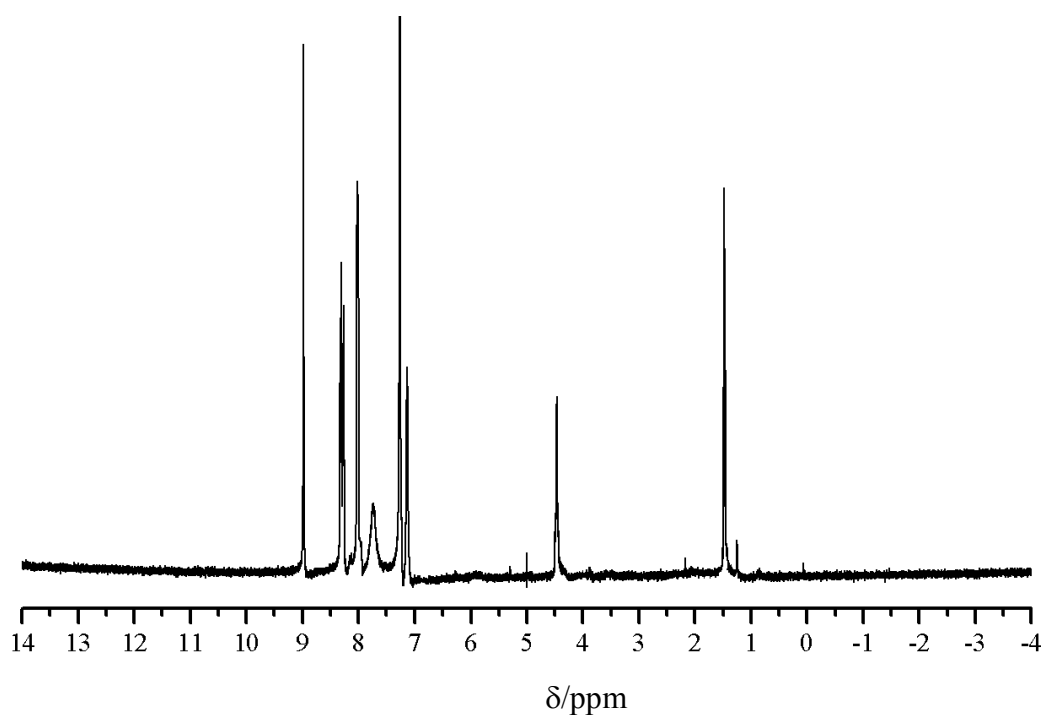
**Figure A-33.**  $^{13}\text{C}$  NMR spectrum of compound **18**.



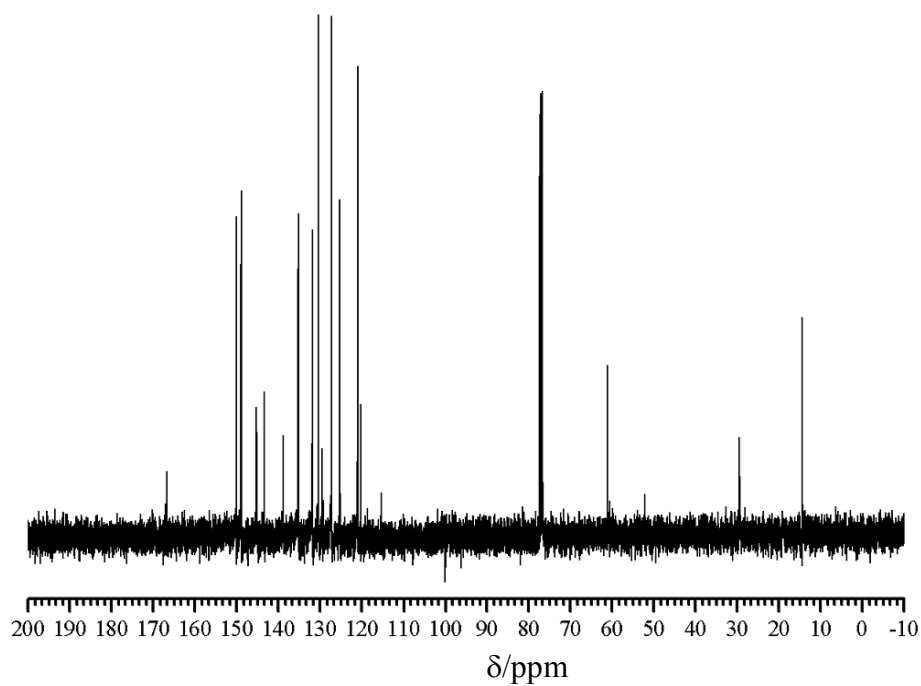
**Figure A-34.** Mass spectrum of compound **18**.



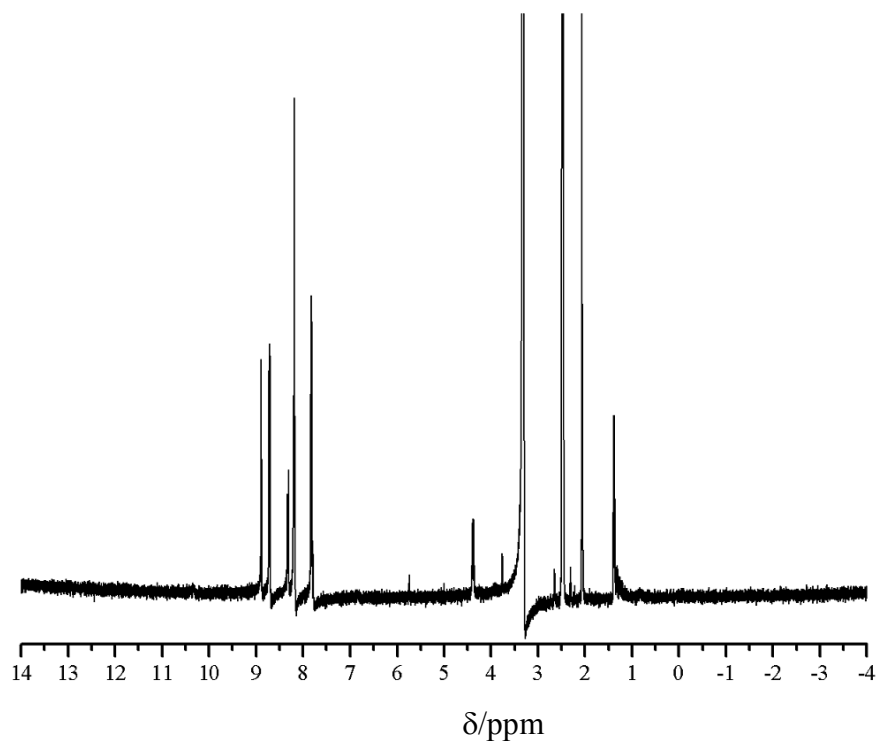
**Figure A-35.** Mass spectrum of compound **19**.



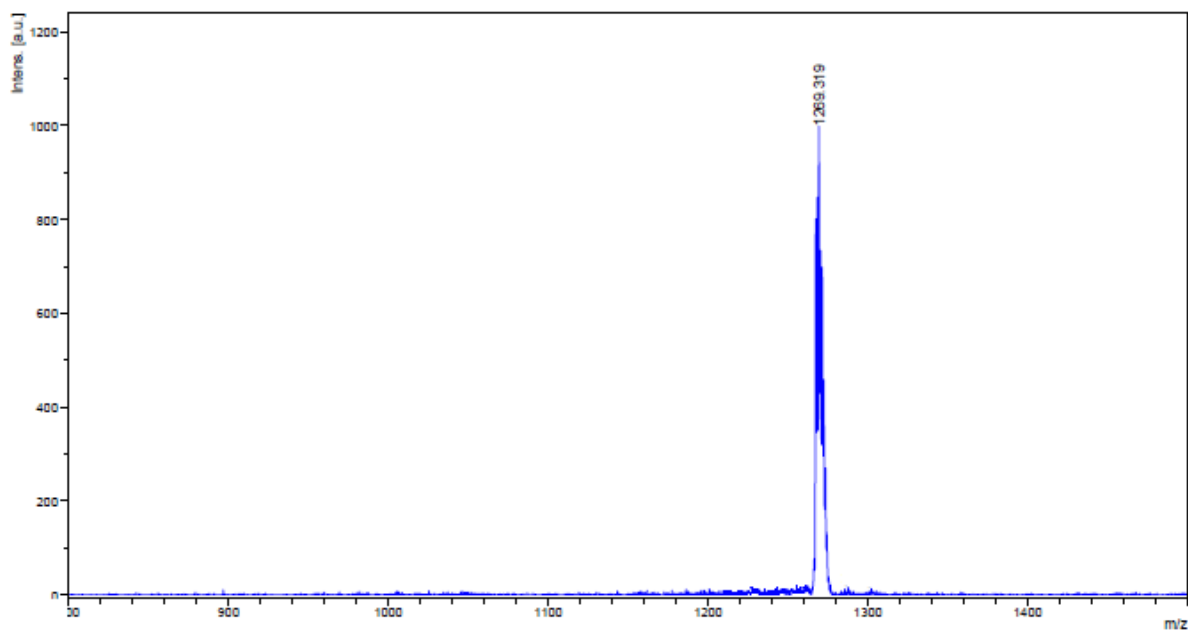
**Figure A-36.** <sup>1</sup>H NMR spectrum of compound **20** in CDCl<sub>3</sub>.



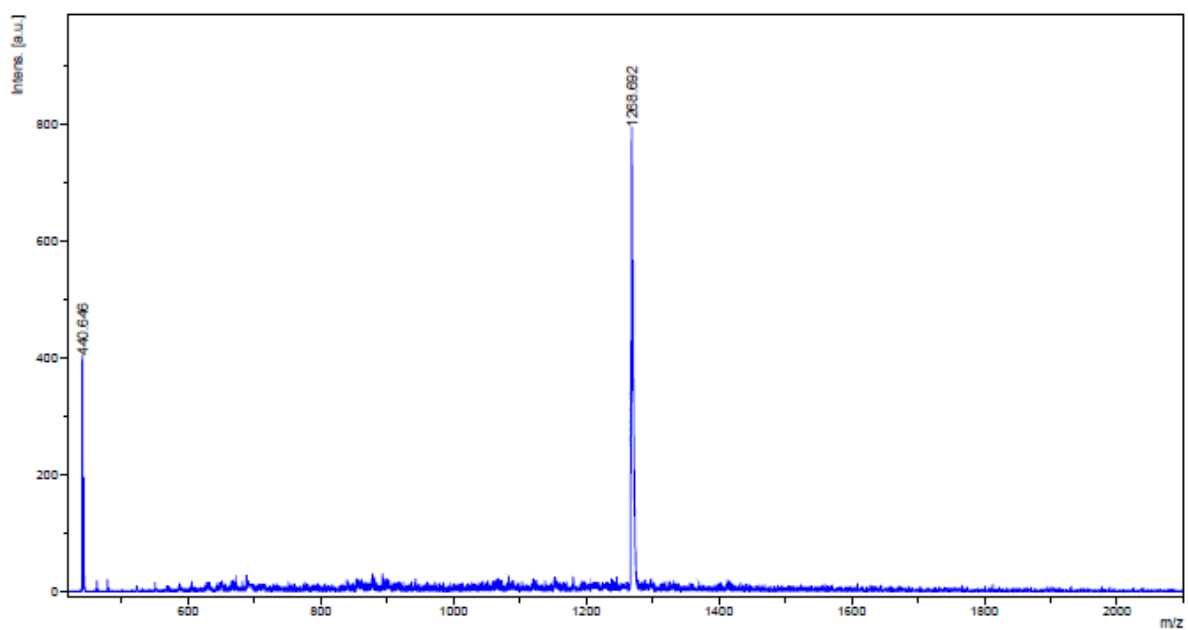
**Figure A-37.**  $^{13}\text{C}$  NMR spectrum of compound **20** in  $\text{CDCl}_3$ .



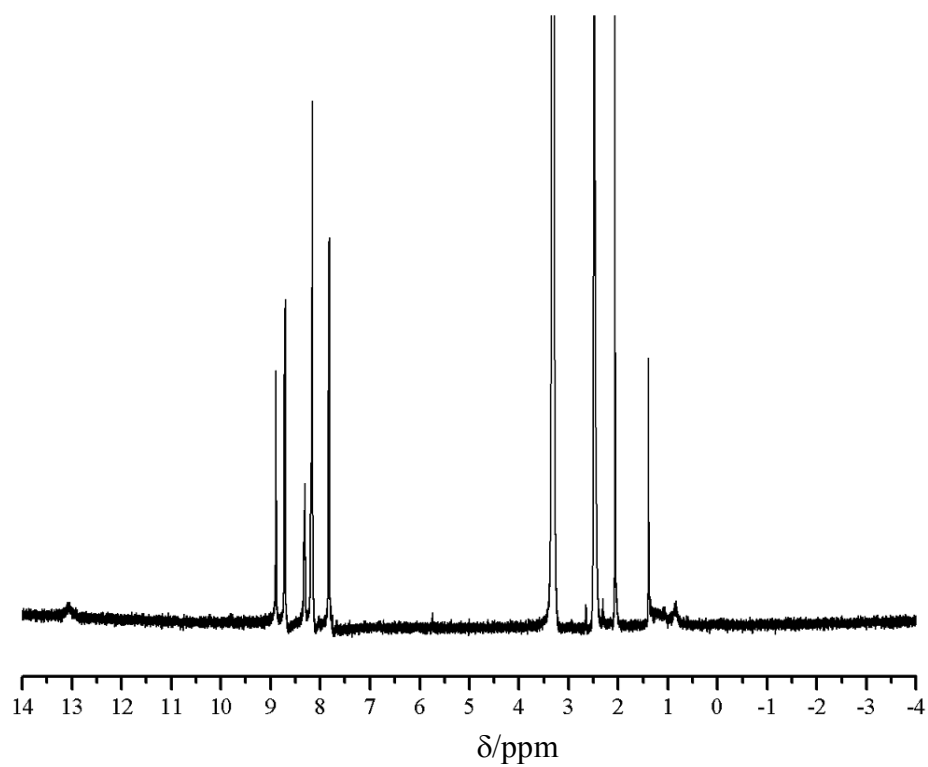
**Figure A-38.**  $^1\text{H}$  NMR spectrum of compound **20** in DMSO.



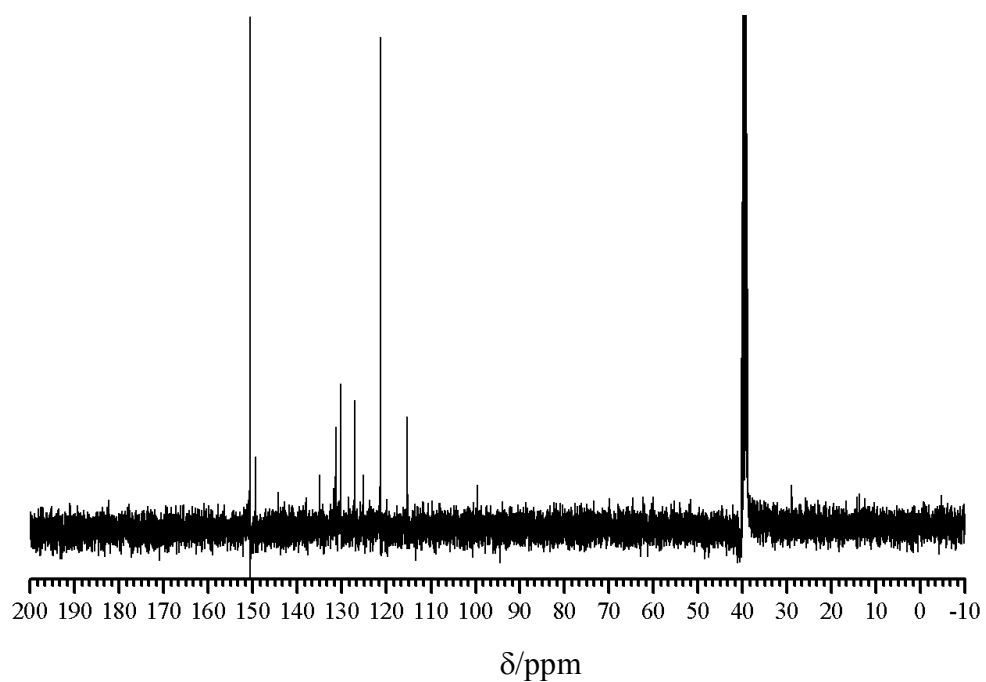
**Figure A-39.** Mass spectrum of compound 20.



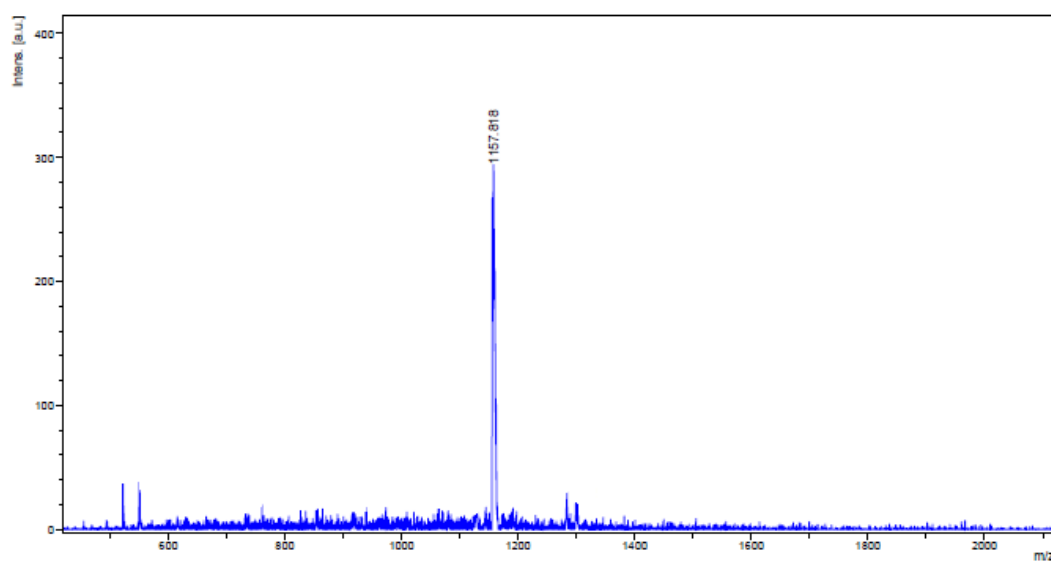
**Figure A-40.** Mass spectrum of compound 21.



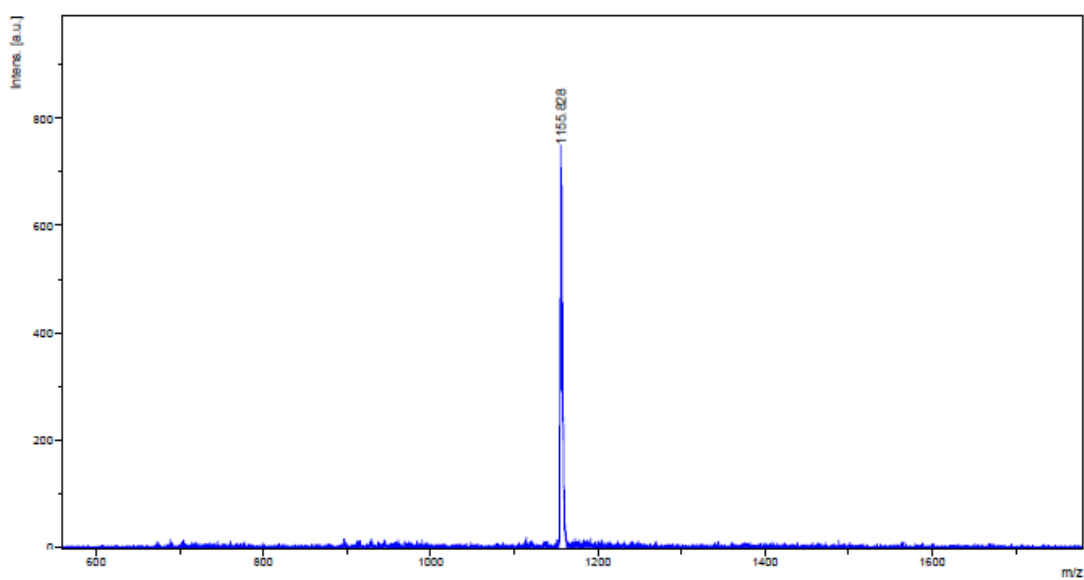
**Figure A-41.**  $^1\text{H}$  NMR spectrum of compound 22



**Figure A-42.**  $^{13}\text{C}$  NMR spectrum of compound 22

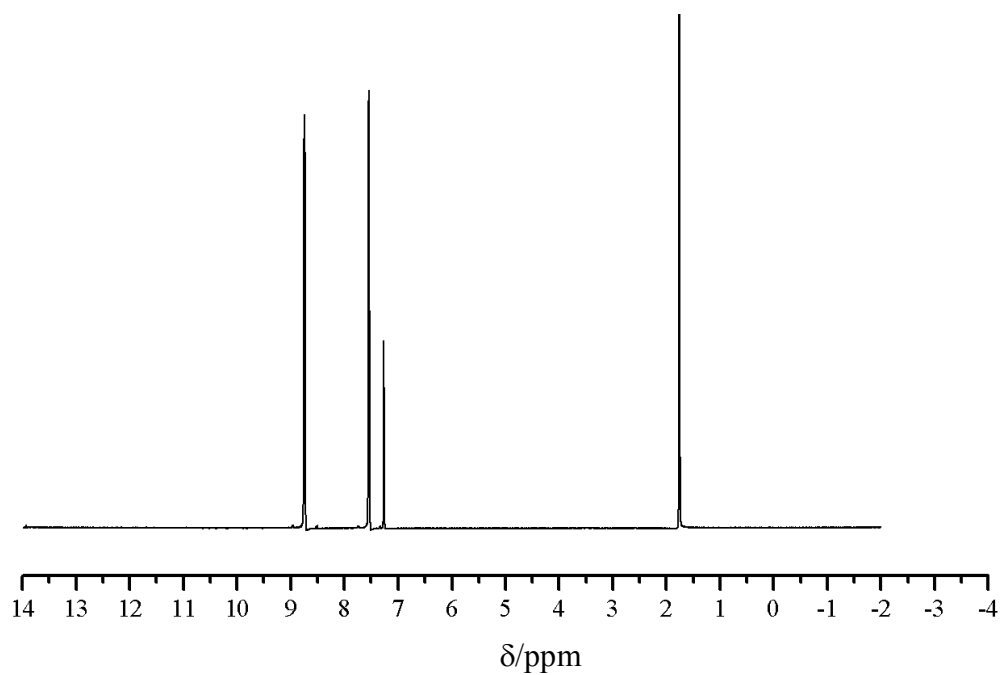


**Figure A-43.** Mass spectrum of compound 22.

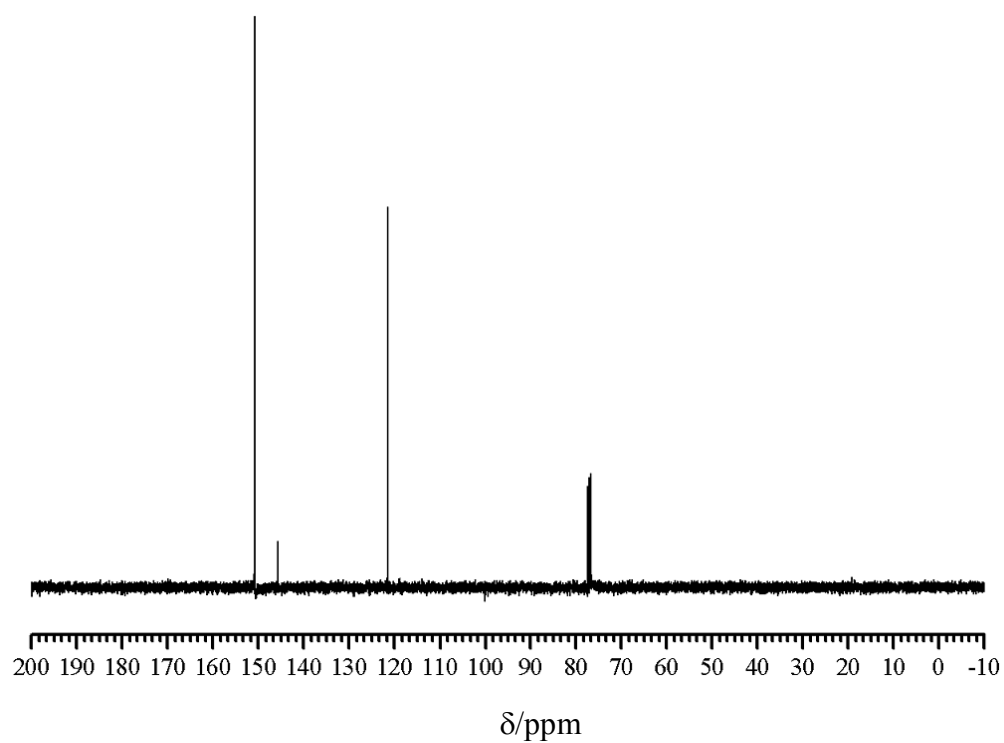


**Figure A-44.** Mass spectrum of compound 23.

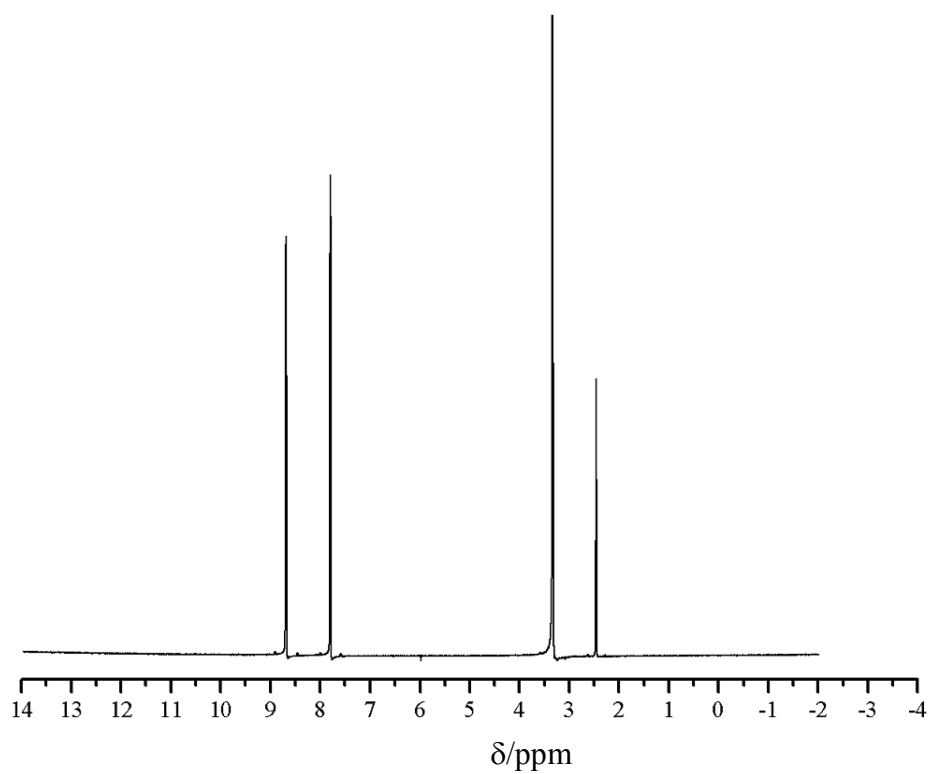




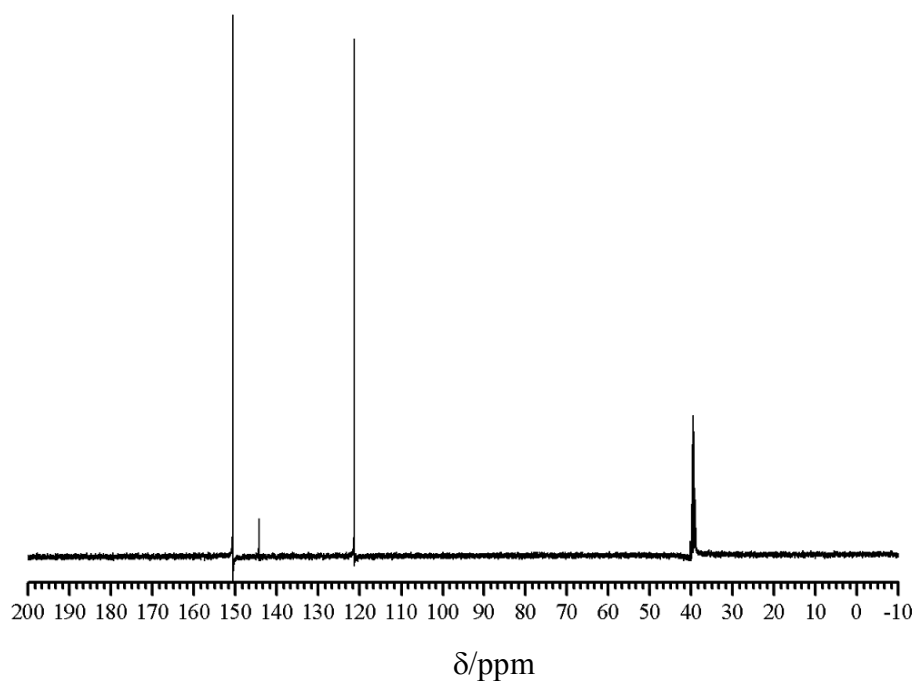
**Figure A-45.**  $^1\text{H}$  NMR spectrum of 4,4'-bipyridine in  $\text{CDCl}_3$



**Figure A-46.**  $^{13}\text{C}$  NMR spectrum of 4,4'-bipyridine in  $\text{CDCl}_3$

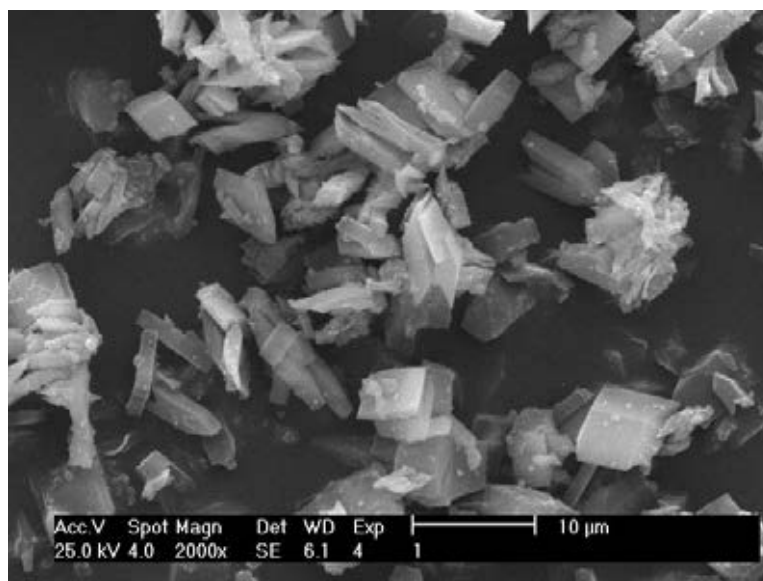


**Figure A-47.**  $^1\text{H}$  NMR spectrum of 4,4'-bipyridine in DMSO

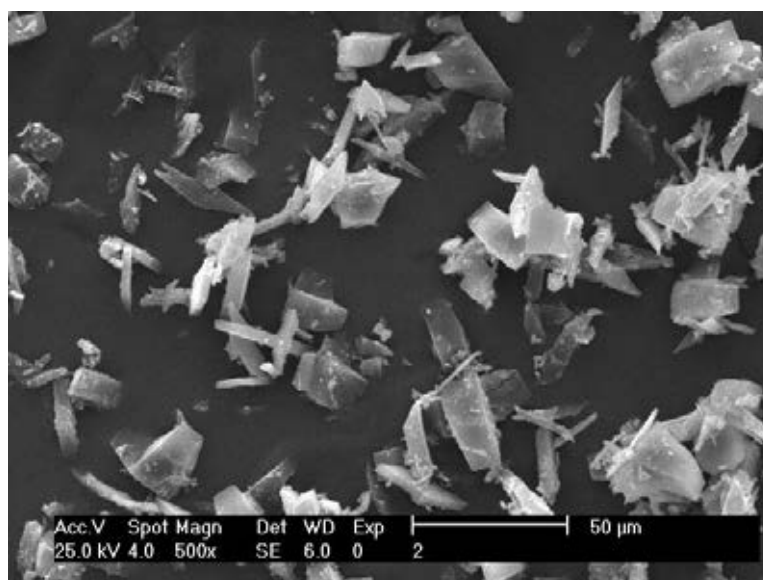


**Figure A-48.**  $^{13}\text{C}$  NMR spectrum of 4,4'-bipyridine in DMSO

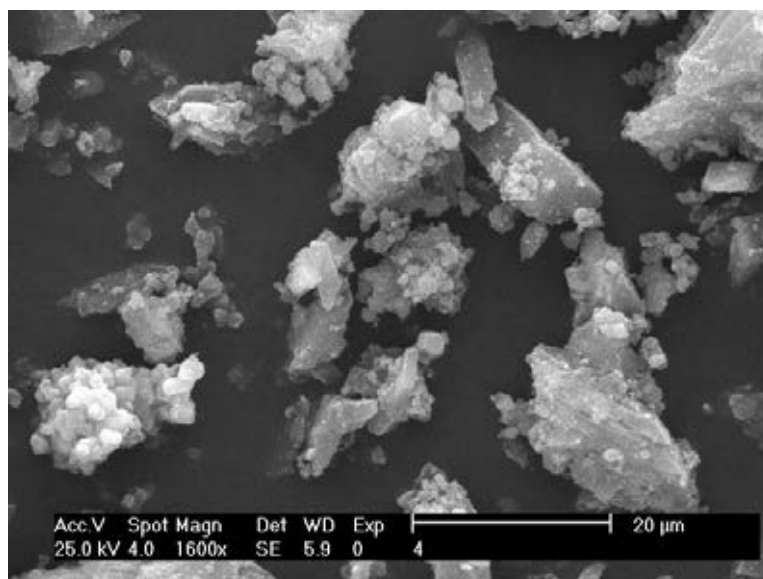
## **APPENDIX B**



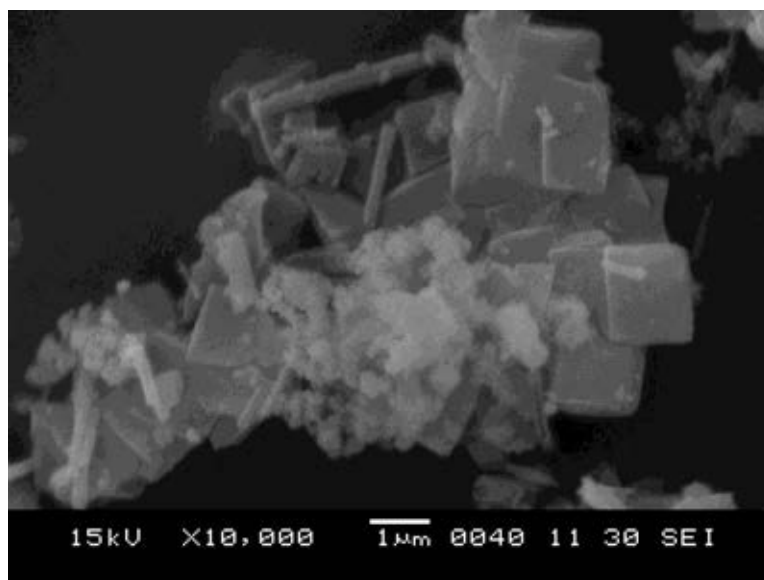
**Figure B-1.** SEM image of MOF 2A with magnification 2,000x



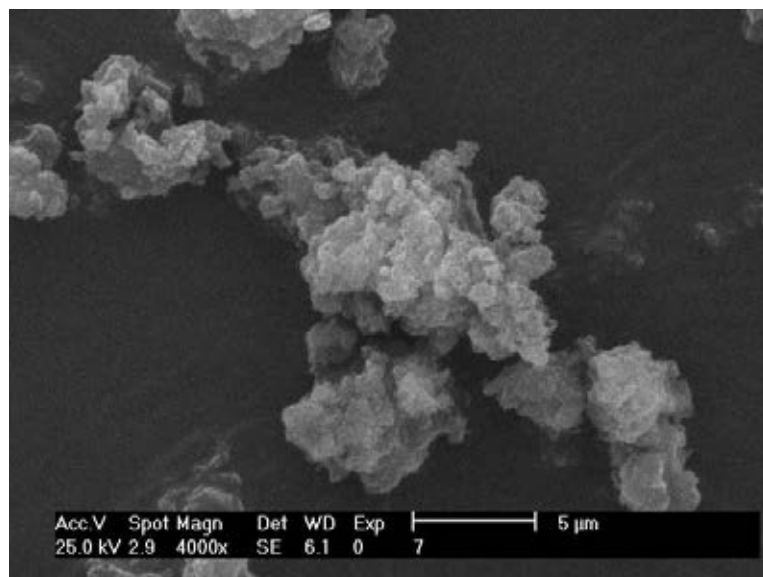
**Figure B-2.** SEM image of MOF 3A with magnification 500x



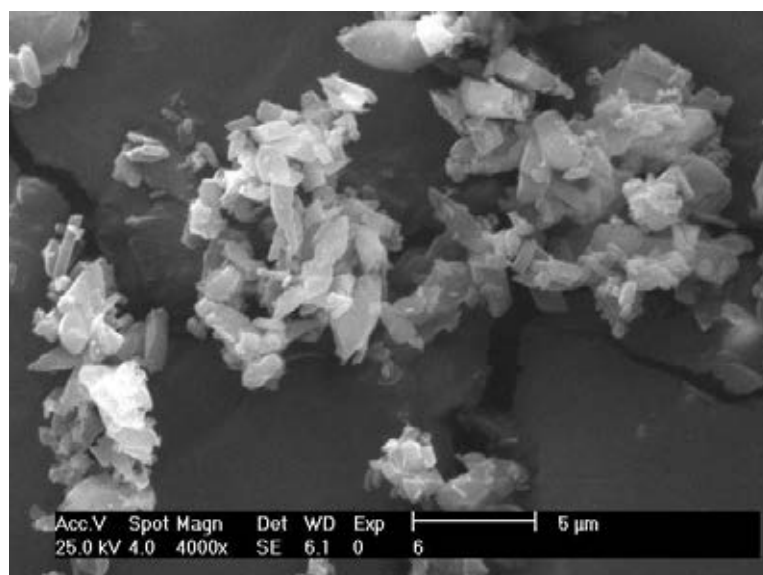
**Figure B-3.** SEM image of MOF 5A with magnification 1,600x



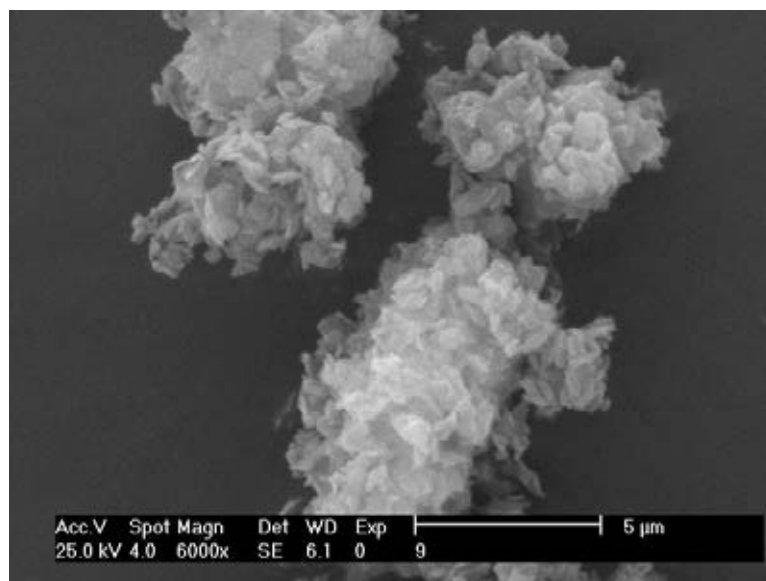
**Figure B-4.** SEM image of MOF 8A with magnification 10,000x



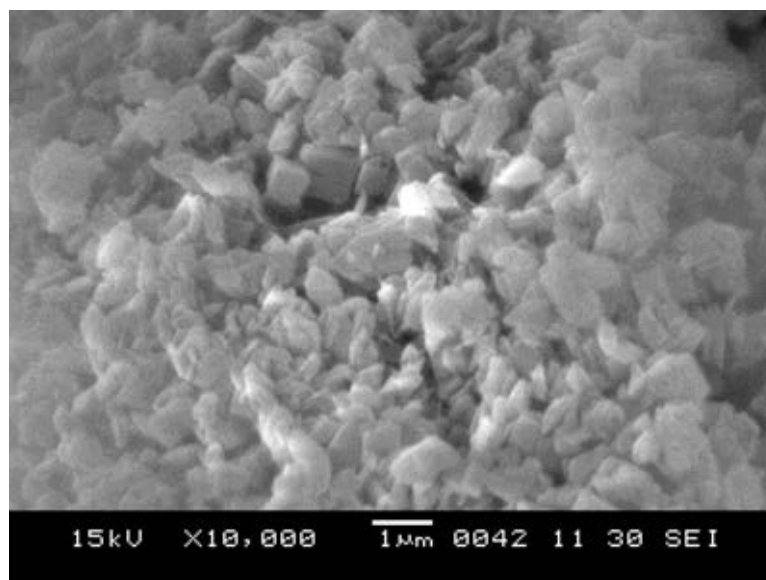
**Figure B-5.** SEM image of MOF **10B** with magnification 4,000x



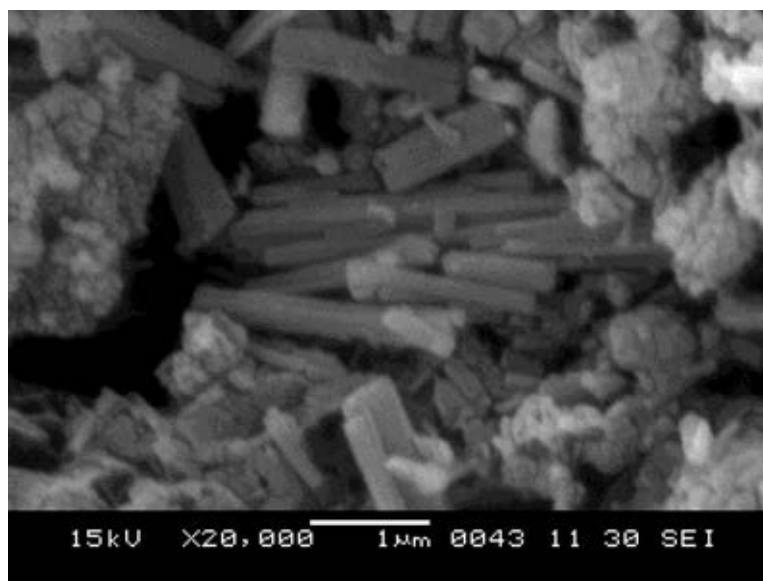
**Figure B-6.** SEM image of MOF **11B** with magnification 4,000x



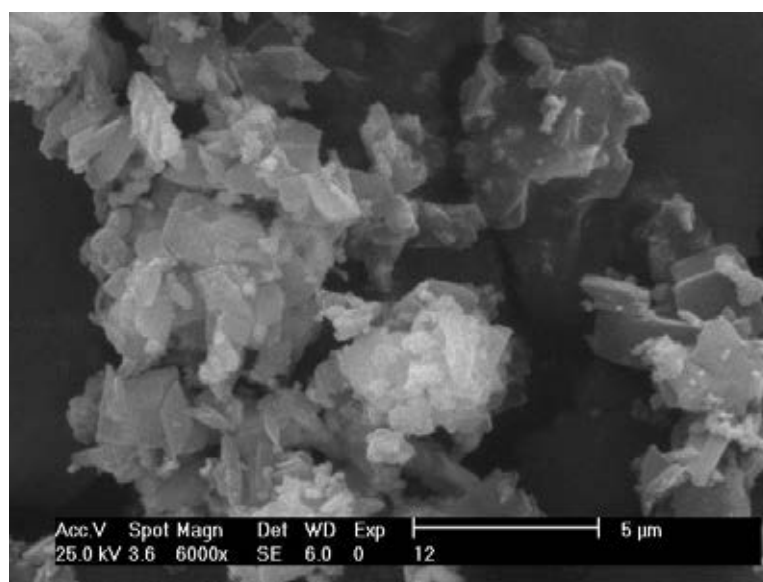
**Figure B-7.** SEM image of MOF 12B with magnification 6,000x



**Figure B-8.** SEM image of MOF 13B with magnification 10,000x

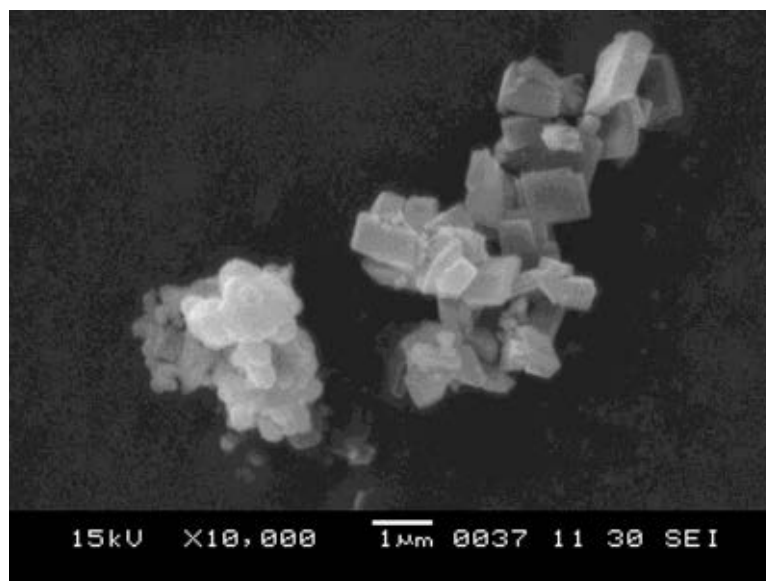


**Figure B-9.** SEM image of MOF **14B** with magnification 20,000x

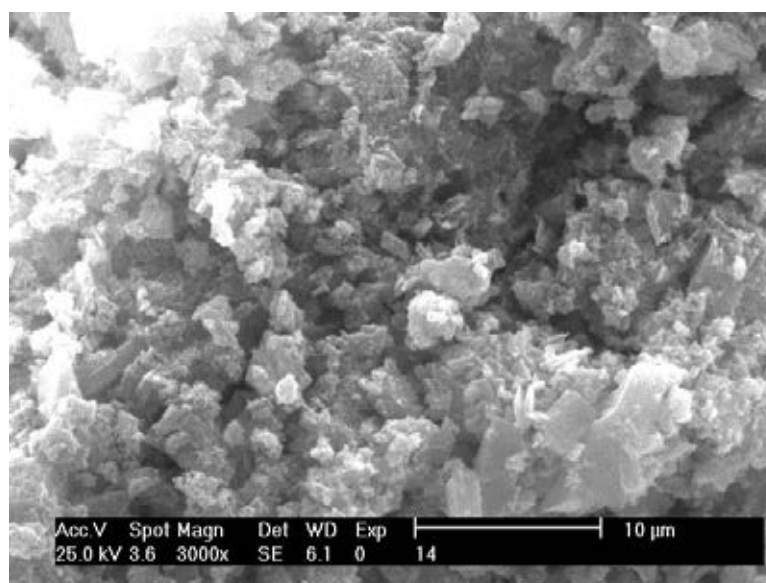


**Figure B-10.** SEM image of MOF **15B** with magnification 6,000x

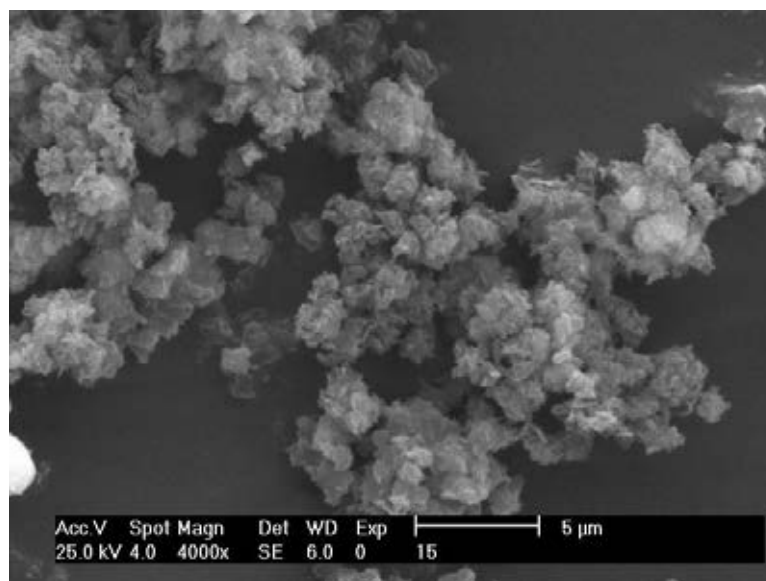




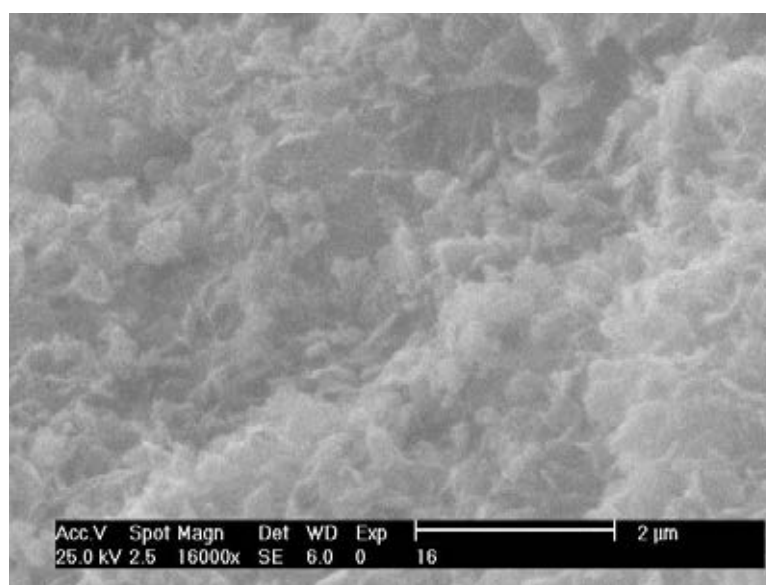
**Figure B-11.** SEM image of MOF 16C with magnification 10,000x



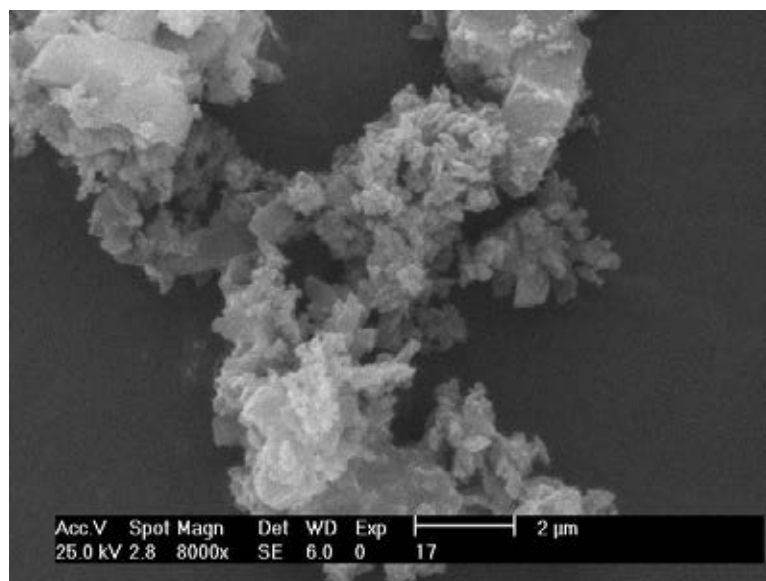
**Figure B-12.** SEM image of MOF 19C with magnification 3,000x



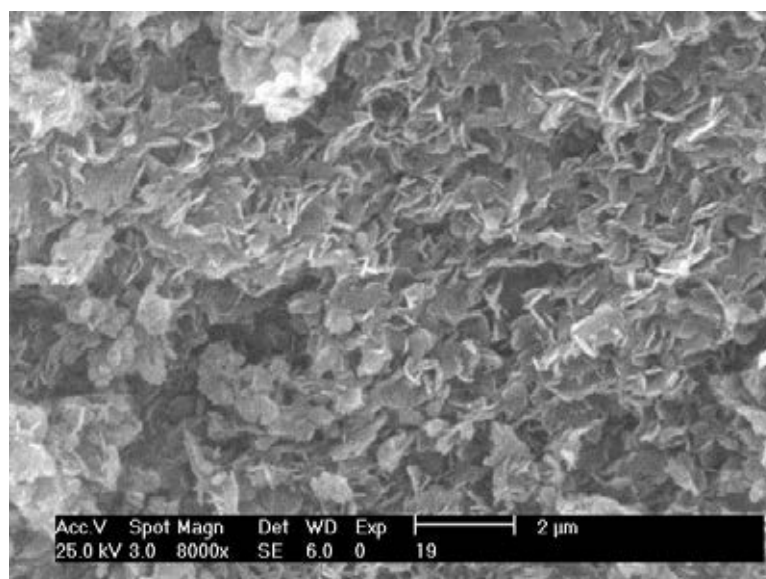
**Figure B-13.** SEM image of MOF 20C with magnification 4,000x



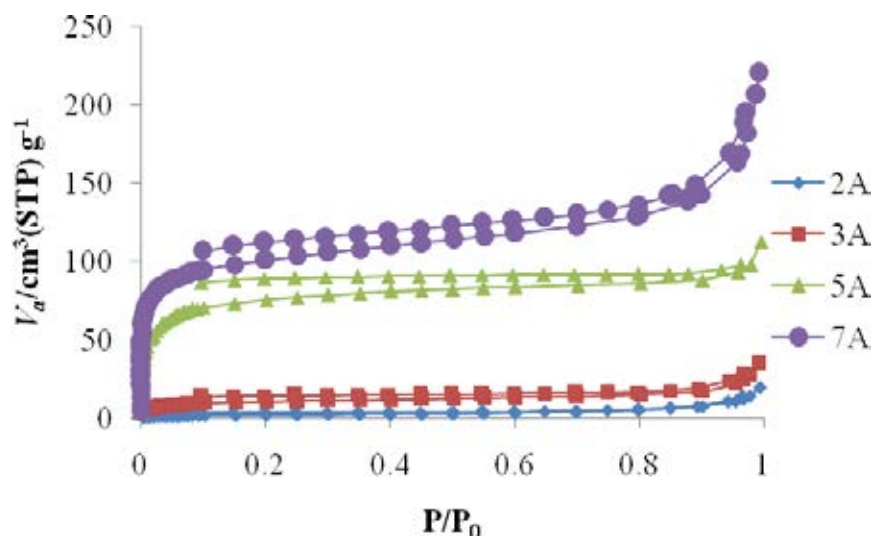
**Figure B-14.** SEM image of MOF 21C with magnification 16,000x



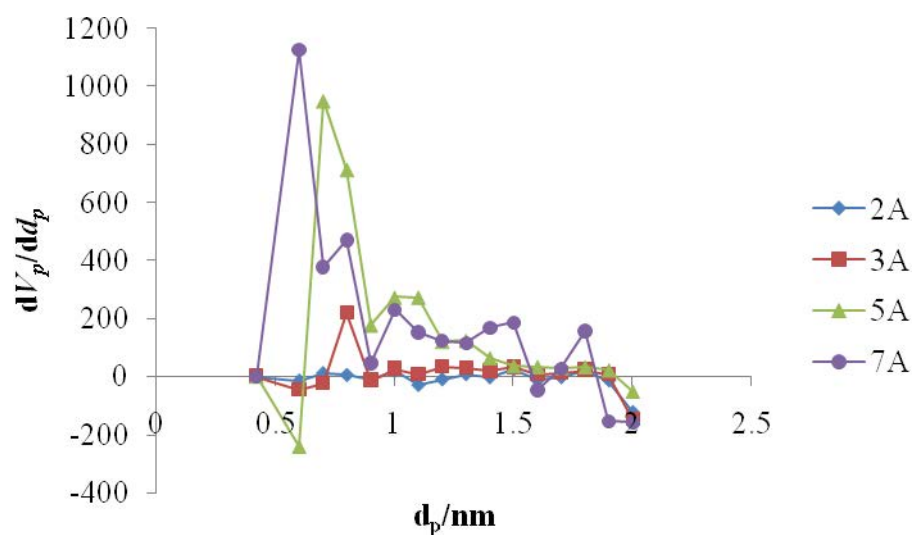
**Figure B-15.** SEM image of MOF 22C with magnification 8,000x



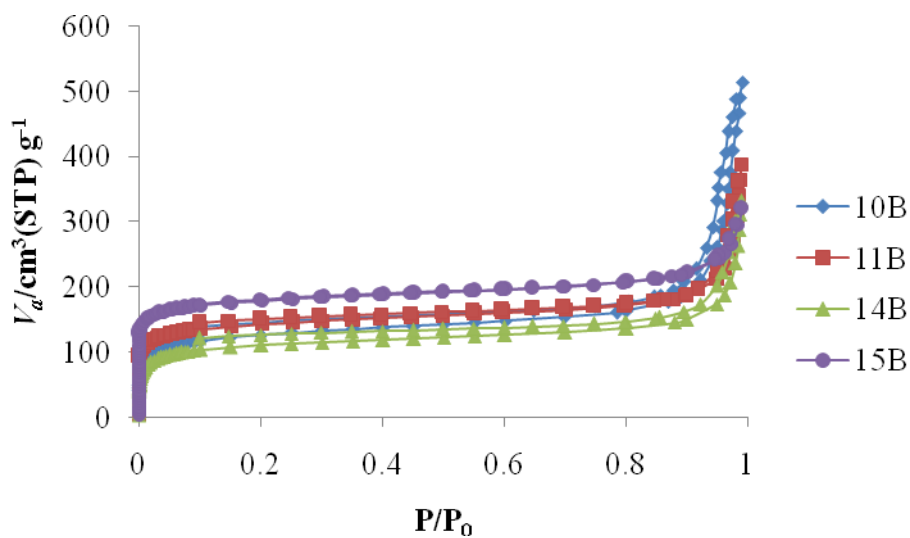
**Figure B-16.** SEM image of MOF 23C with magnification 8,000x



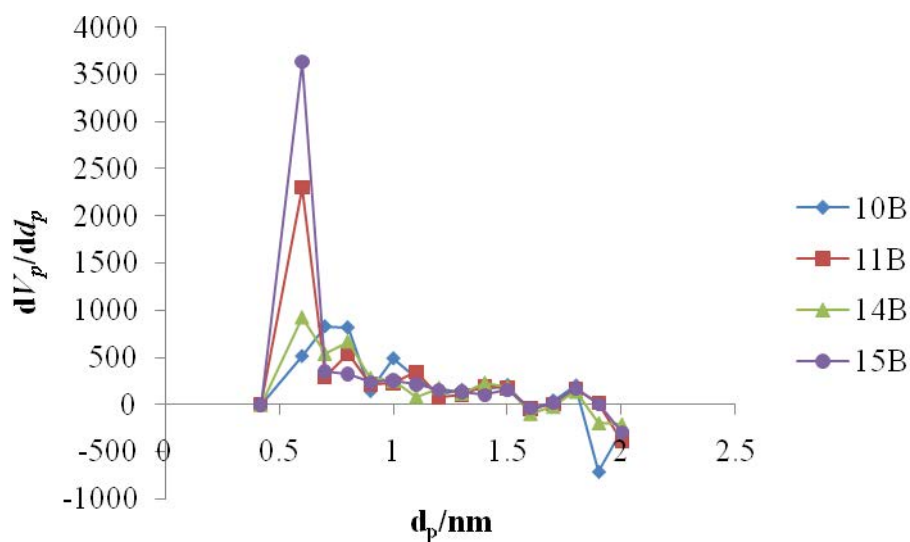
**Figure B-17.** Nitrogen adsorption-desorption isotherm of porphyrin-based MOFs synthesized via pathway A: **2A**, **3A**, **5A** and **7A**



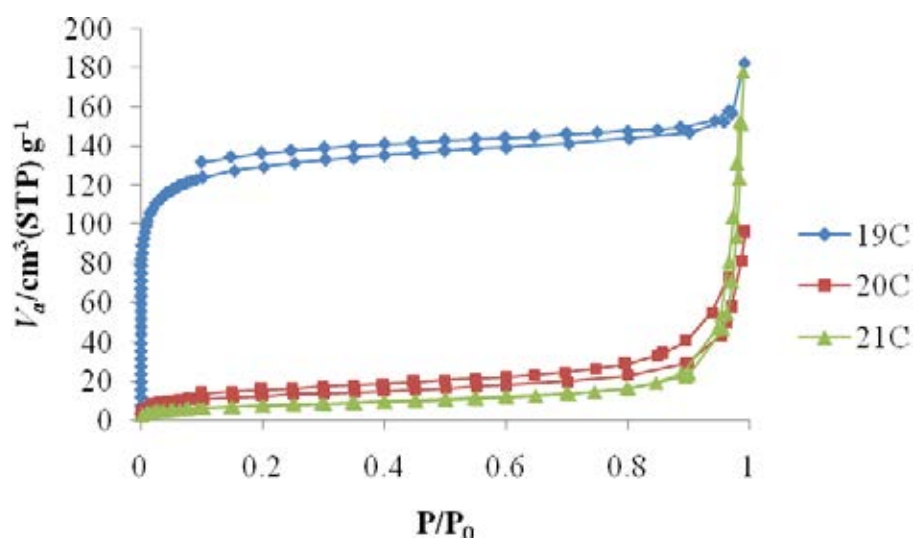
**Figure B-18.** MP pore-size distribution of porphyrin-based MOFs synthesized via pathway A: **2A**, **3A**, **5A** and **7A**



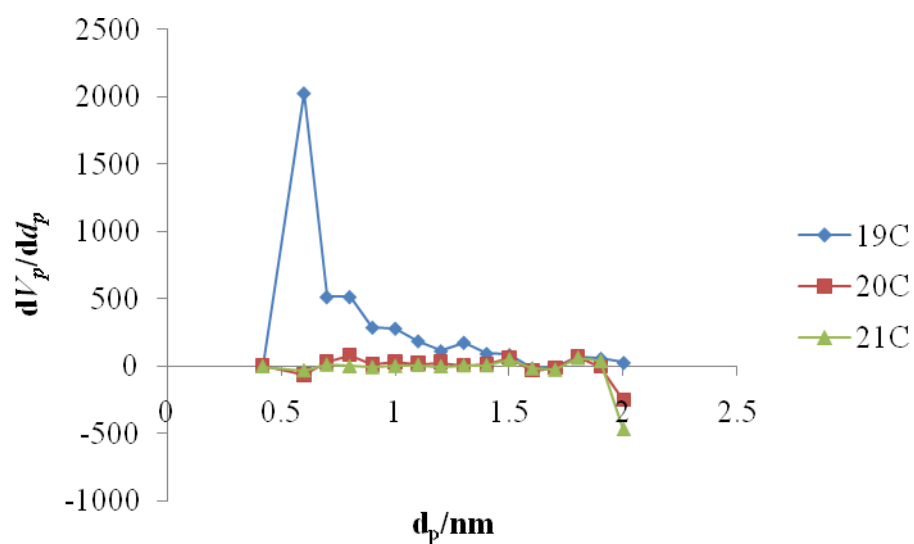
**Figure B-19.** Nitrogen adsorption-desorption isotherm of porphyrin-based MOFs synthesized via pathway B: **10B**, **11B**, **14B** and **15B**



**Figure B-20.** MP pore-size distribution of porphyrin-based MOFs synthesized via pathway B: **10B**, **11B**, **14B** and **15B**



**Figure B-21.** Nitrogen adsorption-desorption isotherm of porphyrin-based MOFs synthesized via pathway C: **19C**, **20C** and **21C**



**Figure B-22.** MP pore-size distribution of porphyrin-based MOFs synthesized via pathway C: **19C**, **20C** and **21C**

## VITA

Miss Salinthip Laokroekkiat was born on August 10, 1985 in Bangkok, Thailand. She got a Bachelor Degree of Chemistry from Faculty of Science at Chulalongkorn University, Bangkok in 2008 with getting the scholarship from Research Professional Development Project under the Science Achievement Scholarship of Thailand (SAST) Chulalongkorn University during 2004 to 2008.

After that, she was admitted into a Master Degree Program in Petrochemistry and Polymer Science, Faculty of Science, Chulalongkorn University, Bangkok in 2008 and completed the program in 2012. During the study in Master program, she got many scholarships: Teaching Assistant Scholarship from Chulalongkorn University during 2008 to 2010, Research fund from Center of Innovative Nanotechnology, Chulalongkorn University during 2009 to 2010 and Research Assistant Scholarship from Chulalongkorn University during 2010 to 2012.